2nd International Workshop

23th – 24th March 2015
Stuttgart, Germany

Integration of Point- and Area-wise Geodetic Monitoring for Structures and Natural Objects

Proceedings

Published by:
Siberian State University of Geosystems and Technologies
Institute of Engineering Geodesy, University of Stuttgart, Germany

2nd International Workshop

“Integration of Point- and Area-wise Geodetic Monitoring for Structures and Natural Objects”

Proceedings

23th – 24th March 2015

Organizers:
Institute of Engineering Geodesy, University of Stuttgart
Siberian State University of Geosystems and Technologies, Novosibirsk, Russian Federation

In collaboration with:
University of Applied Sciences Karlsruhe

Published by:

Alexander P. Karpik, Volker Schwieger, Argina Novitskaya, Otto Lerke

These proceedings can be ordered from:

rektorat@ssga.ru
sekretariat@ingeo.uni-stuttgart.de

ISBN: 978-3-00-049116-0

http://www.uni-stuttgart.de/ingeo/

Printed at Printing Laboratory, SSUGT
8, Plakhotnogo St., Novosibirsk, 630108

ORGANIZING COMMITTEE

Chairman:

Prof. Dr.-Ing. **Volker Schwieger**	Director, Institute of Engineering Geodesy, University of Stuttgart, Chair of FIG Commission 5 “Positioning and Measurement”, Germany
Prof. Dr. **Alexander P. Karpik**	Rector, Siberian State University of Geosystems and Technologies, Russian Federation

Vice Chairman:

Prof. **Vladimir A. Seredovich**	Vice Rector for Scientific and Innovative Activities, Siberian State University of Geosystems and Technologies, Russian Federation
Prof. Dr.-Ing. **Reiner Jäger**	University of Applied Sciences Karlsruhe, Institute of Geomatics, Honorary Professor of Siberian State Academy of Geodesy, Germany
Dr. **Ivo Milev**	Managing Director, “technet-rail 2010 GmbH”, Chair of FIG Commission 6 “Engineering Surveys”, Germany
Dr.-Ing. **Martin Metzner**	Deputy Director, Institute of Engineering Geodesy, University of Stuttgart, Germany

Secretaries:

Argina Novitskaya	Siberian State University of Geosystems and Technologies, Russian Federation
Ekaterina I. Gorokhova	Department of Engineering Geodesy and Mine Surveying, Siberian State University of Geosystems and Technologies, Russian Federation
Otto Lerke	Institute of Engineering Geodesy, University of Stuttgart, Germany

Contact

Prof. Dr.-Ing. **Volker Schwieger**
Institute of Engineering Geodesy
University of Stuttgart
Geschwister-Scholl-Str. 24D
70174 Stuttgart, Germany

Email:
volker.schwieger@ingeo.uni-stuttgart.de

Prof. **Vladimir A. Seredovich**
Vice Rector for Scientific and Innovative Activities
Siberian State University of Geosystems and Technologies
10, Plakhotnogo St.
Novosibirsk, 630108, Russian Federation
Email:
v.seredovich@list.ru

General information

Monitoring of structures and natural objects with regard to movements and deformations is one of the main tasks of engineering geodesy. The object of interest can be monitored with a specific measurement technique at specific individual points and at specific time. The point-based methods, like GNSS or total station, provide highly precise information for individually characterized points. The area-based methods, like Terrestrial Laser Scanning or Photogrammetry, provide the complete shape of the object with a high resolution but very often with a reduced accuracy. The accuracy and reliability of the area wise measurement methods can be improved through the precise point wise measurement methods. On the basis of those considerations the first international workshop took place in Novosibirsk, Russian Federation on 14. - 15. April 2014.

During the first workshop numerous monitoring objects and specific measurement techniques as well as area-wise evaluation methods were presented and discussed. Keywords like multi-sensor integration, change detection, geometric, semantic and dynamic modelling could be identified as future research fields.

On 23.- 24. March 2015 the second international workshop on "Integration of Point- and Area-wise Geodetic Monitoring for Structures and Natural Objects" will take place in Stuttgart, Germany. The event serves as an opportunity for further development of ideas and solutions with respect to monitoring tasks that were analyzed and discussed during the first meeting.

The main focus on the measurement side will be on Global Navigation Satellite Systems, Laser Scanning and Photogrammetry. 3-D Object Modelling and different integrated deformation analysis approaches will be the main part on the modelling and analysis side.

The objects under observation can be: Industrial and civilian, public utilities (hydro technical constructions, atomic and thermal power plants), mining plants, minery, shafts, tunnels, linear structures (highways, roads, pipelines, power transmission lines), landslides, glaciers, etc.

This workshop aims at strengthening the scientific elaboration among the Siberian State University of Geosystems and Technologies, the University of Stuttgart, the University of Applied Sciences Karlsruhe and the technet-rail 2010 GmbH. Mainly young scientists who present their researches and their projects will participate. Joint research activities should be identified and future projects should be developed.

TECHNICAL PROGRAM

MONDAY, 23.03.2015	
09:00 - 09:30	Registration of participants and visitors
09:30 - 10:00	Opening Ceremony of the workshop **2nd International workshop on “Integration of Point- and Area-wise Geodetic Monitoring for Structures and Natural Objects”** • Prof. **Stephan Staudacher,** Dean of Faculty for Aerospace Engineering and Geodesy, University of Stuttgart, Germany • **Christine Müller**, International Affairs, University of Stuttgart, Germany • Prof. **Vladimir A. Seredovich,** Siberian State University of Geosystems and Technologies, Russian Federation • Prof. **Volker Schwieger,** University of Stuttgart, Germany
10:00 - 11:00	**TECHNICAL SESSION 1**: **3-D Object Monitoring and Modelling**
	Chair: Prof. **Vladimir A. Seredovich**, Siberian State University of Geosystems and Technologies, Russian Federation **Andrey V. Sementsov**, **Vyacheslav N. Nikitin, Alexander Yu. Chermoshentsev**, Siberian State University of Geosystems and Technologies, Russian Federation **3D Object Modelling from Images taken by Non-Metric Digital Cameras: Problems and their Solutions** **Reiner Jäger,** University of Applied Sciences Karlsruhe, Germany **Geometry & Gravity Space related 3D Integrated Geomonitoring - Feasilibity, Advantages and Implementation into the GOCA-System** *POSTER CONTRIBUTION:* ***Evgeny I. Avrunev, Elena S. Plyusnina****, Siberian State University of Geosystems and Technologies, Russian Federation,* ***Deformation Model-Building for Engineering Objects***
11:00 - 11:30	**COFFEE BREAK**
11:30 - 12:30	**Dmitry N. Vetoshkin, Sergey R. Gorobtsov**, Siberian State University of Geosystems and Technologies, Russian Federation **3D Monitoring of Fixed Assets under Construction for the Purpose of Consistent Cadastral Registration** **Tatyana Yu. Bugakova, Mariya M. Shlyakhova, Alexander V. Seredovich, Andrei V. Ivanov, Oksana R. Miftakhudinova,** Siberian State University of Geosystems and Technologies, Russian Federation **3D Modelling and Visualizing Surface Deformations of Man-Made Objects** *POSTER CONTRIBUTION:* ***Alexey V. Dubrovsky, Olesya I. Malygina****, Siberian State University of Geosystems and Technologies, Russian Federation* ***Topographic Monitoring on Oil-and-Gas Fields***

12:30 - 13:30	**LUNCH**
13:30 - 15:00	**TECHNICAL SESSION 2: GNSS- SOLUTIONS I**
	Chair: Prof. **Volker Schwieger**, University of Stuttgart, Germany **Julia Diekert,** University of Applied Sciences Karlsruhe, Germany **New Developments and Applications for Low Cost GNSS/MEMS-based Monitoring** **Alexander P. Karpik, Leonid A. Lipatnikov,** Siberian State University of Geosystems and Technologies, Russian Federation **Application of Low Cost GNSS Equipment for Geodetic Monitoring of Engineering Structures and Natural Objects** **Ashraf Abdallah,** Institute of Engineering Geodesy, University of Stuttgart, Germany **The Effect of Convergence Time on the Static- PPP Solution**
15:00 - 15:30	**COFFEE BREAK**
15:30 - 17:00	**TECHNICAL SESSION 3: GNSS- SOLUTIONS II**
	Chair: **Andrei Ivanov**, Ph.D., Siberian State University of Geosystems and Technologies, Russian Federation **Joël van Cranenbroeck**, Creative Geosensing sprl-s, Belgium, Europa **Mariya M. Shlyakhova**, Siberian State University of Geosystems and Technologies, Russian Federation **Significant Contribution of Compass/ Beidou New Chinese GNSS Constellation for Monitoring Applications** **Wei Zhang, Li Zhang**, University of Stuttgart, Germany **Time Series Analysis of Different Shieldings of Low Cost GPS Receiver** **Li Zhang**, University of Stuttgart, Germany **Reducing Multipath Effects by Considering Spatial Correlations**
17:00 - 18:00	**TIME FOR DISCUSSIONS DAY 1**

TUESDAY, 24.03.2015	
09:00 - 10:30	**TECHNICAL SESSION 4: Laser Scanning Applications**
	Chair: Prof. **Reiner Jäger**, University of Applied Sciences Karlsruhe, Germany **Maxim A. Altyntsev, Vladimir A. Seredovich,** Siberian State University of Geosystems and Technologies, Russian Federation **Accuracy Analysis of DEM Generation and Computing Volumes of Excavation and Rock Fillings by Laser Scanning Data**

	Ekaterina I. Gorokhova, Siberian State University of Geosystems and Technologies, Russian Federation **Geomonitoring of Engineering Structures and Forecasting Their Deformations Using Laser Scanning Data** **Desislava Staykova, Nico Zill,** technet-rail 2010 GmbH, Germany **Kinematic and Static Laser Scanning Methods for Infrastructure Monitoring**
10:30 - 11:00	**COFFEE BREAK**
11:00 - 12:30	**TECHNICAL SESSION 5: Modeling for Laser Scanning**
	Chair: Dr. **Ivo Milev**, technet-rail 2010 GmbH, Germany **Stephanie Kauker**, University of Stuttgart, Germany **Approach for a Synthetic Covariance Matrix for Terrestrial Laser Scanner** **Bimin Zheng, Lifan Zhang,** University of Stuttgart, Germany **Denoising of the Point Cloud for Deformation Analysis**
12:30 - 13:30	**LUNCH**
13:30 - 15:00	**TECHNICAL SESSION 6: Geometric and Deformation Analysis**
	Chair: **Joël van Cranenbroeck**, Creative Geosensing sprl-s, Belgium **Sergey G. Mogilny,** Prydniprovs'ka State Academy of Civil Engineering and Architecture, Department of Land Management, Road-Building and Geodesy, Ukraine, **Andrii A. Sholomytskyi, Vladimir A. Seredovich, Alexander V. Seredovich, Andrei V. Ivanov,** Siberian State University of Geosystems and Technologies, Russian Federation **The Analysis of Methods for Determining the Geometric Parameters of Rotating Machines** **Annette Schmitt,** University of Stuttgart, Germany **Deformation Analysis of a Timber Pavilion** *POSTER CONTRIBUTIONS:* ***Boris T. Mazurov***, *Siberian State University of Geosystems and Technologies, Russian Federation* ***Fawzi Zarzoura, Samira Ahmed***, *Mansoura University, Egypt* ***Deformation Analysis of Cable-Stayed Bridges Using Neural Networks*** ***Igor G. Vovk***, *Siberian State University of Geosystems and Technologies, Russian Federation* ***Positioned Displacements of Engineering Constructions and Natural Objects Obtained from Geodetic Monitoring***
14:00 - 14:30	**COFFEE BREAK**

14:30 - 15:30	**TECHNICAL SESSION 7: Optical Methods for Street Mapping**
	Chair: Dr. **Martin Metzner**, University of Stuttgart, Germany **Rolf Kemper-Böninghausen,** Emscher Genossenschaft**, Nico Zill,** technet-rail 2010 GmbH, Germany **Street Inventory Based on Mobile Laser Scanning** **Bara Al-Mistarehi,** Institute of Engineering Geodesy, University of Stuttgart, Germany **Automated Detection for Pavement Crack for Mobile Mapping Data** *POSTER CONTRIBUTION:* ***Tatyana Yu. Bugakova****, Siberian State University of Geosystems and Technologies, Russian Federation* ***Modelling of Spatio-Temporal Variations for Engineering Structures and Natural Objects by Geodetic Monitoring Data***
15:30 - 16:00	**DISCUSSIONS AND CONCLUSIONS, CLOSURE OF THE WORKSHOP**

Content

TECHNICAL SESSION 1: 3-D OBJECT MONITORING AND MODELLING 11

3D Object Modeling from Images Taken by Non-Metric Digital Cameras: Problems and Their Solutions 12

Andrey V. Sementsov, Vyacheslav N. Nikitin, Alexander Yu. Chermoshentsev

Geometry & Gravity Space related 3D Integrated Geomonitoring - Feasibility, Advantages and Implementation into the GOCA-System 19

Reiner Jäger

Deformation Model-Building for Engineering Objects.. 20

Evgeny I. Avrunev, Elena S. Plyusnina

3D Monitoring of Fixed Assets under Construction for the Purpose of Consistent Cadastral Registration 26

Dmitry N. Vetoshkin, Sergey R. Gorobtsov

3D Modelling and Visualizing Surface Deformations of Man-Made Objects 33

Tatyana Yu. Bugakova, Maryia M. Shlyakhova, Alexander V. Seredovich, Andrei V. Ivanov, Oksana R. Miftakhudinova

Topographic Monitoring on Oil-and-Gas Fields 38

Alexey V. Dubrovsky, Olesya I. Malygina

TECHNICAL SESSION 2: GNSS – SOLUTIONS I 44

New Developments and Applications for LowCost GNSS/MEMS based Monitoring.................................... 45

Julia Diekert

The Effect of Convergence Time on the Static- PPP Solution... 58

Ashraf Abdallah

TECHNICAL SESSION 3: GNSS – SOLUTIONS II 70

Time Series Analysis of Different Shieldings of Low-Cost GPS Receiver 71

Wei Zhang, Li Zhang

Reducing Multipath Effects by Considering Spatial Correlation... 83

Li Zhang

TECHNICAL SESSION 4: LASER SCANNING APPLICATIONS.. 84

Accuracy Analysis of DEM Generation and Computing Volumes of Excavation and Rock Fillings by Laser Scanning Data... 85

Maxim A. Altyntsev, Vladimir A. Seredovich

Geomonitoring of Engineering Structures and Forecasting Their Deformations Using Laser Scanning Data . 91

Ekaterina I. Gorokhova

Kinematic and Static Laser Scanning Methods for Infrastructure Monitoring 97

Desislava Staykova, Nico Zill

TECHNICAL SESSION 5: MODELLING FOR LASER SCANNING 101

Approach for a Synthetic Covariance Matrix for Terrestrial Laser Scanner 102

Stephanie Kauker, Volker Schwieger

Denoising of the Point Cloud for Deformation Analysis 111

Lifan Zhang, Bimin Zheng

TECHNICAL SESSION 6: GEOMETRIC AND DEFORMATION ANALYSIS 118

The Analysis of Methods for Determining the Geometric Parameters of Rotating Machines 119

Sergey G. Mogilny, Andrii A. Sholomytskyi, Vladimir A. Seredovich, Alexander V. Seredovich, Andrei V. Ivanov

Deformation Analysis of a Timber Pavilion 131

Annette Schmitt

Deformation Analysis of Cable-Stayed Bridges Using Neural Networks 138

Boris Mazurov

Positioned Displacements of Engineering Constructions and Natural Objects Obtained from Geodetic Monitoring 144

Igor G. Vovk

TECHNICAL SESSION 7: OPTICAL METHODS FOR STREET MAPPING 150

Street Inventory Based On Mobile Laser Scanning 151

Rolf Kemper-Böninghausen, Nico Zill

Automated Detection for Pavement Crack for Mobile Mapping Data 157

Bara' AL-Mistarehi, Volker Schwieger

Modelling of Spatio-Temporal Variations for Engineering Structures and Natural Objects by Geodetic Monitoring Data 170

Tatyana Yu. Bugakova

LIST OF AUTHORS 176

TECHNICAL SESSION 1: 3-D OBJECT MONITORING AND MODELLING

3D Object Modeling from Images Taken by Non-Metric Digital Cameras: Problems and Their Solutions

Andrey V. Sementsov, Vyacheslav N. Nikitin, Alexander Yu. Chermoshentsev
Siberian State University of Geosystems and Technologies, Russian Federation

Abstract
At the given stage of technological development, three-dimensional modeling of real objects is widespread in many fields of human activity. The article describes one of the main problems encountered when modeling by means of non-metric digital camera. Original solution of this problem was suggested, theoretically proved and confirmed in practice.

Keywords
3D- modeling, non-metric cameras, calibration

1 INTRODUCTION

Due to the prevalence of digital cameras, close-range photogrammetry experienced a rebirth. It is increasingly used for three-dimensional modeling of objects. In comparison with other methods of survey such as laser scanning and ground survey via total stations this method is more available since it does not require expensive equipment, but allows construction a model of the object with a given accuracy.
Close-range photogrammetry is used not only in the topography, but also in other fields of science and technology due to the speed of photography in conjunction with the objectivity and accuracy of the results. For example this method is successfully used in construction surveying in the mountains when surveying steep slopes and rocky cliffs along the river banks. Images can be successfully used to determine the volume of materials, evaluate the situation on the coal mines and perform the analysis of deformation structures.
In general the following scopes of close-range photogrammetry applications can be distinguished:

- engineering;
- archaeology;
- architecture & preservation;
- biology;
- geology;
- accident reconstruction & forensics;
- films, gaming and animation.

Images used for these applications are taken by non-metric digital cameras.

2 PARTICULARITIES OF USING NON-METRIC CAMERAS

Non-metric digital cameras are characterized by low cost and weight, compactness, efficiency of taking image and control of its quality, but the images are especially influenced by systematic errors due to distortion of bundles and therefore are not originally suit to solve measuring tasks.
In addition to obtain precise results high-quality images should be used. Achieving this task can be provided by using cameras equipped with a sufficiently large CCD and lens with good optical properties.

2.1 General Approaches to Camera Calibration

Any lenses are subjected to aberrations. To restore a bundle for the purpose of taking into account the distortion of images their parameters and elements of interior orientation have to be determined. This process is called calibration.

Calibration of cameras used in close-range survey can be divided into two main approaches - a self-calibration and calibration by test object.

Self-calibration is performed within the process of solving the main problem, for example construction of three-dimensional model of the structure. This approach saves time because the required parameters are determined by the same working images. However for reliable determination of the calibration parameters entire field of every image should be relatively equally covered by the points. This condition is not always kept in this approach. Also the required height difference of points and the availability of reference data are not always provided to properly eliminate deformation of images. In addition for large lens distortion self-calibration may not work. Thus, the calibration is not always feasible.

Independent calibration process includes taking images of a special calibration test object. It creates special conditions of exposure, allowing more reliable and accurate determination of the required parameters.

Traditional methods of calibration assumes taking images of the spatial test object consisting of a large number of points whose coordinates are determined by geodetic methods. In this case height difference between points must exceed 20% of the distance.

In modern software for three-dimensional modeling calibration via a flat test objects is realized. The examples of the test objects are presented in Figure 1:

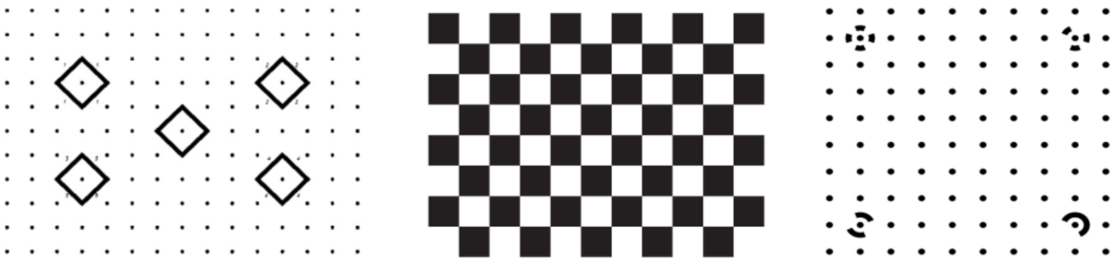

a) **b)** **c)**

Figure 1: Examples of flat test-objects:
a) Topcon Image master
b) GML Camera Calibration Toolbox
c) PhotoModeler

Due to the fact that these sheets have a size less than A1, it can be concluded that shooting conditions differ from the real objects.

However, in practice there are cases when self-calibration is used in order to save time and money. This ultimately affects the resulted accuracy of the work.

2.2 Methods Of Non-Metric Cameras Calibration Used At The Department of Physical geodesy And Remote

On the basis of the Department of Physical Geodesy and Remote Sensing of the Siberian State University of Geosystems and Technologies (SSUGT) original version of calibration has been proposed.

For this purpose special calibration test object was developed and created. The main feature of such test object is composition of patterns (Figure 2).

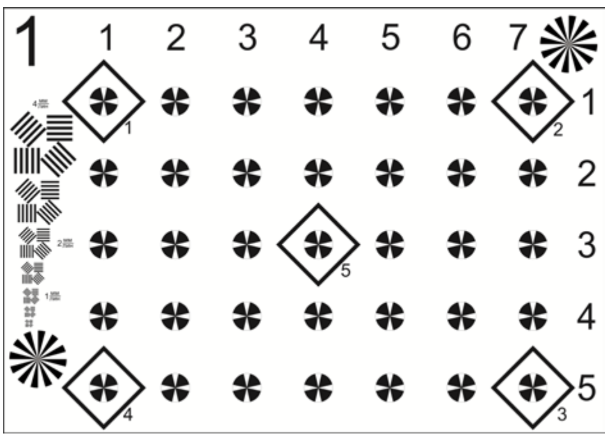

Figure 2: Pattern of test-object SSUGT

Each sheet contains 35 marks in the form of a Maltese cross. Five marks have special labeling.
Round mark is chosen as a shape of the point of test object (Figure 3) It is optimally suited for automatic identification. Combination with a Maltese cross provides comfortable manual identification of points in the image.

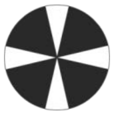

Figure 3: Shape of the mark of test-object

Except marks, each sheet contains radial test targets and sets of dashed targets that allows determining camera resolution image and its field distribution in parallel with the calibration in order to correctly determine the accuracy of the measurements.
The use of patterns allows creating test objects of different shapes and sizes to provide the most optimal shooting conditions close to real operating conditions, such as increasing the distance between the camera and the subject. An example of such test-object located in the room is shown in Figure 4.

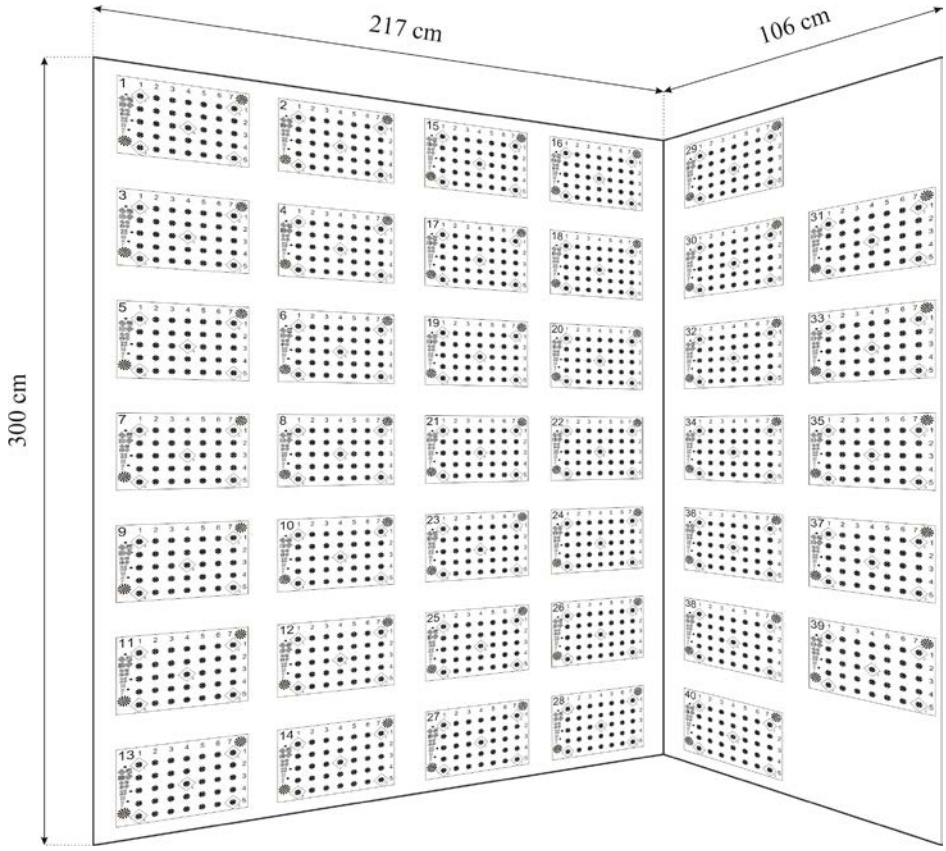

Figure 4: The scheme of the test object SSUGT

This test object satisfies the following requirements:
- does not require much labor and financial costs;
- rapid to set;
- provides greater density of points (1400 marks, 200 with special marking).

Photographing carried out from one center to obtain nine images with a slope of the optical axis according to the scheme (Figure 5).

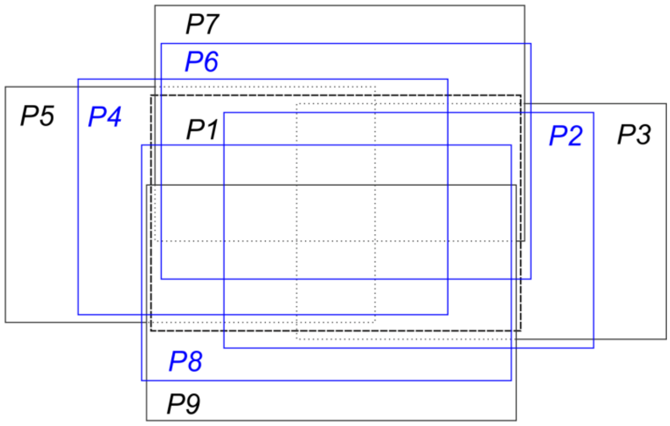

Figure 5: Scheme of the mutual arrangement of nine images when shooting from one point in space

It should be noted that when turning camera on the tripod head the center of photographing will be shifting as shown in Figure 6 and Figure 7.

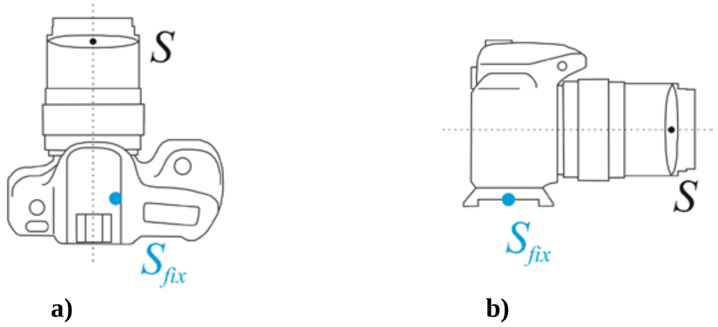

Figure 6: Discrepancy between the center of photograph and the point of mounting camera on a tripod: a) top view; b) side view

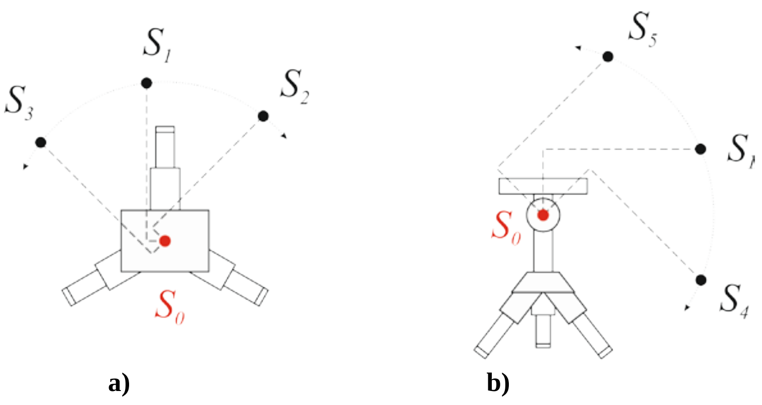

Figure 7: The shift of the center of photograph with respect to the point of rotating the camera on a tripod: a) in the horizontal plane; b) in a vertical plane

Obviously the centers of photographs during rotation of camera will be disposed on spherical surface (Figure 8).

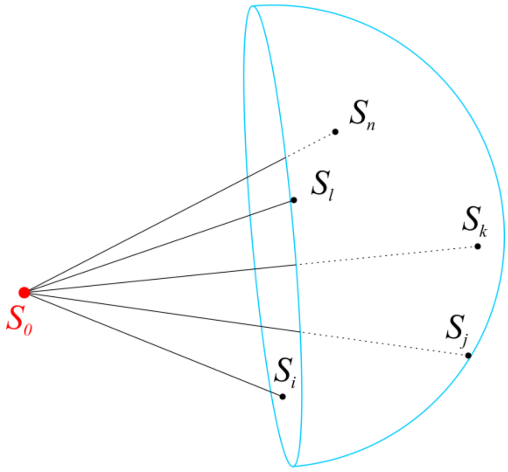

Figure 8: Position of the centers of the photographs relative to the point of rotating tripod head

In general the mathematical model of the tripod can be described by the following formula

$$S_i = S_0 + A_i \cdot l \ , \qquad (1)$$

where S_i - the coordinates of the i-th center of the photograph; S_0 - coordinates of the point of rotation of the tripod head; A_i - the transition matrix from the spatial coordinate system in the image to an external coordinate system; l – displacement vector of the center of photograph with respect to the point of rotation of the tripod head in the spatial coordinate system.

For calibration of digital cameras by the developed technique (Figure 9) it is necessary to fulfill the following conditions:

- apply mathematical model of the tripod according to formula (1) as an additional geometric conditions;
- use at least four images to determine parameters of the sphere along which the center of photograph is moving;
- use the condition of collinearity instead of equality of coordinates in the transformed images;
- set an additional condition on the placement points of test object, such as the condition of the plane $aX + bY + cZ + d = 0$.

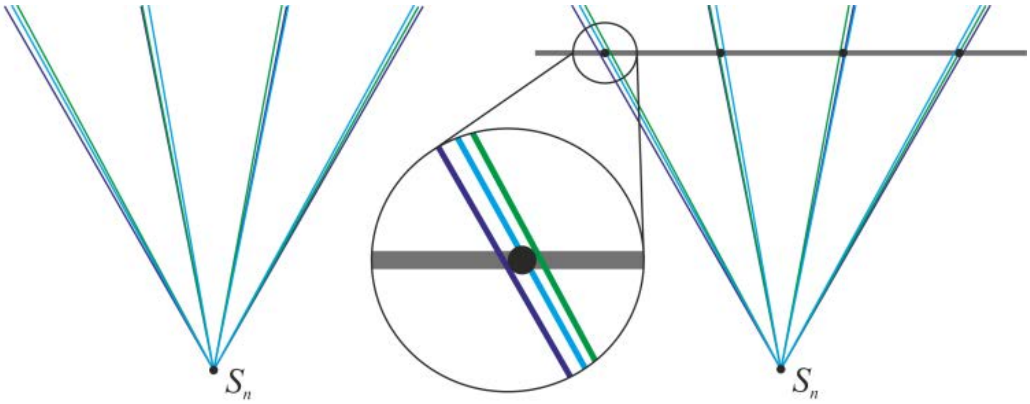

a) **b)**

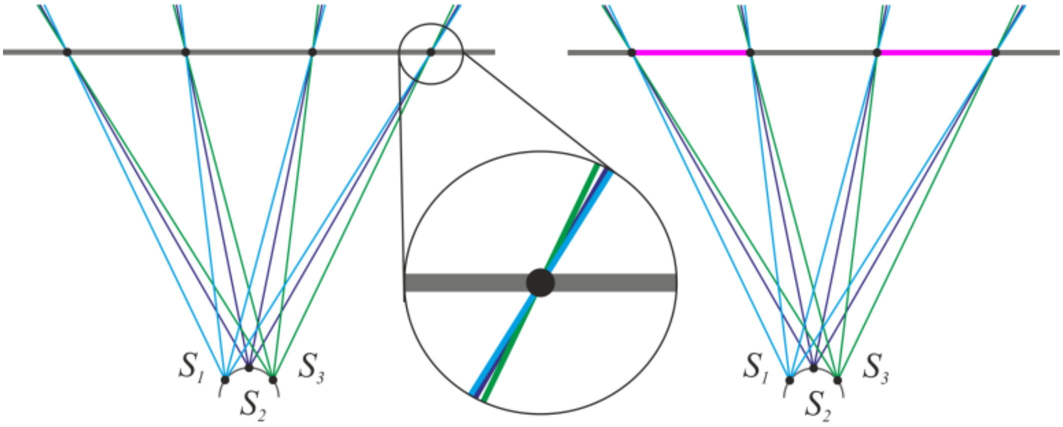

c) d)

Figure 9: The process of determining calibration parameters using a mathematical model of the tripod: a) solution of the system under the condition of equality of the coordinates in the transformed images; b) calculation of the approximate coordinates of the points of the test object based on the condition of placement of points on the test object; c) solution of the system under the condition of collinearity with the use of a mathematical model of the tripod head; d) using additional geometric conditions on the mutual arrangement of the points of the test object

Measurement of corresponding points and data processing (Figure 10) is performed in software developed at the Department of Photogrammetry and Remote Sensing.

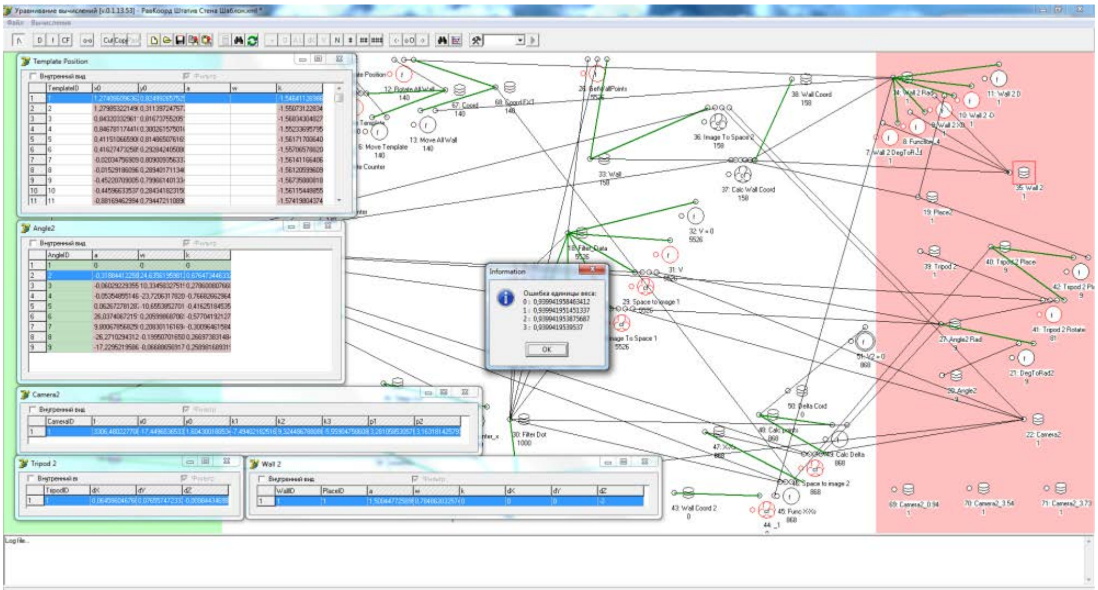

Figure 10: Data processing in a computing environment Equilibrium

The result of processing is information about parameters of distortion depending on the chosen model and elements of interior orientation.

The correctness of the proposed method was confirmed in practice. During the experiments the parameters of calibration were used for recovering a bundle comparable with the bundles recovered by traditional methods of calibration: spatial test object with the coordinates of the points whose coordinates were accurately determined by geodetic methods and images of the night sky.

3 CONCLUSIONS

When using images taken by non-metric digital cameras for measuring tasks it is necessary to perform the calibration. Sensitivity to the presence of significant systematic errors, conditions of taking images and the redistribution of errors due to deformation of the model in the adjustment does not allow using self-calibration as a reliable and basic calibration method. For creating high-accurate models independent calibration should be performed. The presented method allows performing calibration which could be compared with traditional methods. Thus it has more flexibility at the expense of using new test object, additional geometric conditions and special software.

REFERENCES

Journal articles:

ALCHINOV, A.I.: *Terrestrial digital photography*, Geoprofi, 4/2006, p.13-15, 2006.

NIKITIN, V.N., SEMENTSOV, A.V.: Camera Calibration using images of flat test object, Geodesy and Aerophotosurveying, 2/ 2014. p. 71–80, 2014.

NIKITIN, V.N., SEMENTSOV, A.V.: Using additional geometric conditions in solving problems of geodesy and photogrammetry, Vestnik SGGA, 4/2012, p. 41-45, 2012.

NIKITIN, V.N., SEMENTSOV, A.V.: Definition of resolution of the for oblique images using radial test targets, Interexpo Geo-Siberia-2012, V.1/2012, p. 52-57, 2012.

NIKITIN, V.N., SEMENTSOV, A.V.: Experience of orthophoto construction by large-scale aerial photographs taken with nonmetric digital camera, Interexpo Geo-Siberia-2013, 1/2013, p.12-18, 2013.

NIKITIN, V.N., NIKOLAEVA, T.V.: Calibration of digital non metric camera on the images of the star sky, Interexpo Geo-Siberia-2013, 1/2013, p.12-18, 2013.

RAKOV, D.N., NIKITIN, V.N.: Choosing a digital non-metric camera for unmanned aerial complex. Interexpo Geo-Siberia-2012, V.1/2012, p. 27-36, 2012.

SEMENTSOV, A.V.: Camera calibration without using solid reference data, Geodesy and cartography, 4/2014, p. 26-30, 2014.

SEMENTSOV, A.V.: Development of the test-object for digital camera calibration, Interexpo Geo-Siberia-2012, 1/2012, p.60-65, 2012.

SEMENTSOV, A.V., NIKITIN, V.N.: Influence of nonrigorous observance of geometrical conditions on the accuracy of interior orientation elements determination at cameras calibration, Interexpo Geo-Siberia-2014, 1/2014, p.73-81, 2014.

USTAVICH, G.A. POSHIVAYLO, Ya.G.: About the application of non-metric digital cameras for geodetic measurements, Geodesy and cartography, 8/2005, p. 19-24, 2005.

Geometry & Gravity Space related 3D Integrated Geomonitoring - Feasibility, Advantages and Implementation into the GOCA-System

Prof. Dr.-Ing. Reiner Jäger
Institute of Applied Research, University of Applied Sciences Karlsruhe, Germany

Abstract

Since its standardization in the 1970ies, geodetic monitoring is based on network adjustment, using the observations of terrestrial sensors (total-stations, levelling instrumentation), followed by the use of GNSS results (baselines, networks). Traditionally the network adjustment was carried out by mapping the 3D contents of the above sensor observations into a vertical and a horizontal component. This leads to the separation of the 3D-geometry into a 1D and a 2D network, and is not always completely free from simplified assumptions concerning the reductions from 3D to (1D/2D). The splitting into 1D/2D should however always be an option for the above standard sensor types, as it is even compulsory in geo-monitoring software in case of spirit or hydrostatic levelling networks (e.g. for a subsidence monitoring), where the following 3D network adjustment types would not work.

There are however several reasons to extend the spectrum of geodetic network approaches at present to the so-called integrated 3D geometry & gravity field related network adjustment, which dates back to the 1980ies, but was so to say forgotten, when GNSS came up. Reading $\mathsf{l} = \mathsf{l}(\mathbf{x}, W(\mathbf{x}, \mathbf{p}))$, any scalar or vector observation l is regarded here as a function of the 3D space coordinates **x** and the gravity potential W with parameters **p**. The integrated 3D model $\mathsf{l} = \mathsf{l}(\mathbf{x}, W(\mathbf{x}, \mathbf{p}))$ is related to the fixed boundary-value problem, and appropriate and hypothesis-free for the above classical geo-monitoring observations and - in opposite to (1D/2D) - the common denominator to include as well the observation equations of all further modern geo-monitoring sensors, such as laser-scanners, lidar sensors, camera-tachymeters and GNSS/MEMS sensors.

The feasibility of the integrated 3D adjustment is actual due to the availability of precise global gravity potential models W, such as the EGM2008, and further due to the method developed at HSKA to map global gravity models with parameters **p** to regional gravity field models, which have a much smaller (computable) number of parameters **p'**. Last but not least, the integrated 3D model $\mathsf{l} = \mathsf{l}(\mathbf{x}, W(\mathbf{x}, \mathbf{p}))$ is obligatory for any inclusion of gravity field related observations such as gravity measurements g and zenith-camera based vertical deflection observations (η, ξ). These observations types are informative in geo-monitoring network types, where big masse changes occur (e.g. mining areas, oil-exploitation, or geodynamic networks).

The presentation shows, how to use the integrated 3D model $\mathsf{l} = \mathsf{l}(\mathbf{x}, W(\mathbf{x}, \mathbf{p}))$ for the modelling of the above sensor-data observation equations, and discusses the reduction of the integrated model to the so-called quasi-integrated 3D model in case of special types of geo-monitoring networks.

The final part of the presentation describes the implementation of the integrated 3D geometry & gravity field based network adjustment and of the quasi-integrated 3D model, into the geo-monitoring chain modelled by the IAF/HSKA geo-monitoring software GOCA (www.goca.info).

Keywords

Geo-Monitoring, (1D/2D) and 3D Geodetic Network Approaches, Integrated 3D geometry & gravity field related network adjustment, Quasi-Integrated 3D Network Adjustment, Gravity and Vertical Deflections Observations, Multi-Sensor Geo-monitoring, GOCA Geo-Monitoring System and Software.

Deformation Model-Building for Engineering Objects

Evgeny I. Avrunev, Elena S. Plyusnina
Siberian State University of Geosystems and Technologies, Russian Federation

Abstract
Conceptual approaches to the problem of deformation model-building for engineering objects are considered. Mathematical tools offered by the authors allows for deformation model building by n-dimensional vector of geodetic measurements. It also makes it possible to evaluate accuracy of deformation mark displacements by mathematical treatment of m-dimensional vector of geodetic observations epochs.

Keywords
Deformation mark, deformation model, mean-root-square error (RMS error), parametric equation, rectangular coordinate system

The significance of geodetic monitoring for engineering objects state has been time and again discussed in scientific and technical literature [KARPIK A.P. 2004, SEREDOVICH V.A. 2004, AVRUNEV E.I., 2010, AVRUNEV E.I., 2014]. This procedure is aimed at the object deformation model-building to evaluate the critical stress of the structure and (in case of necessity) take preventive measures on strengthening the building load-bearing elements, as well as make changes in the cadastral value.

Deformation marks on the engineering object body serve as reference data for model-building. The number of marks (n) and their location depend on the building structure and its load-bearing elements position. These requirements are to be considered at the stage of planning the detailed project on geodetic observations for geodetic monitoring.

Positions of deformation marks in spatial rectangular coordinate system are determined by 3D laser scanning or reflectionless total station. Laser scanning enables creating the point cloud for continuous model-building, and total station measurements (horizontal (β) and vertical angles (ϒ), horizontal distance of line (S)) allow for discrete deformation model-building which (in our judgment) is preferable for analytical calculations and relevant decision-making.

As a result of geodetic measurements, we have n-dimensional vector of geodetic measurements epochs $t_i = \{t_1, t_2, \dots \dots \dots t_m\}$; (time interval (Δt) is determined based on the engineering object structure, foundation soil type, and the predicted rate of subsidence and deformations development); for each epoch, n-dimensional vector of geodetic measurements $x_i = \{\beta_1, \gamma_1, S_1;\ \beta_2, \gamma_2, S_2; \dots \dots \beta_n, \gamma_n, S_n\}$; T –dimensional vectors of spatial coordinates of deformation marks $X_i = \{X_1, Y_1, Z_1;\ X_2, Y_2, Z_2; \dots \dots \dots \dots \dots .. X_t, Y_t, Z_t\}$ and their mean-square errors $m_i = \{m_1, m_2, \dots \dots m_t\}$.

In coordinate space, components of vector m_i are calculated by the following formula of least squares method:

$$m_i = \sqrt{m_{Xi}^2 + m_{Yi}^2 + m_{Zi}^2}\ , \tag{1}$$

where m_X, m_Y, m_Z, - mean-square errors of deformation marks coordinate determination by corresponding coordinate axes; i – deformation mark number.

To determine the RMS error of deformation mark (m_I) correlation matrix should be calculated by the following equation:

$$K = \mu^2 * (A^T * P * A)^{-1}, \tag{2}$$

where μ is a RMS error of the unit weight which (at the stage of the project accuracy evaluation) is taken as equal to the RMS error of the measured angle:

$$\mu = m_\beta \,, \tag{3}$$

and at the stage of mathematical treatment of geodetic measurements results, it is calculated by formula

$$\mu = m_\beta \,, \tag{4}$$

where r is the number of redundant measurements for determination of deformation mark spatial coordinates (polar intersection method, r=1);
P – weights of conducted measurements calculated by formulae (12);
V – measurement vector corrections which are calculated by compensation (with r≥2), for example, when a single deformation mark coordinates are determined from two reference points.
In input equation (2) A is a matrix of parametric coupling equation. For angles and line lengths, parametric coupling equations have the following form [AVRUNEV E.I. 2010]:

$$V_{\beta_{K'}} = \left(a_{KJ} - a_{KJ}\right)\Delta X_K + \left(b_{KJ} - b_{KJ}\right)\Delta Y_K + a_{JK}\Delta X_J + b_{JK}\Delta X_J - a_{IK}\Delta X_I - b_{IK}\Delta X_I \;, \tag{5}$$

where $V\beta_{K'}$ – corrections for measured angles values (unknown at the stage of project accuracy evaluation) denoting matrix rows A;
k' – order number of the design angle;
k, i, j – indices of parametric equation corresponding to the numbers of initial and desired points making up the design angle;
$\Delta X_I, \Delta Y_I$ – corrections for approximate coordinate values of points to be determined (unknown at the stage of project accuracy evaluation), denoting matrix rows A;
a_{JK}, b_{JK} – coefficients, calculated by formulae:

$$a_{JK} = \rho\frac{\sin\alpha_{KJ}}{L_{KJ}}; \quad b_{JK} = -\rho\frac{\cos\alpha_{KJ}}{L_{KJ}}, \tag{6}$$

where $\alpha_{KJ}, \mathbf{L}_{KJ}$ – directional angle and the line length from the reference point to the deformation mark, respectively.
The second parametrical coupling equation may be written as

$$V_{L\,I-J} = -\cos\alpha_{I-J}\Delta X_I - \sin\alpha_{I-J}\Delta Y_I + \cos\alpha_{I-J}\Delta X_J + \sin\alpha_{I-J}\Delta Y_J \,, \tag{7}$$

To solve matrix equation (2) we derive parametric coupling equation for the vertical angle.

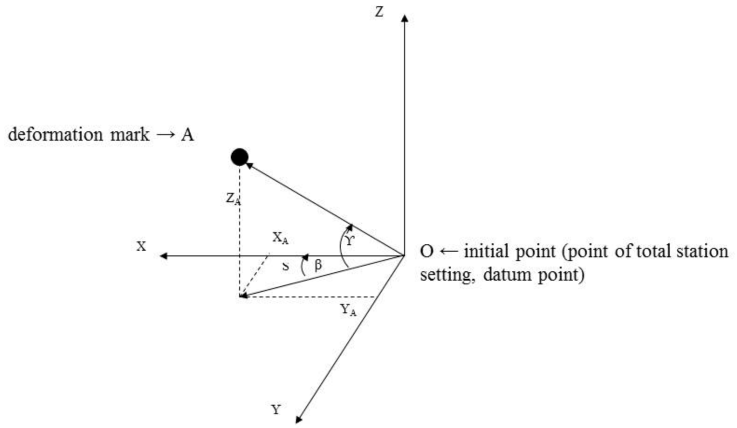

Figure 1: The location diagram of deformation mark in spatial coordinate system

Let vertical angle ϒ be a function of spatial coordinates of the initial point (0) and deformation mark (A):

$$\Upsilon = f(X_0, Y_0, Z_0, X_A, Y_A, Z_A,) = arctg\frac{h}{s} = arctg\frac{Z_A - Z_O}{\sqrt{(X_A - X_O)^2 + (Y_A - Y_O)^2}} \quad . \tag{8}$$

If datum point (Fig. 1) is transferred to the initial point (0), then equation (8) will transform into the following form:

$$\Upsilon = f(X_0, Y_0, Z_0, X_A, Y_A, Z_A,) = arctg\frac{h}{s} = arctg\frac{Z_A - Z_O}{\sqrt{(X_A - X_O)^2 + (Y_A - Y_O)^2}} \quad . \tag{9}$$

The final version of the parametrical coupling equation is as follows:

$$V_\gamma = \left(\frac{\partial f}{\partial X_A}\right)\Delta X_A + \left(\frac{\partial f}{\partial Y_A}\right)\Delta Y_A + \left(\frac{\partial f}{\partial Z_A}\right)\Delta Z_A \ , \tag{10}$$

where the values of partial derivatives (coefficients of parametrical coupling equations) may be calculated by formulae:

$$\left(\frac{\partial f}{\partial X_A}\right) = -\frac{X_A \cdot Z_A}{(X_A^2+Y_A^2+Z_A^2)\cdot\sqrt{X_A^2+Y_A^2}}; \quad \left(\frac{\partial f}{\partial Y_A}\right) = -\frac{Y_A \cdot Z_A}{(X_A^2+Y_A^2+Z_A^2)\cdot\sqrt{X_A^2+Y_A^2}}; \quad \left(\frac{\partial f}{\partial Z_A}\right) = \frac{\sqrt{X_A^2+Y_A^2}}{(X_A^2+Y_A^2+Z_A^2)} \quad . \tag{11}$$

Matrix P in equation (2) determines weights of design measurements, which (taking into account the accepted condition (3)) are calculated by formulae:

$$P_\beta = \frac{\mu^2}{m_\beta^2} = \frac{\mu^2}{m_\beta^2} = 1; \quad P_L = \frac{\mu^2}{m_L^2} = \frac{m_\beta^2}{m_L^2}; \quad P_\gamma = \frac{\mu^2}{m_\gamma^2} = \frac{m_\beta^2}{m_\gamma^2} \ , \tag{12}$$

The calculated elements of correlation matrix allow for determining accuracy characteristics for all deformation marks of the engineering object:

$$m_i = \sqrt{m_{Xi}^2 + m_{Yi}^2 + m_{Zi}^2}, \quad m_{Xi} = m_\beta * \sqrt{Q_{Xi}}; \quad m_{Yi} = m_\beta * \sqrt{Q_{Yi}}; \quad m_{Xi} = m_\beta * \sqrt{Q_{Zi}} \ , \tag{13}$$

In the event that the deformation marks coordinates are determined by laser scanning, the results may be presented as a measured directional angle (α), line length (S) and height difference (h).
Parametrical coupling equations for directional angle and line length are calculated by standard equations (7) and

$$V_\alpha = a_{IJ}\Delta X_I + b_{IJ}\Delta Y_I - a_{IJ}\Delta X_J - b_{IJ}\Delta Y_J \, . \tag{14}$$

For deriving the third equation, let us write the height difference as a function of vertical angle and the line length:

$$h = f(\gamma, S) = tg\gamma * S = tg\gamma * \sqrt{X_A^2 + Y_A^2 + Z_A^2}, \tag{15}$$

then parametrical coupling equation for the height difference will have the following form:

$$V_h = \left(\frac{\partial f}{\partial X_A}\right)\Delta X_A + \left(\frac{\partial f}{\partial Y_A}\right)\Delta Y_A + \left(\frac{\partial f}{\partial Z_A}\right)\Delta Z_A \ , \tag{16}$$

The values of partial derivatives values (coefficients of parametrical coupling equations) may be calculated by formulae:

$$\left(\frac{\partial f}{\partial X_A}\right) = \frac{tg\gamma \cdot X_A}{\sqrt{X_A^2+Y_A^2+Z_A^2}}\ ;\ \left(\frac{\partial f}{\partial Y_A}\right) = \frac{tg\gamma \cdot Y_A}{\sqrt{X_A^2+Y_A^2+Z_A^2}}\ ;\ \left(\frac{\partial f}{\partial Z_A}\right) = \frac{tg\gamma \cdot Z_A}{\sqrt{X_A^2+Y_A^2+Z_A^2}}. \quad (17)$$

Components of matrix P (of laser determinations weight) based on the accepted condition (3) and the principle of equal effect may be calculated as follows:

$$m^2 = m_\alpha^2 + m_L^2 + m_\alpha^2. \quad m_\propto = m_L = m_h = \frac{m}{\sqrt{3}}. \quad m_\alpha = \frac{m*\rho}{\sqrt{3}*L}; \quad m_L = \frac{m}{\sqrt{3}}; \quad m_h = \frac{m}{\sqrt{3}}.$$

$$P_\alpha = \frac{\mu^2}{m_\alpha^2} = \frac{m_\alpha^2}{m_\alpha^2} = 1. \quad P_L = \frac{m_\alpha^2}{m_L^2} = \frac{3*m^2*\rho^2}{3*L^2*m^2} = \frac{\rho^2}{L^2}. \quad P_h = \frac{m_\alpha^2}{m_h^2} = \frac{\rho^2}{L^2}. \quad (18)$$

where m is a laser scanner precision.

On comparing coordinate vectors of geodetic measurements epochs ((t_1, t_2) deformation mark displacement in space is calculated by formula:

$$f = S_{Ai} = \sqrt{\left(X_{Ai}^{t1} - X_{Ai}^{t2}\right)^2 + \left(Y_{Ai}^{t1} - Y_{Ai}^{t2}\right)^2 + \left(Z_{Ai}^{t1} - Z_{Ai}^{t2}\right)^2} = \sqrt{\Delta X_{Ai}^2 + \Delta Y_{Ai}^2 + \Delta Z_{Ai}^2}. \quad (19)$$

Applying the known formula of mean-square error of parameters function in equation (19) we derive the following equation:

$$m_{S_{Ai}} = \mu * \sqrt{\frac{1}{P_{S_{Ai}}}}, \quad (20)$$

where the weight of the function to be estimated may be calculated by formula:

$$\frac{1}{P_{Sa}} = \|f_1, f_2, f_3\| * \left\| \begin{matrix} Q_{\Delta X_A} & Q_{\Delta X_A} & Q_{\Delta X_A} \\ & Q_{\Delta X_A} & Q_{\Delta X_A} \\ & & Q_{\Delta X_A} \end{matrix} \right\| * \left\| \begin{matrix} f_1 \\ f_2 \\ f_3 \end{matrix} \right\|,$$

where f_1, f_2, f_3, are partial derivatives of the desired function (line lengths) by the corresponding parameters (coordinates of deformation mark).

$$f_1 = \left(\frac{\partial f}{\partial \Delta X_A}\right) = \frac{\Delta X_{Ai}}{\sqrt{\Delta X_{Ai}^2+\Delta Y_{Ai}^2+\Delta Z_{Ai}^2}}, f_2 = \left(\frac{\partial f}{\partial \Delta Y_A}\right) = \frac{\Delta Y_{Ai}}{\sqrt{\Delta X_{Ai}^2+\Delta Y_{Ai}^2+\Delta Z_{Ai}^2}}, \quad f_3 = \left(\frac{\partial f}{\partial \Delta Z_A}\right) = \frac{\Delta X_{Ai}}{\sqrt{\Delta X_{Ai}^2+\Delta Y_{Ai}^2+\Delta Z_{Ai}^2}} \quad (21)$$

Suppose the scheme of geodetic measurements remains unchanged in process of transition from one cycle to another, then formula (20) will have the following final form:

$$m_{S_{Ai}} = \mu * \sqrt{\frac{1}{P_{S_{Ai}}}} = \mu * \sqrt{\frac{1}{2\left\{\|f_1, f_2, f_3\| * \left\| \begin{matrix} Q_{X_A} & Q_{X_AY_A} & Q_{X_AZ_A} \\ & Q_{Y_A} & Q_{Y_AZ_A} \\ & & Q_{Z_A} \end{matrix} \right\| * \left\| \begin{matrix} f_1 \\ f_2 \\ f_3 \end{matrix} \right\| \right\}}}. \quad (22)$$

The most important thing in deformation model-building is to determine the significance of deformation mark displacement.

The displacement is accepted for a fact, if statistical criterion (22) is satisfied, if not, displacement of deformation mark is considered as being within the limits of accuracy

$$S_{Ai} \geq t * m_{S_{Ai}} = 2 * m_{S_{Ai}}, \quad (23)$$

where t is a statistical coefficient depending on the probability of significance determination for the deformation mark displacement (with β=0.95, t=2).

If condition (23) is satisfied for deformation marks, then to develop deformation model t, it is appropriate to divide dimensional vector of deformation mark coordinates into L fragments, determined by the design of engineering objects (for example, the fragment may be represented by the floor or the whole building). The fragments borders are determined by deformation bench marks (Fig. 2). Hence, the fragment is represented by parallelepiped with four facets. As the facet is determined by two planes there will be 8L planes in the building (if necessary, the deformation model may be supplemented by the building foundation and intermediate floors).

For the initial state of the engineering object at time t_1 the matrix, determining the initial state is presented by the following equations:

$$B_{t_1} = \begin{Bmatrix} A_1(X - X_J) + B_1(Y - Y_J) + C_1(Z - Z_J) = 0 \\ A_2(X - X_U) + B_2(Y - Y_U) + C_2(Z - Z_U) = 0 \\ \dots\dots\dots\dots\dots\dots\dots\dots\dots\dots\dots\dots\dots\dots \\ A_K(X - X_V) + B_K(Y - Y_V) + C_K(Z - Z_V) = 0 \end{Bmatrix}, \tag{24}$$

where X, Y, Z – variables denoting random point belonging to the corresponding plane;
J, U, V – indices designating the names of deformation marks forming the corresponding plane;
K –plane number (the range of changing K from 1 to 8L)

$\begin{Bmatrix} A_1, A_2, \dots . A_K \\ B_1, B_2, \dots . B_K \\ C_1, C_2, \dots . C_K \end{Bmatrix}$ –matrix of normal vectors coordinates, calculated at the instant of time t_1, using the following equation (for example, for the first plane, formed by deformation marks A, B, and F)

$$N_{t_1} = \begin{Bmatrix} A_1 = (Y_B - Y_A) * (Z_F - Z_A) - (Z_B - Z_A) * (Y_F - Y_A) \\ B_1 = (X_F - X_A) * (Z_B - Z_A) - (Z_F - Z_A) * (X_B - X_A) \\ C_1 = (X_B - X_A) * (Y_F - Y_A) - (X_F - X_A) * (Y_B - Y_A) \end{Bmatrix}. \tag{25}$$

In a similar way coordinates of normal vectors of other planes are calculated.

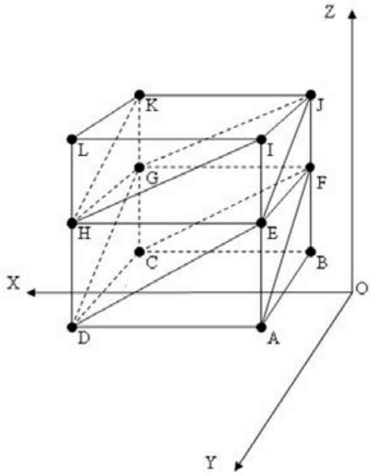

Figure 2: The position of engineering object in spatial coordinate system

As a result of geodetic monitoring of the object state for the successive instants of time, we have m “observation epochs”. In this case deformation model is built on the basis of comparing the matrix of the initial state of object B_{t_1} and the current one B_{t_I} (absolute strain of the object) or B_{t_I} and $B_{t_{I+1}}$ (relative deformation of the object).

Discrepancy between the respective elements of the state matrixes determines displacement of the object under observation in three-dimensional coordinate system. On the basis of the displacement data comparison with standard tolerable limits, the conclusion is made on either the engineering structure stability in space, or on the maximum stressed state of its load-bearing elements.

REFERENCES

Journal articles:

AVRUNEV E.I. Geodetic support of national real-estate cadastre / E.I. Avrunev. Novosibirsk. SSGA, 2010.

AVRUNEV E.I. *Geodetic Monitoring of Natural Object Conditions (by the example of a landslide) /* E.I. Avrunev, I.A. Giniyatov, D.Yu. Terentyev, M.V. Meteleva - Siberian State Academy of Geodesy. T. l. Integration of Point- and Area-wise Geodetic Monitoring for Structures and Natural Objects. P. l. proceeding of International Workshop, 14-15 April 2014, Novosibirsk. - Novosibirsk: SSGA, p. 118-122.

KARPIK A.P. *Methodological and technological basis for GIS support of the territories*: Monograph. – Novosibirsk: Siberian State Academy of Geodesy (SSGA), 2004 – 260 p.

KARPIK A.P. *Creation of territories uniform geo-environment to improve geodetic dataware for national real-estate cadastre /* A.P. Karpik, V.I. Obidenko. – Interexpo Geo-Siberia-2013. T. l. Economics of nature management and property. P. l. proceeding of IX International Scientific Congress and Exhibition Interexpo Geo-Siberia-2013, 24-26 April 2013, Novosibirsk. - Novosibirsk: SSGA.

KARPIK A.P. *Horoshilov V.S. Essense of territories GIS environment as common base for national real-estate cadastre development //* News of higher educational institutions. Geodesy and Aerophotography. – 2012. - № 2/1. – p. 134-136.

SEREDOVICH V.A. et. al. *Movements and stressedly-deformed state of self-organizing geodynamic systems identification by complex geodetic and geophysical observations:* Monograph / V.A. Seredovich, V.K. Pankrushin, Y.I. Kyznetsov, B.T. Mazurov, V.F. Lovyagin; SSGA. – Novosibirsk, 2004. – 356 p.

3D Monitoring of Fixed Assets under Construction for the Purpose of Consistent Cadastral Registration

Dmitry N. Vetoshkin, Sergey R. Gorobtsov
Siberian State University of Geosystems and Technologies, Russian Federation

Abstract
The challenges of cadastral registration for fixed assets under construction are considered. 3D monitoring of capital construction projects and mobile laser scanning techniques are offered for these problems solution.

Keywords
3D monitoring, 3D cadastre, capital construction project (fixed asset under construction), real property unit, cadastre, cadastral registration, laser scanning

1 INTRODUCTION

Nowadays monitoring of urban infrastructure is an important challenge. Current techniques for mobile laser scanning allow for developing accurate 3D models with greater details for various buildings, structures, road network projects, electrified transport network, tram and railway lines, tunnels and bridges. Onrush of such technologies, reduction of facilities size and costs as well as new automated algorithms for surveying results processing increase their range of application. One of the most promising fields is 3D cadastral surveying of capital construction projects for the purpose of consistent cadastral registration.

By cadastral survey is meant special type of surveying works, which involve identification and description of the real estate for its further cadastral registration. As a result of cadastral survey the real estate unit has to obtain characteristics which provide its unique identification and determination of the unit as property (object of law) and object of registration, and characteristics required for transactions, valuation and taxation. Traditionally, cadastral survey involves terrestrial (total station surveying) or cartometric (including photogrammetric) methods. For many years these methods have met the requirements of national cadastral systems. However, with the advance of architecture and civil engineering, with many capital construction projects having complex architecture and design as well as non-standard shape, traditional techniques would not do. They are incapable of taking into account the multilevelness in structures (multi-level junctions, bridges and tunnels, etc.).

2 REAL-ESTATE TYPOLOGY

Russian legislation is developing a complicated concept of real property. As opposed to the majority of European countries where the objects (units) of property are traditionally land plots whereas buildings and structures are considered as their secondary improvements, in Russia, on the contrary, land plots, buildings, structures and premises are considered as independent real-estate units, i.e. they are particular objects of cadastral registration, rights, valuation and taxation.

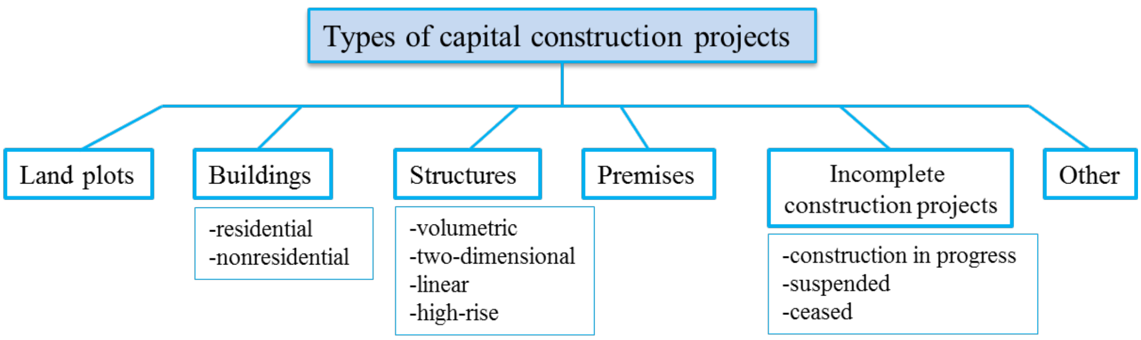

Figure 1: The structure of real property units in Russia

Current system of cadastral registration of real property has been functioning since March, 2008, when Federal law "On the State Real Estate Cadastre" came into effect. In 2008 – 2010 the law applied only to land plots, but capital construction projects were registered by technical inventory bodies. Since 2010 capital construction projects have been registered in national real property cadastre. Technical inventory bureaus scanned and transferred all the operating records and data on capital construction projects to cadastral registration bodies. Thus, the initial cadastral database was established. In accordance with the changes in legislation, the procedures for preparation of cadastral data on the projects, as concerns capital construction projects (cadastral works), cadastral registration and information provision were developed.

Now cadastral surveying of capital construction projects is conducted by cadastral engineers who were licensed for this work in 2010. In the course of works a cadastral engineer determines the structure location on the land plot, other data are given on the basis of the project documentation and its maintenance permit. In some cases, when project documentation and maintenance permit are not required, technical plan of the structure is made on the basis of the declaration prepared by the its owner.

Technical plan of the structure drafted by a cadastral engineer consists of graphical and textual parts.

Technical plan is made in electronic form, as XML-format document according to the established scheme, certified by digital electronic signature of the cadastral engineer. The documents attached to the technical plan are presented in PDF format, graphical forms within the plan – as JPEG files.

In accordance with the established requirements technical plan of the structure includes the following characteristics of the capital construction projects.

Table 1: Structure characteristics

№	Characteristic name
1	Cadastral number of structure
2	Previously assigned state registration number of structure (cadastral, inventory, conventional)
3	Cadastral number of land plot(s) on whose territory the structure is located
4	Number of cadastral unit(s) within which the structure is located
5	Address (location description) of structure
	Other description of location
6	Purpose of structure
7	Name of structure
8	Number of structure floors
	including underground
9	in operation since (year)
	construction finished in (year)
10	Basic characteristic of structure

In process of capital construction project registration the body of cadastral registration has limited powers concerning examination of the documents and data on the project. Actually they examine only the applicant's permission to apply for cadastral registration of the project, and the presented technical plan for conformity with the established requirements.

Thus, the existing techniques for capital construction projects description for their further cadastral registration suffer from grave shortcomings:

1. The key function of cadastral survey and registration of real property is to provide its unique identification as an object of law and transaction. Moreover, the project is to be supplied with characteristic, which allows for its unequivocal delimitation and separation from other property units. As concerns land plots the problem may be efficiently solved by determining plane rectangular coordinates of the boundary turning points. As for capital construction projects presented as individual real property units, such description is insufficient. The buildings and structures with complex design (highly engineered) cannot be unequivocally

described and demarcated in two-dimensional space. The capital construction plane projection may overlap another’s land parcel.

a) b)

Figure 2. a) Technopark building, Novosibirsk; b)”Gate of Europe”, Madrid

Therefore, for the complete identification of capital construction projects their spatial parameters should be determined in 3D coordinate system.

2. Applying the existing cadastral surveying techniques cadastral engineer actually measures only the outer contour of the capital construction unit. All basic parameters are introduced in technical plan from the project documentation. Thus, knowing that actual parameters of the unit (height, total structural volume, etc.) may differ from the design, modern technologies admit some erroneous information introduced in real property cadastre. There is no way of comparing the project actual parameters and the design parameters. i.e. determining its functional suitability. Moreover, cadastral registration may be performed for the capital construction project which belongs to another unit (according to the project documentation). In cadastral works we should use the techniques which make it possible to determine the established list of the object spatial parameters which may be compared with those of the design.

3. The list of project characteristics to be determined and introduced in real estate cadastre has reduced as compared with the previously used one. It no longer meets the requirements of wear-out estimation and evaluation by cost-is-no-object (reconstruction) approach, etc. Current techniques allow for considerable increase of the characteristics list, including determination of spatial parameters for capital construction projects or of their certain structural components (height, depth, height difference, volume, etc.)

The above mentioned problems can be efficiently solved by current techniques of mobile 3D-laser scanning of capital construction projects, and their description, visualization in 3D cadastre system.

3 3D CADASTRE

The idea of 3D cadastre introduction is not new. Most of the developed countries used to face the problem of registration as concerns complicated multilevel projects of capital construction (junctions, bridges, and tunnels, nonstandard shape buildings with overhanging floors). In a number of countries (Australia, Netherlands, Sweden, Greece) current cadaster has 3D elements. Thus, in Greece height component of object description is applied for the territories with compact terrace planning, with major part of the real property unit being projected on the roof of the building locating lower down the slope. In the Netherland special code system is used for designating underground structures, with the notice of the existing underground structures being placed at the level of the land plot surface.

Practical experience of Russia in developing 3D cadastre goes back to 2010 when the Federal Service of State Registration, Cadastre and Cartography (Rosreestr) and the Agency of Cadaster, Land Registration and Cartography (the Netherland) created pilot project on modeling 3D real-estate cadastre. The projected resulted in 3D description of the basic types of capital construction projects: underground structures, buildings, etc.

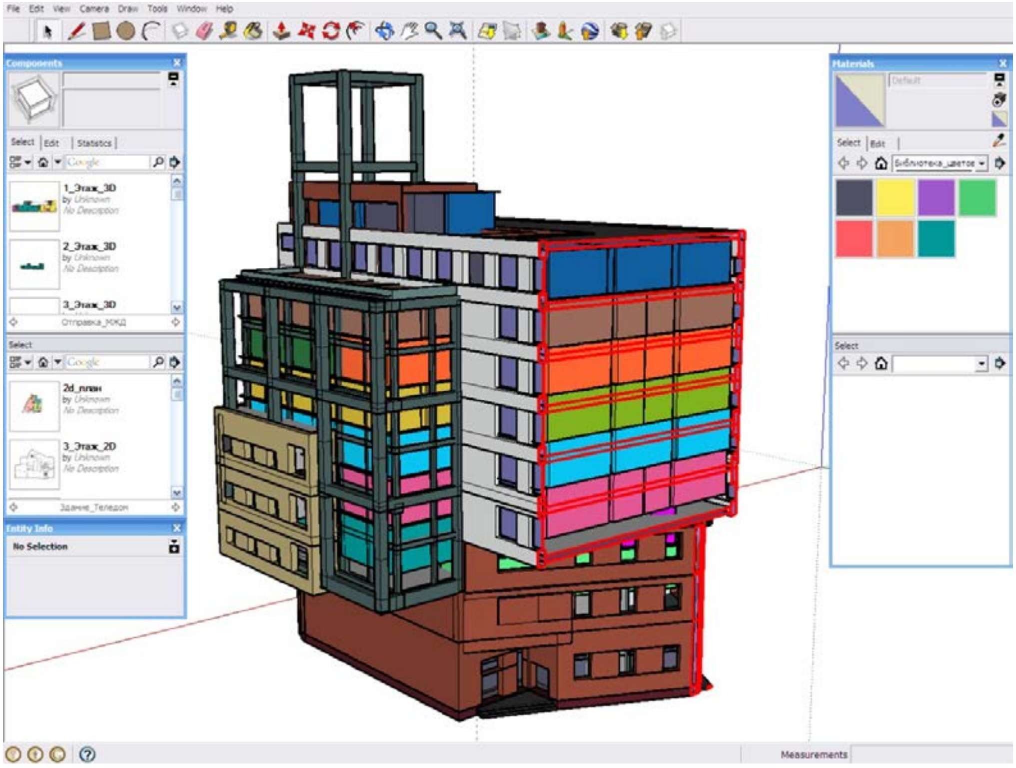

Figure 3: 3D model of “Pilot project “Telehouse”

However, this project has not been further developed. The obtained results have been introduced neither into the real-estate cadastre nor into the normative base.

Application of 3D laser scanning data for description of capital construction projects may be considered by the example of the Bugrinsky Bridge. The works on its 3D modeling were conducted by the Siberian State University of Geosystems and Technologies.

The Bugrinsky Bridge was launched in Novosibirsk, Russia on October 8, 2014. The bridge length being 2.1 km (total, 5.4 km), it took over 24,000 tons of metal, 45,000 cubic metres of concrete, 30,000 tons of fabricated metals (aggregate value, 14.8 billion roubles) to build it. Its capacity is about 60,000 cars per 24 h. The bridge is a combined structure. Constructively, it is a beam structure set on 30 reinforced concrete saddles on boring piles.

Figure 4: Bugrinsky Bridge, Novosibirsk

The Bugrinsky Bridge is a unique structure as concerns certain characteristics. The length of arch span, 380 m, is the greatest in Europe. The arch height is 70 m. The arch dome is made of metal filled with cable-stay. The technique of arch mounting by launching along the contour of the dome was used for the first time in the world. The bridge ranks among the five most impressive bridges built in Russia lately. The world record in arch bridges is held by China, with its arch foundation being 55 m, but that bridge has no cable-stay system. Arch-cable-braced bridges have been built for the last decade, but they are still few in number. The Bugrinsky Bridge is an original design, which may be referred to the unique structures on the world scale.

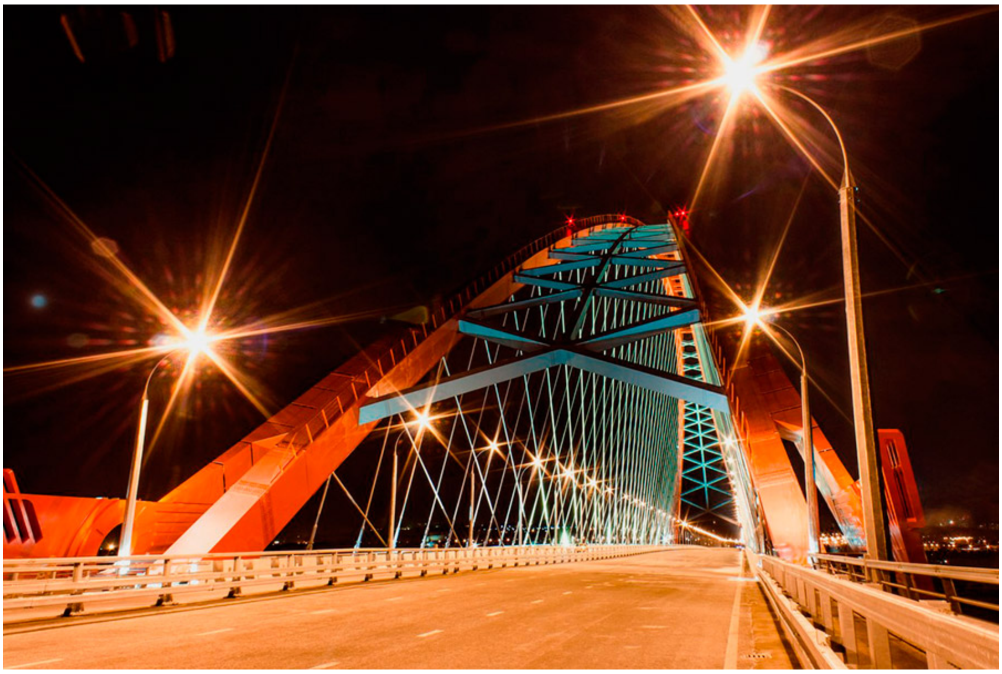

Figure 5: The Bugrinsky Bridge arch

The Siberian State University of Geosystems and Technologies has conducted a complex of experimental and production works on 3D laser scanning of the Bugrinsky Bridge, from the initial stage of arch launching to the bridge deformation monitoring in process of testing. Terrestrial laser scanner (TLS) Leica ScanStation C10 was chosen for 3D laser monitoring. It features high accuracy and measurement rate, and high-precision compensatory device for TLS leveling.

Figure 6: Terrestrial laser scanner Leica ScanStation C10

High scanning rate and precise measurement (of the point cloud) capabilities give advantages to laser scanning relative to other technologies applied for capital construction projects surveying. Laser scanning provides redundancy of precise information. In combination with software products for laser scanning data processing this technique gives opportunity for high-precision modeling of construction objects, in particular, detection of displacements and deformations with accuracy up to 1 mm.

The work resulted in high-precision detailed 3D model of the Bugrinsky Bridge presented below.

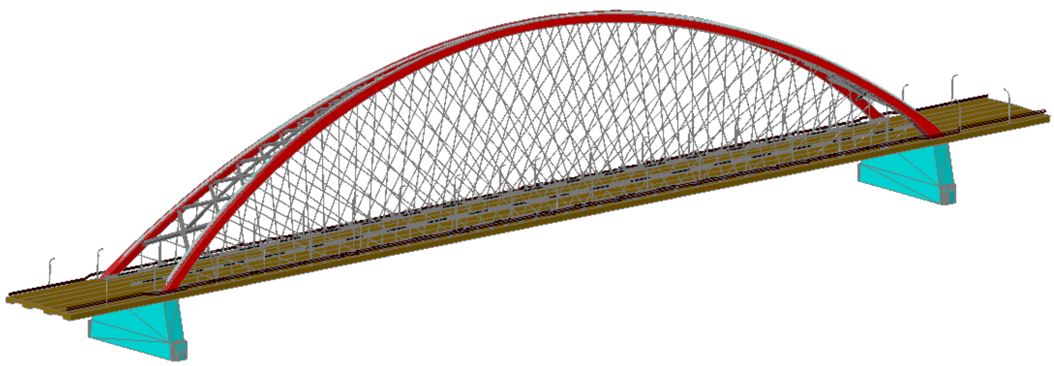

Figure 7: 3D model of the Bugrinsky Bridge

The developed 3D bridge model permits eliminating the above mentioned shortcomings of the system for capital construction projects registration in real-estate cadastre.

1. The given model may serve as a basis for the system of 2D or 3D real estate registration.

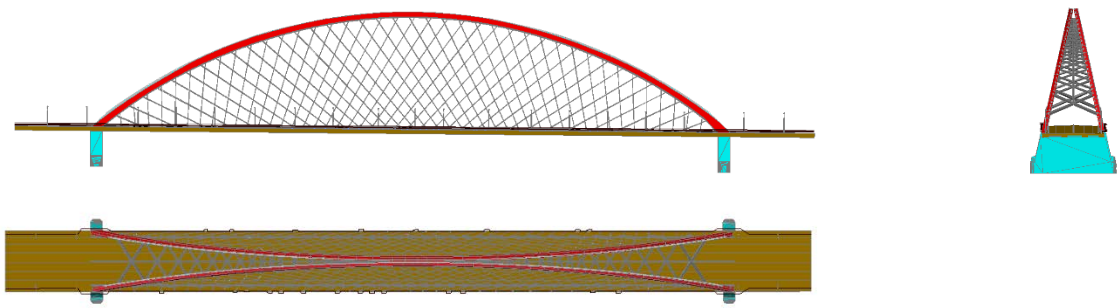

Figure 8: 2D model of the Bugrinsky Bridge

The bridge as a spatial real property object can be presented in concept of boundary plane according to ISO/DIS 19152 Annex B:

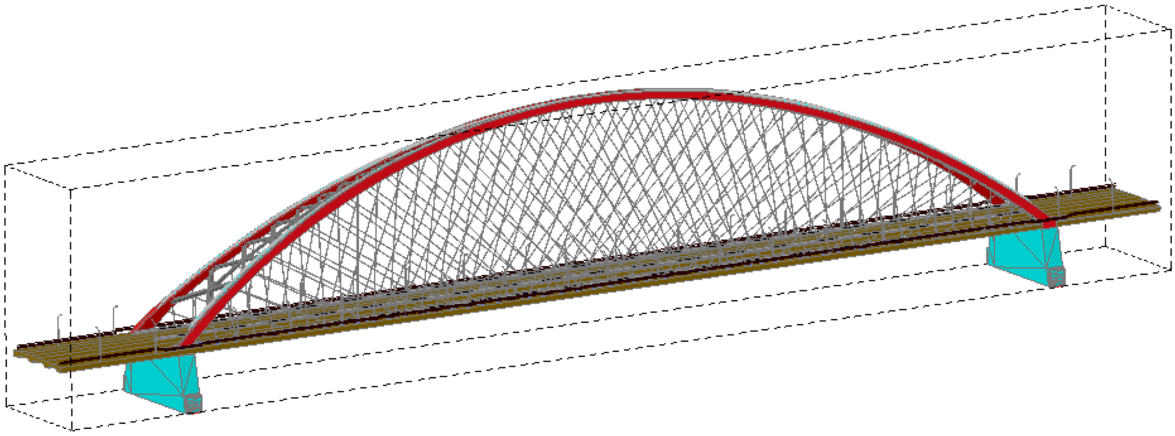

Figure 9: 3D model of the Bugrinsky Bridge as a real property unit under ISO/DIS 19152 Annex B

2. The developed 3D bridge model enables obtaining a wide range of spatial characteristics for capital construction project:

- configuration of structures and elements, size, vertical and horizontal position;
- column heights, span lengths, junction sections and other geometrical parameters whose values predetermine deformation of different elements.

These parameters may be used in cadastral registration and in design parameters conformity test.

4 CONCLUSION

According to the experience of the Siberian State University of Geosystems and Technologies in 3D modeling of capital construction projects, mobile laser scanning techniques are going to find a new field of application, i.e. cadastral surveying of real-property units for further registration and geodetic monitoring as well. The given approach allows for considerable improvement of cadastral information quality concerning capital construction projects without essential increase in job costing. The approach is to increase efficiency of cadastral system as a whole.

REFERENCES

Journal articles:

GERASIMOVA S.G., IBRAGIMOV M.B., PETROV M.V.: Perspectives of creating 3D cadastre in Russia, Geoprofi, p. 5-8, 2013.

MOHAMED EL-MEKAWY, JESPER PAASCH, JENNY PAULSSON: Integration of 3D Cadastre, 3D Property Formation and BIM in Sweden, 4th International Workshop on 3D Cadastres, p. 17-34, 2014.

NIKOLAEVA T.V., NIKITIN V.N.: Cadastre in 3D format, Interexpo Geo-Siberia-2014, p. 219-225, 2014.

SNEZHKO I.I.: Comparative analysis of creating a 3D cadastre in Russia and the Netherlands, Geodesy and Aerophotosurveying, p. 100-104, 2013.

YASHNOV A.N., SEREDOVICH V.A., IVANOV A.V.: Techniques for determining bridge span sliding displacement by terrestrial laser scanning in Novosibirsk, Interexpo Geo-Siberia-2013, p. 144-150, 2013.

Links:

URL, Federal law of 24.07.2007 #221-ФЗ (edited, 29.12.2014) "On Real Estate Cadastre" (revised and supplemented, with changes introduced, 22.01.15)
http://www.consultant.ru/document/cons_doc_LAW_170233/

URL, Order of Ministry for Economic Development, R.F., 23.11,2011, #693 (edited, 25.02.14) "On approval of structure technical plan form and requirements"
http://www.consultant.ru/document/cons_doc_LAW_164154/

3D Modelling and Visualizing Surface Deformations of Man-Made Objects

Tatyana Yu. Bugakova, Maryia M. Shlyakhova, Alexander V. Seredovich, Andrei V. Ivanov, Oksana R. Miftakhudinova
Siberian State University of Geosystems and Technologies, Russian Federation

Abstract
Spatial state of man-made objects is not invariable. It changes under the environmental impact or interior processes. Spatial state variations show in motions and deformations of the object resulting sometimes in irreversible impacts (from construction failure to human toll). In connection with the above said, one of the major problems of geodetic monitoring is determination of changes in man-made object spatial state. The example of man-made object deformation determined by laser scanning data is presented.
The models developed by laser scanning are static. With static 3D model of the object spatial state referred to the fixed instant of time *t*, we can reveal surface deformation by its superposing on the design surface. Real model deviation from the design one by the value greater than allowable testifies to the surface deformation.

Keywords
3D modeling, terrestrial laser scanning, spatial state, man-made objects, surface deformation, deformation visualization

1 INTRODUCTION

Safe operation of man-made objects (buildings, structures, industrial and civil facilities) is impossible without proper malfunction diagnostics, which involves control of some parameters determining performance characteristics of buildings, structures and facilities. To obtain complete and reliable data on the object conditions we should apply information-engineering system comprising geodynamic, hydrological, geodetic and other subsystems for conditions control. The most important of them are geodetic subsystems. They are to estimate spatial state (position, deformation, and geometrical characteristics) of objects. Modern geodetic instruments allow for conducting high-precision prompt measurements for estimating spatial state of the man-made object. For example, laser scanner makes possible 3D determinations of any complex or inaccessible surfaces. The result of laser scanner operation is a set (cloud) of points of X, Y, Z coordinates. Laser scanning data are processed by software, to develop real 3D metric models of the object. On their basis information on the spatial position of the object and its geometric characteristics (distance, volume, and area) are obtained.
Laser-based models are static, but the spatial state of man-made objects is not invariable. Their state changes due to environmental factors or internal processes. Variations of spatial state might result in irreversible impacts, from construction failure to loss of life. Thus, one of the most important objectives of geodetic monitoring is determination of spatial objects variations.

2 EXPERIMENT

The focus of the article is 3D modeling and visualization of man-made object surface deformation by terrestrial laser scanning.
The dome of Novosibirsk planetarium was chosen as an object of research. The survey was conducted from the inside of the building.
The data on the object were obtained by the universal compact laser scanner Leica ScanStation C10. It is one of the most popular instruments of ScanStation series, ensuring high efficiency and performance in process of topographic surveying. Pulse laser system provides scanning operation at the distance up to 300 m, with the rate of 50,000 points a second that makes it possible to produce detailed 3D images. The scanner field of view is 270° vertically and 360° horizontally. The high-resolution built-in video camera provides real detailed sharp images to be later superimposed over the scanned point cloud. As a result of scanning, one scan was obtained. Measurement data were presented and corrected in software Cyclone by horizontal level, with compensator

precision of 4 mm. The model was determined in the uniform coordinate system OXY, coordinates Z were determined in real system of heights (Fig.1).

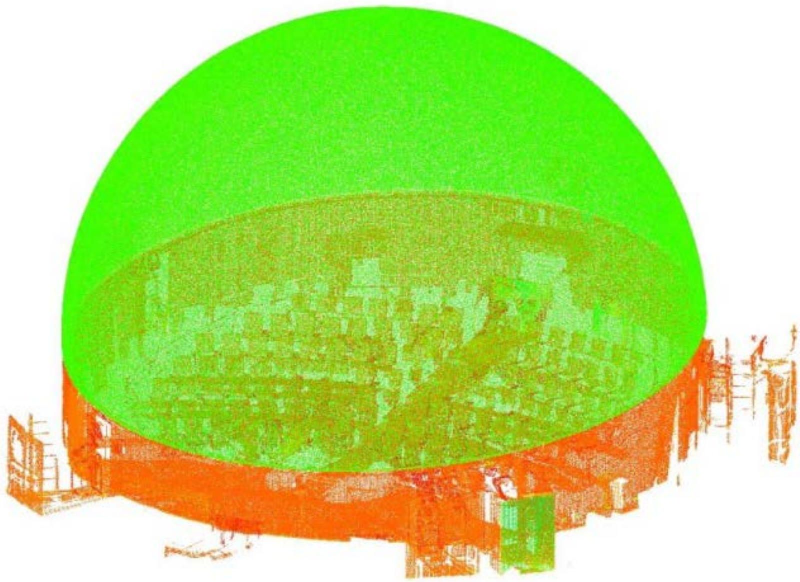

Figure 1: The planetarium dome from terrestrial laser scanning

Software Rapidform XOR was chosen for data processing. It is a program which allows for transition from 3D scan to completely parametrical CAD model. Whereas most of 3D-scanning data-processing programs are focused solely on optimization of polygonal grid or development of high-quality NURBS-surfaces by 3D scan, Rapidform XOR complements optimization functions of the grid and generation of NURBS-surfaces with new capabilities of CAD modeling. It provides new toolbox for 3D scans transformation into parametrical CAD-models. The software comprises a number of functions aimed at the solution of reverse engineering problems to ensure finite model built with the set accuracy relative to the object to be scanned. The patent Accuracy Analyzer built in XOR guarantees that the model will be built with the desired admissible error relative to the original and provides time for the repeated control in third-party software and making repeated alterations in geometry.

With static 3D model of the object spatial state corresponding to the fixed instant of time *t*, surface deformation may be determined by its superimposing over the design surface. Real model deviation from the project one by the value greater than admissible will testify to this surface deformation.

The work on determination and visualization of the planetarium dome surface deformation was conducted in three stages:

1. The point cloud was imported in software Rapidform XOR.
2. TIN surface of the dome was constructed (points rarefaction, noise removal, triangulation). The result is presented in Fig. 2.
3. To determine the dome surface deformation, approximation was performed, i.e. superposition of TIN surface and the design data, with the sum of squares of the real surface points coordinates deviation being minimal. The sphere preset by the equation was chosen as the design surface.
4.

$$(x - x_0)^2 + (y - y_0)^2 + (z - c_0)^2 = R^2 \tag{1}$$

where R is the sphere radius.

Approximation result is given in Fig. 3.

4. The value of the standard deviation (of the planetarium dome) from the project sphere was determined. The vector of standard deviation value $\overline{V} = \overline{V}(\overline{v_1, v_n})$ was obtained, where *n* is the number of root-mean-square error values. Mean values of deviations are 36 mm. The 3D object model with surface deformation zones image is shown in Fig.4.

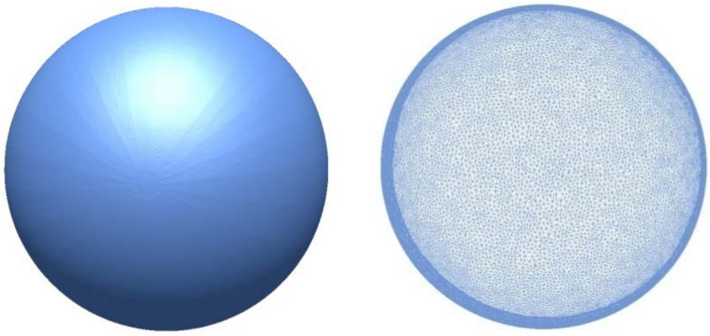

Figure 2: TIN surface of planetarium dome

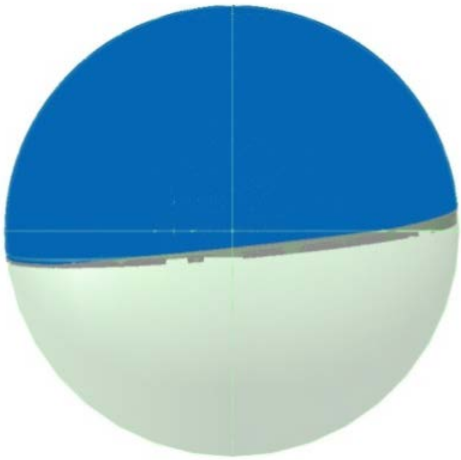

Figure 3: Approximation result

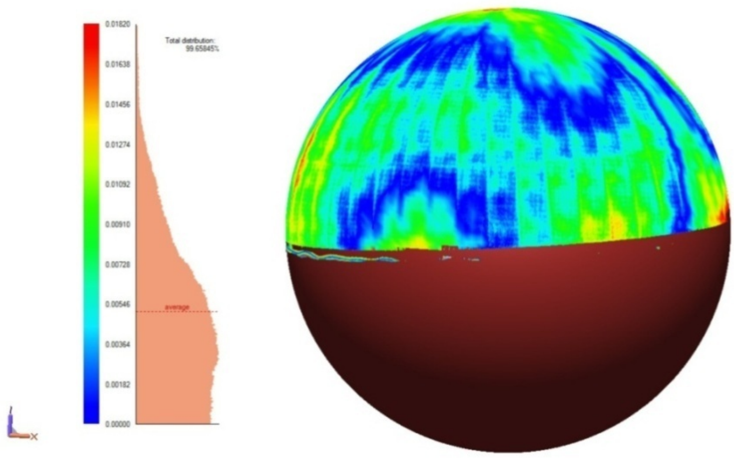

Figure 4: 3D model of the planetarium dome surface with image of deformation zones, and the result of mean square error estimation

Object deformation is a process taking place in time, it is determined as a function of time $D(t_i)$, where t_i belongs to time interval *T*, $i = 1..k$, *k* – the number of instants of time in interval *T*. Therefore to determine functions $D(t_i)$ on the whole time interval *T* there must be *k* static models. Thus to determine deformations of the object surface throughout the whole time gap *T* by the method of static models, superimposition *k* iterations should be performed.

To reduce the number of iterations the experiment was conducted. The possibility of three models superimposition is considered in the given work.

In this connection simulation of the dome deformation surface was developed. Height coordinates of its upper parts were changed, then the model was superimposed on the design model. Mean deviation values are 38 mm (Fig.5).

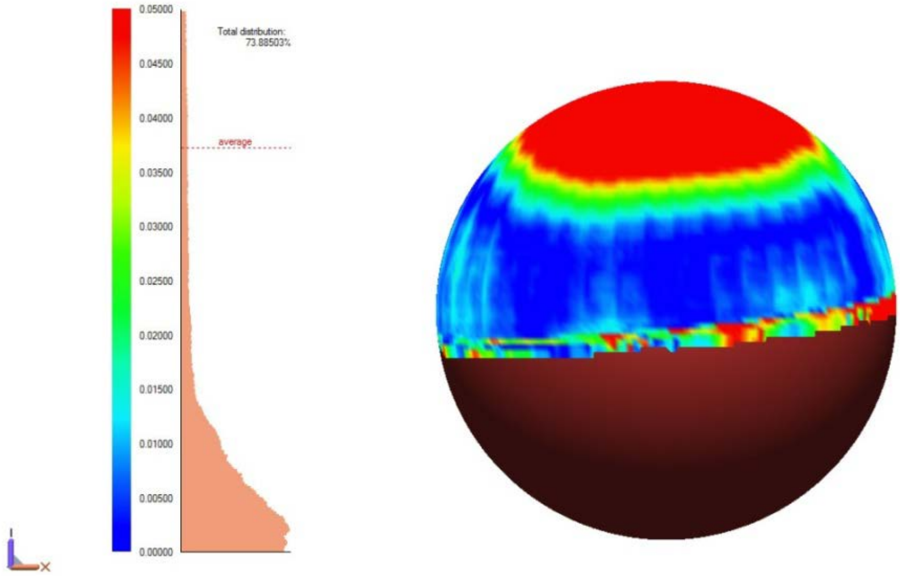

Figure 5: 3D model of the deformed design dome

In Fig. 6 the experiment result is presented, i.e. 3D dome model, obtained by superimposition of three models: design model, set by equation (1), real one, obtained by the results of laser scanning, and the deformed model.

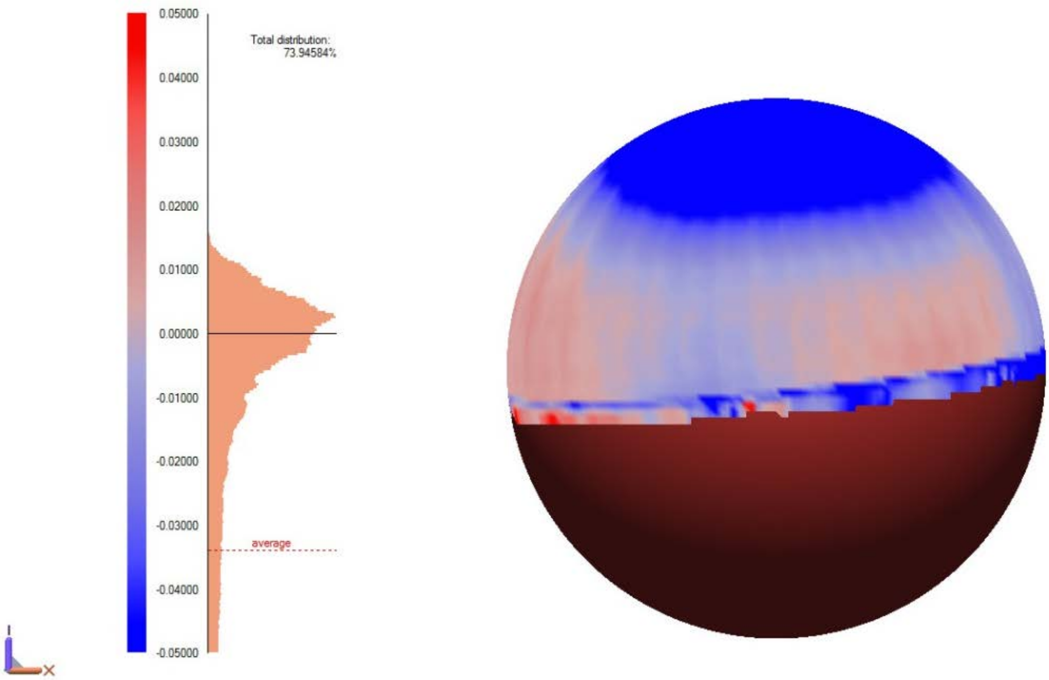

Figure 6: The result of three 3D models superimposition

The model is a result of three surface models averaging. It is not informative; the object deformation process is not represented.

3 CONCLUSION

The conclusion was made by the research results:
Using laser scanning for determining man-made object surface deformation we obtain complete visual information by superimposition of two 3D models. Applying quantitative characteristics, we receive mean square deviations of one model from the other.

1. Object deformation is a time dependent dynamic process that presupposes the work with the data time series. By the results of laser scanning the information on the object deformation at the set instant of time may be received. However the process is laborious. Function $D(t_i)$ in this case was determined discretely. For analysis, interpretation and prediction of deformation processes $D(t_i)$ should be determined as a continuous function that is impossible without mathematical simulation techniques.
2. Determination and visualization of man-made object surface deformations by laser scanning is well suited for reconstruction of buildings and structures and monitoring of geometric parameters by determining deviations from the design values.

REFERENCES

Books:

SEREDOVICH, V.A.: *Terrestrial laser scanning*. Siberian State Academy of Geodesy, Novosibirsk, 2009.

Journal articles:

BUGAKOVA, T.YU., *Objects state stability estimation by geodetic data using phase space method*. Author's abstract of dissertation for Candidate's degree, Siberian State Academy of Geodesy, Novosibirsk, 2005.

BUGAKOVA, T. YU., VOVK, I.G., *Mathematical simulation of systems time-space variations by geometric properties*, VIII International scientific congress, International scientific conference "Geodesy, geomatics, cartography, mine survey", Interexpo GEO-Siberia-2012, Vol. 3, Novosibirsk: SSGA, p. 26 – 31, 2012.

BUGAKOVA T. YU., VOVK I.G. *Mathematical simulation of system spatio-temporal variations by geometric properties, and man-made risk estimation by exponential smoothing*, Vestnik SSGA, 4/2012, p. 47-58, 2012.

BUGAKOVA, T.YU., *Problem of geoengineering systems risk evaluation by geodetic data*, VII Interexpo GEO-Siberia -2011, Vol.1, p. 151-157, 2011.

BUGAKOVA, T. YU., VOVK, I.G., *Determination of object rotational motion by repeated geodetic measurements*, Interexpo Geo Siberia – 2013: IX International scientific congress "15-26 April 2013, International scientific conference "Early warning and management under crisis and emergency situations: measures and their realization by means of cartography, geoinformation, GPS and remote sensing", Novosibirsk, SSGA, p. 88-92, 2013.

IVANOV, A. V., GOROKHOVA, E. I., GOROKHOVA, L. I., MURASHOV, K. V. *Creating a 3D model of the planetarium SSGA according to terrestrial laser scanning for modernization of the star hall*, Interexpo Geo Siberia – 2014: Xth International scientific congress "8-18 April 2014, International scientific conference "Geodesy, geomatics, cartography, mine survey", Novosibirsk, SSGA, p. 150-155, 2014.

Topographic Monitoring on Oil-and-Gas Fields

Alexey V. Dubrovsky, Olesya I. Malygina
Siberian State University of Geosystems and Technologies, Russian Federation

Abstract
Topographic monitoring is a system of continuous detecting of changes in spatial objects on the Earth surface and subsequent updating of their digital models. The system of oil-and-gas field monitoring is a complex multi-level process. Analysis of anthropogenic load structure on the oil-field territory reveals prevailing number of infrastructure objects (84 % of the total number of objects), this testifying to the mostly linear character of lands disturbance.

Keywords
Topographic monitoring, technogenic geodynamic events, geodetic control, anthropogenic natural territorial complexes

1 INTRODUCTION

According to article 3 of Federal law № 209-ФЗ "On geodesy and cartography" (of December 26, 1995) topographic monitoring refers to federal-purpose geodetic and cartographic works. Topographic monitoring is a system of continuous detecting of changes in spatial objects on the Earth surface and subsequent updating of their digital models.

The system of oil-and-gas field monitoring is a complex multi-level process including the following work stages:

- development of normative legal basis for topographic monitoring and requirements for the information accuracy, storage and representation results;.
- preparation of hardware and maintenance basis for works implementation;
- establishment of systems for continuous monitoring of territories state;
- automation of digital cartographic materials preparation and updating (for oil-and-gas field territory);
- organization of constant control over the topographic monitoring system.

Features of oil-and-gas complexes (by the example of Siberian region):

- remote and hard-to-reach location (most of the oil-and-gas fields)
- lack of the required density of geodetic control for the oil field territory;
- prevalence of linear disturbances of lands;
- high concentration of infrastructure determining the character of anthropogenic load on the territory;
- ecological and anthropogenic risks of pipe maintenance
- frigid climate and permafrost;
- technogenic geodynamic events caused by oil pumping;
- petrochemical pollution of the environment;
- long period of soil restoration;
- abundance of watered and swampy areas on the fields.

Due to its size, oil production volume, life of well, and features of geographic position, the changes in the oil fields landscape are the greatest in the region, with the area of completely disturbed lands exceeding 20 %. On the whole, there are almost no undisturbed natural territorial complexes NTC) left in the region. We can speak only about anthropogenic natural territorial complexes (ANTC). It should be mentioned that alongside with anthropogenic factors the most important and sometimes determining role in ANTC formation is plaid by the structure of primary undisturbed natural territorial complexes and their natural dynamics.
The most important effect on ANTC formation is made by the following NTC components:

- mechanical composition of soils and earth, which make up the surface, mostly tundra-gley and gley soils;

- composition and qualitative indicators of lignose, mainly, low vegetation;
- the degree of swampiness: more than 60% of the territory is swampy, covered by multiple small lakes;
- type of sand recovery (quarrying or hydraulic), determining the technique for intrafield road-bed filling. It’s a decisive factor in the absolute value of the territory disturbance and its type (linear or linear-areal);
- secondary current exogenous processes such as underflooding and thermokarst.

Environment of oil and gas fields territory is deteriorating, with lands being highly disturbed and contaminated. As concerns disturbed lands area, it grows insignificantly, with no more than 5 – 7 % of new objects arising on the fields (usually, multiple well fills). The areas of some multiple well platforms are growing with growing diking areas in process of oil spill recultivation. The area of open pits for common mining operations is also increasing.

The degree of the oil field land disturbance may depend on anthropogenic and natural factors.
Anthropogenic factors embrace:

- field area;
- oil production volume;
- application of special techniques, in particular, “superplatforms” development;
- cities and settlements with developed infrastructure on the oil field territory;
- main communications on the territory;
- technogenic geodynamic events (seismic events, subsidence, gaps, faults of the Earth surface) resulting from the hydrocarbon field development.

- Natural factors include: Soil cover;
- hydrocarbon occurrence depth;
- erosion processes (both water and wind ones)
- sea ice drifts;
- swamps and lakes of glacial origin on the territory.

2 ANALYSIS OF ANTHROPOGENIC LOAD STRUCTURE ON THE OIL-FIELD TERRITORY

Analysis of anthropogenic load structure on the oil-field territory reveals prevailing number of infrastructure objects (84 % of the total number of objects), this testifying to the mostly linear character of lands disturbance.
As concerns the oil fields territory contamination, it features:

- new oil spills and reservoir water overflow;
- some old oil spills areas growth due to pollutants migration;
- secondary changes in the environment state of some lakes with previously noticed oil slick.

Special attention should be paid to the degree of lakes pollution dynamics. Many of the lakes with previously observed oil slick reveal depositions of oil heavy fractions on their banks and bottom with vivid degradation of aquatic vegetation and intensive ‘bloom”.

The extent of contaminated and disturbed lands areas depends on a number of factors including oil production intensity, field size, its operation period, maintenance and transportation level, the way of landfilling (if any), communications state, and the territory landscape conditions. The latter affect ANTC (anthropogenic natural territorial complexes) formation in two ways: on the one hand, different NTC have different anthropogenic resistance levels, on the other hand, NTC structure itself in many cases determines the types and scales of these impacts. Fig. 1 presents the diagram of oil production units distribution by their actual area:

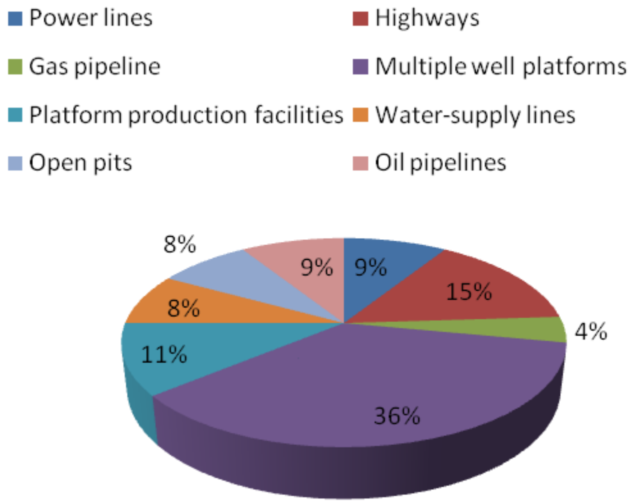

Figure 1. Diagram of oil production units distribution by their actual area

According to the diagram analysis the largest land area (55 %) is occupied by multiple well platforms, test holes, open pits and platform production facilities. Smaller areas are taken by highways, oil pipelines, water-supply lines, gas pipelines, and power lines. This distribution pattern is caused by the field structure, mostly by its the territory being oversaturated with production wells. The specific anthropogenic load density is over 15 %.

General scheme of topographic monitoring system for oil and gas field territory is shown in Fig.2.

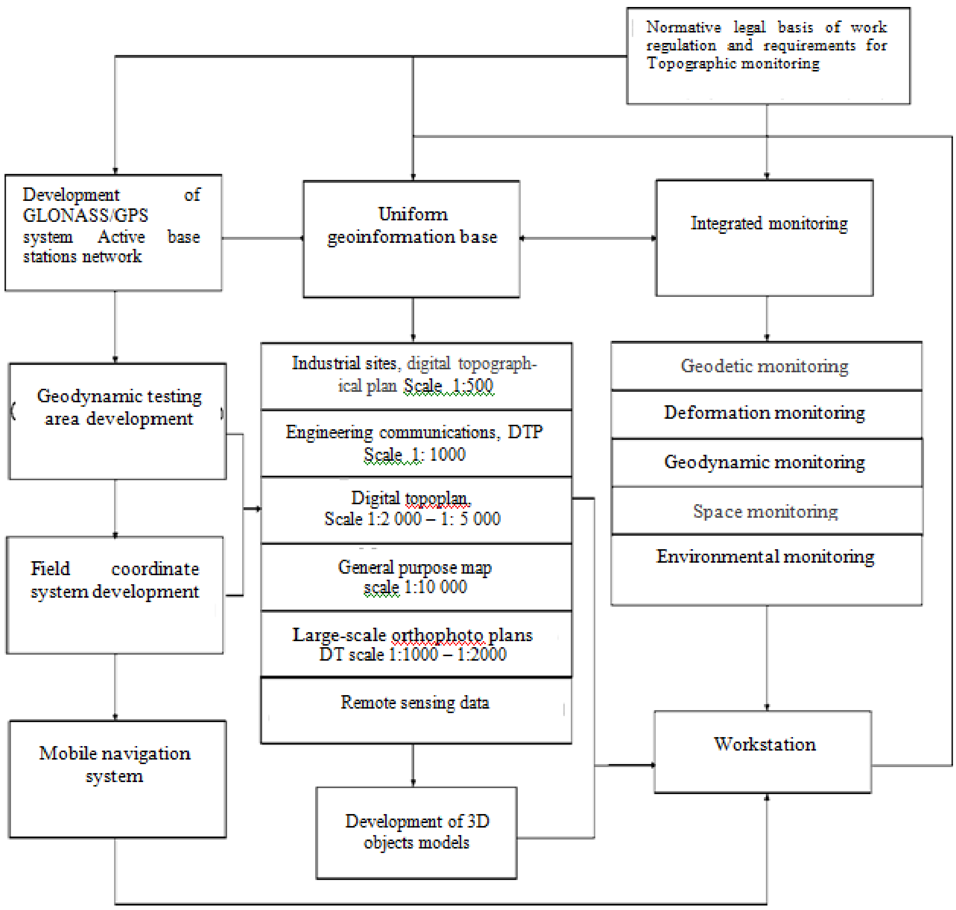

Figure 2: Scheme of topographic monitoring system arrangement on the territory of oil and gas field

3 STAGE OF GIS DEVELOPMENT

Improvement of engineering projects reliability, operating life and accident prevention has always been a pressing problem. This requires high-class topographic and geodetic backup by automated noncontact methods with optimum filtering, modeling, analysis, interpretation and forecasting. Geoinformation systems (GIS) may serve as an instrument for efficient application of integrated field observation results concerning the objects and processes under study. As a result, a uniform geoinformation basis for oil and gas field territory is created.

In home and foreign practice there is no sufficient experience in creating large-scale GIS with data bases of monitoring results concerning complex time-space relationship between engineering projects, geological conditions and environment as well as corresponding subsystems for management, mathematical treatment and modeling. GIS development is needed for timely accident and catastrophe prevention, optimization of the terms for preventive maintenance and repair works including the programs of integrated field observations. Therewith GIS efficiency is going to increase if mathematical modeling subsystems are supplied with the software for calculating the strength of engineering structures support frames by predictive estimates of deformations. Mathematical simulation allows for determining quantitative laws of deformation to be applied to the same-type engineering structures constructed and used under the same geological and environmental conditions. Knowledge of general regularities increases efficiency of designing, construction and maintenance of engineering projects. Thus, the authors suggest studying the affecting factors, geological environment and engineering projects as a uniform system. The idea of integrated topographic monitoring is offered. Not only new objects development, but also deformation processes are considered in ecological terms. Taking into account accuracy requirements for engineering solutions it is necessary to develop large-scale GIS for ecological cadaster and monitoring of the environment including engineering projects.

In accordance with the instructions “On mine surveying works” all the current changes taking place in the field are entered into mining-surveying plans quarterly. If topographical situation on the terrain changes by more than 35 % as compared with its representation on the plan, then a new mine-survey is to be conducted. The example of topographic and geodetic works results on oil-and-gas field territory is shown in Fig.3.

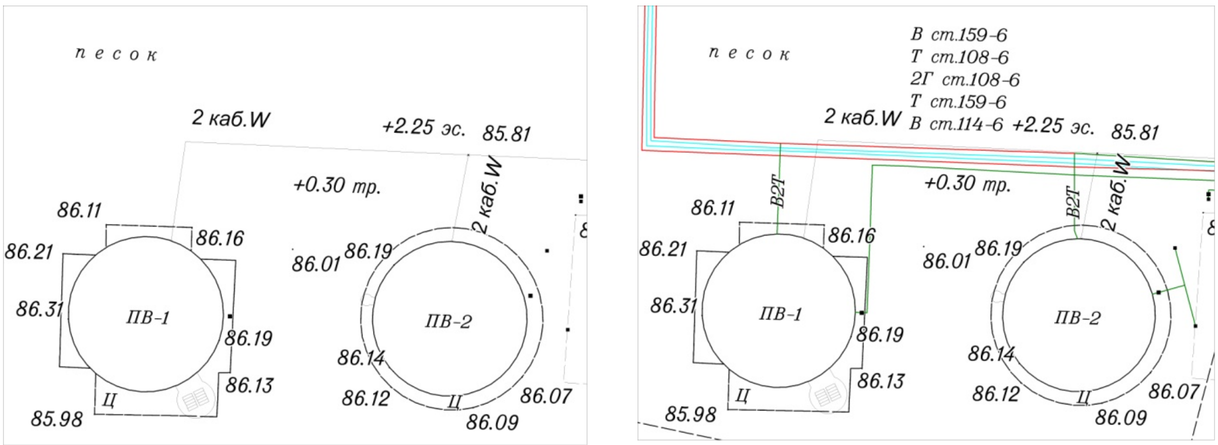

a) b)

Figure 3: Example of large-scale mapping: a) the territory before pipeline construction; b) updated topographic plan of the territory

The next stage of GIS development for the territory of oil-and- gas field involves development of techniques and software for joint intercycle mobile horizontal and vertical adjustment of networks and mathematical models identification. Therewith the mechanism of optimum filtration should be used to improve the accuracy of deformation detection and evaluate the model adequacy and accuracy. In process of creating dynamic models for processes and phenomena under study analogous mathematical treatment of other types of integrated field observations should be conducted.

The final step is the transition to kinematic and dynamic models for predicting each case of deformation process under study and their accuracy evaluation. To solve methodological problems, at the final stage it is necessary to develop hardware configuration and the structure of GIS program-technical complex subsystems interaction. Evidently, they should be developed based on the available technical and economic facilities, taking into account the results of previously solved problems. Development of GIS for geoecological and deformation monitoring is a challenge to be considered by specialists of different fields. However, geodetic methods of mathematical treatment and modeling are to prevail. Hence, it is topography and geodesy professionals that are to play the leading role as concerns scientific and technical basis of GIS development.

It should be noted that in home and foreign practice of oil production great attention is paid to technogenic geodynamic events: subsidence and fracture of the Earth crust and anomalous earth quakes on oil-and gas field territories. In connection with the above mentioned, development of expert-model GIS is an urgent problem. The systems are united by the common user interface of ordinary GIS with expert system shell and mathematical simulation block. Establishment of the uniform multipurpose system is not the only purpose considered by the authors. The existing software package is to be used for implementing a number of algorithms for topographic and geoecological monitoring of the territory. The research should be based on geoinformation involving the data of oil-production lands inventory. In the first place, it's large-scale digital topographic plans and maps, combined raster-vector models of the territory, land management projects, cadaster plans, registers of movable and real property of oil-and- gas production companies as well as digital maps of the territory anthropogenic load based on the above mentioned information.

4 CONCLUSIONS

Alongside with traditional geodetic methods the growing potential of precise gravimetry is emphasized. Combined with other research methods, gravimetry facilitates geodynamic monitoring problems, i.e. fractures, caverns, slides, tear-off fissures, registration of underground waters filtration regime, and classification of geological structures. On the basis of precise gravimetric measurements, low amplitude local gravity anomalies and their changes dynamics may be determined. That allows for obtaining detailed geological density characteristics of engineering structures foundations and estimating anthropogenic impact thereon.

REFERENCES

Books:

KHORUZHAYA, T.A. *Assessment of ecological danger. Kniga service, Moscow, 2002.*

Journal articles:

BUDAROVA V.A., DUBROVSKY A.V., KALENITSKY A.I., *Technique for processing the results of geodetic surveying for 3D prospecting seismology on oil-and-gas field territory*. Vestnik SGGA: scientific and technical journal/founded, GOU VPO "SGGA". Issue 1(12). Novosibirsk: SGGA, p. 21-27, 2010.

DUBROVSKY, A.V., *Formation of anthropogenic natural territorial complexes of oil-and-gas fields in North Siberia.* Collected scientific works of post-graduate students and young scientists, Siberian State Academy of Geodesy/edited by T.A. Shirokova, Novosibirsk, p. 19 – 24, 2004.

DUBROVSKY, A.V., *Mapping of anthropogenic load on oil-and-gas complex territory*. Materials of conference. Irkutsk, IrGTU, 2004.

DUBROVSKY, A.V., *Development and introduction of new geoinformation technologies for automating the process of oil-and-gas complexes lands inventory and establishing information basis for territories geomonitoring*. Brief outline reports, 9th Russian educational and practical conference "Organization, technology and experience of cadastral works", Moscow, GIS-Association, p. 16-18, 2004.

DUBROVSKY, A.V. *Mapping of anthropogenic load on oil-and-gas complex territory.* Materials of conference "Geodesy, cartography, cadaster of Baikal lands", Irkutsk, IrGTU, 2004.

Federal law of 26 December, 1995, № 209-FA "On geodesy and cartography"[Text] "Rossiyskaya gazeta", № 7, 13.01.1996.

RD 07-603-03 *Instructions for mine surveying works* (approved by Gostechnadzor of R.F., 6 June, 2003. N 73) to be introduced, 29 June 2003 [electronic resource] - http://www.iscgroup.ru/index.php?go=Files&in=view&id=346.

SEREDOVICH, V.A., *Mathematical simulation and identification of complex self-organizing geodynamic systems.* Progress report on the research work/SSGA; headed by V.A. Seredovich, № GR 012001.15981, Novosibirsk, SSGA, 2003.

SEREDOVICH, V.A., KALYUZHIN V.A., DUBROVSKY A.V., *Development of technologies for oil- and-gas complexes lands inventory on the basis of integrated data processing.* Brief outline reports, international production forum "Geoform+", Moscow, p. 28-29, 2005.

SEREDOVICH, V.A., KALYUZHIN V.A., DUBROVSKY A.V., *Development of GIS for territories of anthropogenic natural territorial complexes of oil-and-gas fields.* Materials of international scientific and technical conference on 225th anniversary of MIIGAiK, Moscow, MIIGAiK, p. 133-138, 2004.

TECHNICAL SESSION 2: GNSS – SOLUTIONS I

New Developments and Applications for LowCost GNSS/MEMS based Monitoring

Dipl.-Ing. (FH) Julia Diekert
Institute of Applied Research, University of Applied Sciences Karlsruhe, Germany

Abstract
Geo-Monitoring of buildings and natural structures is increasingly supplemented by Structural Health Monitoring (SHM). The measurements are set in relation to the physical parameters of the structure which are usually defined as a finite element model (FEM), in order to detect and localize changes in these parameters. The dynamic SHM has the advantage in respect to static SHM, that the mass matrix and damping matrix of moving structures are includes, so in addition to displacements $\mathbf{u}$ the velocity $\dot{\mathbf{u}}$ and acceleration $\ddot{\mathbf{u}}$ a are taking into account.
Therefore the complete navigation state vector has to be determined. In order to achieve this economically, L1 GNSS receivers are fused with MEMS-IMU. However, an advanced modeling is required to achieve a sufficient accuracy for monitoring for example by integrating inequality constraints into the robust adjustment. These problems can be solved with Simplex or algorithms for Quadratic Programming Problem, for example the Active Set Algorithm, that is shortly described herein.

After the theoretical discussions, a suitable low-cost MEMS sensor and the software GOCA GNSS control to control and define the GNSS receivers and sensor networks. The measurements taken at the Stuttgart TV tower with an GNSS/IMU are investigated in regard to various aspects of a frequency analysis to determine the natural frequency of the tower for a simplified SHM. It turns out that the fused speed from GNSS and MEMS is very suitable for the frequency ranges below 1 Hz, which is the range of the natural frequency of many towers. But accelerometers that can be installed within the structure measure, can determine the high-frequency oscillations, that are in some applications just as interesting as the Eigen frequency itself.

Keywords
LowCost GNSS, MEMS, Dynamic Structural Health Monitoring, Frequency Analysis, Inequality Constraints, Robust Adjustment

1 INTRODUCTION

One of future challenges, especially for growing and densely-populated cities is limited space. Therefore new infrastructure and buildings often have to be built in a closely spaced environment or based upon already existing structures. Therefore the need for a reliable and secure monitoring of building and structures alongside construction sites is constantly increasing.

This concerns not only the static monitoring but also monitoring of moving, e.g. vibrating buildings and towers. A change for example in the natural frequency of the vibration may indicate on a material defect or on an already critical damage to the building. This can be detected and localized with the methods of Structural Health Monitoring (SHM).

High frequency vibrations must be recorded therefore by suitable sensors that can detect these vibrations. These are in particular accelerometers and gyroscopes, that are coupled as an Inertial Measurement Unit (IMU). IMUs combined with GNSS can capture both slow oscillations, as well as fast vibrations. For the high-precision positioning two-frequency GNSS receiver are used, but also increasingly L1 receivers, if the ambiguities can be fixed in a static or quasi-static mode and with a nearby reference station. The combination of raw-capable L1 receivers with an IMU as a LowCost solution is therefore very well suited for structural health monitoring. However, if the ambiguities cannot be reliably fixed, it immediately goes hand in hand with an accuracy reduction, which is mostly not acceptable in geo monitoring. So the IMU in a coupled GNSS/MEMS system can also hold the position accuracy in the case of short-time "Loss of Fix".

2 MONITORING AS DATA COLLECTION, MODELING, REPORTING AND REACTION

Monitoring can be seen as a chain of different interacting processes, including geo data acquisition, modeling, reporting and alerting on reaching critical states (Fig. 1). The following section will have particular regard to the modeling. Here, an improved modeling both by introducing conditions that can be tailored to the application and by exact modeling of dynamic SHM, the advanced modeling can achieve a better performance compared to classical deformation analysis.

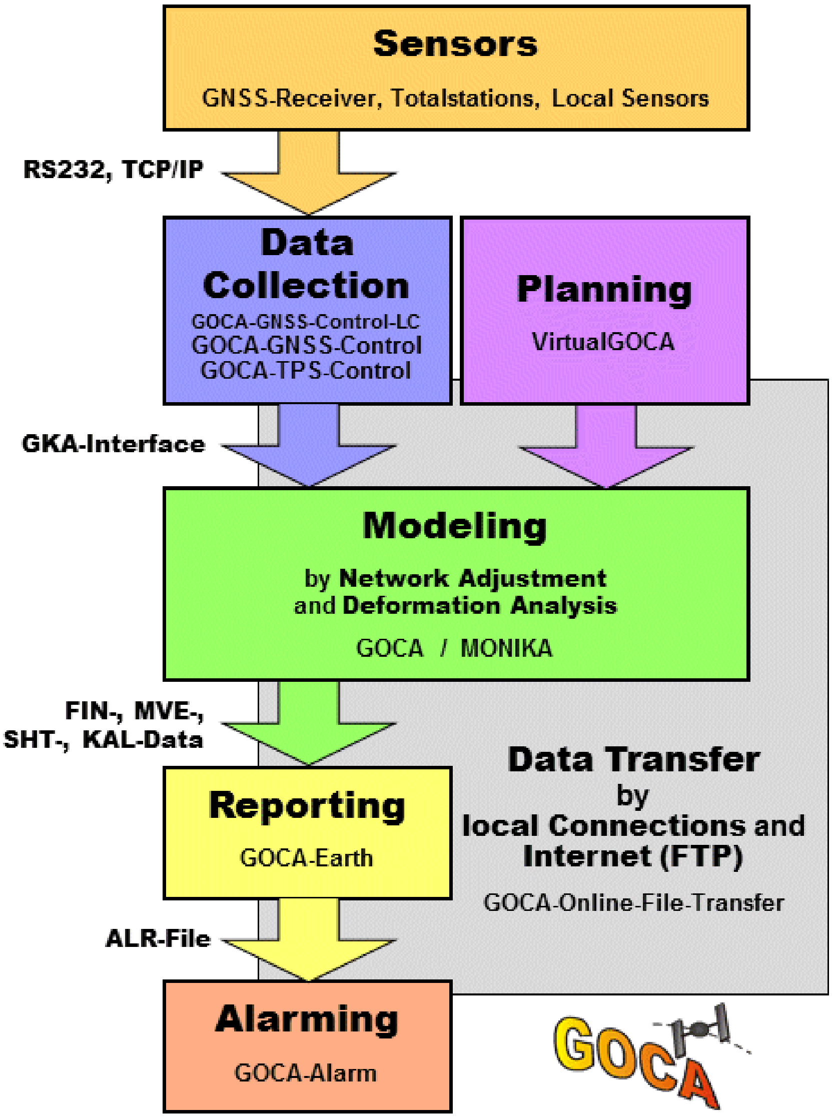

Figure 1: Components of the geomonitoring chain at the example of the GOCA-System

2.1 Advanced Modelling with Equations as Constraints in a Robust Adjustment

As monitoring usually is a very specific applications, additional conditions can often be defined that cannot be assumed in other navigation applications, for example, that a sensor (physically) can only be in a certain maximum inclination, or that other sensors only move as a unit. These additional conditions may be introduced either as additional equations or inequalities into the system model.

There are different approaches to include constraints into the adjustment, as investigated in [SIMON], for example by a model reduction (rendering) or projection onto a constraint surface. A simple and straight-forward integration is to use "perfect observations", if the conditions can be represented as equations of the form $\mathbf{Bx} = \mathbf{b}$. They can equally be introduced into a standard Least Squares adjustment, as well as into a robust adjustment. Perfect observations are virtual observations that can be considered in the observations covariance matrix $\mathbf{C_{ll}}$ with a very small standard deviation.

As an example for robust adjustment the classic Huber estimator is based on the following loss and influence functions, as it is described in [JÄGER ET AL., 2005]:

Loss function:
$$\rho(\bar{\varepsilon}) = \begin{cases} \frac{1}{2} \cdot \bar{\varepsilon}^2 & \text{for } |\bar{\varepsilon}| < k \\ k \cdot |\bar{\varepsilon}| - \frac{1}{2} k^2 & \text{for } |\bar{\varepsilon}| \geq k \end{cases} \tag{1}$$

Influence function:
$$\psi(\bar{\varepsilon}) = \frac{d\rho(\bar{\varepsilon})}{d\bar{\varepsilon}} = \begin{cases} \bar{\varepsilon} & \text{for } |\bar{\varepsilon}| < k \\ \frac{k \cdot \bar{\varepsilon}}{|\bar{\varepsilon}|} & \text{for } |\bar{\varepsilon}| \geq k \end{cases} \tag{2}$$

The continuous loss function of the Huber estimator is thus within the interval [-k,k] identical to the least-squares adjustment, outside of this interval it is linear. Therefore the influence function is limited and the estimation is considered robust against gross errors.

To determine the unknown parameters $\hat{\mathbf{x}}_\mathbf{M}$, an iterative approach can be used, where the estimator weight matrix $\mathbf{W}(\hat{\mathbf{x}}_\mathbf{M}^\mathbf{k})$ is calculated at each iteration step k to determine a new estimation of $\hat{\mathbf{x}}_\mathbf{M}^{k+1}$.

Iterative parameter estimation:
$$\hat{\mathbf{x}}_\mathbf{M}^\mathbf{k+1} = \left(\overline{\mathbf{A}}^\mathbf{T} \cdot \mathbf{W}^\mathbf{k} \cdot \overline{\mathbf{A}}\right)^{-1} \cdot \overline{\mathbf{A}}^\mathbf{T} \cdot \mathbf{W}^\mathbf{k} \cdot \bar{\mathbf{l}} \tag{3}$$

with the weight matrix
$$\mathbf{W}^k = diag\left\{w_i^k\right\} \tag{4}$$

$$\text{with } \mathbf{w}^\mathbf{k} = \frac{\boldsymbol{\psi}\left(\overline{\mathbf{A}} \cdot \hat{\mathbf{x}}_\mathbf{M}^\mathbf{k} - \bar{\mathbf{l}}\right)}{\overline{\mathbf{A}} \cdot \hat{\mathbf{x}}_\mathbf{M}^\mathbf{k} - \bar{\mathbf{l}}} \tag{5}$$

In equation (5) $\overline{\mathbf{A}}$ and $\bar{\mathbf{l}}$ are the homogenized Jacobi matrix respective observation vector. This homogenization can be achieved with $\overline{\mathbf{A}} = \mathbf{C_{ll}}^{-\frac{1}{2}} \cdot \mathbf{A}$ and $\bar{\mathbf{l}} = \mathbf{C_{ll}}^{-\frac{1}{2}} \cdot \mathbf{l}$.

Virtual observations should be excluded from the iterative weighting process due to their strict behavior. On the other hand, if virtual observations from constraints are weighted down, this could also hint on an erroneous system model.

Alternatively to the iterative adjustment described herein, the L1-norm estimation can also be calculated with other algorithms, for example the Barrodale-Roberts-Algorithms [BARRODALE & ROBERTS, 1974].

2.2 Solving Inequalitiy Constraints with the Active Set Method (Quadratic Programming)

There are multiple approaches to introduce inequality constraints that have different advantages. Since most investigations focus on least squares adjustment, the introduction of inequality constraints into L2-Norm is thoroughly investigated in [ROESE-KOERNER ET AL]. To solve the problem of inequality constraints, algorithms for quadratic programming problems are used, for example the interior point approach and active set method, that is very popular.

The greater-than inequality constraints can be transformed into smaller-than inequality by multiplying the equation with minus 1, so the equality constraint can be defined in the form $\mathbf{B^T} \cdot \mathbf{x} < \mathbf{b}$.

For solving the resulting quadratic programming problem the objective minimization function $\mathbf{v^T P v} = \min$ from the least squares adjustment is substituted into the new objective function $\gamma_1 \mathbf{x^T} \cdot \mathbf{Cx} + \gamma_2 \mathbf{c^T x} = \min$, as derived in [ROESE-KOERNER ET AL] with:

$$\mathbf{C} = 2 \cdot \mathbf{A^T P A} \quad \text{and} \quad \gamma_1 = \tfrac{1}{2} \qquad (6)$$
$$\mathbf{c} = -2 \cdot \mathbf{A^T P l} \qquad \gamma_2 = 1$$

The active set method itself is an iterative approach, with the following steps, that are described below:

- (Step 1) Choosing an initial parameter state x^0
- (Step 2) Calculate the search direction p^i
- (Step 3) Compute step length q^i
- (Step 4) Update $\mathbf{x^{i+1}} = \mathbf{x^i} + q^i \cdot \mathbf{p^i}$
  - If one of the inequality constraints is violated, it becomes active, and the iteration starts anew from Step 2
  - (Step 5) Otherwise calculate the Lagrange multipliers k. If all Lagrange multipliers are positive, the optimal solution is found, otherwise all constraints with k<0 are inactivated and the iteration goes back to Step 2.

The search direction (from Step 2) is calculated by the vector difference of the initial parameter state x0 and the adjusted parameters from solving the unconstrained problem

$$\mathbf{p^i} = \hat{\mathbf{x}} - \mathbf{x}^0 \text{ with} \qquad \hat{\mathbf{x}} = \left(\mathbf{A^T P A}\right)^{-1} \cdot \mathbf{A^T P l} = -\mathbf{C}^{-1}\mathbf{c} \qquad (7)$$

The length of the search direction **p** has to be chosen, so that a subset of constraints are exactly fulfilled (the active set), while the other constraints, that are not fulfilled are inactive. For a complete calculation scheme of Step 3, including calculation of the active set matrix W, see [ROESE-KOERNER ET AL].

If no constraints are violated after the update step 4, the objection function can be extended to the general Lagrange function

$$\mathbf{\Phi}(\hat{\mathbf{x}}, \mathbf{k}) = \tfrac{1}{2}\mathbf{x^T C x} + \mathbf{c^T x} + \mathbf{k^T} \cdot \left(\mathbf{B^T x} - \mathbf{b}\right) \qquad (8)$$

The Lagrange multipliers k for step 5 can be calculated by using the active set matrix W and solving the linear equation system $\mathbf{p}^{*(\mathbf{i+1})} = \overline{\mathbf{W}}^{\mathbf{i+1}} \mathbf{k}^{\mathbf{i+1}}$. If all Lagrange multipliers k are positive, then the optimal solution is found.

One of the drawbacks of the active set method, as well as of other quadratic programming approaches is, that no stochastic information about the estimated parameters x is calculated. This issue could be addressed for example with a Monte Carlo Simulation.

Another approach for solving a minimization problem that is constrained with inequalities is by using Linear Programming techniques, such as Simplex. The restrictions, benefits and problems of these algorithms [DANTZIG & THAPA] for a geodetic monitoring problem are one of the main topics of further research.

2.3. Dynamic Structural Health Monitoring

The parameters $\mathbf{y}(t) = [\mathbf{u}(t), \dot{\mathbf{u}}(t), \ddot{\mathbf{u}}(t)]^T$ (displacement, velocity and acceleration), which are part of the navigation state, can be used to determine the physical parameters p of an integrated deformation analysis, that can defined as FEM model. In the integrated deformation analysis changes $\Delta\mathbf{p}$ in these parameters can be detected, which could result from damage or material weaknesses.

In the case of static FEM-based structural health monitoring only changes in the stiffness matrix $\mathbf{K}(p_K)$ are considered. In contrast, in the dynamic case as for example, in case of vibrations, also changes in the mass and damping matrix $\mathbf{M}(p_M)$ and $\mathbf{C}(p_C)$ of a structure are detectable.

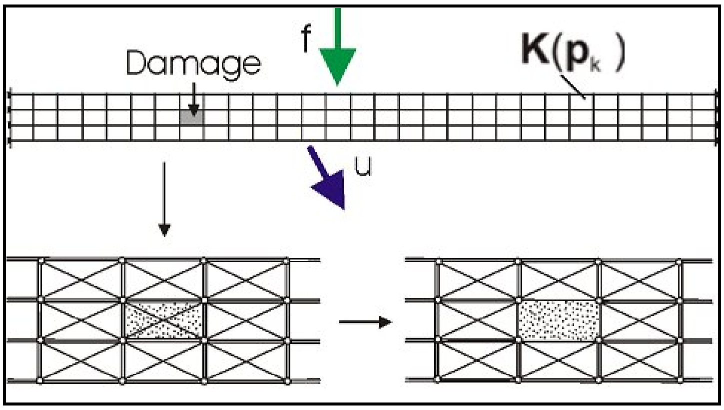

Figure 2: Integrated deformation analysis in the static FEM approach at the example of a dam [JÄGER, 2014]

The vibration, which is stimulated by an external force f (t), and the so-called natural or Eigen vibrations with f (t) = 0 can be represented in dependency of the mass and damping matrix $\mathbf{M}(p_M)$ and $\mathbf{C}(p_C)$ and the stiffness matrix $\mathbf{K}(p_K)$ as:

General damped vibrations: $$\mathbf{K}(\mathbf{p}_K)\cdot\mathbf{u}(t) + \mathbf{C}(\mathbf{p}_C)\cdot\dot{\mathbf{u}}(t) + \mathbf{M}(\mathbf{p}_M)\cdot\ddot{\mathbf{u}}(t) = \mathbf{f}(t) \qquad (9)$$

Damped Eigen vibrations: $$\mathbf{K}(\mathbf{p}_K)\cdot\mathbf{u}(t) + \mathbf{C}(\mathbf{p}_C)\cdot\dot{\mathbf{u}}(t) + \mathbf{M}(\mathbf{p}_M)\cdot\ddot{\mathbf{u}}(t) = \mathbf{0} \qquad (10)$$

2.3.1 Dynamic Structural Health Monitoring in the Time Domain

One way for a dynamic SHM provides the state transition matrix of the geometric parameters. Considering the state transition matrix of the damped Eigen vibrations (that is derived in [JÄGER, 2004]), it can be stated that the parameters $\dot{\mathbf{u}}$ and $\ddot{\mathbf{u}}$ are directly related to the physical parameters (Equation 11).

State transition of Eigen vibrations:

$$\begin{bmatrix} \mathbf{u_O(t+\Delta t)} \\ \dot{\mathbf{u}}_\mathbf{O}\mathbf{(t+\Delta t)} \\ \ddot{\mathbf{u}}_\mathbf{O}\mathbf{(t+\Delta t)} \end{bmatrix} = \begin{bmatrix} \mathbf{I} & [\mathbf{\Delta t}] & \left[\frac{1}{2}\mathbf{\Delta t}^2\right] \\ \mathbf{0} & \mathbf{I} & [\mathbf{\Delta t}] \\ \mathbf{0} & [-\mathbf{M(p_M)}^{-1}\cdot\mathbf{K(p_K)}\cdot\mathbf{\Delta t}] & [\mathbf{I}-\mathbf{M(p_M)}^{-1}\cdot\mathbf{C(p_C)}\cdot\mathbf{\Delta t}] \end{bmatrix} \cdot \begin{bmatrix} \mathbf{u_O(k)} \\ \dot{\mathbf{u}}_\mathbf{O}\mathbf{(k)} \\ \ddot{\mathbf{u}}_\mathbf{O}\mathbf{(k)} \end{bmatrix} \qquad (11)$$

In most cases, the physical properties, namely $\mathbf{p} = (\mathbf{p_K}, \mathbf{p_C}, \mathbf{p_M})^T$ of the building, will be well known from the FEM model based on the construction structural analysis. But there are also objects, where these parameters are unknown and have to be determined. One of the possible solutions is to estimate these parameters in a Kalman Filter. While the structure is stimulated with a known force or vibrating with Eigen vibrations, displacement, velocity and acceleration at different positions are measured and the parameters p are determined and stored over a longer period of time. In the following stages, these parameters and their stability can be monitored.

2.3.2 Dynamic Structural Health Monitoring in the Frequency Domain

Another possibility for a dynamic Structural Health Monitoring offers the transformation into the frequency domain, the so-called spectral approach [JÄGER 1988].

In case of undamped Eigen vibrations (with $\mathbf{C}(\mathbf{p}_C) = \mathbf{0}$) the following equations can be derived [ZIENKIEWICZ].

$$[\mathbf{K}(\mathbf{p}_K) - \omega^2 \cdot \mathbf{M}(p_M)] \cdot \varphi(\mathbf{x}) = \mathbf{0} \tag{12}$$

With the solution of this equation system (with the dimension *n* from matrix **K** and **M**), the *n* Eigen frequencies ω_i can be calculated with n Eigen nodes $\varphi_i(\mathbf{x})$, that are the normalized Eigen vectors of equation (12) and depending on the position x.

After differentiating the equation (analogue to the time domain dynamic approach), we can derive the following equation set [JÄGER, 1988], that parameterizes the changes of the Eigen frequencies and Eigen nodes in respect to changes of the stiffness and mass matrices **K** and **M**.

$$\Delta\omega_i^2(\Delta\mathbf{p}_K, \Delta\mathbf{p}_M) = \boldsymbol{\varphi}_i^T \cdot [d\mathbf{K}(\Delta\mathbf{p}_K) - \omega_i^2 \cdot d\mathbf{M}(\Delta\mathbf{p}_M)].\boldsymbol{\varphi}_i \tag{13}$$

$$\Delta\boldsymbol{\varphi}_i(\Delta\mathbf{p}_k, \Delta\mathbf{p}_M) = -\frac{\boldsymbol{\varphi}_i^T \cdot d\mathbf{M}(\Delta\mathbf{p}_M) \cdot \boldsymbol{\varphi}_i}{2} + \sum_{\substack{j=1,\\ j\neq i}}^{n} \frac{1}{\omega_i^2 - \omega_j^2} \boldsymbol{\varphi}_i^T \cdot [d\mathbf{K}(\Delta\mathbf{p}_K) - d\mathbf{M}(\Delta\mathbf{p}_M)] \cdot \boldsymbol{\varphi}_j \tag{14}$$

The solution to (13) and (14) is a so-called inverse Eigen value-Eigen-vector problem, that is the task to calculate the changes in the parameterization (right side of the equation system) based on the changes in the spectral characteristics (left side) of the Eigen value problem.

The changes in the frequency can be determined with a frequency analysis from acceleration, velocity or displacement measurements, as it is done in Chapter 3.2.

3 THE MONITORING CHAIN IN PRACTICE

3.1 Geo Data Acquisition with Low-Cost GNSS and MEMS

The sensor network for monitoring must be adapted to the expected result. This refers both to the accuracy of the individual sensors, as well as other properties such as data rate, robustness against external influences and error characteristics of individual sensors, as well as installation and maintenance costs. Although the sensor network as a whole must be able to measure all the desired parameters, below only geo data sensors are considered.

For many monitoring projects, a network can be set up, for example with few total stations and GNSS receivers, which cover together a large number of points. In the case of an oscillating structure, however, fewer points need to be measured continuously with high frequency. Therefore in particular GNSS and MEMS are suitable.

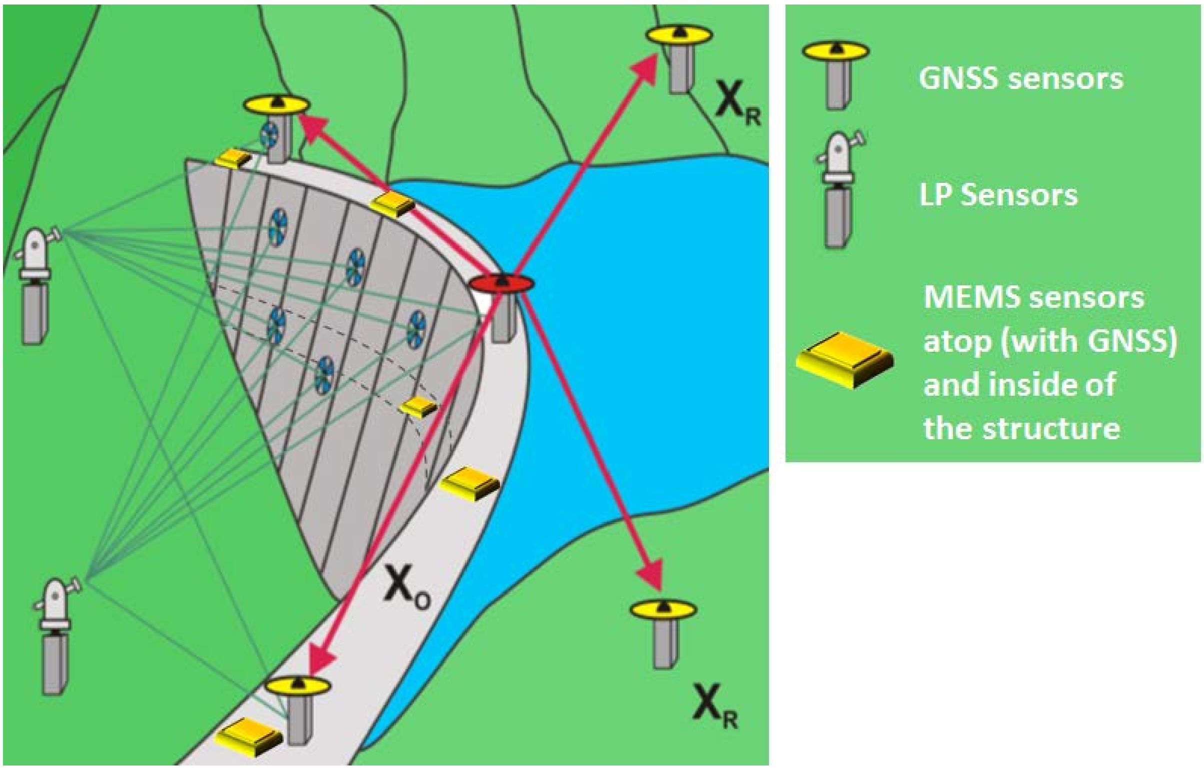

Figure 3: Network of GNSS, LP and MEMS sensors for geomonitoring

While pure GNSS is very suitable for the determination of vibrations with low frequency (< 10 Hz), a good choice for higher frequency are MEMS sensors. As part of the joint project "GNSS/INS multi sensor systems for a mobile platform navigation" (www.navka.de) a sensor platform has been developed which is optimized primarily for navigation tasks. This "Robinette GM1", assembled by the company teXXmo mobile Solutions, Böblingen (www.texxmo.de), is used, but "MEMS-boxes" in many designs and for different accuracy requirements are available.

Figure 4: GNSS&MEMS navigation-box “Robinette GM1” with interfaces.

For the data acquisition of the GNSS receiver, the software module GOCA GNSS Control (www.goca.info) is used, that simplifies the configuration of networks with multiple GNSS receivers and can perform the direct integration of data into the GOCA software for deformation analysis.

Each receiver can be controlled individually or together in a GNSS array. GOCA GNSS Control allows to create multiple networks, which are changed iteratively after certain time intervals (Fig. 5). This allows the detection of systematic errors from the network design. GOCA GNSS Control can respond to various problem situations, such as the failure of a GNSS receiver or poor satellite visibility at one location. An interface to the software module GOCA alarm allows the alarm on different hardware problems.

For the GNSS processing there are several possibilities:

- RINEX Data Collection for post-processing analysis
- RINEX processing for near-line analysis
- RTK processing with
  - internal hardware processors
  - external WANNINGER SOFTWARE WA1 processing engine
  - integrated GNSS RTK processing based on RTKLIB1functions and methods:
    RTKLIB is an open source software package for GNSS processing. More information can be found at www.rtklib.com

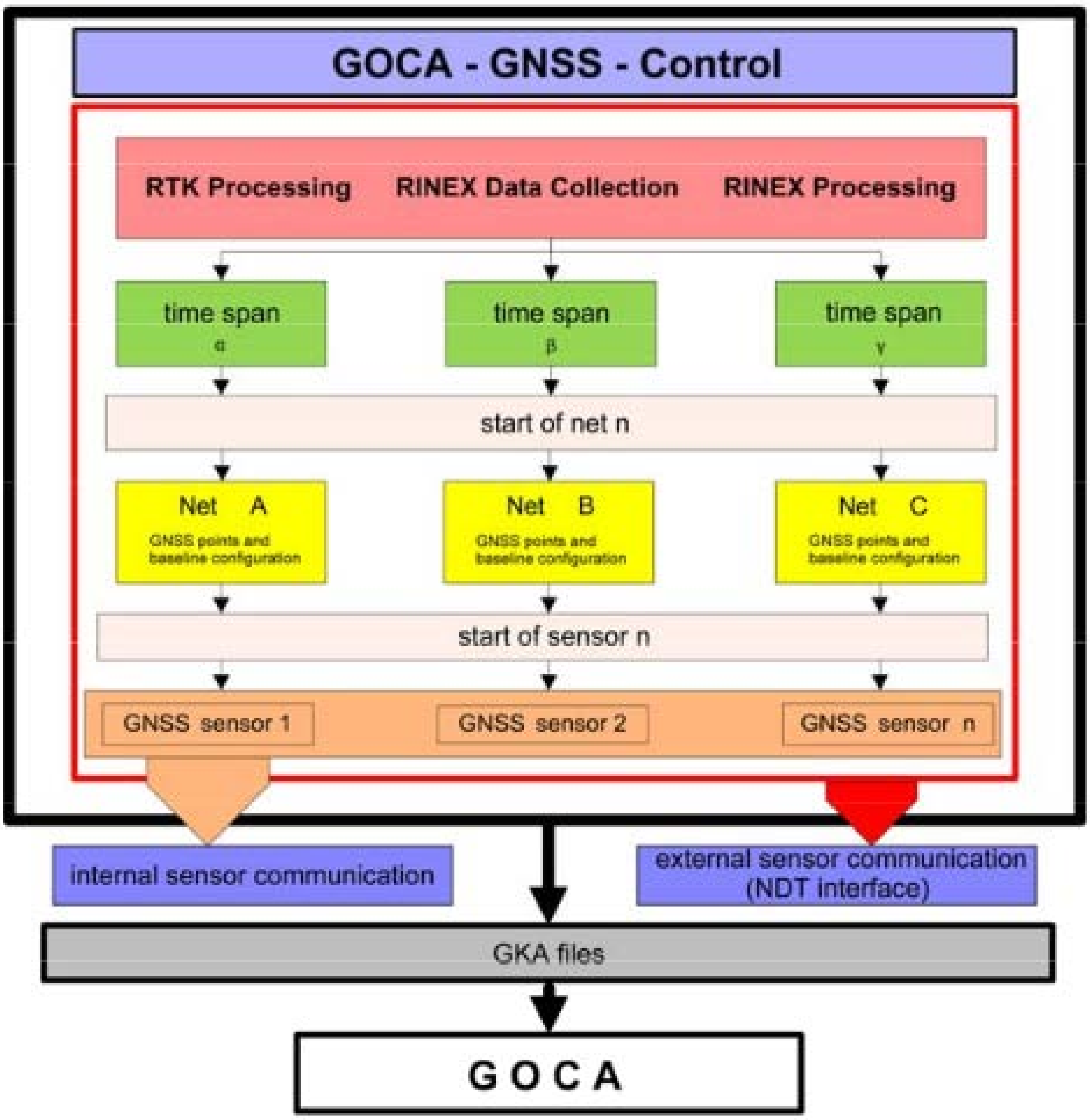

Figure 5: GNSS network design in GOCA GNSS Control

3.2 SHM on the Example of Stuttgart Television Tower

As part of a Bachelor thesis [BAIER], the Stuttgart TV tower could be monitored for several days with different weather conditions. In addition to the Robinette GM1 a Leica GNSS two frequency receiver was used, which was operated automatically with GOCA-GNSS-Control LowCost ("LC"), that is a simplified software version. This receiver was operated in differential mode with a SAPOS reference station.

The aim of the thesis [BAIER] was to investigate the influence of weather, especially wind and solar insolation on the vibration behaviour of the tower. For that purpose only the GNSS receiver was used that could determine the position of the antenna that was attached to the tower with high accuracy.

Figure 6: Robinette GM1 and Leica Antenna are installed above the visitors platform [Photo: BAIER]

It was found that the amplitude and the shape of the elliptical oscillating movement strongly depends on the weather conditions (see table 1), but the natural frequency of the tower is independent and very stable with 0.195 Hz. The following values of the oscillation behaviour of the tower were determined with this high-precision GNSS solution:

Table 1: Extract from the tables of [BAIER] for the oscillation frequency and amplitude on days with different wind conditions, determined with two frequency DGNSS solution

Date	Wind velocity [m/s]	Wind azimuth [°]	Ø of semi-minor [cm]	Ø of semi-major [cm]	Frequency [Hz]
18.11.14	8-9.5	275 – 285	2.0	3.5	0.196
11.12.14	15-23	220-235	3.0	8.5	0.195
12.12.14	15-18	218-228	2.0	12.0	0.195
03.01.15	15-16	330-350	4.0	6.0	0.196
09.01.15	16-20	220-230	2.5 - 5.0	6.0 – 9.0	0.195

Due to its stability the primary objective in the context of structural health monitoring could be to monitor the natural frequency of the tower. The two frequency GNSS solution is very well suited for this task, as it is shown in [BAIER], as well as in other investigations [BREUER ET AL.]. However, cost-effective and high-frequency MEMS sensors, determine further system-relevant frequencies in addition to the natural frequency.

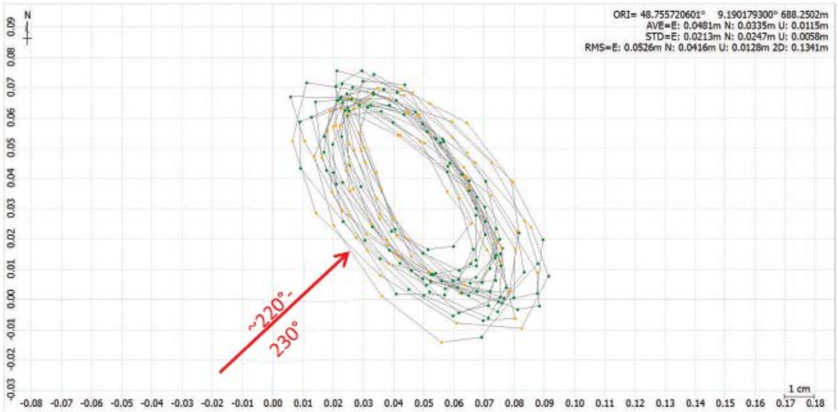

Figure 7: Plot of the GNSS antenna position, taken on 09.01.15 during a 180 sec measurement interval with strong wind coming from azimuth 220 – 230 °[BAIER]

3.2.1 Frequency Analysis of Acceleration Data

The data from the accelerometers in different time periods have been transformed by a Fast Fourier transformation into the frequency domain. The measurements were taken on a windless day. Considering the frequency spectrum of the acceleration data it can be seen that in addition to the natural frequency more oscillations can be found whose amplitude can be higher than the natural frequency.

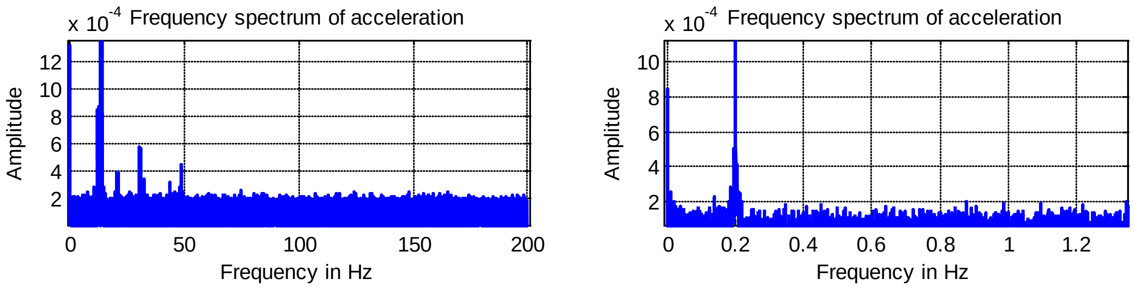

Figure 8: Left: Complete Frequency spectrum of the Robinette GM1 data with 25 min measurement interval and 400 Hz sampling rate. Right: Zoom on the frequency region of the Eigen frequency

In this examination the natural frequency can be significantly determined at a measuring period of 25 min. The oscillation in the range of 13.5 Hz is a vibration of the aluminum lattice, where the sensor is attached to, while the vibration of about 46 Hz is resulting from the movements of the elevator, since its mechanical room was in close proximity to the sensors.

Since the natural frequency of the tower is interesting, the data can also be sampled in a lower frequency in order to enable a faster calculation. In the case of the available noisy acceleration data, a sampling frequency in the order of 25 Hz is sufficient to determine the natural frequency, below thatthe frequency cannot be significantly distinguished from noise.

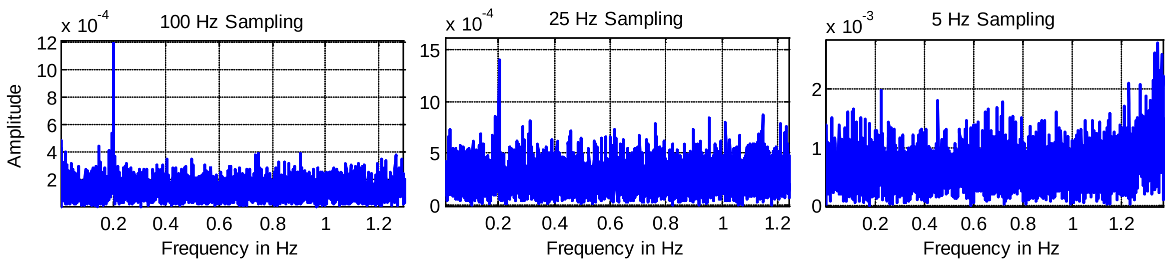

Figure 9: Zoom on the frequency spectrum with 100 Hz, 25 Hz and 5 Hz sampling rate (from left to right)

In order to detect the natural frequency, shorter time intervals may be chosen, so that a shift of the frequency may be detected reliably even after a few oscillation cycles. Therefore the measurement set was divided into time series of 1 min, 2 min and 5 min and the frequency spectrum of each period was calculated separately.

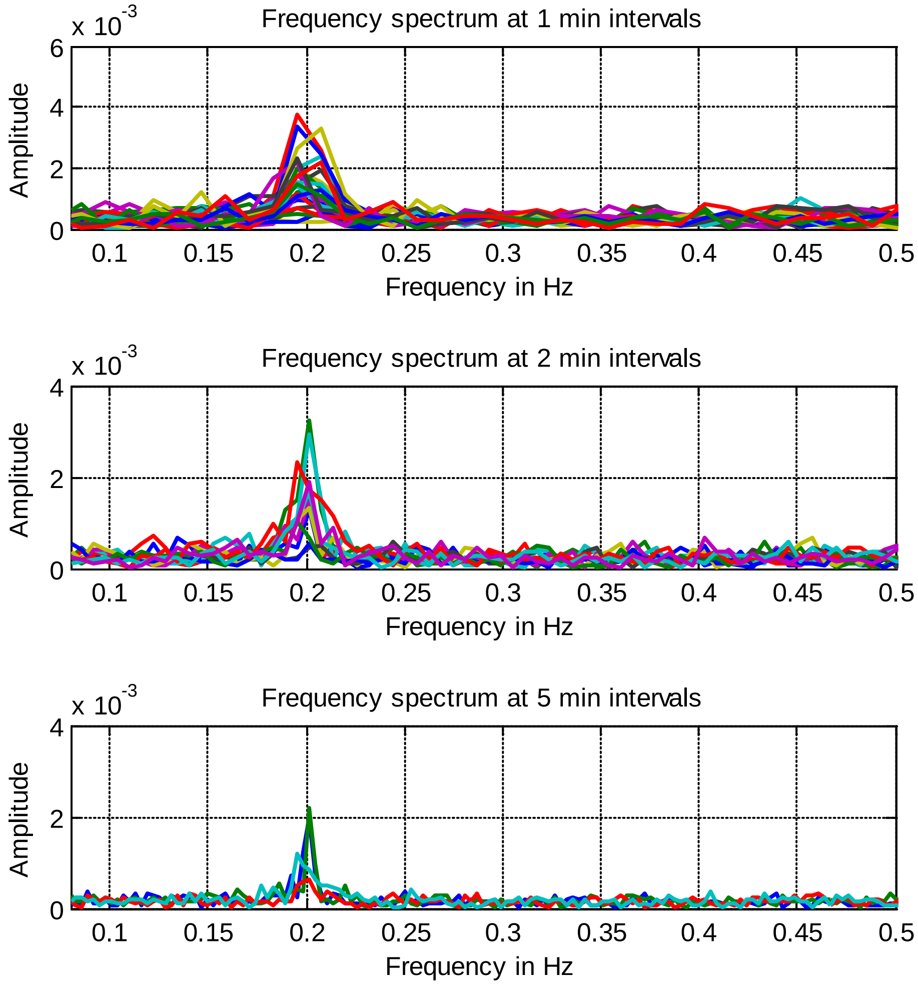

Figure 10: Frequency spectrum of 1 min, 2 min and 5 min measurement intervals (from top to bottom) for each time series

It turns out that a time interval with at least 2 minutes, or better with 5 min length should be chosen, to determine the natural frequency with the acceleration sensor that was used in this case. If smaller measurement periods are chosen, the frequency could not be detected in each time series, so a false alarm could be raised.

3.2.2 Frequency analysis of the velocity data

If the GNSS receiver of the Robinette is active, the GNSS velocity and the IMU data can be fused in a loose coupled Kalman filter with a navigation state, that consists only of the velocity and sensor errors. The fusion of GNSS raw data (Pseudoranges, Phase and Doppler measurement) with IMU raw data is only interesting, if the position is also to be determined.

This adjusted velocity from the fusion of GNSS and IMU can also be used as an input into the FFT. It can be seen that it is even better suitable to measure the natural frequency of the tower, but that increased accuracy comes with the disadvantage of a sufficient satellite visibility.

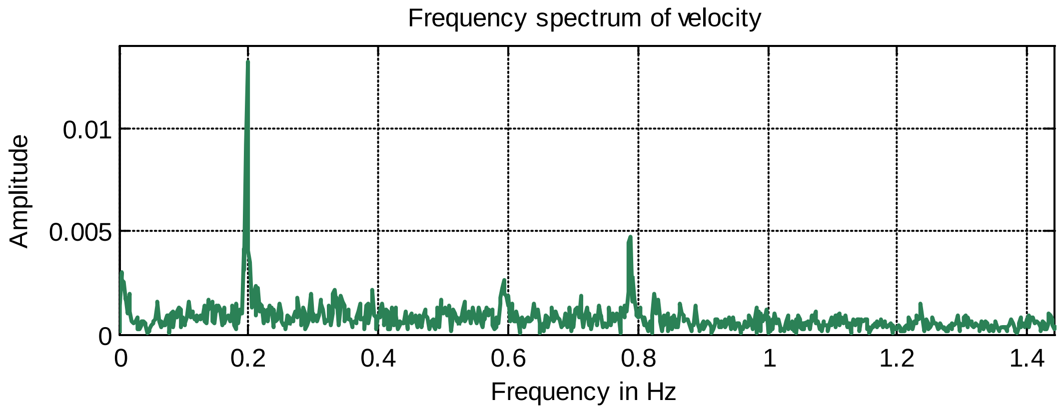

Figure 11: Frequency spectrum from velocity data (GNSS/INS fusion)

4 OUTLOOK

The GNSS position solution of the L1 GNSS receivers cannot be used directly. Due to the low number of satellites in the measurements (in general only 5 or 6 satellites were visible) and the low-cost antenna that is not secured against multipath, the ambiguities for the differential solution in this setup could not be fixed. The float solution is in turn influenced too much by other effects, to determine the elliptical movement of the tower. The ambiguity solution can be improved, however, through the use of inequalities and other constraints that are tailored to the specific location of the GNSS receivers in the monitoring, so a fixed solution can be calculated. Another approach that is investigated in near future is a new ambiguity solving strategy based on the Ambiguity Function (ZEBHAUSER).

With the increasing number of satellites of GALILEO new algorithms can be rediscovered, for example the linear combination of phase and code measurements that reduces ionospheric errors. Through OPPP new opportunities are created, especially if a reference station cannot be set up nearby.

If this improved GNSS solution is in turn fused with IMU data, the complete navigation state vector can be calculated, in particular $\dot{\mathbf{u}}$ and $\ddot{\mathbf{u}}$. This serves as a direct input into the Structural Health Monitoring, described in chapter 2.3.

5 CONCLUSION

A frequency analysis to determine the natural frequency of vibrating structures provides an important contribution to structural health monitoring, and is, as in the presented case of the Stuttgart Television Tower, often independent of outside weather conditions. This frequency analysis may be carried out with low-cost GNSS / MEMS sensors. Especially suitable is a fusion of GNSS velocity and acceleration or an advanced fusion of GNSS raw data (Pseudoranges, Phase observations and Doppler) with IMU data, however, this results in the need for good satellite visibility. With the data fusion of MEMS and GNSS and an advanced modeling (such as constraints) the full spectrum of SHM is opened because there are also velocity and displacement available, next to accelerations. With a sufficient number of sensors this allows in accordance with the dynamic FEM Structural Health Monitoring the detection and the localization of a damaged structure in a building.

ACKNOWLEDGMENTS

The research in this paper was carried out with measurements, that were carried out in the context of the Bachelor Thesis of Mr. David Baier from the Hochschule für Technik, Stuttgart. We would like to thank him for his support and all the participants, especially Mr. Messmer from Messmer Consult, Stuttgart, and the SWR.

REFERENCES

Books:

BREUER P. et. al.: *Messung der Auslenkung von Türmen und Kaminen mittels GPS-Methoden. Monitoring displacements of towers and chimneys applying GPS methods.“*, published by Hochschule für Technik Stuttgart, 2008.

DANTZIG G., THAPA M.: *Linear Programming: Theory and Extensions*, Springer-Verlag, ISBN 0-387-98613-8, 1997

JÄGER R., MÜLLER T., SALER H., SCHWÄBLE R.: *Klassische und robuste Ausgleichungsverfahren*, Wichmann-Verlag Heidelberg, 2005

SIMON D.: *Kalman Filtering with State Constraints, A Survey of Linear and Nonlinear Algorithms*, published at Cleveland State University, USA, 2009

ZEBHAUSER B.: *Zur Entwicklung eines GPS-Programmsystems für Lehre und Tests unter besonderer Berücksichtigung der Ambiguity Function Methode*, Dissertation der Technischen Universität München, 1999

ZIENKIEWICZ O.C. (1984): *Methode der finiten Elemente*. Carl Hanser Verlag, München, Wien, 1984

Journal articles:

BAIER D.: *Systementwicklung zur GNSS-Komponente zum dynamischen Online Structural Health Monitoring (SHM) des Fernsehturms Stuttgart*, Bachelorarbeit an der Hochschule für Technik Stuttgart, 2015

BARRODALE, I. and ROBERTS ,F.D.K: *Algorithm 478, Solution of an Overdetermined System of Equations in theL1 Norm*. Comm. ACM 17, page 319-320, 1974

JÄGER R.: Methods and Approaches for Integrated Deformation Analysis, Proceedings to the International Workshop "Integration of Point- and Area wise Geodetic Monitoring for Structures and Natural Objects", Novosibirsk, Russian Federation, 2014

JÄGER R. *Analyse und Optimierung geodätischer Netze nach spektralen Kriterien und mechanische Analogien*. Deutsche Geodätische Kommission. Reihe C (Dissertationen), Nr. 342, München, 1988

JÄGER, R.,BERTGES M.: *Integrierte Modellbildung zum permanenten Monitoring von Bauwerken und geotechnischen Anlagen*. Proceedings to the 61. DVW-Fortbildungsseminar, 27./28. September 2004, DVW-Schriftenreihe, Band 46/2004.. page 101-140, 2004

ROESE-KOERNER I., KRASBUTTER, SCHUH W.-D.: *A constrained quadratic programming technique for data-adaptive design of decorrelation filters*, Proceedings to the VII Hotine-Marussi Symposium on Mathematical Geodesy, page 165-170, 2009

The Effect of Convergence Time on the Static- PPP Solution

Ashraf Abdallah
Institute of Engineering Geodesy (IIGS), Stuttgart University, Stuttgart, Germany.

Abstract
Recently, the Precise Point Positioning (PPP) technique has been deeply investigated in surveying researches to achieve distinguished coordinates accuracy using one dual frequency GNSS instrument. In this research study, four SAPOS stations with 24 hours observation data in Baden-Württemberg State, Germany were selected to be processed. The station's observation times were divided into different convergence times (1-hour, 2-hours, 4-hours, 6-hours, 8-hours, 12-hours and 24-hours). This paper aims to evaluate the accuracy of the static PPP solution with different convergence times using three PPP software packages, the APPS-PPP online service, the CSRS-PPP online service, and Bernese V. 5.2 software.

Together, the study indicates that, APPS-PPP online service in position$_{3D}$ after 4-hours 1 cm; the solution is steady after 6-hours up to 24-hours. CSRS-PPP online service shows a stable solution after 6-hours with a position$_{3D}$ of 1.2 cm. Bernese software provides a position$_{3D}$ of 1.44 cm after 6-hours and this solution is still improved to reach 1 cm after 24-hours convergence time. Obviously for this case study, the APPS-PPP online service provides the best PPP coordinate solution.

Keywords
Static GNSS-PPP, Convergence time, APPS-PPP, CSRS-PPP, Bernese software

1 INTRODUCTION

Precise Point Positioning (**PPP**) is a positioning technique using only one single antenna. This method is different from differential GNSS (**DGNSS**), which needs one or more reference stations (GRINTER & ROBERTS, 2011). The GNSS Precise Point Positioning (PPP) technique is one of the most challenging surveying methods to realize a high accurate positioning (GAO, 2006). The estimation of PPP is based mainly on the ionosphere free linear combination (IF) for code (ρ_{IF}) and phase (ϕ_{IF}) measurements for dual frequency GNSS data. These combinations are formed in equation (1) and (2) (MIRSA & ENGE, 2010).

$$\rho_{IF} = \frac{f_{L1}^2}{(f_{L1}^2 - f_{L2}^2)}\rho_{L1} - \frac{f_{L2}^2}{(f_{L1}^2 - f_{L2}^2)}\rho_{L2} = r + c(\delta^R - \delta^S) + T_z \cdot m(el) + \varepsilon_\rho \qquad (1)$$

$$\phi_{IF} = \frac{f_{L1}^2}{(f_{L1}^2 - f_{L2}^2)}\phi_{L1} - \frac{f_{L2}^2}{(f_{L1}^2 - f_{L2}^2)}\phi_{L2} = r + c(\delta^R - \delta^S) + T_z \cdot m(el) + \lambda_{IF} \cdot N_{IF} + \varepsilon_\phi \qquad (2)$$

Where,

f_1, f_2 :the frequencies of the GPS L_1 and L_2 signals,

ρ_{Li}, ϕ_{Li} :the measured code and phase data,

r :the true geometric range, it can be calculated as a function of the satellite position (X_S, Y_S, Z_S) and receiver position (X_R, Y_R, Z_R) as follow,

$$r = \sqrt{(X_S - X_R)^2 + (Y_S - Y_R)^2 + (Z_S - Z_R)^2} \qquad (3),$$

c :the vacuum speed of light,

δ^R , δ^S :the receiver and the satellite clock offset,

N_{IF}, λ_{IF}	:the combination integer ambiguity and the combination carrier wavelength,
$T_z \cdot m(el)$	:the troposphere zenith delay including mapping function,
$\varepsilon_\rho,\ \varepsilon_\phi$	:measurement noises including the multipath.

The ionosphere-free combination removes the first order ionospheric error. Therefore, higher order ionospheric terms have to be modelled (KEDER, ET AL., 2003); the related equations are reported in BASSIRI & HAJJ (1993). The troposphere refraction is modelled in the equations (1) & (2) using the term of $T_z \cdot m(el)$, which refers to the troposphere delay including the mapping function. The troposphere delay consists of two components, the hydrostatic dry delay, which can be predicted and includes nearly 90 % of the troposphere delay (HOFFMANN-WELLENHOF ET AL., 2000). The second part is known as the wet component, and it is not easy to predict (LEICK, 1995). For further information regarding troposphere delay modelling, it is recommended to see HOPFIELD (1969), MARINI (1972), NIELL (1992) and SAASTAMOINEN (1973). In addition to precise orbit and satellite clock data, other biases should be considered to obtain a highly PPP accuracy such as the absolute phase center variation for satellite and receiver antenna (PCV) (NGS, 2015), atmosphere tidal loading; see (RAY & PONTE, 2003) & (GGFC, 2015), and ocean tidal effects; see (LE PROVOST & LYARD, 1997) & (SCHERNECK, 2011).

PPP is an important area of interest within the field of surveying; therefore, this research paper introduces a study of the accuracy of the static PPP technique with different convergence times. Additionally, three PPP software packages will be utilized in this study: the APPS-PPP (**A**utomatic **P**recise **P**oint **S**ervice) online service, the CSRS-PPP (**C**anadian **S**patial **R**eference **S**ystem) online service, and Bernese V. 5.2 software. Data from Four SAPOS (**SA**telliten**POS**itionierungsdienst der deutschen Landesvermessung) stations in Baden-Württemberg State, Germany were processed with different convergence times, 1-hour, 2-hours, 4-hours, 6-hours, 8-hours, 12-hours, and 24-hours. The paper investigates the accuracy at different convergence times with the different processing software packages.

2 PPP SOFTWARE PACKAGES

Regarding this study, the data sets were processed to assess the effect of convergence times. They were processed using the APPS-PPP online service, the CSRS-PPP online service and Bernese software V. 5.2. The next chapter describes the properties and the processing parameters for each software package.

2.1 APPS-PPP Online Service

Automatic Precise Positioning Service of the Global Differential GPS System (GPDGPS) is an online service from the JPL (**J**et **P**ropulsion **L**aboratory- California Institute of Technology). The APPS online service is currently based on JPL's GIPSY-OASIS software, v 6.3 (GREGORIUS, 1996). It provides a PPP solution for the uploaded RINEX files in the static or kinematic techniques. Currently, it deals only with dual frequency data. The result is shown on the web page interface for the static technique (APPS, 2015). The available options for APPS online service are illustrated in Figure 1. The registered user can select the processing mode, L1 code type and model the pressure data if the meteorological model will be modelled. The online service also supplies the possibility to change the elevation angle (APPS, 2015).

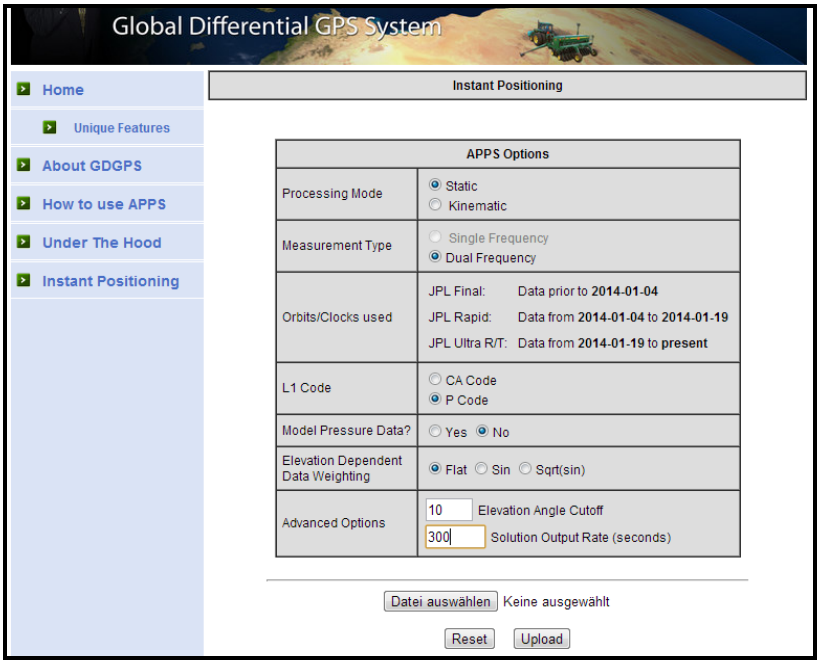

Figure 1: APPS-PPP online service technique (APPS, 2015)

The processing parameters, which are used in the PPP processing, are illustrated below:

- Reference system :ITRF2008,
- Coordinate format :Cartesian (XYZ) and ellipsoidal (LLH),
- Satellite orbit and clock ephemeris :JPL (JPL, 2015),
- Satellite and receiver phase center offsets :IGS ANTEX (ANTEX, 2015),
- Tropospheric model
  - Dry :$1.013 \cdot 2.27 \cdot \exp^{-0,00011 \cdot h}$ (m), where h refers to the ellipsoidal height of the site,
  - Wet :standard (0.1) + Gradient model (JPL, 2010),
  - Mapping function :GMF (Global Mapping Function),
- Ionospheric model :Second order ionospheric delay,
- Elevation angle :10°,
- Interval :30 seconds.

2.1 CSRS-PPP Online Service

CSRS-PPP is an online service, which is provided by the Natural Resources of Canada (NRC) for PPP solution (CSRS-PPP, 2004). It processes a single or dual frequency, and it processes also static or kinematic data. CSRS-PPP online service is one of the most famous PPP online services. This service is available on the website of the NRC (NRC, 2015). Figure 2 depicts the procedure of the online service. In this procedure, the acquired data is uploaded to the website in RINEX format. Finally the results are sent to the user via e-mail with all solution details (CSRS-PPP, 2004).

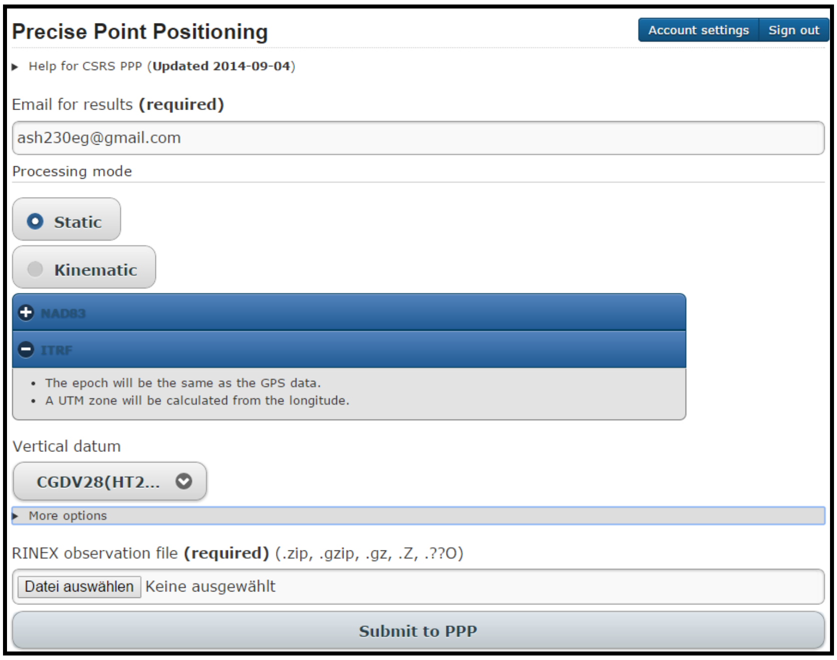

Figure 2: CSRS-PPP online service technique (NRC, 2015)

The processing parameters are reported below (CSRS-PPP, 2004):

- Reference system :ITRF2008,
- Coordinate format :Cartesian, ellipsoidal, UTM,
- Satellite orbit and clock ephemeris :IGS (IGS, 2015),
- Satellite and receiver phase center offsets :IGS ANTEX (ANTEX, 2015),
- Tropospheric model
  - Dry :Davis (GPT) (BÖHM, ET AL., 2007),
  - Wet :Hopfield model (GPT) global pressure and temperature data (BÖHM, ET AL., 2007),
  - Mapping function :GMF (Global Mapping Function),
- Ionospheric model :Second order ionospheric delay CSRS online services with regard to IERS convention notes (IERS-CONVENTIONS, 2010),
- Elevation angle :10°,
- Interval :30 seconds.

2.2 Bernese Software

Bernese software V. 5.2 is a high quality GNSS processing software using the post processing mode. It provides many possibilities for the GNSS measurement data in the case of static or kinematic measurement data. Additionally, it processes the data in double-difference (Differential GNSS) and zero-difference (PPP solution) techniques. This software is developed at the Astronomical Institute of the University of Bern (AIUB), Switzerland (DACH, ET AL., 2007). The documentation of the software is given in a user manual, which is available online in PDF format. Moreover, solved examples are available, which are related to data processing under DACH & WALSER (2014). The software has the option to obtain the PPP solution in an automatic procedure, which is called (**B**ernese **P**rotocol **E**ngine (BPE)). As seen in figure 3, the processing flowchart starts with downloading the orbit data and other related parameters from CODE (**C**enter for **O**rbit **D**etermination in **E**urope) ftp server (CODE, 2015). The RINEX files are smoothed from outliers and cycle slips using pre-processing tools. The orbit data and the smoothed RINEX files are inserted for clock synchronization of the receiver clock with respect to the GPS time. Finally, the parameter estimation is received using the least square adjustment theory to obtain the final static–PPP solution (DACH, ET AL., 2007).

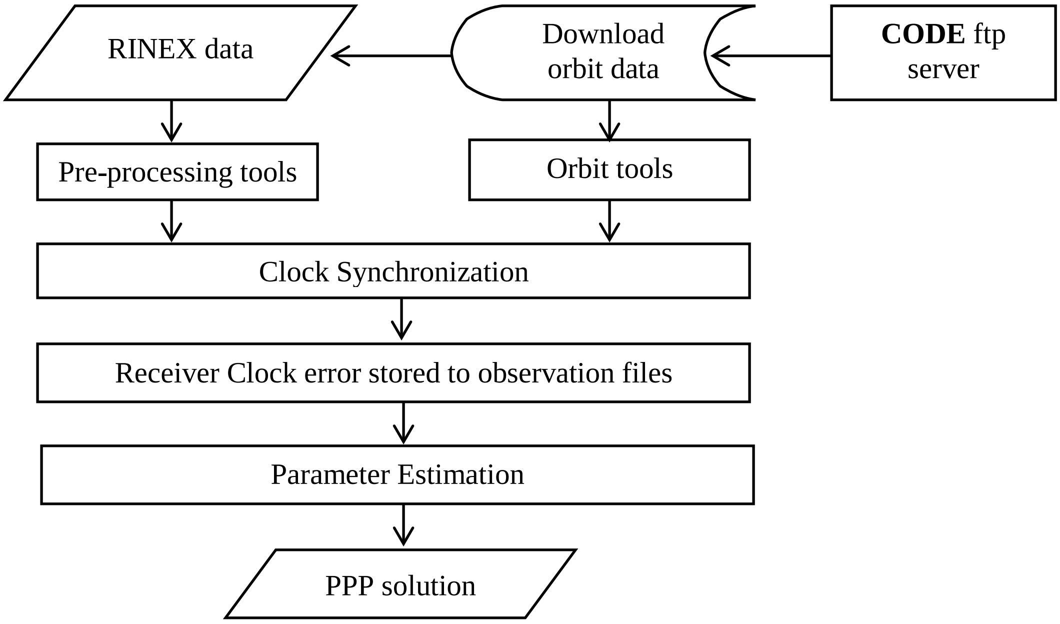

Figure 3: Bernese processing schedule

As shown below, the processing parameters are listed:

- Reference system :ITRF2008,
- Coordinate format :Cartesian,
- Satellite orbit and clock ephemeris :CODE (CODE, 2015),
- Satellite and receiver phase center offsets :PCV.I08 (IGS08 format) (NGS, 2014),
- Tropospheric model
  Dry :Dry GMF,
  Wet :Wet GMF,
  Mapping function :GMF (Global Mapping Function),
- Ionospheric model :Linear ionospheric free combination,
  :Higher order parameters,
- Elevation angle :10°,
- Interval :30seconds.

3 EXPRIMENTAL DATA, EVALUATION METHODOLOGY AND ANALYSIS

Four SAPOS stations in Baden Württemberg State, Germany, were processed for the static PPP solution with different convergence times. Figure 4 displays the layout of the processed stations. The data were divided using TEQC software to different convergence times: 1-hour, 2-hours, 4-hours, 6-hours, 8-hours, 12-hours and 24-hours (TEQC, 2015). TEQC software is executable software working under Windows or Linux operating systems. It provides the capability to check the quality of GNSS data and to divide the observation times. For more information, it is advisable to see TEQC (2015). Figure 5 shows the properties of estimation stations.

Figure 4: Layout of SAPOS's Stations, Baden-Württemberg State, Germany © Google Earth

<table>
<tr>
<td>
ID : 0384,
City : Stuttgart,
Antenna type : TRM59800.00 SCIS,
Receiver type : TRIMBLE NETR5.</td>
<td>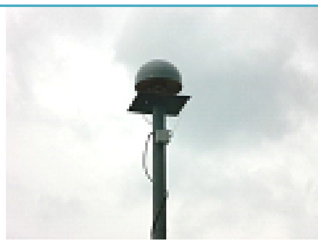
ID : 0386,
City : Heilbronn,
Antenna type : TRM59800.00 SCIS,
Receiver type : TRIMBLE NETR5.</td>
</tr>
<tr>
<td>
ID : 0391,
City : Geislingen,
Antenna type : TRM59800.00 SCIS,
Receiver type : TRIMBLE NETR5.</td>
<td>
ID : 0400,
City : Tübingen,
Antenna type : TRM59800.00 SCIS,
Receiver type : TRIMBLE NETR5.</td>
</tr>
</table>

Figure 5: SAPOS stations properties (SAPOS, 2015)

From the quality check of these stations using TEQC software, properties of the processed stations can be established as follow:

- Observation date : 01 July, 2012,
- Observation interval : 30 seconds,
- GNSS system : GPS+GLONASS,
- No. of tracked satellites/Epoch : 10 to 22 satellites (varied),
- Data gap for in 0391 station for 4 minutes.

The PPP solution was evaluated with respect to the known coordinates for the stations in the UTM projection and for the ellipsoidal heights. The difference values $\delta_{i,j}$ between the reference known coordinates *M* and the PPP results *M'* are as reported in equation (4). Moreover, the error in 2D $\delta_{2D,i,j}$ and in 3D $\delta_{3D,i,j}$ is calculated as shown in equation (5) and (6).

$$\delta_{i,j} = M - M' \quad (4),$$

$$\delta_{2D,i,j} = \sqrt{\delta_E^2 + \delta_N^2} \quad (5),$$

$$\delta_{3D,i,j} = \sqrt{\delta_E^2 + \delta_N^2 + \delta_h^2} \quad (6).$$

Where,

i	:is station number,
j	:is E or N or h,
E, N, h	:are East, North and ellipsoidal height,
δ_E, δ_N, δ_h	:are the difference values in East, North and height.

3.1 APPS-PPP Results

The observation data with different convergence times were uploaded using the registered account to the free online services. The estimated PPP results were different with the known values; Figure 6 illustrates the error values in position$_{2D}$ and height directions. The horizontal axis refers to the convergence time in hours, up to 24-hours. The vertical axis shows the error value in cm and the results are labelled with different colours.

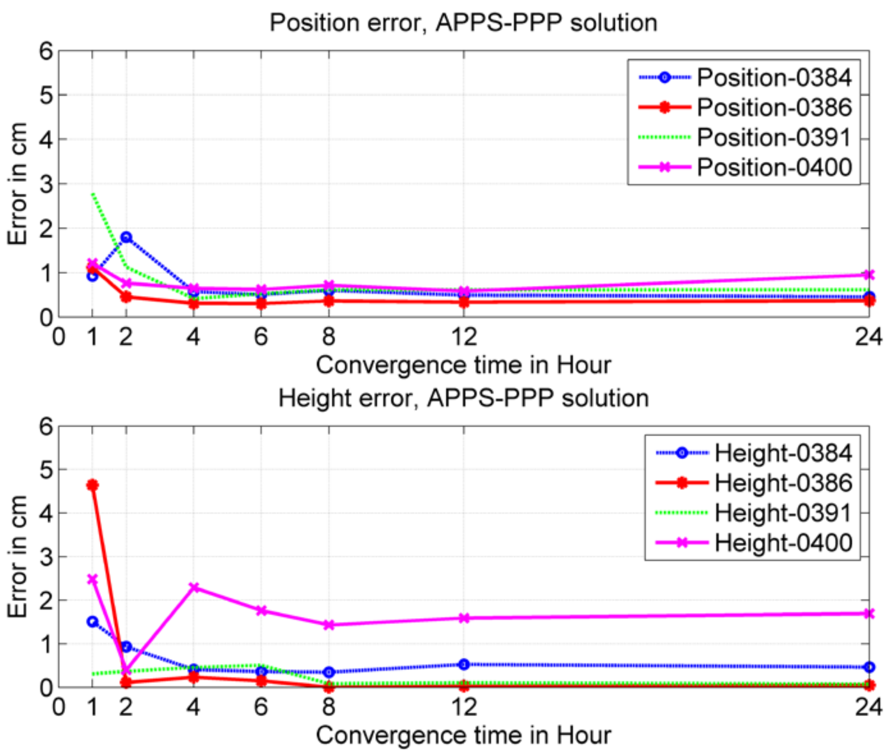

Figure 6: PPP error form APPS-PPP online service

As presented in this figure, for 1-hour convergence time, the position solution shows an error of 3 to 1 cm for position$_{2D}$ and up to 5 cm for height. The solution remains unreliable even after 2-hours. After 4-hours, the solution significantly improved to reach sub-cm level in the position$_{2D}$ and the height; only station 0400 shows an error higher than 2 cm in height direction up to 24 hours. Afterwards, the solution slightly varies, but it remains in the mm level. After 8-hours, there is not any improvement in the accuracy up to 24-hours; the static-PPP solution shows millimetre level.

3.2 CSRS-PPP Results

As like the APPS-PPP online service, the RINEX files with different convergence times were uploaded to the service, and the PPP solution was sent to the user to the e-mail address with the Cartesian and UTM coordinates. Figure 7 shows that the PPP solution after 1-hour provides an error in position$_{2D}$ and height of 3 to 1 cm. This error decreases after 2-hours up to 1.5 cm and up to 2 cm for position$_{2D}$ and height respectively. After that, the solution is improved to reach sub-cm level for position$_{2D}$ and less than 2 cm for height direction. The solution is stable after 8-hours with a millimetre level for position$_{2D}$ and up to 1.5 cm for the height direction.

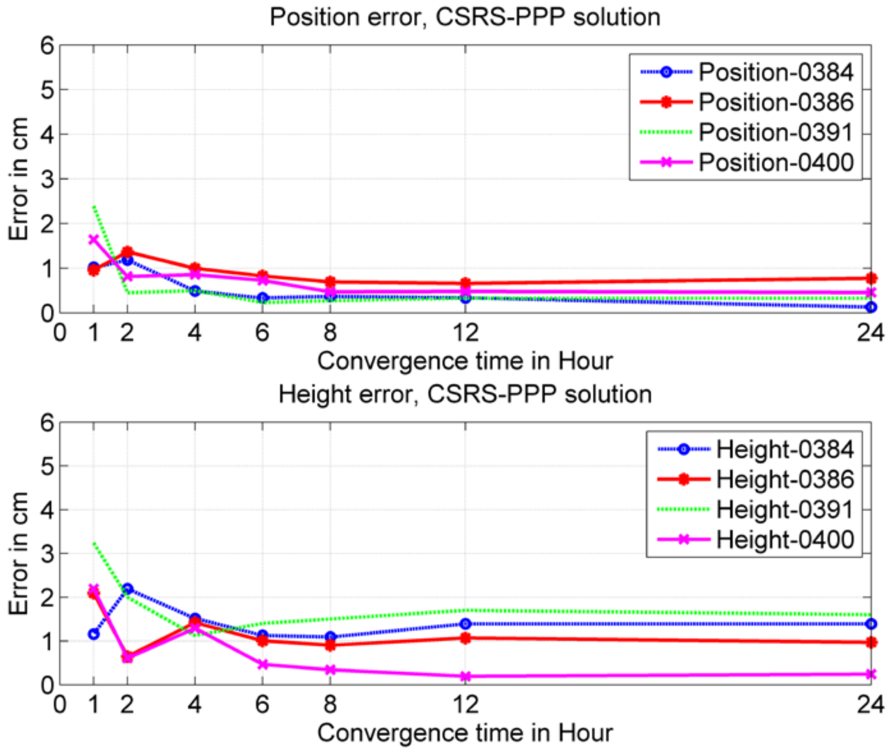

Figure 7: PPP error form CSRS-PPP online service

3.3 Bernese Software

Using different convergence times in Bernese software, Figure 8 reports the error values in cm for the position$_{2D}$ and the height for the four stations with various convergence times. The figure is gridded in the vertical direction in the relevant studied times.

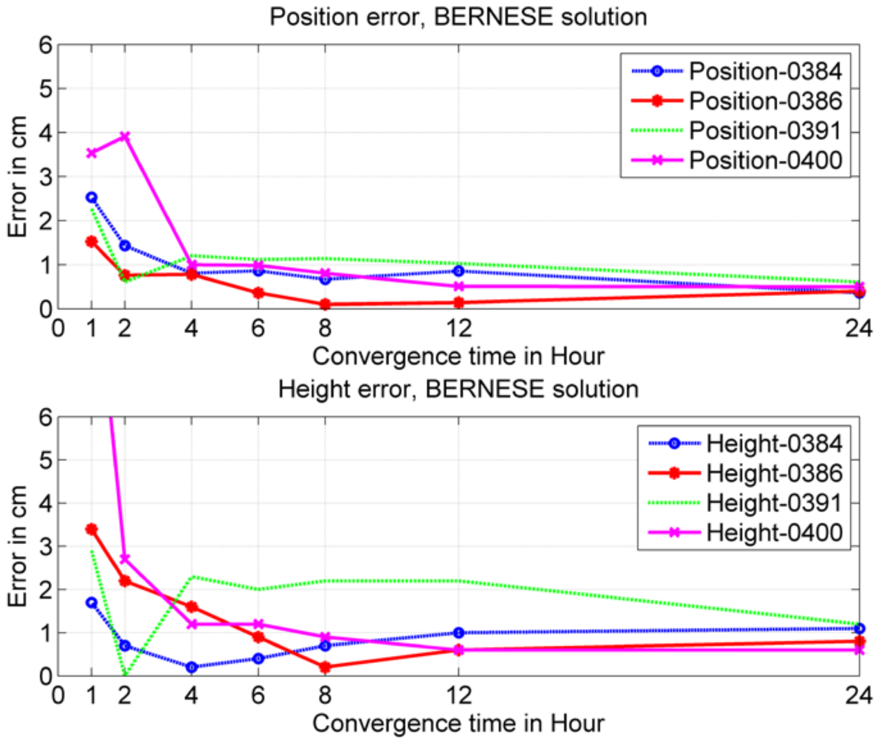

Figure 8: PPP error form Bernese software

In position$_{2D}$ graph, the solution shows non-reliable solution for the 1-hour and 2-hours with an error on 4 to 1 cm. The highest error in reported for from station 0400. After 4-hours, the accuracy significantly improved for all stations to reach an error of 1.30 cm to 8 mm; this accuracy reaches values up to 1 cm after 12-hours. After 24-hours, the solution achieves 5 mm level for all stations. Regarding the height graph, the solution reaches up to 4 cm for all stations except the station 0400 for up to 2-hours. After 4-hours, the solution shows up to 2.2 cm accuracy level. Excluding the station 0391, the error improved to reach 1 cm after 8-hours and remains stable up to 24-hours.

3.4 Summary

This study has gone some way towards investigating of the PPP coordinate solution with different convergence times. PPP coordinate solution was carried through using three PPP processing tools. Therefore, Table 1 concludes the mean error in position$_{3D}$ for the four stations. The APPS-PPP online service provides in position$_{3D}$ after 4-hours 1 cm, and after 6-hours the error is stable up to 24-hours.

Table 1: Overall statistics for all PPP software packages

Convergence time	**Position$_{3D}$ (cm)**		
	APPS-PPP	**CSRS-PPP**	**BERNESE**
1-hour	3.02	2.65	5.38
2-hour	1.13	1.77	2.32
4-hour	1.02	1.53	1.69
6-hour	0.89	1.19	1.44
8-hour	0.82	1.10	1.22
12-hour	0.84	1.23	1.28
24-hour	0.89	1.19	1.04

Similar to APPS-PPP, the CSRS-PPP online service shows a stable solution after 6-hours with an error in position$_{3D}$ of 1.2 cm. Regarding Bernese software, the solution is still improved after 6-hour convergence time and reports 1 cm after 24-horurs. Obviously for this study, the APPS-PPP online service provides the best PPP coordinate solution.

4 CONCLUSIONS

The main goal of this study was to investigate the effect of convergence time of static-PPP solutions. The observation data of 24 hours for 4 CORS stations in Germany were divided to 1-hour, 2-hours, 4-hours, 6-hours, 8-hours, 12-hours, and 24-hours. Three tools were utilized to get the static-PPP solution: the APPS-PPP online service, CSRS-PPP online service, and Bernese software. The first two tools provide the user with the PPP solution for free without any specific processing’s effort. The second tool was a licensed copy of Bernese software, which needed more effort to obtain the solution. On the other side, Bernese software has many parameters to be changed during the process, which offers the possibility to study each element in the PPP solution.

Regarding the finding of this study, APPS-PPP shows a sub-cm level after 4-hour convergence times and a stable solution after 6-hours with a position_{3D} of 9 mm. CSRS-PPP delivers sub-cm level for position_{2D} and 1 cm level in height after a convergence time of 6-hour. This solution remains stable up to 24-hours. Bernese software offers a reliable solution after 4-hourrs with 1 cm in position_{2D} and up to 2 cm in height. The solution improves to deliver sub-cm in position_{2D} and 1 cm for height after 8-hours. After that, the solution is steady up to 24-hours to report a 1 cm level in position_{3D}.

Finally, the strength key of this research paper is the longer convergence time delivers a better PPP coordinate accuracy. Moreover, the high number of satellites is an effective parameter for getting a better PPP solution. From this data set, APPS-PPP online service slightly out behaves the solution of CSRS-PPP online service and Bernese software with respect to the accuracy. The free online services could offer a good PPP solution for the user. On the other side, Bernese software could provide the researchers with a high ability to study the different elements of PPP solutions.

For comparison with previous researches, GRINTER & JANSSEN (2012) & ABDALLAH (2013) studied the static solution of the CSRS-PPP online service. They reported that, the solution of CSRS-PPP after 2-hours shows a high difference comparing to the reference solution. This solution is significantly improved between 4-hours and 12-hours and a stable solution after 12-hours to 24-hours. These findings are matching of our case study. OCALAN, ET AL. (2013) & ABDALLAH & SCHWIEGER (2015) studied also the comparison between CSRS-PPP and APPS-PPP. They found that APPS-PPP online service provides a more reliable solution than the CSRS-PPP solution, which is similar to our outcomes.

Extended efforts are needed: (i) improving the obtained accuracy from Bernese software and (ii) studying the tropospheric parameters achieved from the different PPP software packages. Furthermore, (iii) studying the accuracy of the static PPP solution with a limited number of satellites, (iv) increasing the studied stations.

REFERENCES

Books:

ABDALLAH, A.: *Accuracy Assessment Study of Precise Point Positioning for Static and Kinematic Surveying.* Master of science, Not published, Signatur: S7-2013,6 ed. Stuttgart University, Institute of Engineering Geodesy (IIGS), 2013.

CSRS-PPP:*On-line Precise Point Positioning ‘How to Use’ Document.* Ver 1.1 Hrsg. Canada: Natural Recourses Canada.

DACH, R., FRIDEZ, P., HUGENTOBLER, U. & MEINDL, M.: *User manual of the Bernese GPS Software Version 5.0.* Bern, Switzerland: Astronomical Institute, University of Bern, 2007.

GREGORIUS, T.: *GIPSY-OASIS II: How it works.* University of Newcastel upon Tyne, 1996.

HOFFMANN-WELLENHOF, B., LICHTENEGGER, H. & COLLINS, J.: *GPS: Theory and Practics.* 4 ed. New York: Springer-Verlag/Wien, 2000.

IERS-CONVENTIONS: *IERS Technical Note No. 36*. Frankfurt am Main, Germany: Verlag des Bundesamts für Kartographie und Geodäsie, Petit, G.; Luzum, B. (editors), 36: 137-147, 2010.

LEICK, A.: *GPS Satellite Surveying.* 2nd ed., Wiley, New York, 1995.

MIRSA, P. & ENGE, P.: *Global Positioing System Signals, Measurements, and Performance*. Revised second ed., Ganga-Jamuna Press, 2010.

Journal articles:

ABDALLAH, A. & SCHWIEGER, V.: *Static GNSS Precise Point Positioning Using Free Online Services for Africa*. Journal of Survey Review, Accepted, DOI 10.1179/1752270615Y.0000000017, 2015.

BASSIRI, S. & HAJJ, G.: *Higher-order ionospheric effects on the GPS observables and means of modeling them*. Manuscripta geodaetica, Springer-Verlag, 18(5), p. 280-289, 1993.

BÖHM, J., HEINKELMANN, R. & SCHUH, H.: *A Global Model of Pressure and Temperature for Geodetic Applications*. Journal of Geodesy, 81(10), p. 679-683, 2007.

GAO, Y. & SHEN, X.: *A New Method for Carrier Phase Based Precise Point Positioning*. Journal of the Institute of Navigation, 49(2), p. 109-116, 2002.

GRINTER, T. & JANSSEN, V.: *Post-Processed Precise Point Positioning: A Viable Alternative?*. Wollongong, New South Wales, Australia, Proceedings of the 17th Association of Public Authority Surveyors Conference (APAS2012), 2012.

GRINTER, T. & ROBERTS, C.: *Precise Point Positioning: Where are we now?*. Sydney, Australia, Proc. IGNSS2011, 2011.

HOPFIELD, H.: *Two-quartic topospheric refractivity profile for correcting satellite data*. Journal of Geophysical Research, 74(8), 4487-4499, 1969.

KEDER, S., HAJJ, G., WILSON, B. & HEFLIN, M.: *The effect of the second order GPS ionospheric correction on receiver positions*. Geophysical Research Letters, 30(16), 2003.

MARINI, J.: *Correction of satellite tracking data for an arbitrary tropospheric profile*. Journal of Radio Science, 7(2), 223-231, 1972.

NIELL, A.: *Global mapping functions for the atmosphere delay at radio wavelengths*. Journal of Geophysical Research, 101(B1), 3227-3246, 1992.

OCALAN, T., ERDOGAN B., TUNALIOGLU N.: *Analysis of web-based online services for GPS relative and precise point positioning techniques.* Boletim de Ciências Geodésicas, 19(2), 191-207, 2013.

LE PROVOST, C. & LYARD, F.: *Energetics of the M2 barotropic ocean tides: an estimate of bottom friction dissipation from a hydrodynamic model*. Progress in Oceanography, 40(1-4), 37-52, 1997.

RAY, R. D. & PONTE, R. M.: *Barometric tides from ECMWF operational analyses.* Annales Geophysicae, 21, 1897-1910, 2003.

SAASTAMOINEN, J.: *Contribution to the theory of atmospheric refraction*. Bulletin géodésique, 107(1), 13-34, 1973.

Links:

ANTEX: *NGS Antenna information*, http://www.ngs.noaa.gov/ANTCAL/documents/format.txt, last accessed on January, 2015.

APPS: *Automatic Precise Point Service,* http://apps.gPDGNSS.net/index.php, last accessed on February, 2015.

CODE: *CODE ftp server*, ftp://ftp.unibe.ch/aiub/CODE/2012/,last accessed on February, 2015.

DACH, R. & WALSER, P.: *Bernese GNSS Software Version 5.2 Tutorial*. http://www.bernese.unibe.ch/docs/TUTORIAL.pdf, last accessed on February, 2015.

GGFC (2015): *Atomsphere Tide Loading Calculator from Global Geophysical Fluid Center*. http://geophy.uni.lu/ggfc-atmosphere/tide-loading-calculator.html, last accessed on February, 2015.

IGS: *IGS orbit and clock data products*, http://igscb.jpl.nasa.gov/components/prods.html, last accessed on February, 2015.

JPL: *JPL orbit and clock data products*, https://gipsy-oasis.jpl.nasa.gov/index.php?page=data, last accessed on February, 2015.

NGS: *Antenna Absolute Calibrations,* http://www.ngs.noaa.gov/ANTCAL/, last accessed on February, 2015.

NRC: *Natural Resources Canada,* http://webapp.geod.nrcan.gc.ca/geod/tools-outils/ppp.php?locale=en, last accessed on February, 2015.

TEQC: *TEQC manual*, http://facility.unavco.org/software/teqc/tutorial.html, last accessed on February, 2015.

SAPOS: *SAPOS Baden-Württemberg, Germany*, http://www.sapos-bw.de/karte.php, last accessed on February, 2015.

SCHERNECK, H.G.: *Chalmers/Onsala Sapce Obsevatory*. http://holt.oso.chalmers.se/loading/, last accessed on February, 2015.

TECHNICAL SESSION 3: GNSS – SOLUTIONS II

Time Series Analysis of Different Shieldings of Low-Cost GPS Receiver

Wei Zhang[1], Li Zhang[2]
[1]Master Program Geodesy and Geoinformatics, University of Stuttgart, Germany
[2]Institute of Engineering Geodesy, University of Stuttgart, Germany

Abstract
The geodetic monitoring is one of the central tasks in engineering geodesy. By monitoring the geometric surface of a test object, changes, movements and deformations over certain time periods can be detected. Nowadays, the GNSS (Global Navigation Satellite System) has been increasingly used in monitoring as it has been developed rapidly in recent years. On the one hand, the accuracy reaches at centimetre or even millimetre level. On the other hand, the measurements can be achieved continuously and autonomously, which is the trend of monitoring measurement (Schwieger 2009). In the Institute of Engineering Geodesy at the University of Stuttgart (IIGS), the low-cost single frequency GPS receiver (u-blox receiver) has been studied for a long time. To improve the accuracy of measurements, different shieldings are constructed to reduce undesirable multipath effects. In this paper, the qualities of the different shieldings were explored by time series analysis. A method to improve the accuracy of low-cost GPS by reducing the multipath effects was introduced.

Keywords
Time series, low-cost GPS, multipath effects, geodetic monitoring.

1 INTRODUCTION

Monitoring can be used for detecting movements of artificial and natural objects such as dams, roads, tunnels, bridges, overpasses, buildings, foundations, construction sites, mining and mines, slopes and volcanic slopes, earthquake areas (Welsch et al. 2000). Especially for the prediction of natural disasters, monitoring measurements are meaningful. For example, if a volcanic eruption can be detected by the geodetic monitoring in near real time or as soon as possible, potential affected population can be informed and evacuated with less loss. An automatic monitoring system using low-cost single-frequency GPS receiver, which was developed in the Institute of Engineering Geodesy at the University of Stuttgart (IIGS), has been introduced in Zhang and Schwieger (2013). The data collection and transmission are achieved in real time and the data processing is in near real time, the results can be delivered to users in every 20 or 30 minutes, makes it possible to return GPS positioning results in near real time.

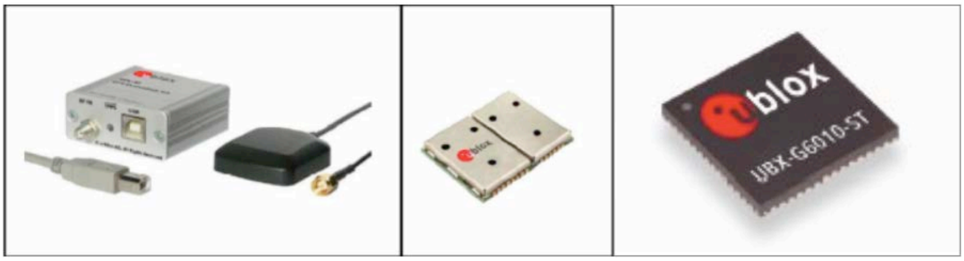

Figure 1: Ublox GPS Positioning evaluation kit, modules and chips (U-Blox 2014)

The investigated low-cost single-frequency GPS Receiver is equipped with positioning chips from the company "u-blox" (see figure 1). Comparing to average cost of €20,000 for a geodetic receiver, the receivers, e.g. the u-blox receivers, costs only about €100 to €300. Although the u-blox LEA 6T GPS-receiver with ANN-MS antenna can already obtain an accuracy, which almost meets the requirements of geodetic applications (see Zhang and Schwieger 2013), there is great potential to improve the accuracy, especially in shadowing environment. The dominant error of short baselines, especially in shading environment, is caused

by multipath. Using shieldings such as ground plate and choke ring can reduce the multipath effects. One so-called L1-optimized choke ring ground plate was constructed at IIGS. Its performance will be investigated and compared with other shieldings in this paper. The multipath effects can cause periodic deviations in the coordinates, which are, depending on obstructions in the near vicinity, about several millimetres to centimetres. The periodicities will be investigated through time series analysis.
In this paper, after a short introduction and motivation, the basics of precise positioning with GPS and time series analysis will be given. Then, the test of different shieldings will be presented and the results will be shown and discussed.

2 PRECISE POSITIONING WITH GPS

2.1 GPS Observation Model

Positioning is well known in daily life as it is embedded in smartphones based on satellite navigation systems. The GNSS is a general name for existing and future global satellite systems such as GPS (Global Positioning System) from USA, GLONASS from Russia, the EU's Galileo and Chinese Beidou. Here in this paper, the GPS measurements are to be investigated. The basic principle is the same for all systems. Signals from at least four satellites must be simultaneously received by the GPS-receiver, in order to determine the position (X, Y and Z-coordinate) and the receiver clock error.
The GPS-signals are transmitted from the satellites to the user receiver on ground through the atmosphere. Two kinds of errors are generated in transmission, these are ionospheric and tropospheric error caused by atmospheric refraction and internal errors from the satellite and user receiver.
The accuracy is depending on GPS devices and measurement methods. There are essentially two different methods, namely the code phase measurements and the carrier phase measurements (Bauer 2011). The code phase measurement, the so-called pseudo range, is based on measuring the run time of the satellite signals from the satellite to the receiver. The typical applications of the code phase measurement with low accuracy requirements can be found as navigation in daily life, for example navigation functionality on phones or car-based equipment. Since the accuracy of the pseudo range (code phase) is only in the decimetre or even meter, which is not sufficient for the application of geodetic monitoring measurements, the carrier phase measurement is used in this study, whose accuracy can reach some millimetres to centimetre rang. In carrier phase measurements the carrier phases of the signals sent from satellites are compared with the phase of the receiver reference signal and the phase difference is determined. Furthermore, the integer number of wave cycles, the so-called ambiguity has to be determined.

2.2 Differential GPS

To get the accuracy of GPS measurement in millimetre to centimetres range the differential GPS method has to be applied. In differential GPS there is a reference station with known position and a rover station with unknown position. The coordinate’s difference (or baseline) between the two stations will be calculated. If the baseline is determined, then the position of the rover station can be determined by adding the baseline to reference station.
In general, a longer baseline between the reference and rover station leads to a greater loss of accuracy, since many errors cannot be regarded as the same for two stations. In engineering geodesy, the extensions of monitoring objects are normally a couple of kilometres for the baselines. For this reason, high-precision positioning in the millimetre to centimetre range can be realized by using the carrier phase measurement combined with differential GPS.
In differential GPS or in relative modus most of the satellite errors, the atmospheric errors can be reduced (compare table 1). Multipath, signal diffraction and antenna phase centre variation are not reduced.

Table 1: Errors of GPS measurement for carrier phase measurement (Rost 2011)

Sources of errors		Magnitude	
		Absolut	Relative
Satellite error	Satellite clock error	5 - 100 m	0.0 ppm
	Satellite track error	5 - 50 m	0.2 - 2.0 ppm
Signal propagation	Ionospheric refraction	0.5 - 100 m	0.1 - 50.0 ppm
	Tropospheric refraction	0.01 - 0.5 m	0.1 - 3.0 ppm
	Multipath error	mm/cm	mm/cm
	Signal diffraction	mm/cm	mm/cm
Receiver error	Variation of antenna phase centre	mm/cm	mm/cm

2.3 Multipath Effect

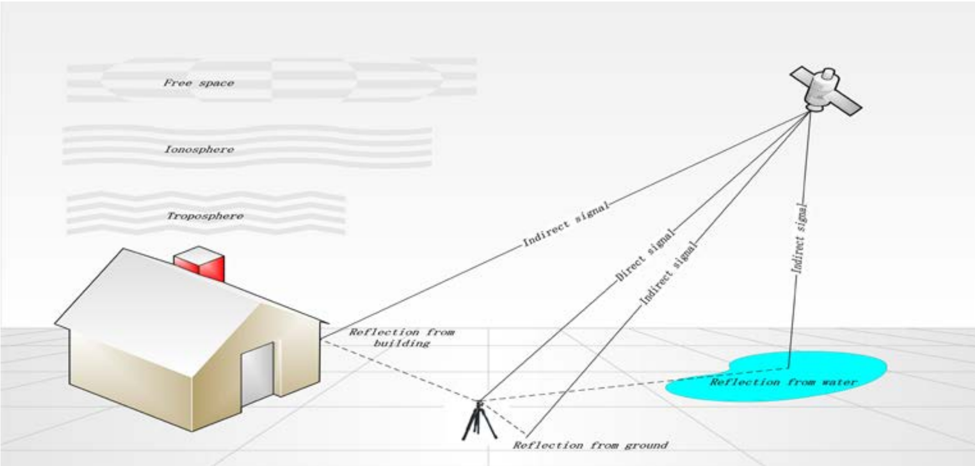

Figure 1: Description the cause of multipath effects

However the multipath error cannot be reduced in differential GPS. The multipath effect arises when in the vicinity of antenna objects that reflected GPS signal are located, e.g. buildings and trees and ground. The signals transmitted by the satellites are reflected by objects and go towards to the antenna. This will be superimposed with the direct signal and it leads to a time-shifted signal. Up to now there exist many methods to reduce multipath errors, but none of them can reduce the multipath completely (Rost 2011). Therefore, reducing the multipath influence is the objective of this paper.

It is possible to reduce the influence by using special shieldings for the antenna. For example, a round ground plate (GP) or the so-called choke ring ground plate (CRGP) which consists a round ground plate and a series of concentric cylinders, can be used to prevent the antenna from indirect or reflected signals, especially the signals from ground. Another way to reduce the multipath effect is through the data processing.

The multipath error of the carrier phase can be maximum ¼ of the wavelength that means for GPS-L1-frequecy it may be maximum of 4.7 cm. The multipath effects can cause periodic variation in the coordinates. For the typical antenna height of 1.5 m, the periodicities vary from several minutes to 1 hour (Zeimetz at al. 2009).

The periodicities of the different shieldings will be analysed through time series analysis. The periodic effects will be modelled and subtracted from the measurements values, so that the accuracy of the results will be improved.

3 DATA PRE-PROCESSING

3.1 Test Scenario

To evaluate the improvement of accuracy and the changes of periodicity by different shieldings, four combinations of antennas and shieldings are tested (compare figure 3):

a) Antenna without shielding (TBIII): a low-cost GPS antenna, model Trimble Bullet III, is set without shielding. The used receiver is a single-frequency GPS receiver U-blox EVK-6T of the company U-Blox.
b) Antenna with ground plates (TBIII+GP): the same GPS antenna as a) is assembled with a ground plate to avoid possible indirect signals from the ground.
c) Antenna with choke rings ground plate (TBIII+CRGP): the L1 frequency-optimized choke ring is used in a). The principle of choke rings is that the ring depth is equal to one-quarter of the L1 carrier wavelength namely approximately 4.5 cm.
d) Geodetic antenna (Leica AX1203): for comparison, the measurement as a reference by a geodetic antenna of the company Leica and a geodetic receiver Leica GX1230. For comparison the measurement are only processed with GPS L1 frequency.

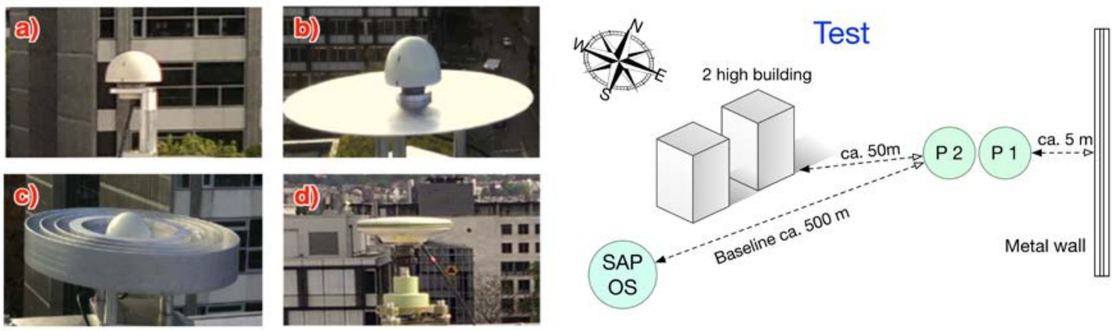

Figure 3: Shape of the four antennas and overview of test scenario

Table 2: Overview for test of antennas and shieldings

Session Nr.	Data	Antennas and shieldings	
		P1	**P2**
1	**24.10.13**	TBIIII+CRGP	TBIII+GP
2	**27.10.13**	TBIII+GP	TBIIII+CRGP
3	**26.04.14**	Leica AX1203 (only L1)	TBIII
4	**27.04.14**	TBIII	Leica AX1203(L1 only)

The four types of antennas with shielding and receivers are built on the points P1 and P2 for measurements on four days (compare table 2). The antennas are located near a metal wall about 5 meters away (compare figure 3). A SAPOS reference station is located about 500 meters from the measurement site, this SAPOS station is taken as reference station for our test. SAPOS is the abbreviation for the satellite positioning service of the germen state survey, which operates many continuously operating GNSS reference stations in Germany (Mansfeld 2010). The RINEX data of the reference stations are available via internet. The multipath errors are the main errors for such short baselines. In our case, it may be originated from the ground and the wall. In addition, it can be seen from the right picture of Figure 3 that there is two high buildings in about 50 meters away. Such objects can also cause multipath effect with different periods, which may be analysed by means of time series analysis.

3.2 Processing the Raw Data

The raw data of u-blox receiver are in binary UBX format. They are converted into RINEX (Receiver Independent Exchange Format) format and edited by using the free software TEQC (TEQC 2013).

Figure 4: Processing of the raw data

The calculation of the baseline is done by the software wa1 from the company Wasoft (Wa1 2013). The output of wa1 is the baseline or the coordinates in UTM (Universal Transverse Mercator)-coordinates system. If the ambiguities of the carrier phase measurements are not fixed to integers, the results will be marked as “float”-solution.

Next, the pre-processing phase is divided into three steps - detection of outliers, missing data interpolation and elimination of linear trends. The three steps are analysed in the time domain. In order to analyse the data in the frequency domain, the data should be free from outliers and linear trends. These steps are needed to have a stationary and equidistant time series.

3.3 Detection of Outliers

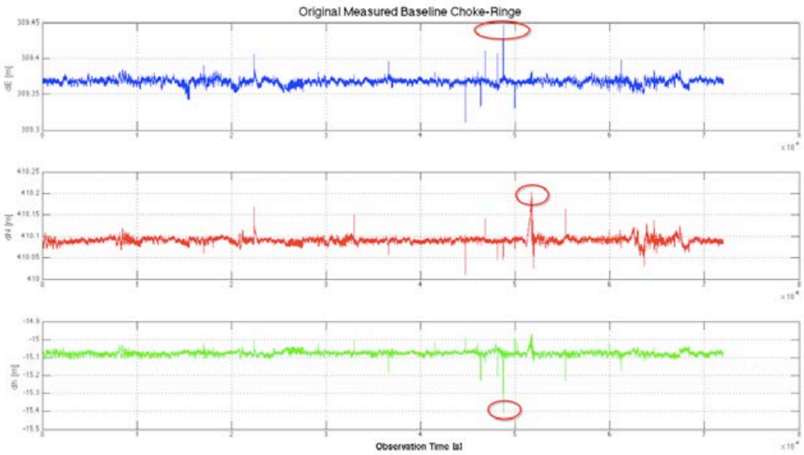

Figure 5: Original baseline component dN, dE, dh (choke ring ground plate)

Figure 5 represents an example of an original output of the wa1 software, which is one measured baseline of test scenario. The outliers can be clearly seen. In general, the rate of outliers shows the reliability of the GPS receiver. The deviations of outliers account for about several centimetres, sometimes even a decimetre. Here is the normal distribution is applied for outlier detections. The confidence intervals can be defined by the use of standard deviation σ. The area within 1σ corresponds to the probability of 68% and 95% within 2σ and 99,7% for 3σ (Schwieger 2012). The more the deviations are permissible, the greater is the corresponding confidence interval. All measured values that lie outside the 3σ region are identified as outliers. This means that about 0.3% of the deviating measured values are identified as outliers. The ambiguity for some measurements could not be fixed, which is also identified in the algorithm as an outlier.

3.4 Interpolation of Data Gaps

Normally the data gaps can be caused by the loss in transmission or due to elimination of outliers. In our test thanks to the stabile hardware there are few data gaps from the loss in transmission but due to the last step by eliminating the outliers. To provide the data for further processing, the resulting data gaps need to be filled. To compute the missing data the neighbouring points are in the taken into account. There are several methods to approximate and complement the gaps, for example 'linear', 'spline' and 'nearest'. Here the method of "linear" interpolation is used to remain the trend of the data. After interpolation the outliers are no longer recognized and data gaps are filled. The interpolated data gaps guarantee the continuity of the time series in order to transform into the frequency domain afterwards.

3.5 Elimination of the Linear Trend

When a linear trend exists in the time series, the series is non-stationary and this may cause problems in frequency domain. The reorganized the potential periodicity will become wrong.

$$\Phi(x) = a_0 + a_1 x + a_2 x^2 + a_3 x^3 + \ldots + a_n x^n \tag{3.1}$$

$$l = \Phi(x) \quad \text{corresponding to coordinate E,N,h} \tag{3.2}$$

$$x = \begin{bmatrix} a_0 & a_1 & a_2 & a_3 \end{bmatrix} \tag{3.3}$$

$$A = [1 \quad x \quad x^2 \quad x^3] \tag{3.4}$$

In general, the polynomial model used to eliminate the linear trend. It looks like equation 3.1 according to Foppe and Neitzel (2014). After trying and due to the large amount of data, the polygon of grade 3 is used. The measured coordinates are regarded as observations and coefficients as unknown parameters. Through the establishment of the functional model, the unknown parameters by least square adjustment can be calculated. Next, the calculated parameters must be assessed by significance tests. Since the degree of freedom and the number of observation is very large in the adjustment, the significance test is carried out according to normal distribution instead of the t-distribution.

$$\text{Quantile:} \quad Y = y_{1-\frac{\alpha}{2}} \tag{3.5}$$

$$\text{Test statistic:} \quad y = \left| \frac{a_i}{s_{a_i}} \right| \qquad i = 0, 1, 2, 3 \tag{3.6}$$

If the test statistic (formula 3.6) is greater than the quantile, the parameter is significant. If one parameter is not significant, it must be deleted in accordance with the model and the adjustment is performed iteratively until all parameters are significant.

3.6 Results after Pre-Processing

Table 3: Comparison of the accuracy of the results after -pre-processing

Quality	TBIII	TBIII+GP	TBIII+CRGP	Leica AX1203
Outlier [%]	5.4	3.9	3.0	3.3
s_E [mm]	7.2	5.9	3.5	3.9
s_N [mm]	10.7	8.5	5.4	6.1
s_h [mm]	18.2	14.5	9.0	10.0
s_{3D}[mm]	22.3	17.8	11.1	12.3

Table 3 shows the results of measurement data from the test after pre-processing. The average accuracy in the static GPS measurements is about 1 to 2 cm. The antenna without shielding has an worst accuracy of 22.3 cm. With the ground plate, the accuracy can be improved by 20 %. This means that the ground plate can prevent some indirect signals, in particular the reflected signal from the floor. Obviously the antenna constitutes the specific form of the choke rings achieved the best result and namely the accuracy is improved by about 50%, which is even better than the high-priced geodetic receiver with geodetic antenna (here are the Leica AX1203 GPS antenna with GX1230 GPS receiver).

4 PROCESSING OF PERIODS

After pre-processing of time series analysis and the elimination of the linear trend the basic conditions, for further analysis are met. First, the time series are transformed by the Fast Fourier Transform (FFT) into the frequency domain. After transformation, the periodogram can be calculated. It represents the power spectrum for different frequencies. In the following the task is to find out periods in the periodogram with the highest power.

For a discrete time series, it should be ensured that the recognition of the periodicity has an upper limit. The highest frequency that can be found is called the Nyquist frequency (Paulo et al., 2002). The Nyquist frequency is, according to the Nyquist-Shannon theorem, half the sampling frequency. That is, it is impossible to read the information on data in a wider range than the sampling frequency. For example, if a change in the temperature of two cycles per day is observed, then the data must be collected by the Nyquist-Shannon theorem at least four times a day.

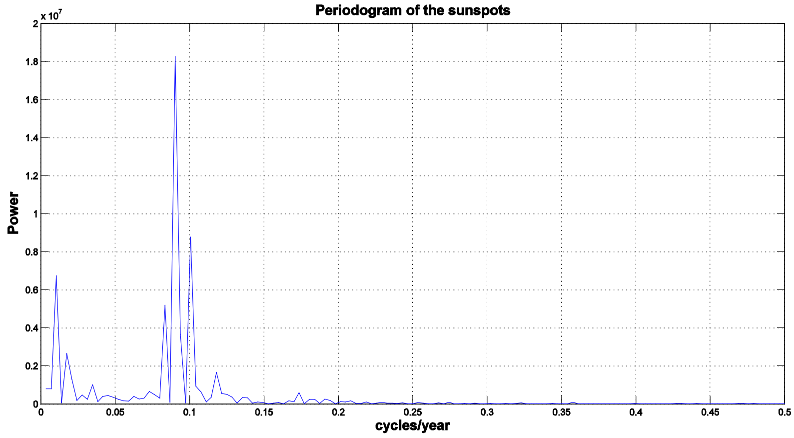

Figure 6: Periodogram of the sunspots (Mathworks 2007)

In figure 6 shows an example of the application of the periodogram to determine the periodicity of the sunspots. Here you recognize a relatively good spectral dissolution. There are four clear peaks. From the illustration it can be concluded that the frequency of the tall peaks is less than 0.1 cycles per year. This can be seen as the cycle of sunspots has an average value of eleven years.
In the following the periodogram of the coordinate time series is presented (figure 7). The periodic trend in the time series is obviously visible from the periodogram. In this case, all the points match to the corresponding frequencies. The peak in the periodogram indicates the strong potential frequency behind the data.

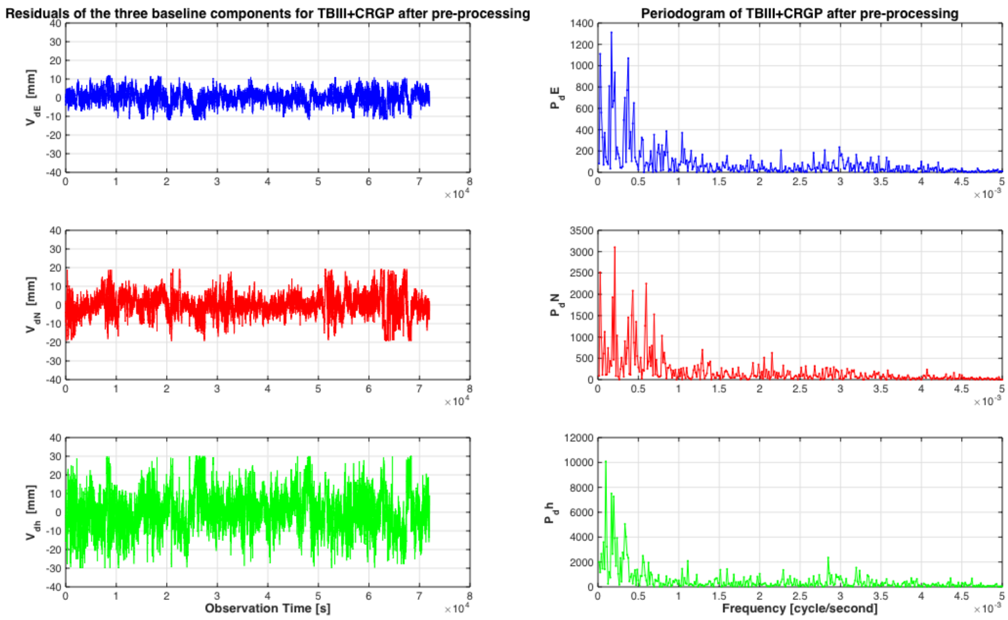

Figure 7: Residuals of the baselines components in dN, dE, dh and their periodogram of choke ring after the pre-processing (TBIII+CRGP)

4.1 Modelling and Estimation of the Periodic Trend

In order to eliminate the periodical trend of the identified frequency, the model is given below. The sine-cosine form of the Fourier series is used (formula 4.1). Each time only single frequency is modelled and there are three unknown parameters a_0, a_j and b_j to be estimated.

$$f(x) = \frac{a_0}{2} + \sum_{j=1}^{\infty}\left(a_j \cdot \cos\left(2\pi f_j x\right) + b_j \cdot \sin\left(2\pi f_j x\right)\right) \qquad (4.1)$$

$$l = f(x) \quad \text{corresponding to coordinate E,N,h} \qquad (4.2)$$

$$x = \begin{bmatrix} a_0 & a_j & b_j \end{bmatrix} \tag{4.3}$$

$$A = \begin{bmatrix} \frac{1}{2} & \cos(2\pi f_j x) & \sin(2\pi f_j x) \end{bmatrix} \tag{4.4}$$

The identified frequency f_j is used in the functional model. Analogous to the modeling of the linear trend, here the three unknown parameters are estimated by least square adjustment (Niemeier 2008). After the calculation of the unknown parameters, each parameter must be tested using a significance test. If the test statistic (formula 3.2) is greater than the quantile, the parameter turns out to be significant. If there is not significant parameter, it must be deleted in accordance with the model and the compensation is performed iteratively until all parameters are significant.

4.2 Results after the Periodic Trends Elimination

The periodic trend is modelled with the identified frequency in the periodogram. Next, the oscillation of the modelled data can be extracted. The accuracy is improved. Normally, the multipath effect can cause several periodic variations depending on the shading in the area. Therefore, the process is performed iteratively for the elimination of the periodic trends to locate all potential periods. But there are also some periods that are not due to the multipath effects, but may be regarded as white noise, which should have small amplitude. In general, the periods that are not caused by multipath effects should not be significant and then the iteration should be terminated. However, this is here not the case with the elimination of the periodic trends. The parameters are still significant after 300 iterations. Therefore it is very important to define a threshold to terminate the iteration. This issue will be resolved in the next section with appropriate values. Here the authors present the possible increase in accuracy by the elimination of the periodic trends.

Table 4: Standard deviations after elimination of the largest 10 periods

Quality	TBIII		TBIII+GP		TBIII+CRGP		Leica AX1203	
	before	after	before	after	before	after	before	after
s_E [mm]	7.2	6.3	5.9	5.3	3.5	3.1	3.9	3.6
s_N [mm]	10.7	9.3	8.5	7.6	5.4	4.9	6.1	5.5
s_h [mm]	18.2	15.9	14.5	13.4	9.0	8.0	10.0	9.1
s_{3D} [mm]	22.3	19.5	17.8	16.3	11.1	9.9	12.3	11.2
Improvement [%]	12.6		8.4		10.8		8.9	

Table 5: Standard deviations after elimination of the largest 50 periods

Quality	TBIII		TBIII+GP		TBIII+CRGP		Leica AX1203	
	before	after	before	after	before	after	before	after
s_E [mm]	7.2	4.5	5.9	4.3	3.5	2.5	3.9	2.9
s_N [mm]	10.7	6.7	8.5	6.2	5.4	3.9	6.1	4.2
s_h [mm]	18.2	11.5	14.5	11.0	9.0	6.7	10.0	7.5
s_{3D} [mm]	22.3	14.0	17.8	13.3	11.1	8.1	12.3	9.1
Improvement [%]	37.2		25.2		27.0		26.0	

Table 6: Accuracies after elimination of the largest 300 periods

Quality	TBIII		TBIII+GP		TBIII+CRGP		Leica AX1203	
	before	after	before	after	before	after	before	after
s_E [mm]	7.2	2.3	5.9	2.7	3.5	1.7	3.9	1.7
s_N [mm]	10.7	3.6	8.5	3.8	5.4	2.6	6.1	2.5
s_h [mm]	18.2	6.1	14.5	7.1	9.0	4.5	10.0	4.5
s_{3D} [mm]	22.3	7.4	17.8	8.5	11.1	5.5	12.3	5.4
Improvement [%]	66.8		52.2		50.5		56.1	

Tables 4, 5 and 6 indicate the accuracy and its improvement after the elimination of the most powerful 10, 50 and 300 periods behind the entire time series of 24 hours. After the elimination of the ten largest periods the accuracy of all three coordinate components has improved by about 10%. The improvement of antenna without shielding is the largest by 12.6%. It shows also that periods in the periodogram can still be found. The 3D accuracy after 50 iterations is achieved approximately 1 cm and, after 300 iteration even below 1 cm. If the three tables considered together, the following observations can be made: more periods are eliminated, the more increases the accuracy. In addition, the antenna without shielding always achieved the greatest improvement. The reason may be that the antenna without shielding is influenced stronger by multipath effects than the others, so it benefited more from the elimination of the periods.

4.3 Threshold Determination

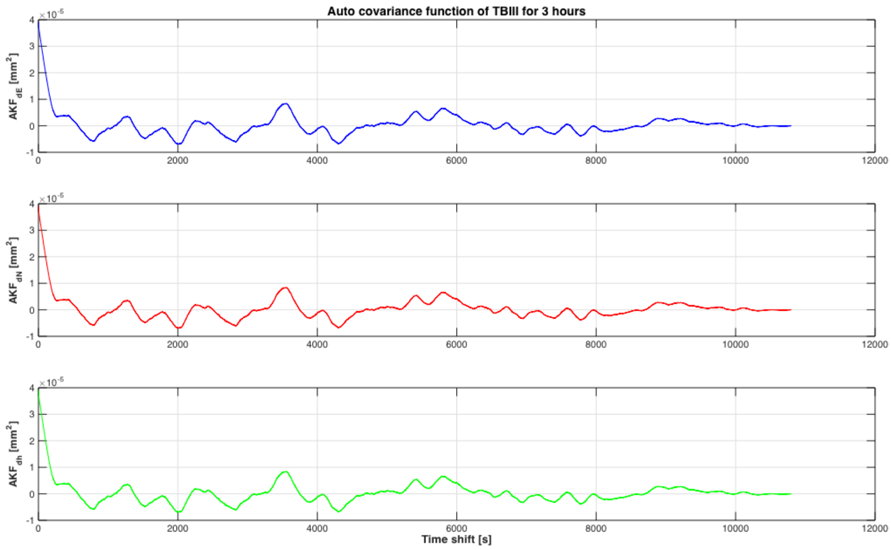

Figure 8: Auto covariance function of one baseline

The periodogram can discover all dominant periods. The accuracy of the time series can be improved if the identified periods of the time series are eliminated. This sequence can always be performed iteratively, because there is always a next strongest period. Therefore the question arises whether it actually makes sense to eliminate more and more periods. The answer is of course "no" and a suitable threshold is to be given instead of the significance test to terminate the iteration. The threshold replaces the quantile. The amplitude of the oscillation is compared with the threshold T. The parameters a_j and b_j are calculated from the adjustment in a final step (equation 4.5).

$$A_j = \sqrt{a_j^2 + b_j^2} \tag{4.5}$$

$$T = \sqrt{\hat{C}(0) - \hat{C}(1)}, \text{ with } \hat{C}(k) = \frac{1}{n-k-1}\sum_{j=1}^{n-k}(x_j - \bar{x})(x_{j+k} - \bar{x}) \tag{4.6}$$

The threshold is defined in terms of the white noise of the auto covariance function. The figure 8 shows the auto covariance function. Since the function of the zero time shift quickly falls down and close to zero, so that this process is quite similar to that of the white noise characteristic. It can be assumed that the white noise is represented by the difference between the value at the zero time shift and in the time difference of one represents. The threshold value is given with the white noise (equation 4.6).
Only if the test magnitude, which is determined from the modeling by means of adjustment theory, is greater than the threshold, the modeled vibration can be described as a distinct periodic effect. If this significance test is integrated into the program, it reveals how much iteration is expired at each antenna with different screens and what periods are eliminated from it.

Table 7: Periodic effects by the shieldings in the iteration until the threshold

Antenna	Number of iteration			Period [min]		
	d_E	d_N	d_h	d_E	d_N	d_h
TBIII	12	15	8	20-25	18-30,60-80	16-30,70-90
TBIII+GP	3	4	3	50,70,200	50,170,400	75,300,400
TBIII+CRGP	0	0	0	-	-	-

Table 7 and Figures 9 to 11 show an overview of the alteration of the periodic effects and the threshold in the periodogram. Under the application of the threshold value, the results can differ for different antenna shielding combinations. The antenna without shielding needs up to 15 iterations, to reach the threshold. The antenna with ground plate needs only 3 to 4 iteration for and for the antenna with choke ring even no significant periods can be found. That supports the positive effect of the shielding that with respect to elimination of the multipath effects. Furthermore, it can be seen that the period of 15 min to 30 min, which is identified in the case of no shielding does not occur for the other. This means that most of short periodic effects, which may be mainly the reflected from the ground, are successfully removed by using the shielding. Incidentally, the periods of about one hour at the antenna without shielding and ground plate which are not conditioned for the the multipath error from the ground, may be caused by the wall in the vicinity.
Although is no period be found in the antenna with the choke rings, there are also some strong periods that can be seen in figure 11, which may be caused by multipath effects. This means that another threshold can be defined in the future and the accuracy can be improved even more and multipath effects can be furthermore reduced.

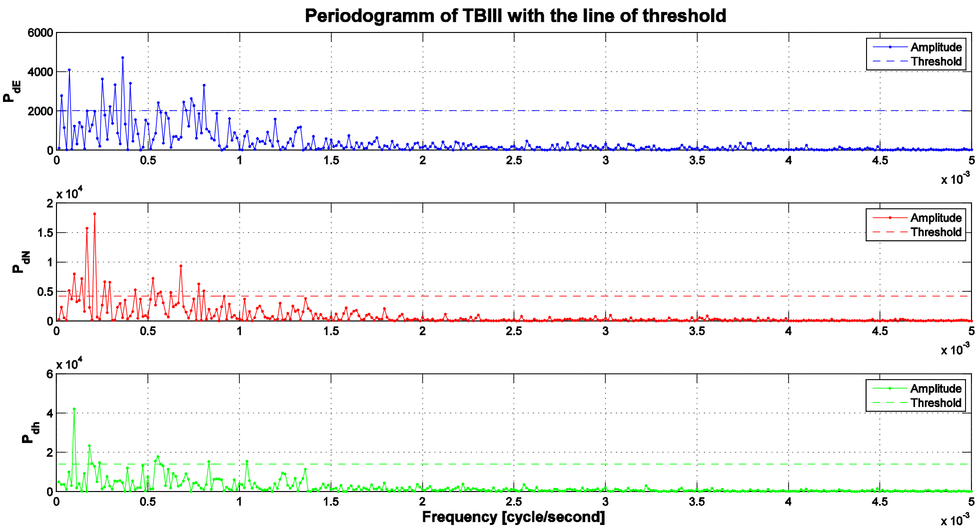

Figure 9: Periodogram for antenna without shieldings considering threshold

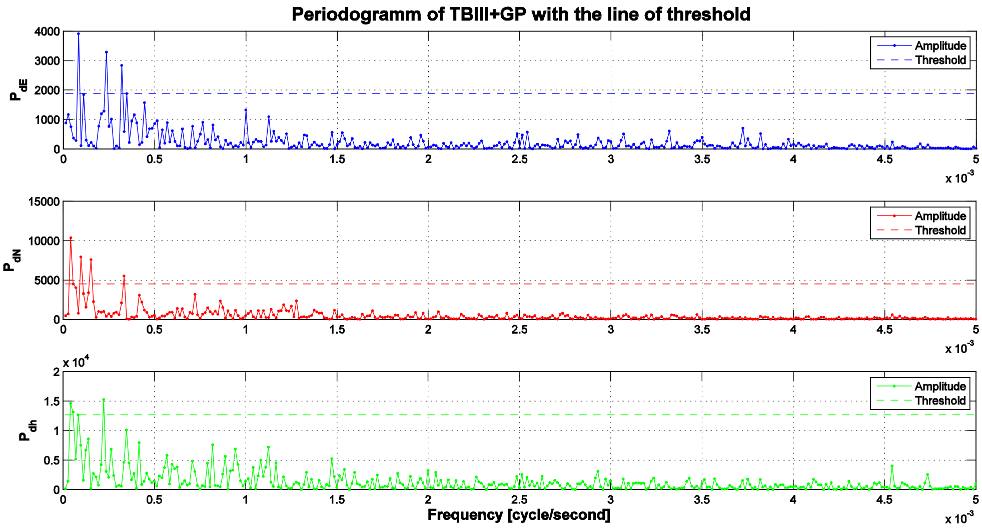

Figure 10: Periodogram of antenna with ground plate considering threshold

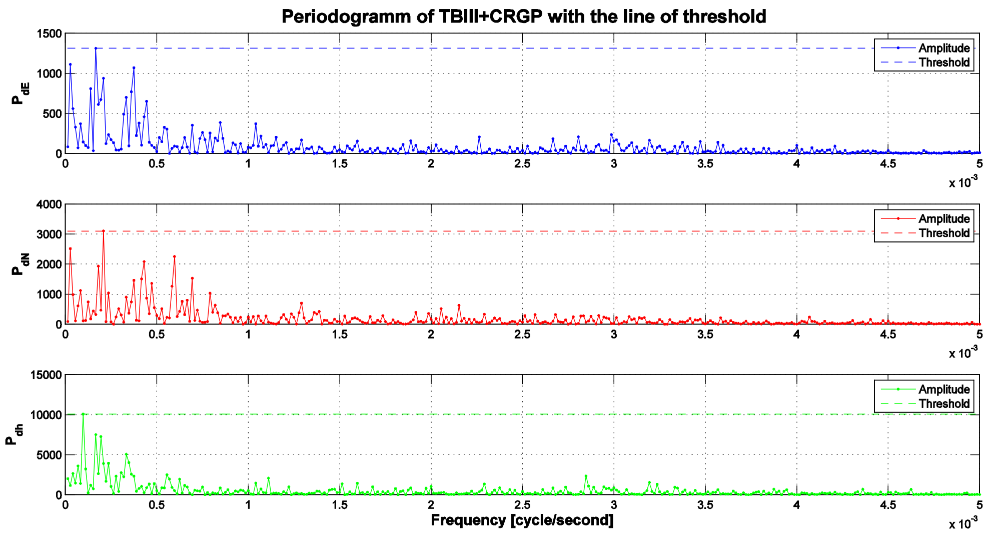

Figure 11: Periodogram of antenna with choke ring considering threshold^

5 CONCLUSIONS

In summary, this paper deals with comparing different shieldings by time series analysis for low-cost GPS receivers. In chapter 3 the accuracy and reliability of the collected coordinate time series have been improved by the data pre-processing, namely removing outliers and filling gaps. Compared to the antenna without shielding, the antennas equipped with ground plate and choke rings achieve better reliability and higher accuracy. Especially the Trimble Bullet III antenna with choke ring can already obtain an accuracy of 1 cm to 2 cm in 3D-position. This accuracy is almost the same for the Leica geodetic antenna and receivers combination, which have measured in the same position.

Chapter 4 shows that the multipath error could be reduced efficiently by the shieldings, because mainly indirect signals reflected from the ground can be eliminated. After the transformation of the time series in the frequency domain and a suitable definition of a threshold value can be seen that the apparent periodic trends in antennas with and without shielding are different. For the antenna without shieldings, periods are detected at around 15 to 20 min and 50 to 70 min. This may explain why the antennas with shieldings can gain a better accuracy. For geodetic monitoring, these low-cost receiver antenna shielding combinations, especially the choke rings may be applied.

As outlook, although the periodogram can help identifying periods in order to reduce multipath effects, it is difficult to define a threshold to locate multipath errors by distinguishing anomaly periods. One method to define the threshold based on white noise is developed in this paper, however there are still visible oscillation in the time series, other methods for definition of the threshold can be explored in future investigation.

ACKNOWLEDGEMENTS

The authors thank Wa1 software provider, Prof. Dr. Wanninger from Geodetic Institute of Technical University of Dresden. The authors thank also Mr. Martin Knihs of the IIGS for their help with the practical measurement and the construction of the ground plate and the choke ring.

Next, I want to thank to Prof. Dr.-Ing. Schwieger and all colleagues at the Institute of Engineering Geodesy for the good study atmosphere and their helpfulness. Furthermore, I would like to thank my colleges and friends for the beautiful and exciting period of study in Stuttgart, Germany. My very special thanks go to my parents who supported my studies and were always at my side.

REFERENCES

Books:

BAUER, M.: *Vermessung und Ortung mit Satelliten. 5. neu bearbeitete Auflage*. Herbert Wichmann Verlag, Heidelberg, 2011.

MANSFELD, W.: *Satellitenortung und Navigation: Grundlagen, Wirkungsweise und Anwendung globaler Satellitennavigationssysteme, 3. Auflage*. Vieweg+Teubner, GWV Fachverlage GmbH, Wiesbaden, 2010.

MATHWORKS: *MATLAB 7: Data Analysis*. The Mathworks, Inc., 2007.

NIEMEIER, W.: Ausgleichungsrechnung. Walter de Gruyter, Berlin, New York, 2008.

PAULO, S. R. D.; EDUARDO, A. B. d. S.; SERGIO, L. N.: *Digital Signal Processing: System Analysis and Design.* Cambridge University Press, 2002.

SCHWIEGER, V.: *Skript: Statistik und Fehlerlehre.* Institut für Ingenieurgeodäsie, Universität Stuttgart, Stuttgart, 2012.

WELSCH, W.; HEUNECKE, O.; KUHLMANN, H.: *Auswertung geodätischer Überwachungs- messungen. In: Möser, Müller, Schlemmer(Hrsg.): Handbuch Ingenieurgeodäsie*. Herbert Wichmann Verlag, Heidelberg, 2000.

Journal articles:

FOPPE, K.; NEITZEL, F.: *Von der Zufallsgröße zur Trendschätzung im vermittelnden Ausgleichungs-Modell - Grundlagen zur Zeitreihenanalyse für Praktiker*. In 129. DVW- Seminar: Zeitabhängige Messgrößen - Ihre Daten haben (Mehr-)Wert, 26.- 27. February 2014 in Hannover.

ROST, C.: *Phasenmehrwegereduzierung basierend auf Signalqualitätsmessungen geodätischer GNSS-Empfänger*. In C-Reihe der Deutschen Geodätischen Kommission (DGK), DGK München, München, 2011.

SCHWIEGER, V.: *Accurate High-Sensitivity GPS for Short Baselines*. FIG Working Week, Eilat, Israel, 03.-08.05.2009.

ZEIMETZ, P.; ELING C.; KUHLMANN H: *Analyse von GPS-Referenzstationsbeobachtungen mit Methoden der Zeitreihenanalyse.* In 85. DVW-Seminar: Zeitabhängige Messgrößen – Verborgene Schätze in unseren Daten. 07. - 08. September 2009 in Kassel.

ZHANG, L.; SCHWIEGER, V.: *Investigation regarding different antennas combined with low-Cost GPS receivers*. FIG Working Week, Abuja, Nigeria, 06.-10.05.2013.

Links:

TEQC : http://facility.unavco.org/software/teqc/teqc.html. Last accessed: February 2013.

U-BLOX : http://www.u-blox.de/de/gps-modules/pvt-modules.html. Last accessed: August 2014.

Wa1 : http://www.wasoft.de/wa1/index.html. Last accessed: February 2013.

Reducing Multipath Effects by Considering Spatial Correlation

Li Zhang
Institute of Engineering Geodesy, University of Stuttgart, Germany

Abstract
At the Institute of Engineering Geodesy of the University of Stuttgart (IIGS), low-cost single frequency GPS receivers were investigated for many years, the goal is applying these low-cost GPS receivers for monitoring tasks.
The multipath effect is the dominant error for short baselines. To improve the accuracy of the measurement, the spatial correlation of coordinate’s residuals of several closely-spaced low-cost GPS antennas were analyzed using time series analysis. Methods to improve the accuracies and reliabilities of the low-cost GPS receivers will be introduced and the results will be shown.
The aim is the development of a method, which can deliver an accurate and reliable result in near-real-time, using time and spatial correlations of multiple low-cost GPS receivers to enable structural health monitoring.

Keywords
Low-cost GPS, monitoring, multipath effects, spatial correlation, time series

TECHNICAL SESSION 4: LASER SCANNING APPLICATIONS

Accuracy Analysis of DEM Generation and Computing Volumes of Excavation and Rock Fillings by Laser Scanning Data

Maxim A. Altyntsev, Vladimir A. Seredovich
Siberian State University of Geosystems and Technologies, Russian Federation

Abstract
The issue of large volume of laser scanning data is considered. The task of point cloud reduction is stated. Point cloud reduction algorithms are outlined. Accuracy analysis of digital elevation model generation by thinned laser scanning data is given. Volume calculation as a technique for accuracy estimation of DEM generation is presented. Volume calculation methods are outlined. The results of analysis for laser scanning data of an open-cut mine are shown.

Keywords
Laser scanning, DEM generation, volumes of excavation and rock fillings, accuracy

1 INTRODUCTION

Generation of digital elevation models (DEM) is the integral part of majority of surveying works. Digital elevation models can be represented both with a part of a topographic plan in display mode by contours and elevation points and with three-dimensional surfaces which are divided into regular, irregular and statistical ones. Regular DEM is considered as an array of points placed in corners of equally sized grid cells, whereas irregular DEM is considered as a grid with irregular shapes, for example, triangle grids also called triangulated irregular network (TIN). Statistical models are based on application of second and third linear interpolation where points for model generation are chosen by random distribution similar to uniform FEDOTOV & POSPELOV (2007). For example, such models are always included into three-dimensional models of territories where there are some complicated engineering structures.

DEM can be generated on the basis of various geodetic data, but more exact, detailed and dense model can be obtained only using laser scanning. The quality of DEM generation using laser scanning data directly depends on their preprocessing including calibration and adjustment of laser points, and classification results where ground points should be correctly classified in big datasets MENG, CURRIT & ZHAO (2010).

But when generating DEM using laser scanning data it should be taken into account that these data contain great number of redundant information. The better approach is to reduce the volume of data. It's necessary to find or to develop an algorithm of point cloud reduction for generated DEM not to have lower accuracy. Such an algorithm should analyze initial point cloud with the object to choose laser points which have to be included in a resulting point cloud. That means DEM based on the resulting thinned point cloud will be simplified. Simplified DEM has to have almost the same accuracy as DEM based on the initial point cloud.

A volume of excavation and rock fillings can be a criterion of DEM accuracy. This volume is calculated between two models generated on the basis of multitemporal laser scanning data. For volume computation it is enough to choose calculation algorithm and to select at first DEM generated for the data collected earlier, and then – for those collected later. If one compares the volume determined between multitemporal initial DEMs with the volume determined between resulting ones, it's likely to be almost the same. The less difference between volumes is, the more accurate the simplified DEMs are.

Accuracy of DEM generation can be estimated using the volume calculation approach even if there are only data gathered in one period of time. In this case volume should be calculated between DEM generated on the basis of initial point cloud and simplified DEM. The less the calculated volume is, the more accurate simplified DEM we get. Difference between excavation and filling also should be less to get a more accurate simplified DEM.

2 VOLUME CALCULATION METHODS

There are several methods of volume calculation between two surface models: grid method, the average end area method, the prismoidal method and the composite method SCACCO (2005).

In the grid method volumes of excavation and fillings are calculated in each equally sized grid cell which are obtained by means of comparison and dividing corresponding multitemporal surfaces. Total volumes are equal to sum of all cell volumes. The lower size of cells is the more accurately the total volumes will be calculated.

The average end area method uses evenly spaced parallel cross-sections cut through the site to compute volume differences. At each cross-section, the area bound by two surfaces is calculated. This area is then averaged with the area calculated for the adjacent section and multiplied by the distance between the sections. The sum of these calculations is the total site volume.

The prismoidal method is a more accurate method which uses a form of finite element analysis to calculate volumes. Each side of the triangles representing the upper TIN surface is projected onto the lower TIN surface. The points where the TIN lines from each surface intersect are then projected back onto the triangles to define a subarea on each triangle. These subareas are then averaged and multiplied by the distance between the centroid of the subareas to yield volumes; they are then summed to get total site volume.

The composite method is the most accurate method which creates a new triangulated surface based on points from both surfaces. It determines where a triangle edge or point from the proposed surface crosses an edge or point from the existing surface and calculates the elevation difference at these locations. This data is then used to create the new TIN.

3 POINT CLOUD REDUCTION ALGORITHMS

There are several different algorithms for point-based surface model simplification, including clustering BRODSKY & WATSON (2000), particle simulation TURK (1992), and iterative simplification ALEXA et al. (2001), ALEXA et al. (2003), DYN, ISKE & WENDLAND (2007). Iterative simplification algorithms are usually applied. These algorithms include thinning, a recursive point removal scheme, where the points are removed according to some suitable removal criterion. Thinning algorithms are efficient methods for the construction of a point data hierarchy.

In this article 3 algorithms for point-based surface model simplification will be compared. The first algorithm is the simplest. By means of this algorithm regularly distributed points at constant intervals in both X and Y directions are included in a simplified grid model SOININEN (2014). Constant distance between laser points in the grid model should be specified.

The second algorithm is an iterative process that consists of several stages SOININEN (2014). The process of including points in a simplified model starts by searching for initial points inside rectangular regions of a given size. One has to specify a rectangle size. The rectangle size corresponds to a minimum point density in the whole point cloud. The lowest and the highest source point inside each rectangle are classified as a key point and those are used to create an initial triangulated model. During each iteration loop the algorithm searches for source points which are beyond the given tolerance above or below the current model. Such tolerances should be preliminarily specified. If such points are found, the highest or lowest points are classified and added to the model.

The third algorithm is a meshfree thinning algorithm DYN, ISKE & WENDLAND (2007). This algorithm is based on local surface approximation for estimating the significance of a point. The local approximation relies on principal component analysis for the estimation of a local tangent plane and a kernel-based smoothing approximation using compactly supported radial basis functions. During the surface simplification only the nearest neighbours of some point x should be used to reconstruct the surface in its neighbourhood. The number of neighbours is a fixed parameter determined at the beginning of the algorithm. A detailed description is given in BUHMANN (2003).

4 DATA SOURCE AND PREPROCESSING

For accuracy analysis of DEM generation and computing volumes of excavation and rock fillings laser scanning data of an open-cut mine in the site of Bugotakskiy deposit occurrence in Novosibirsk Region were taken. These data were gathered by Riegl VZ-400 scanner. Surveying was carried out by the Siberian State University of Geosystems and Technologies (SSUGT) on the 6th of September and the 1st of October 2014. The area of the analyzed open-cut mine part is approximately 22000 m^2. Before the point cloud reduction and the volume calculation the ground points were classified. The number of ground points collected in September is 2771467, in October – 2853265. Excavation and rock filling volumes were calculated between these 2 data sets.

5 ACCURACY ANALISYS OF DEM GENERATION

For implementation of accuracy analysis of DEM generation source laser scanning data were thinned several times using 3 algorithms described in the section 3. During the thinning process various parameters of each algorithm were used. When applying the grid method the values of grid spacing were specified as 10, 30 and 100 centimeters. When using the key point classification algorithm, the minimum point density was specified as 50, 100 and 500 centimeters whereas tolerance above or below the current model as 1, 2, 5, 10 and 50 centimeters. When using the meshfree thinning algorithm number of neighbours was specified as 5 and 10.

For volume calculation the grid method was chosen. Grid size of 20 centimeters was used. At first volumes were calculated between multitemporal DEMs obtained when using the same parameters. In Fig. 1 the correlation between the number of ground points and the difference excavation volume is shown. The number of ground points collected only in October is given in next figures. The difference excavation volumes were calculated between the volume of the initial model and the thinned ones.

From Fig. 1 excavation volume is seen to be rather small except this volume for grid spacing value of 100 centimeters. The maximum excavation volume value of about 137 м^3 for the key point classification algorithm is very small in comparison with total site area. If one analyzes the meshfree thinning algorithm excavation, the volume is minimal as well as the volume calculated when using some parameters of the key point classification algorithm. But the number of points obtained as the result of source point cloud thinning by both the grid method and the meshfree thinning algorithm is more than the one obtained by the key point classification algorithm. The key point classification algorithm is concluded to be more appropriate algorithm for point cloud reduction. Fig. 2 shows correlation between difference excavation volume and tolerance for key point classification algorithm. Tolerance is one of this algorithm parameters described in the section 3. It is necessary to determine parameters when the number of point is less as well as the value of difference excavation volume. Theoretically the less number of points the more difference excavation volume is. Comparing Fig. 2 and 3 it can be conclude that the majority of values are rather close to each other. Determining parameters of the key point classification algorithm it can be concluded that the better result was obtained for minimum point density of 100 cm and tolerance of 50 cm. The number of point was reduced in 117 times applying such parameters. Using a more thinned model the volume can be calculated even more accurately than using a less thinned model.

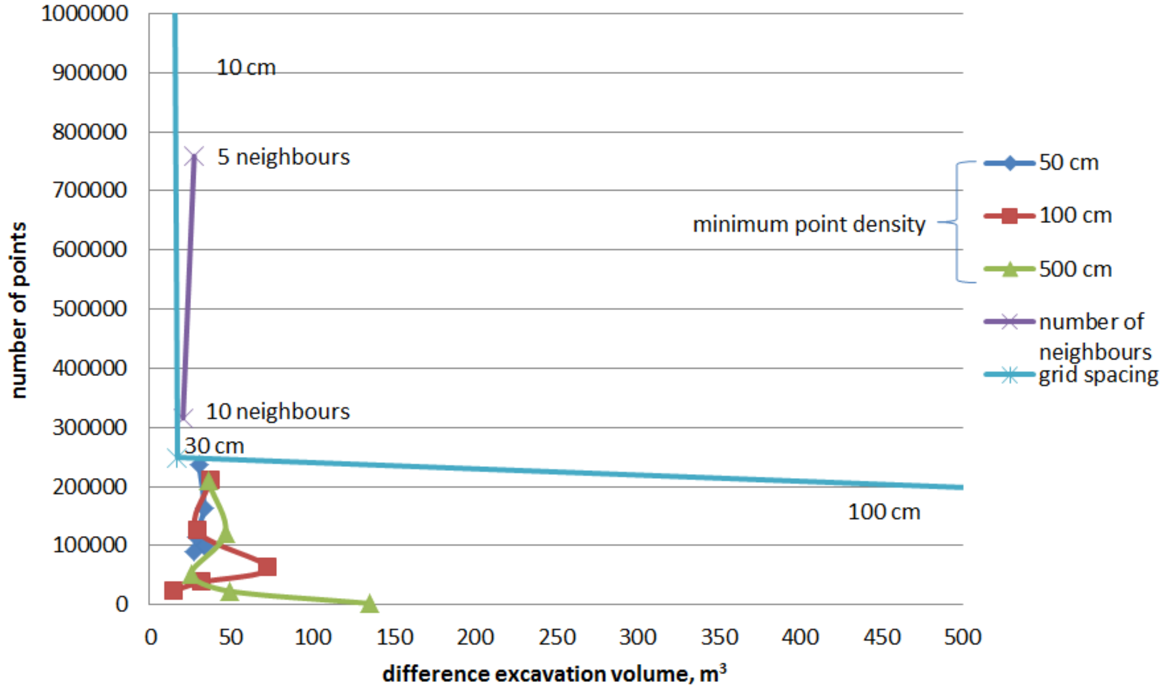

Figure 1: The number of points depending on excavation volume

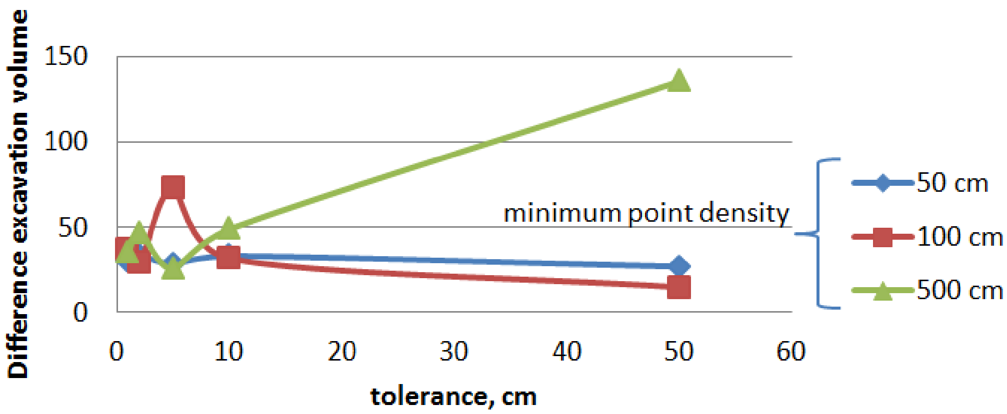

Figure 2: Difference between excavations in initial and thinned model depending on tolerance

The results of this investigation show that difference excavation volume should not be applied as a criterion of DEM accuracy. For this reason another investigation was carried out. Volumes were calculated between initial and thinned DEMs. DEM generated by ground laser points collected in October was chosen. In Fig. 3 the correlation between the number of ground points and the excavation volume is shown. The statement about the greater excavation volume when using the lesser number of points is confirmed in this case. From Fig. 3 it is also seen that DEMs generated on the basis of laser points thinned by the key point classification algorithm generally have better accuracy comparing excavation volumes with the same number of ground points. The number of points which were thinned by different parameters of the key point classification algorithm is quite low.

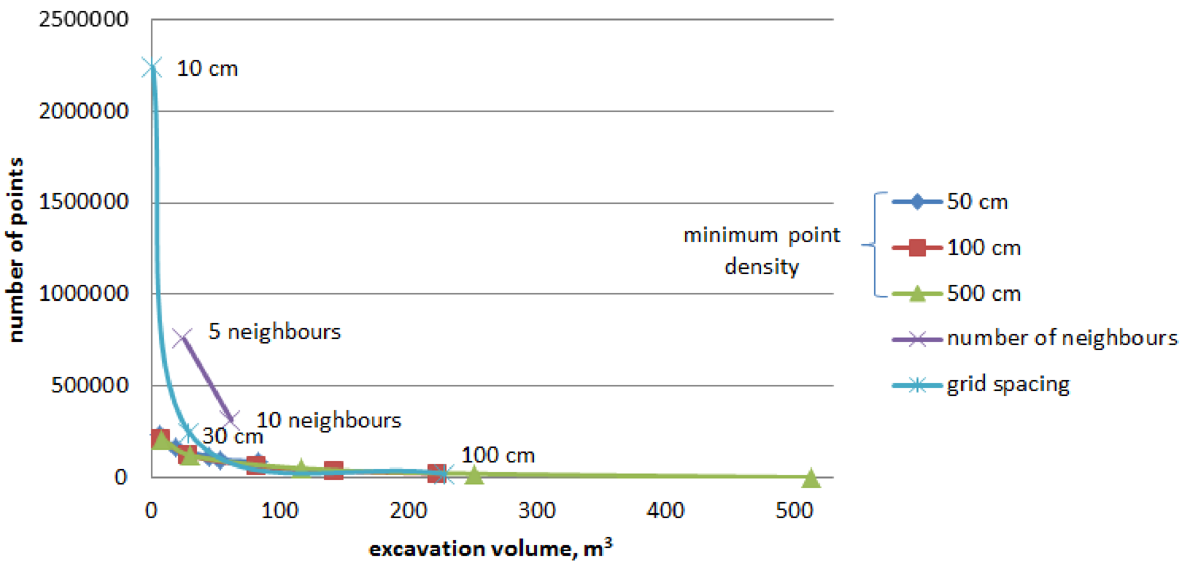

Figure 3: The number of points depending on excavation volume

To choose parameters of the key point classification algorithm for obtaining higher accuracy of DEM generation, Fig. 4 and 5 are necessary to be compared. In Fig. 4 the correlation between excavation volume and tolerance is shown, in Fig. 5 it is shown between the number of points and tolerance. If one looks at Fig. 5, the number of points for the values of minimum point density of 100 and 500 centimeters is rather close to each other. The number of points for these values is much lower than for the value of 50 cm. Therefor the minimum point density value of 50 cm should be rejected. The number of points in DEM generated when using minimum point density values of 100 and 500 cm and using tolerance value of 5 cm is 2 times lower than in DEM generated when using tolerance value of 2 cm. Taking into account this fact, tolerance value of 5 cm is more suitable for thinned DEM generation. If one looks at Fig. 4 excavation volumes for the minimum point density values of 100 and 500 cm from tolerance value of 1 cm to tolerance one of 5 cm are close. The excavation volume for minimum point density of 100 cm and tolerance of 10 cm differs much more from this volume for minimum point density of 500 cm and tolerance of 10 cm. This volume for tolerance of 5 cm and minimum point density of 100 cm is a bit lower than the volume for tolerance of 5 cm and minimum point density of 500 cm. But the number of points when using such parameters is lower when one applies the minimum point density value of 500 cm. Taking into account the fact that excavation volume of 100 м^3 is very small for the area of 22000 m^2 it can be concluded that for generation of the most thinned and accurate DEM the minimum point density value of 500 cm and tolerance one of 5 cm should be chosen.

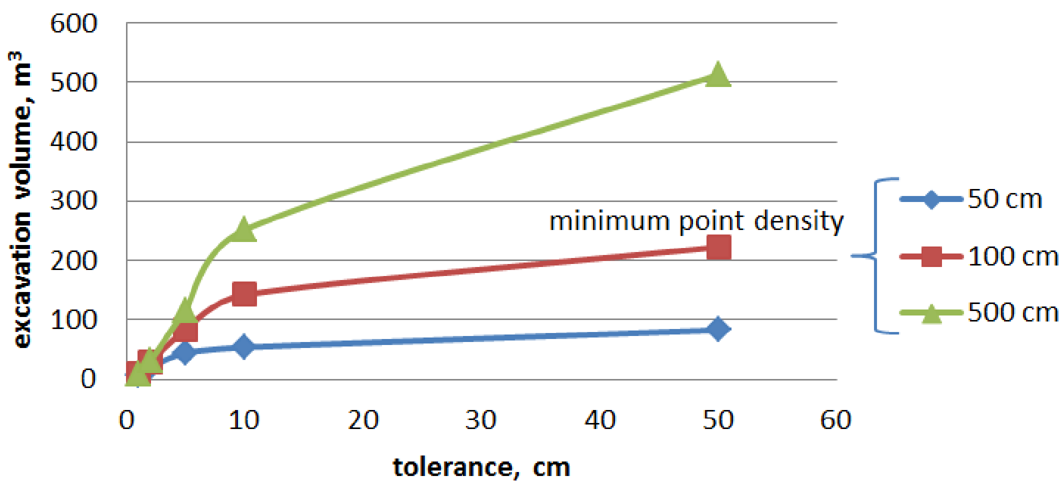

Figure 4: Excavation volume depending on tolerance

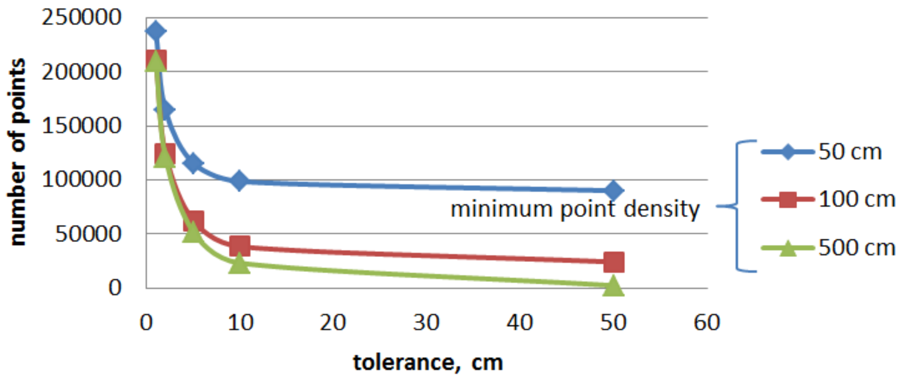

Figure 5: The number of points depending on tolerance

6 CONCLUSIONS

Thus, accuracy analysis of DEM generation by laser scanning data for the open-cut mine was carried out. It was noticed that laser scanning data contain great number of redundant information and these data should be thinned. Thinned data was proved to be appropriate for generation of accurate simplified DEM. Volume calculation of excavation and rock fillings was chosen as the criterion of accuracy estimation of simplified DEM generation. It was shown that for reliable accuracy estimation a volume should be calculated between initial DEM and simplified one. 3 algorithms were used for data thinning. Among these algorithms the key point classification algorithm showed the better and the most accurate results of thinning. Optimal parameters of this algorithm were selected. These are the minimum point density value of 500 cm and tolerance one of 5 cm. Using these parameters point cloud was reduced in 57 times almost without loss of DEM generation accuracy. It was also shown that if one need just to calculate volume between multitemporal laser scanning data, these data can be thinned more than in 117 times. Optimal parameters of the key point classification algorithm for this purpose are as follows: the minimum point density value of 100 cm and tolerance one of 50 cm. Next investigation should be carried out using more numbers of algorithms and parameters.

REFERENCES

Books:

FEDOTOV, G.A., POSPELOV, P. I.: *Encyclopedia of a road maker. Volume 5. Highway design.* Moscow, 2007.

SOININEN, A.: *TerraScan User's Guide*. Finland, 2014.

BUHMANN, M. D.: *Radial Basis Functions*. Cambridge University Press, UK, 2003.

Journal articles:

MENG, X., CURRIT, N., ZHAO, K.: *Ground Filtering Algorithms for Airborne LiDAR Data: A Review of Critical Issues*. Remote Sensing, vol. 2(3), p. 833-860, 2010.

SCACCO, M.: *On the surface with quantity take-off software*. Site Prep Magazine, winter 2005, p. 24-30, 2005.

BRODSKY, D., WATSON, B.: *Model simplification through refinement*. Proceedings of Computer Graphics and Imaging, p. 221–228, 2000.

TURK G.: *Re-tiling polygonal surfaces*. Computer Graphics, vol. 26(2), p. 55-64, 1992.

ALEXA, M., BEHR, J., COHENOR, D., FLEISHMAN, S., LEVIN, D., SILVA., C.T.: *Point set surfaces*. IEEE Visualization, p. 21–28, 2001.

ALEXA, M., BEHR, J., COHENOR, D., FLEISHMAN, S., LEVIN, D., SILVA., C.T.: *Computing and rendering point set surfaces*. IEEE Trans. Vis. Comput. Graph., vol. 9(1), pp. 3–15, 2003.

DYN , N., ISKE, A, WENDLAND, H.: *Meshfree thinning of 3d point clouds*. Foundations of Computational Mathematics, vol. 8, p. 409 - 425, 2007.

Geomonitoring of Engineering Structures and Forecasting Their Deformations Using Laser Scanning Data

Ekaterina I. Gorokhova
Siberian State University of Geosystems and Technologies, Russian Federation

Abstract
Monitoring of engineering structures is one of the main tasks of engineering geodesy. Geometric changes of structure points can be detected with the different surveying instruments. The problems of processing and forecasting structure conditions are also very important. Classification of monitoring types, methods of statistical data processing and general steps of tunnel monitoring using laser scanning data are offered.

Keywords
Geomonitoring, terrestrial laser scanning, deformations, cross-section, engineering structures, forecasting

1 INTRODUCTION

To ensure the safety of engineering structures, geomonitoring is widely used. The purpose of the monitoring is: the timely detection of deformations critical values; determination of their causes; predicting the way the deformations may develop; finding and taking measures for elimination, mitigation and prevention of harmful processes. Forecasting is the most complicated part of the geomonitoring because it requires collection, taking into consideration, registering, storing and processing the results of engineering structures deformation measurements. Prognosis is necessary for getting a scenario of deformation development and insight into the general condition of engineering structures. The aims of geomonitoring of engineering structures and analysis of their deformations are very actual and complicated. They need the maximal accuracy of measurements, observation process automatization, the utmost reliability of geodetic devices, as well as flexible software tools for processing and analyzing the data. At all stages of any engineering structure life cycle (surveying, tracing, staking etc) the results of geodetic measurements and observations are the initial basis for creating a comprehensive system letting us monitor and predict the general condition of the above mentioned structures.

The complex approach to monitoring aims solution includes both the engineering structure condition assessment (processing the results of geodetic observations and getting the quantitative characteristics of condition changes in engineering structure in general, and any of its parts in particular), and the prognostic characteristics definition.

2 GENERAL DEFINITIONS

Statistical analysis of geodetic measurements in different observation epochs allows estimating the deformation processes and coming to conclusions about exploitability of engineering structures.

Mathematical modeling and kinematic analysis of observations for engineering structure's supporting constructions let us to determine quantitative pattern of deformations development and forecast their further progress.

The main phases of geodetic monitoring are:

1. Development of technical specifications;
2. Condition monitoring and technical investigation of the object for the purpose of data collection and systematization before starting the main works;
3. Development of monitoring program;
4. Monitoring, data processing, generation of intermediate progress report;
5. Forecasting of structures condition, report generation and recommendations about further serviceability of structures and reduction of negative factors influence;

6. Completion of monitoring, preparation of final report.

Forecasting is possible only when used all data, complete and comprehensive information about engineering structure condition and its changes based on modeling by the statistical extrapolation method. In this case the choice of approximating function is carried out by taking into account factors and limitations of controlled deformations process development. Thus, statistic pattern is composed from strictly determined single phenomena. Using this pattern it is possible to achieve the reliable predictions only by mathematical tools.
The mathematical model of deformation process can be expressed both in kinematic and dynamic mode depending on completeness and available initial data. The mathematical process descriptions of monitored structure points displacement serve as a kinematic model and show the dependence of the displacements on the time (but without considering the forces causing this movement). The dynamic model is the mathematical process description of monitored structure point’s displacement which takes into account inertial properties of system “structure - environment” and the actions of the main forces causing displacement. It means that dynamic model describes the deformation process with regard to joint effect of time and main influencing factors

There are following types of forecasting:

- searching forecast - determination of possible prognostication object conditions in the future;
- regulatory forecast - ways and periods determination of possible conditions of prognostication objects in the future, accepted as criteria;
- interval prediction – the results are presented as confidential interval or errors corridor of the defined prognostication object characteristics with the specified probability of forecast implementation;
- selective prognosis – the result is presented as unique value of prognostication object characteristics without indication to confidential interval,
- on-line testing forecast- with the forecast period up to 1 month,
- short-term forecast - forecast with time period from 1 month to 1 year,
- middle-term forecast - the forecast with the anticipation period from 1 year to 5 years,
- long-term prognosis - the forecast is carried out from 5 to 15 years,
- very long term forecast - the forecast with anticipation period over 15 years.

For mathematical model verification a check forecasting is performed for the period, which matched with already fulfilled reserve observation epochs.

For representing construction deformation process through numerical parameter characteristics it is necessary to calculate them for each observation epoch, and then to approximate the variation of these characteristics in time for the performed observation epochs. The main numerical characteristics in each observations epoch are mathematical expectation and dispersion, and the dependence level between epochs is expressed by autocorrelation function. Approximation of variations of these numerical characteristics in time represents the multivariable statistical process distribution law found by the results of discrete geodetic observations. The dependence overcrowding of approximating terms is described by correlation parameters for linear case and the correlative relations – for nonlinear case.

The number of observations epoch, preceding to forecast step, must provide the variance, necessary for model parameter estimation.

The prognosis phase consists of extrapolation of modeling parameters on reasonably selected time period and of using the obtained estimates for determination of relative mathematical expectation and dispersion. Thus, within the revealed statistical law the predicted values of specific forecast implementations and errors corridor are estimated.

Forecasting of structures deformation progress must proceed until its stabilizing confirmed by geodetic observations. Thus it is necessary to update data of the previous measurements by getting new monitoring results according to data on change of forecast background. In such a way the observance of the continuous prediction principles is performed.

3 FORECASTING KINEMATIC MODELING ALGORITHM

The accomplished calculations and data analysis serve as a justification for correct using of stochastic functions by forecast modeling. If it is necessary, normalization and linearization of the simulated process are made.

The forecast kinematic model of subsidence process is built as the following two first conditional moment functions (1), (2):

$$\widehat{m}_{Xi}\left(\frac{t_2}{t_1}\right) = \widehat{m}_X(t_2) + \hat{r}_X(t_2, t_1)\frac{\hat{\sigma}_X(t_2)}{\tilde{\sigma}_X(t_1)}\dot{x}_i(t_1) \tag{1}$$

$$\hat{\sigma}_X\left(\frac{t_2}{t_1}\right) = \hat{\sigma}_X(t_2)\sqrt{1 - \hat{r}^2(t_2, t_1)} \tag{2}$$

where: t_1– the end time of previous observations epochs', on which the model is built; t_2 – the end of predictions period (cross-sections on which the forecast is executed); the sign ~ marks statistical estimates of numerical parameters in observed cross-sections; the sign ^ marks the numerical parameters approximated on the forecast base period; $\widehat{m}_{Xi}\left(\frac{t_2}{t_1}\right)$ – the subsidence forecast of i-y mark for timepoint t_2, if $\dot{x}_i(t_1)$, $\widehat{m}_{Xi}(t_2)$, $\hat{r}_X(t_2, t_1)$, $\hat{\sigma}_X(t_2)$ are known. They present centered subsidence value i-y mark at the moment t_2 and estimation of expectation autocorrelation function and standard, which are extrapolated at t_2 by the equations. These equations approximate their developing for base prognosis time. $\hat{\sigma}_X\left(\frac{t_2}{t_1}\right)$ – *is* expected tolerance.

Thus, the contains of the first reference moment function in a formula (1) presents itself expected kinematic model as mathematical expectation $\widehat{m}_{Xi}\left(\frac{t_2}{t_1}\right)$ of i-mark subsidence at t_2 provided that it is known at the time t_1. It is approximate equation of average subsidence $\widehat{m}_{Xi}(t_2)$, extrapolated by the time t_2 and also autocorrelation function (regulated) $\hat{r}_X(t_2, t_1)$, extrapolated on the approximating equation at the time t_2 multiplied at $\frac{\hat{\sigma}_X(t_2)}{\tilde{\sigma}_X(t_1)}$ and centred value i-subsidence $\dot{x}_i(t_1)$ at the observable period t_1.

In fact, this equation expresses a regression line of the i-mark subsidence which is projected on the horizontal plane. The second conditional moment in expression (1) characterizes the expected predictions error (an errors corridor) and represents the standard of the subsidence forecast $\hat{\sigma}_X\left(\frac{t_2}{t_1}\right)$ at the moment t_2, if t_1 is known. It is equal to standard products extrapolated on the approximating equation at the moment t_2 , on the square root of 1 minus a square of the normalized autocorrelation function, extrapolated on the approximating equation at the t_2.

Thus, substantially, expected kinematic modeling is reduced to determination of statistical parameters of the statistical law in each cross-section of the forecast base period and to the following approximation these parameters in time.

Then expected modeling is comparable if the actual forecast errors on a monitoring period are no more than the predetermined standard or (as a last resort) its triple value. Such control check is called as inverse verification. In certain cases there are big variances of expected and actual subsidence values.

There can be following causes:

a) Statistical inhomogeneity the selected group of process implementations. At the same time it is possible with using the method of statistically similar groups criteria selection;

b) Subnormally precise approximation (and then extrapolation) of model parameters.

Often the last case can arise by approximation and extrapolation of average subsidence $\widehat{m}_X(t_2)$, therefore there is a systematic distortion of results. For elimination of this defect it is necessary to use the following effective method – to predict not the subsidence value of specific i-mark, but differences of subsidence values of typical points, for example, which have the maximum and minimum subsidence values. It' that subsidence inhomogeneity between i and l marks is forecasted according to (1) with a formula:

$$\widehat{m}_{\Delta X}\left(\frac{t_2}{t_1}\right)_{il} = \frac{\hat{r}_X(t_2,t_1)\left(\hat{\sigma}_X(t_2)\right)}{\tilde{\sigma}_X(t_1)}\Delta X(t_1)_{il} \tag{3}$$

The tolerance forecast of subsidence values should increase $\sqrt{2}$. But, as a rule, the forecast accuracy of a subsidence rises in case of inaccuracy approximation and extrapolation $\widehat{m}_X(t_2)$. Therefore, it can be used for a value forecast accuracy assessment $\hat{\sigma}_X\left(\frac{t_2}{t_1}\right)$ calculated according to (1).

4 TERRESTRIAL LASER SCANNING FOR GEOMONITORING OF TUNNELS

Among the surveying technologies just the laser scanning is capable to satisfy to the increasing demand for precise kinematic measurements.

Figure 1: A view of subway tunnel

The office processing of TLS data is finished by the assessment of railway tunnel conditions (Fig.1) and determination of geometrical parameters giving evidence of tunnel deformations. To analyse the a tunnel's health the following procedures were used:

1. Comparison of design and actual *K*-sections (obtained by terrestrial laser scanning data) located every 10 m on a smoothed tunnel section. Such technique allows revealing a declination of a tunnel under construction from the designed value, deformation monitoring during construction, when maintenance begins, and during tunnel maintenance (Fig.2).

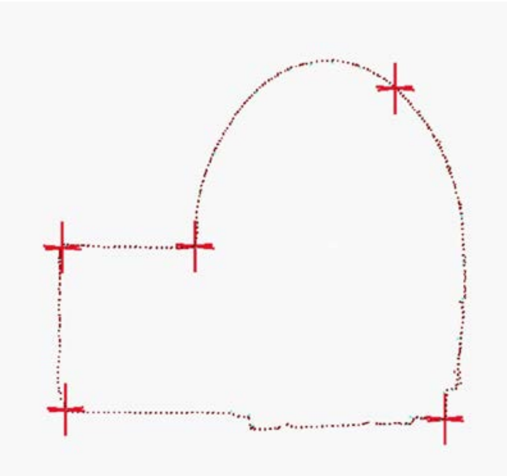

Figure 2: An example of a cross-section with control points in Cyclone

2. Comparison of tunnel cross-sections obtained for different dates of tunnel scanning. In this case the assessment of tunnel condition will be compared with the characteristics of its similar cross-sections obtained for different observation epochs. This technique is aimed at the regular monitoring of railway tunnels. Its advantage is that it allows comparing not only separate cross-sections taken from 3D model, but 3D models of tunnel created for different dates themselves.

3. Than the cross-sections are plotted on spline basis – approximation and least-squares method (Fig.3).

4. Prediction of a status of a tunnel and development of already existing deformations by means of the kinematic analysis and Kallman's filter.

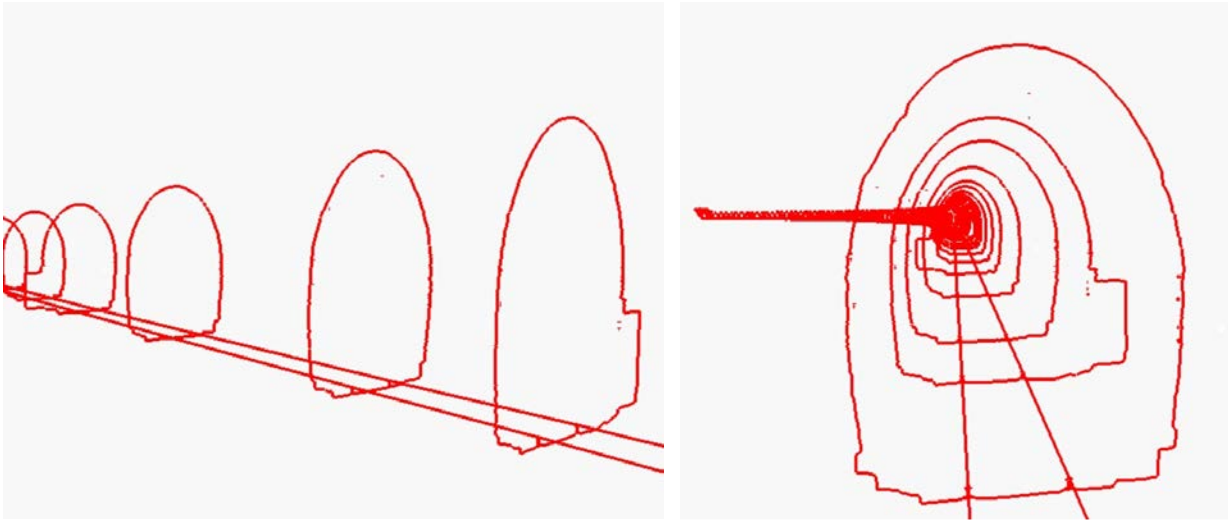

Figure 3: An example of spline basis – approximation of cross-sections

5 CONCLUSIONS

Geomonitoring based on instrumental high-precision geodetic observations makes possible to find and to prevent displacements and deformations of engineering structures. It provided the high level of their safety. Laser scanning technology can be successfully used for geomonitoring of complicated engineering objects and structures and provide the high accuracy (about 1-10 mm). For the forecasting of engineering structures conditions the kinematic and dynamic models are created.

REFERENCES

Books:

SEREDOVICH, V.A.: *Terrestrial laser scanning*. Siberian State Academy of Geodesy, Novosibirsk, 2009.

PIEGL, L., TILLER, W.: *The Nurbs Book*. Springer, Berlin, 1997.

Journal articles:

GOROKHOVA, E.I., *Terrestrial Laser Scanning for Monitoring of Tunnel Deformations*, Siberian State Academy of Geodesy. Integration of Point- and Area-wise Geodetic Monitoring for Structures and Natural Objects. Proceeding of International Workshop, 14-15 April 2014, Novosibirsk. - Novosibirsk: SSGA, p. 83-89.

GOROKHOVA, E.I., IVANOV, A.V., *Experience of application for terrestrial laser scanning technology in railway tunnels*, Proceedings of International scientific congress "Interexpo GEO-Siberia-2009", p. 257 - 260, 2009.

KOMISSAROV, AV., GOROKHOVA, E.I., *Substantiation of parameters for tunnels surveying whis terrestrial laser scanning*, Geodesy and Aerophotography, 3/2011, p. 81 – 85, 2011.

NEUNER, H., SCHMITT, C., NEUMANN, I., *Modelling of terrestrial laser-scanning profile measurements with*, Proceedings of the 2nd Joint international Symposium on Deformation Monitoring, Nottingham, England, 2013.

HEIKER, A., KUTTERER, H., *Integration of observations and models in a consistent least squares adjustment model*, Proceedings of the 1st International Workshop on the Quality of Geodetic Observation and Monitoring Systems, QuGOMs. München, 14.-15.04.2011.

KUTTERER, H., NEUMANN, I., *Recursive least-squares estimation in the case of interval observation data*, International Journal of Reliability and Safety, Jg. 5, 3/4/2011, S. 229–249, 2011.

PAFFENHOLZ, J.-A., ALKHATIB,H., KUTTERER,H., *Direct geo-referencing of a static terrestrial laser scanner*, Journal of Applied Geodesy, Jg. 4, 3/2010, S. 115–126, 2010

KHOROSHILOVA, ZH.A., KHOROSHILOV, V.S., *Engineering structures deformation monitoring as a component of geodetic monitoring*, Proceedings of International scientific congress "Interexpo GEO-Siberia-2012", p. 84-88, 2012.

Kinematic and Static Laser Scanning Methods for Infrastructure Monitoring

Desislava Staykova, Nico Zill
technet-rail 2010 GmbH, Germany

Abstract
In the recent years the usage of state of the art monitoring systems marks a rapid progress especially in engineering area, for the purposes of the local administration authorities and infrastructure management. For different navigation aims, for monitoring and investigation of big areas the classical geodetic methods are being replaced form a modern mobile and terrestrial scanning systems comprising in itself variety of sensors ensuring continuous and accurate data acquisition. The new age system technologies are symbiosis between hardware and software solutions. The combination of a scanning instrument, DMI and INS system is easy to set up and provides fast way for acquisition of spatial data in large areas. Depending on the manufacturer accuracy characteristics and variety of set up combinations this technology can be used for monitoring of surface settlements, in combination with a developed filter algorithm the accuracy of the trajectory resulted from kinematic differential GNNS measurement can be improved up to 2 or 5 cm. With the usage of appropriate post processing software the accuracy of the end results can be raised up to two times.

Key words: Infrastructure monitoring

1 INTRODUCTION

For the last ten years is observed fast development in the technology of combination between sensors within diverse common complex systems. The existence of such systems providing different accuracy levels offers the possibility for their usage in application areas of the engineering surveying, railway and automotive industry, land administration and for navigation purposes.
Because of its flexibility and possibility for fast and continuous data measurement the multisensory integration and fusion rapidly evolved in various applications areas. The object of this paper is to provide an overview for the usage of high-end and low cost systems complexes and software solutions for the purposes of the engineering geodesy, transportation and navigation.

2 TERRESTRIAL LASER SCANNING SYSTEMS FOR DEFORMATION MONITORING

The need of precise modelling and geometrical characterization of large structures and open areas as dams, mines, landslides and others can't be covered by the traditional surveying methods which require the usage a huge number of points for describing the objects surface. The development of the laser scanning technology in the last decade offers new way for deformations measurements and becomes part of the infrastructure monitoring. The high scanning speed, dense measurement of huge amount of points and high accuracy gives advantage of the terrestrial laser scanning (TLS) in comparison with other technologies used for large structural monitoring. Compared with the technologies using single point monitoring approaches where the displacements detection is limed to specific benchmarks, the TLS provides high data redundancy. Combined with proper software products this technique offers the possibility for high accurate surface modeling and displacement detection in the millimeter area. The scanned object consists of big amount of points which allows the implementation of mathematical algorithms for modeling and analyzing the objects behavior. Another advantage of the TLS as remote sensing measurement technology is the minimized impact of the operator over the observed points and network (Milev and Staykova 2014).

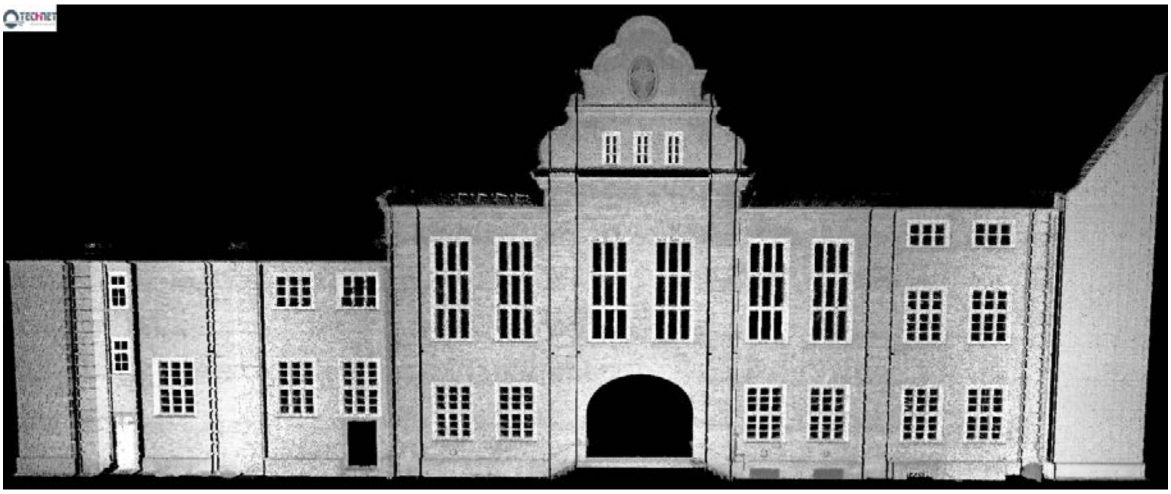

Figure 1: The analyzed object develop into 2D (© technet-rail 2010)

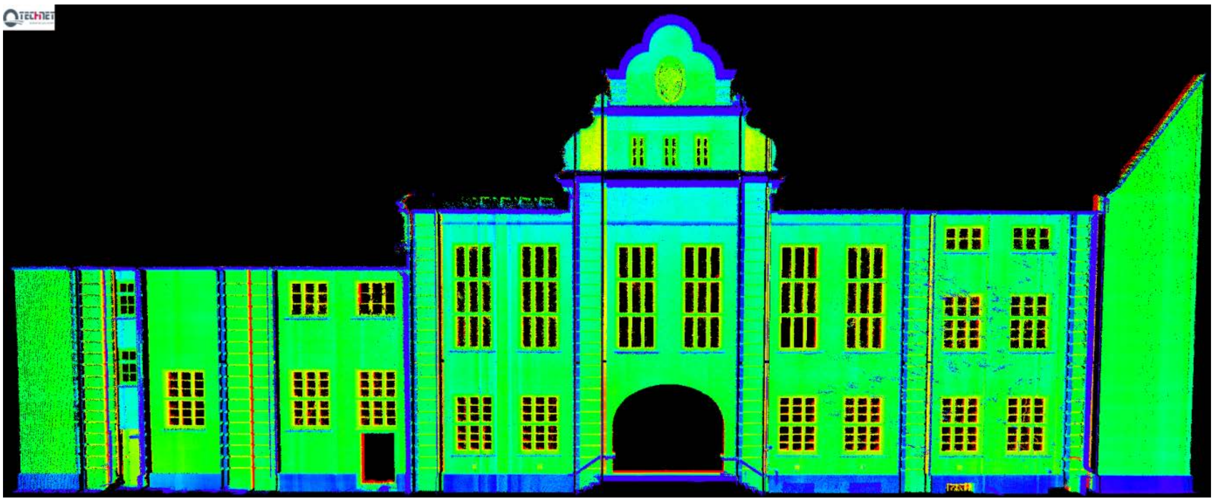

Figure 2: Deformation analysis based on the relative distance of the scanned points to a best fitting plane (© technet-rail 2010)

3 MOBILE LASER SCANNING TECHNOLOGY (MLS)

For different navigation purposes, for monitoring and investigation of wide areas the static measuring methods are being replaced form a modern mobile measuring complexes combination of variety of sensors (high-end and low-cost) which ensure fast, continuous and accurate data acquisition. In the last years the MLS experienced a vast development and proved its usage especially in the area of railway and automotive sector, for deformation analysis, for monitoring and documentation of the as-built street and railway network and the correspondent infrastructure objects.

3.1 Application of the MLS in the Railway and Automotive Areas

The advantages of the MLS technique for fast, high accurate and complete scanning of the surroundings make it a substantial part of the modern railway and road conditions monitoring. The continuous way of data acquisition and processing minimizes the operator errors, reduces significantly the time for performance of the surveying work and the a-posteriori data analysis. For decades the localisation and recognition of the infrastructure objects part of the railway and road environment is of a prior importance in the transportation sector.

For determination and documentation of the as-built railway and street network form the acquired data technet-rail 2010 developed software solutions (SiRailScan and SiRoadScan) for point cloud analysis. The integrated mathematical algorithms ensure the high accurate extraction and adjustment of the as-built left rail, right rail and centre line, as well as of the roads border lines. The so adjusted geometry is further the basis for driving speed control tests, determination of the as-built rail and road environment which comprises the clearance detection and documentation, investigation of the catenary wires deviations, ballast and road settlements, signals position and any changes in the existing situation.

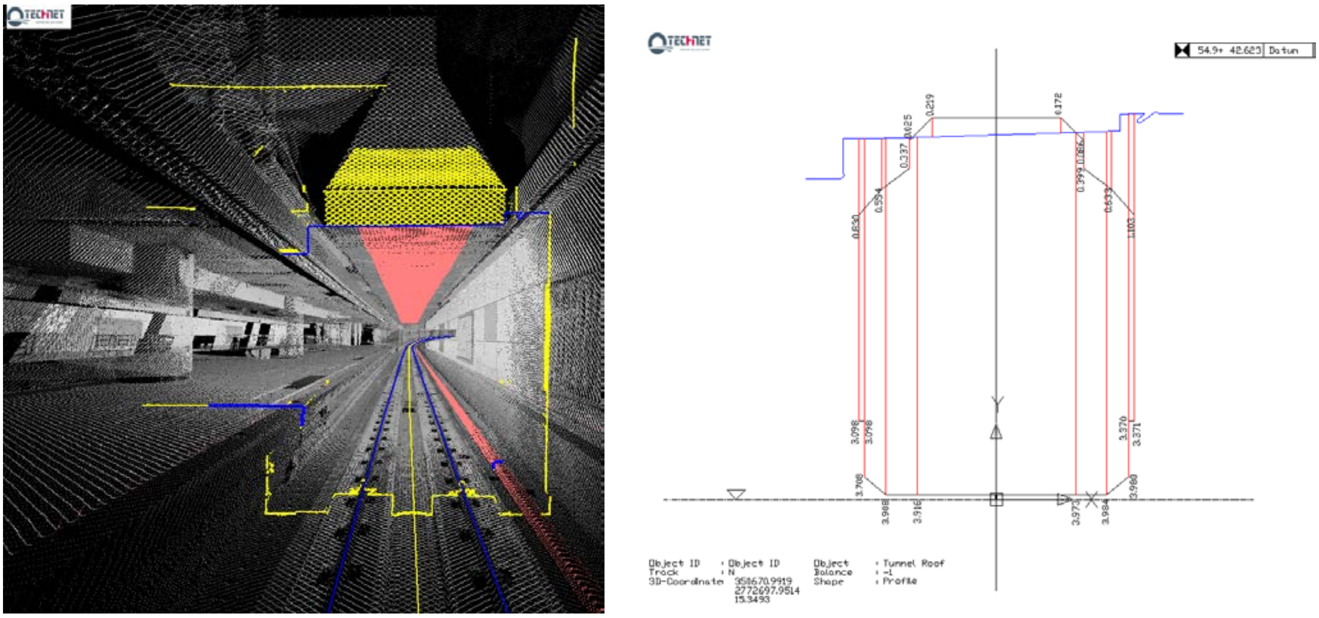

Figure 3: Adjusted as-built rail geometry with SiRailScan used as basis for performance of clearance analysis and documentation in chainage based railway system (© technet-rail 2010)

Figure 4: With SiRoadScan adjusted road border lines. Detection and recognition of the roads signals. (© technet-rail 2010)

In response of the growing interest to the application of MLS technique and a-posteriori data adjustment for monitoring purposes, were developed additional tools for deformation analysis of the structures as tunnel bodies, railway bridge constructions and road surfaces. The integrated software solutions enable the comparison between the designed and as-built situation, epoch-wise analysis, modelling of the structure, development into 2D followed by color-coded deformation map.

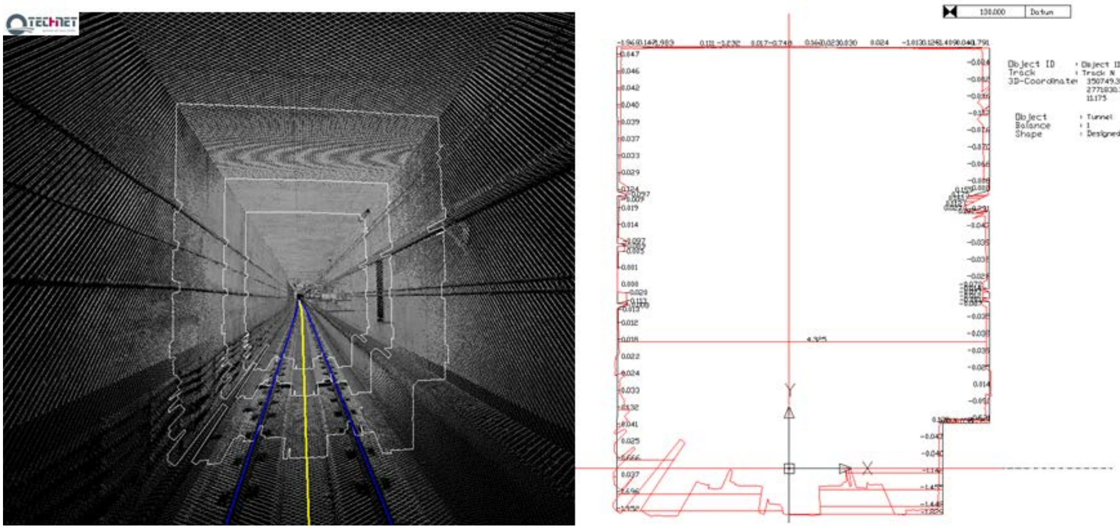

Figure 5: Tunnel deformation analysis performed with SiRailScan based on the as-built rail geometry. Automated calculation of differences between designed and as-built tunnel structure (© technet-rail 2010)

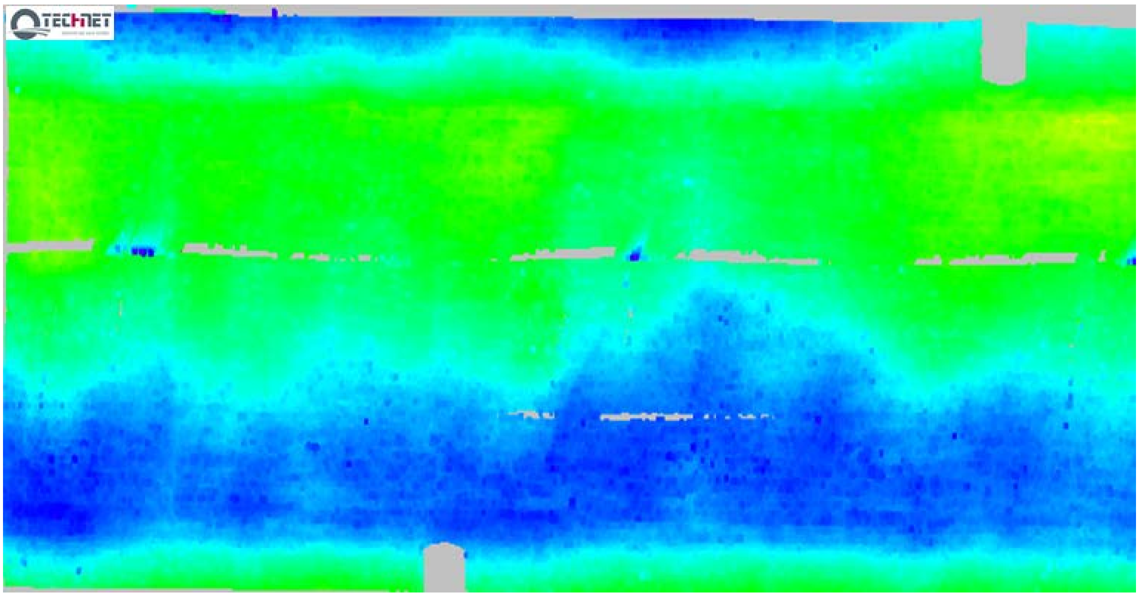

Figure 6: Tunnel deformation analysis with SiRailScan based on a pre-defined form and direction (© technet-rail 2010)

4 CONCLUSIONS

For decades the infrastructure objects such as dam walls, bridges, tunnels, roads and railway tracks, are substantial part of the civil engineering and engineering geodesy. The complicity of their structure requires deep knowledge about the behaviour of these objects and the various methods for their optimal and high accurate monitoring. The fast development evolution of the multisensor integration in combination with laser scanning technology makes it essential method for accurate, continuous and dense measurement for the purposes of the engineering surveys.

REFERENCES

MILEV I., STAYKOVA D., TLS for structure monitoring, 2014, *International Wokshop"Integration of Point- and Area-wise Geodetic Monitoring for Structures and Natural Objects"*, Novosibirsk, Russian Federation, pp.

technet-rail 2010 GmbH: http://www.technet-rail.de

TECHNICAL SESSION 5: MODELLING FOR LASER SCANNING

Approach for a Synthetic Covariance Matrix for Terrestrial Laser Scanner

Stephanie Kauker, Volker Schwieger
Institute of Engineering Geodesy, University of Stuttgart, Germany

Abstract
In this paper, a synthetic covariance matrix for measured values based on an error model for terrestrial laser scanners is presented. First, in order to understand error sources of terrestrial laser scanners, their main structures are investigated. Second, to develop a corresponding synthetic covariance matrix, the details of an elementary error model are explored. Finally, a synthetic covariance matrix by merging the knowledge of the error sources with the fundamentals of the elementary error model is suggested.
The elementary error model consists of 16 parameters classified into the following groups: non-correlated, functional correlated and stochastic correlated. As a result, the user can immediately see the impact of the elementary errors on the variances of a 3D point cloud.

Keywords
Terrestrial laser scanner, elementary error model, synthetic covariance matrix, correlation.

1 INTRODUCTION

The abbreviation *IMCAD* represents a project named *Integrated spatio-temporal modeling using correlated measured values for the derivation of surveying configurations and description of deformation processes*. This work is founded by the *Deutsche Forschungsgemeinschaft* (*German Research Foundation*) and realized in cooperation of the *Institute of Engineering Geodesy, University Stuttgart* with the *Department of Geodesy and Geoinformation, Vienna University of Technology*.
As part of this project a new non-linear space-temporal method for modeling a time-varying object surface will be developed. At the beginning, small sample pieces made of different materials such as wood, metal, fibre-reinforced plastics and cast resin will be used for analysis. Later on, real monitoring objects e.g. bridges and dams will be observed. Due to their size the chosen surveying configuration, such as location and number of laser scanner positions, is very essential.
For this reason, it is important to investigate a method which provides the determination of an optimal surveying configuration by using highly correlated point clouds.
This non-linear sensitivity analysis which examines the influence of input data on the output directly provides conclusions on the appropriate instruments, their quality parameters and the surveying configuration.
The result of the research shall provide a method to model and determine deformations on any point on an object surface.

Traditionally, deformation processes are mostly detected point-wise, e.g. by means of a total station. This means a loss of information since only clearly reproducible points or signalized points can be measured. Reproducing points from epoch to epoch is an important tool for high-quality analysis of deformation. Nowadays, object surfaces can be measured area-wise, e.g. by means of terrestrial laser scanning. The relations among the measured point clouds and the deformation parameters are non-linear. The measured data is highly correlated.

In this paper, an elementary error model is presented. On this basis, a synthetic covariance matrix that represents substantial errors of terrestrial laser scanners, among others, is proposed.
Taking into account an optimal surveying configuration for terrestrial laser scanners, e.g. number of scans and geometric orientation to a target, a variance-based sensitivity analysis will be elaborated.
Approaches for axis errors and tumbling error according to the principle of measurement of a total station have been used by Deumlich and Staiger (2002) and Lichti (2008). In Neitzel (2006c) these approaches are used for investigations of a Z&F Imager 5003.

The sources of errors are classified in three groups: First, there are instrumental errors caused by the production of the hardware. Second, there are errors caused by the atmospheric influence on laser scanner measurements. Furthermore, the monitored objects represent a source of error due to their surface condition and material.

The main contributions of this paper can be summarized as follows:

- Description of the aim of our project
- Definition of an elementary error model and its corresponding synthetic covariance matrix
- Details of the terrestrial laser scanner error budget.

2 ELEMENTARY ERROR MODEL AND SYNTHETIC COVARIANCE MATRIX

In this section, the structure of the elementary error model and how it is linked to the synthetic covariance matrix is described.

2.1 Elementary Error Model

Observing a target provides values such as angles and distances. According to Bessel (1837) and Hagen (1837) these values are treated as random quantities. This is, "any realisation l of a measured random quantity L shows a random deviation ε with respect to its expected value μ_l"(Schwieger 1999). That implies, a sum of v very small elementary errors d_i may represent any random deviation:

$$\mu_l = l - \varepsilon, \quad \text{and} \quad \varepsilon = \sum_{i=1}^{v} d_i \, . \tag{1}$$

It can be assumed, that individual elementary errors comprise the same absolute values. Hereby, negative and positive sign may be equally probable (Hagen 1837). Hence, the expected value of the random deviation μ_ε is determined to zero as follows (Pelzer 1985):

$$\mu_\varepsilon = E(\varepsilon) = \sum_{i=1}^{v} E(d_i) = 0. \tag{2}$$

In case the analysis of a measurement process gets more detailed, their absolute values decrease once the number of elementary errors increases. Assuming infinite elementary errors, their absolute values may be infinitely small. Therefore, a standard normal distribution is assumed as justified for a standardized random deviation $\bar{\varepsilon}$. Consequently, the normal distribution is valid for the measurement quantity L, considering standard deviation σ and variance σ^2 (Pelzer 1985):

$$\bar{\varepsilon} = \frac{\varepsilon}{\sigma} \sim N(0,1), \quad \text{and} \quad L \sim N(\mu_l, \sigma^2). \tag{3}$$

Generally speaking, a sum of very small elementary errors with changing signs are sufficient to model normal distributed measurements. For further modelling two specialisations have to be considered. Firstly, measured values and their random deviations may be multidimensional. This is, the scalars in equations (1) and (2) are n-dimensional vectors (Pelzer 1985):

$$\boldsymbol{\mu_l} = \boldsymbol{l} - \boldsymbol{\varepsilon}, \quad \text{and} \quad \boldsymbol{E(\varepsilon)} = \sum_{i=1}^{v} \boldsymbol{E(d)} = \boldsymbol{0}. \tag{4}$$

Secondly, to handle multi-dimensional data, it is essential to classify elementary errors. In addition, modelling the impact on the measurements is substantial. In this process, influence factors are used to build influence matrices which comprise the effect on the covariance matrix of the observations. As mentioned in Schwieger (1999) three types have to be considered, which are classified and structured as follows:

- p non-correlating error vectors $\boldsymbol{\delta_k}$,
- m functional correlating errors ξ_j,

- q stochastic correlating error vectors $\boldsymbol{\gamma_h}$,

$$\boldsymbol{\delta_k} = \begin{bmatrix} \delta_{1k} \\ \delta_{2k} \\ \vdots \\ \delta_{nk} \end{bmatrix}, k = 1,2,\dots,p, \quad \text{and} \quad \xi = \begin{bmatrix} \xi_1 \\ \xi_2 \\ \vdots \\ \xi_m \end{bmatrix}, \quad \text{and} \quad \boldsymbol{\gamma_h} = \begin{bmatrix} \gamma_{1h} \\ \gamma_{2h} \\ \vdots \\ \gamma_{nh} \end{bmatrix}, h = 1,2,\dots,q \,. \tag{5}$$

The index *n* defines the number of measurements. With regard to the non-correlating errors, *k* describes the kind of elementary error, while *p* represents the number of elementary errors. The index *m* comprises the number of functional correlating elementary errors ξ_j. The index *h* implies the kind of elementary errors and *q* represents the number of stochastic correlating errors.

In the next step, the influence on the measurements is modelled by partial derivatives. The derivatives can be determined analytically or numerically based on the model assumption. Inducing the influences of different elementary errors on the observations requires the integration of the derivatives into influencing matrices (Schwieger 1999). The three aforementioned types of errors can be calculated as follows:

- p matrices $\mathbf{D_k}$ for non-correlating errors,
- one matrix **F** for functional correlating errors,
- q matrices $\mathbf{G_h}$ for stochastic correlating errors.

The influencing matrices describe the projection of the elementary errors into the observation space.

Since each elementary error of the non-correlating and stochastic correlating classes impacts on exactly one measurement quantity functionally, $\mathbf{D_k}$ and $\mathbf{G_h}$ are diagonal matrices (equation (6)).

Contrary to these matrices, the **F** matrix is non-diagonal because one functional correlating error may impact more than one measurement quantity (Schwieger 1999). For illustration, the elements of $\mathbf{D_k}$, **F** and $\mathbf{G_h}$ are defined as follows:

$$\boldsymbol{D_k} = \begin{bmatrix} \frac{\partial l_1}{\partial \delta_{1k}} & 0 & \cdots & 0 \\ 0 & \frac{\partial l_2}{\partial \delta_{2k}} & 0 & \vdots \\ \vdots & 0 & \ddots & \vdots \\ 0 & \cdots & \cdots & \frac{\partial l_n}{\partial \delta_{nk}} \end{bmatrix}, \quad \boldsymbol{F} = \begin{bmatrix} \frac{\partial l_1}{\partial \xi_1} & \frac{\partial l_1}{\partial \xi_2} & \cdots & \frac{\partial l_1}{\partial \xi_m} \\ \frac{\partial l_2}{\partial \xi_1} & \frac{\partial l_2}{\partial \xi_2} & \cdots & \frac{\partial l_2}{\partial \xi_m} \\ \vdots & \vdots & \ddots & \vdots \\ \frac{\partial l_n}{\partial \xi_1} & \frac{\partial l_n}{\partial \xi_2} & \cdots & \frac{\partial l_n}{\partial \xi_m} \end{bmatrix}, \quad \boldsymbol{G_h} = \begin{bmatrix} \frac{\partial l_1}{\partial \gamma_{1h}} & 0 & \cdots & 0 \\ 0 & \frac{\partial l_2}{\partial \gamma_{2h}} & 0 & \vdots \\ \vdots & 0 & \ddots & \vdots \\ 0 & \cdots & \cdots & \frac{\partial l_n}{\partial \gamma_{nh}} \end{bmatrix}. \tag{6}$$

As result, the random deviation vector $\boldsymbol{\varepsilon}$ is calculated directly as the sum of all elementary errors. Hereby, the projection into the observation space is considered by Schwieger (1999) as:

$$\boldsymbol{\varepsilon} = \sum_{k=1}^{p} \boldsymbol{D_k} \cdot \boldsymbol{\delta_k} + \boldsymbol{F} \cdot \boldsymbol{\xi} + \sum_{h=1}^{q} \boldsymbol{G_h} \cdot \boldsymbol{\gamma_h} \,. \tag{7}$$

2.2 Synthetic Covariance Matrix

The elementary error model, presented in the previous section, is fundamental for the computation of a synthetic covariance matrix. In order to determine variances, covariances and correlations for measurements, a covariance matrix is used. For instance, the general symmetric structure of a covariance matrix $\mathbf{\Sigma_{ll}}$ is given below:

$$\boldsymbol{\Sigma_{ll}} = \begin{bmatrix} \sigma_1^2 & \sigma_{12} & \cdots & \sigma_{1n} \\ \sigma_{12} & \sigma_2^2 & \cdots & \sigma_{2n} \\ \vdots & \vdots & \ddots & \vdots \\ \sigma_{1n} & \cdots & \cdots & \sigma_n^2 \end{bmatrix}. \tag{8}$$

Here, σ_n^2 defines the variances which represent the stochastic dependence of one random value, with *n* as number of measurements. The σ-values placed on the secondary diagonals remain the covariances of two random values, e.g. σ_{12} comprises the covariance between measurement 1 and measurement 2. Calculating the correlation coefficient requires both, the covariance and the square root of the variances (see equation (9)) (Niemeier 2008):

$$\rho = \frac{\sigma_{12}}{\sigma_1 \cdot \sigma_2} \quad (9)$$

The degree of the correlation coefficient is independent of the values of the variances. In case $\sigma_{12} = \pm 1$ functional dependence is given. For $\sigma_{12} = 0$, the correlation coefficient indicates stochastic independence. Since the final covariance matrix is constructed of the different types of elementary errors, it is named *synthetic covariance matrix* Σ_{ll}.
The synthetic covariance matrix is based on the *law of error propagation* applied on equation (7) (Schwieger 1999). As result, the new equation is given as follows:

$$\Sigma_{ll} = \sum_{k=1}^{p} D_k \cdot \Sigma_{\delta\delta,k} \cdot D_k^T + F \cdot \Sigma_{\xi\xi} \cdot F^T + \sum_{h=1}^{q} G_h \cdot \Sigma_{\gamma\gamma,h} \cdot G_h^T . \quad (10)$$

$\mathbf{D_k}$, $\mathbf{F}$ and $\mathbf{G_h}$ represent the influencing matrices which are explained in the section above. Their structure is important for determining the covariance matrices of the elementary errors. The covariance matrices are defined as follows:

- $\mathbf{\Sigma_{\delta\delta,k}}$ for the non-correlating errors,
- $\mathbf{\Sigma_{\xi\xi}}$ for the functional correlating errors,
- $\mathbf{\Sigma_{\gamma\gamma,h}}$ for the stochastic correlating errors.

The covariance matrices of the non-correlating errors $\mathbf{\Sigma_{\delta\delta,k}}$ and the functional correlating errors $\mathbf{\Sigma_{\xi\xi}}$ are diagonal matrices (see equation (11)). Consequently, modelling correlations among the elementary errors is avoided, for example, in case k = 1, multiplying $\mathbf{D_1}$ and $\mathbf{\Sigma_{\delta\delta,1}}$ results in a new matrix which is filled only on the primary diagonal.

$$\mathbf{\Sigma_{\delta\delta,k}} = \begin{bmatrix} \sigma_{1k}^2 & 0 & \cdots & 0 \\ 0 & \sigma_{2k}^2 & 0 & \vdots \\ \vdots & 0 & \ddots & \vdots \\ 0 & \cdots & \cdots & \sigma_{nk}^2 \end{bmatrix}, \quad \mathbf{\Sigma_{\xi\xi}} = \begin{bmatrix} \sigma_1^2 & 0 & \cdots & 0 \\ 0 & \sigma_2^2 & \cdots & \vdots \\ \vdots & \vdots & \ddots & \vdots \\ 0 & \cdots & \cdots & \sigma_m^2 \end{bmatrix}, \quad \mathbf{\Sigma_{\gamma\gamma,h}} = \begin{bmatrix} \sigma_{1h}^2 & \sigma_{12h} & \cdots & \sigma_{1nh} \\ \sigma_{12h} & \sigma_{2h}^2 & \cdots & \sigma_{2nh} \\ \vdots & \vdots & \ddots & \vdots \\ \sigma_{1nh} & \cdots & \cdots & \sigma_{nh}^2 \end{bmatrix}. \quad (11)$$

In previous work by Pelzer (1985), the computation of synthetic covariance matrices by using the error types mentioned above was introduced. In Schwieger (1999) stochastic correlating elementary errors are additionally established as method best suited for modelling the synthetic covariance matrix for GNSS measurements.
Matrix $\mathbf{G_h}$ modells functional independent values. Consequently, the covariance matrix $\mathbf{\Sigma_{\gamma\gamma,h}}$ comprises covariances among the elementary errors of one type.
A challenge of the elementary error model is that the variances and covariances, in case of stochastic correlating errors, have to be determined. However, they cannot be computed easily, therefore they may be assigned by using manufacturers' information, empirical values or practical values. Moreover they might be estimated using maximum errors.

3 TERRESTRIAL LASER SCANNER ERROR BUDGET

3.1 Error Sources of a Terrestrial Laser Scanner

Scanning objects is done area-wise by sampling an angular grid. This can be realized through the optics of a rotating sloped mirror (see Figure 1). After the laser beam is generated with very high frequency, it is reflected due to the sloped mirror (see Figure 1b). Further constructions of terrestrial laser scanners are explained, e.g. in Gordon (2008) and Eling (2009).

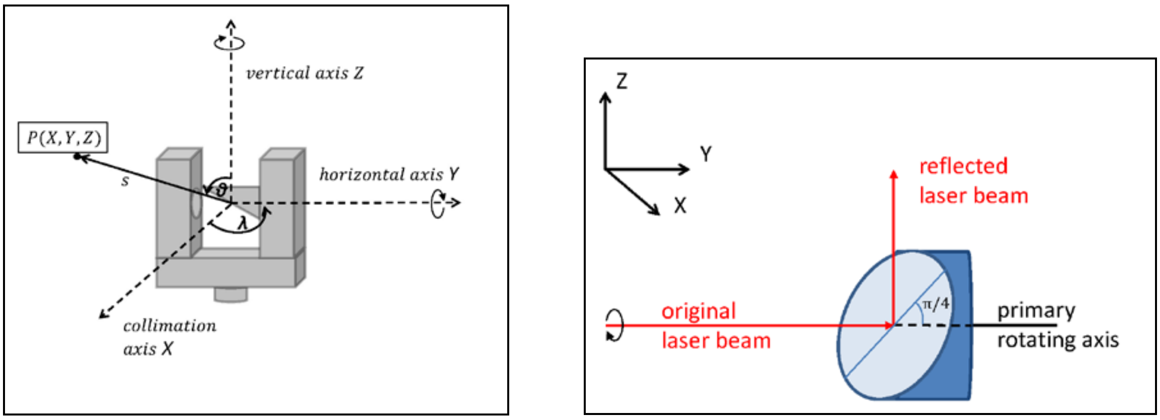

(a) Main observables (b) Reflection of a TLS beam

Figure 1: Main construction elements of a terrestrial laser scanner

The horizontal angle λ, the vertical angle ϑ and the slope distance s define the main observables of terrestrial laser scanning measurements. These parameters must be known to clearly determine the geometric position of the reflected points in observation space. Consequently, for each point Cartesian coordinates can be calculated. In Figure 1a the geometrical relationship between the polar observables and the transformation into Cartesian coordinates is displayed. The Cartesian coordinates are given as follows:

$$\begin{bmatrix} X \\ Y \\ Z \end{bmatrix} = s \begin{bmatrix} \sin\vartheta \cos\lambda \\ \sin\vartheta \sin\lambda \\ \cos\vartheta \end{bmatrix} \qquad (12)$$

The main principle of a terrestrial laser scanner is similar to a total station. According to previous investigations e.g., Deumlich and Staiger (2002), Lichti and Lampard (2008) and Lichti (2010), it is assumed that the main error sources of a total station may also appear for a terrestrial laser scanner. Since their three main axes, such as collimation axis, horizontal axis and vertical axis, are comparable, their errors can be applied to the error modells.
First, the elementary errors are classified into instrumental and atmospheric errors and errors that occur when a laser beam meets a monitored object. In the next step, the error sources are grouped regarding the three types of correlations mentioned in section 2. The results of the grouping are shown in Table 1 below.

Table 1: classification of error sources and correlation types

group	error source	correlation	group	error source	correlation
instrumental	range finder error	functional	atmospheric	pressure	stochastic
	zero point error			partial water vapour pressure	
	collimation axis error		object	colour	stochastic
	horizontal axis error			roughness	
	vertical index error			reflectivity	
	tumbling error			penetration depth	
	eccentricity of the collimation axis			angle of incidence	functional
atmospheric	temperature	stochastic		edges	

3.2 Functional Error Modelling

In order to calculate the numerical impact on a 3D point cloud, the functional relation among the terrestrial laser scanner error sources have to be considered.

4.2.1 Modelling Instrumental Errors

According to Stahlberg (1997), Neitzel (2006a) and Neitzel (2006c) polar observable values can be computed as follows:

$$s_k = k_0 + s \cdot m \tag{13}$$

$$\theta_k = \text{acos}(\cos i \cdot \cos c \cdot \cos(\zeta + \Delta\zeta + h) + \sin i \cdot \sin c) \tag{14}$$

$$\lambda_k = \alpha + \Delta\alpha + \text{atan}\left(\frac{\cos i \cdot \tan c}{\sin(\zeta + \Delta\zeta + h)} + \frac{\sin i}{\tan(\zeta + \Delta\zeta + h)}\right) + \frac{e_z}{s_k \cdot \sin(\zeta + \Delta\zeta + h)} \tag{15}$$

where the index k represents the corrected observables. The further components are defined as below:

s:	measured slope distance	c:	collimation axis error
k_0:	zero point error	i:	horizontal axis error
m:	range finder error	h:	vertical index error
α:	measured horizontal rotation angle	v:	tumbling error
ζ:	measured vertical rotation angle	e_z:	eccentricity of the collimation axis
s_k:	corrected slope distance		
λ_k:	corrected horizontal rotation angle (horizontal angle)		
θ_k:	corrected vertical rotation angle (zenith angle)		

Rotating around the vertical axis causes a tumbling error which affects the 3D point cloud. The tumbling error is investigated by Neitzel (2006c). The impact of this error is approximated by the functional model as follows, whereby α_z represents the horizontal direction of the projection of the zenith angle into the horizontal plane. ζ_z defines the angle between the vertical axis and the direction to the zenith:

$$\Delta\alpha = v \cdot \sin\alpha_z \cdot \cot\zeta_z \tag{16}$$

$$\Delta\zeta = v \cdot \cos\alpha_z \tag{17}$$

Filling the influencing matrices $\mathbf{D_k}$, $\mathbf{F}$ and $\mathbf{G_h}$ requires the calculation of the derivatives of equations (13 - 17). In the next step, it is important to compute influencing values for the construction of the synthetic covariance matrix. In Gordon (2008) some of these error sources are investigated, where the zero point error shows a maximum value up to *5 mm*, the maximum value of the vertical index error is *-17.69 mgon* and the maximum value of the collimation axis error is *-19.62 mgon*.
According to Neitzel (2006a) the maximum value of the horizontal axis error is up to *-14.6 mgon* among others. Hence, these values are used for the approach.
In case the standard deviation σ_k of an error δ_{ik} is not known, it can be calculated assuming normal distribution (Pelzer 1985):

$$\sigma_k \approx 0.3 \cdot \delta_{ik}[max] \tag{18}$$

Table 2 below shows the standard deviations of the instrumental errors to be used for computing the corresponding covariance matrix.

Table 2: standard deviations of instrumental errors

group	error source	standard deviation	source
instrumental	range finder error	1.50 [mm]	Gordon (2008)
	zero point error	0.300018[-]	Gordon (2008)
	collimation axis error	-5.89 [mgon]	Gordon (2008)
	horizontal axis error	-4.38 [mgon]	Neitzel (2006a)
	vertical index error	-5.31 [mgon]	Gordon (2008)
	tumbling error	-0.09 [mm/m]	Neitzel (2006c)
	eccentricity of the collimation axis	0.60 [mm]	Gordon (2008)

3.4 Atmospheric Error Sources

Another group which affects the 3D point cloud are the atmospheric errors. The environmental influences, such as air temperature, pressure and partial water vapour pressure have to be modelled to compute their weight on a terrestrial laser scanner measurement. For this purpose, a commonly known equation for the model is used which is presented in Joeckel et al. (2008):

$$N_L = (n_L - 1) \cdot 10^6 = N_{Gr} \cdot \frac{273.15}{1013.25} \frac{p}{T} \frac{11.27}{T \cdot e} \qquad (19)$$

The definition of the components is given in the following:

n_L:	group refractive index of light with current environment (t, p, e)	t:	temperature in *°C* (T=t + 273.15)
N_L:	reduction of the standard atmosphere to the current atmospheric environment	e:	partial water vapour pressure in *hPa*
N_{Gr}:	group refractive index of light for normal atmosphere	p:	pressure in *hPa*

The total differential is calculated as

$$\partial N_L = \frac{\partial n_L}{\partial t} \cdot dt + \frac{\partial n_L}{\partial p} \cdot dp + \frac{\partial n_L}{\partial e} \cdot de \qquad (20)$$

The mean atmosphere, with temperature of 17 *°C*, pressure of 1000 *hPa* and partial water vapour pressure of 11 *hPa*, results in differential quotients (Joeckel et al., 2002).

$$\frac{\partial n_L}{\partial t} = -1.00 \cdot 10^{-6} \left[\frac{1}{K}\right], \quad \frac{\partial n_L}{\partial p} = 0.29 \cdot 10^{-6} \left[\frac{1}{hPa}\right], \quad \frac{\partial n_L}{\partial e} = -0.04 \cdot 10^{-6} \left[\frac{1}{hPa}\right] \qquad (21)$$

Next, their impact on distance measurements can be calculated (Joeckel et al., 2002):

$$\Delta n \cdot 10^6 = -1.00\, \Delta t + 0.29\, \Delta p - 0.04\, \Delta e \qquad (22)$$

As result of equation (21), a change of $\Delta t = 1$ *°C* affects distance measurements by 1 *ppm*. In case the air pressure changes to 1 *hPa*, the distance measurement is influenced by approximately -0.3 *ppm*. In addition, an error in the partial water vapour pressure of 1 *hPa* causes 0.04 *ppm* impact on distance measurements (Rüeger 1990).
In previous research by Eschelbach (2007), the impact of locally changing temperature on geodetic measurements for laboratory conditions are investigated. Besides, Geiger et al. (1995) established an approach for three dimensional modelling of the refraction for GPS measurements. In the future the standard deviations and the correlations for the meteorological parameters have to be modelled.

3.5 Error Sources on the Surface of Monitored Objects

As soon as a laser beam impinges on an object, it is reflected. Due to physical laws the laser beam is not fully reflected. This loss of intensity is caused by the colour, the roughness, the reflectivity and the penetration depth of an object. Furthermore, the laser beam can be splitted on edges (Gordon 2008). Besides, the angle of incidence is substantial, which is investigated by Eling (2009) and Zámečniková and Neuner (2014). The bigger the angle, the less energy of the laser beam is thrown back. According to *Lambert's cosine law* the intensity of the reflected laser beam *I* is proportional to the cosine of the angle *β* and the reflection area *A* of the laser beam:

$$I(\beta) \sim A \cdot \cos(\beta) \qquad (23)$$

As elementary error the size and the shape of the area *A* and additional characteristics of the object may be understood. Further investigations have to be realized in the future.

4 CONCLUSION AND FUTURE WORK

This paper presents the elementary error model. On this basis an approach for the computation of a synthetic covariance matrix is provided. In addition, essential sources of errors for terrestrial laser scanning measurements are examined, such as range finder error, collimation axis error and vertical index error, among others. Further error sources are caused by the atmosphere, e.g. temperature and pressure. Moreover, monitored objects affect terrestrial laser scanner point clouds, e.g. due to their surface structure, material and roughness.

For future work it is planned to model the impact of meteorological conditions. As well, object based variances have to be defined in order to complete all covariance matrices. As result the synthetic covariance matrix will be computed. On this basis, the generated synthetic covariance matrix shall be evaluated by empirical investigations.

REFERENCES

Books:

DEUMLICH, F., STAIGER, R. (2002): *Instrumentenkunde der Vermessungstechnik*. 9. Auflage, Herbert Wichmann Verlag, Heidelberg.

JOECKEL, R., STOBER, M., HUEP, W. (2008): *Elektronische Entfernungsmessung und ihre Integration in aktuelle Positionierungsverfahren*. 5. Auflage, Herbert Wichmann Verlag.

NIEMEIER, W. (2002): *Ausgleichungsrechnung*. Walter de Gruyter, Berlin, New York.

PELZER, H. (1985): *Grundlagen der mathematischen Statistik und Ausgleichungsrechnung*. In: H. Pelzer (Ed.), Geodätische Netze in Landes- und Ingenieurvermessung. Konrad Wittwer Verlag, Stuttgart.

RÜEGER, J. M. (1990): *Electronic distance measurement: an introduction.* Third totally revised edition, Springer-Verlag, Berlin.

Journal articles:

BESSEL, F. W. (1837): *Untersuchungen über die Wahrscheinlichkeit der Beobachtungsfehler*. Astronomische Nachrichten, Vol. 15, pages 369-404.

ELING, D. (2009): *Terrestrisches Laserscanning für die Bauwerksüberwachung.* DGK – Deutsche Geodätische Kommission, Reihe C, Nr. 641, Verlag der Bayerischen Akademie der Wissenschaften, München.

ESCHELBACH, C. (2007): *Störanfälligkeit geodätischer Präzisionsmessungen durch lokale Temperaturschwankungen*. In: Brunner, F. (Hrsg): Beiträge zum 15. Internationalen Ingenieurvermessungskurs, Graz, 19.-20.04.2007, S. 169-180.

GEIGER, A., COCARD M., HIRTER, H. (1995): *Dreidimensionale Modellierung des Refraktivitätsfeldes in der Atmosphäre*. VPK - Vermessung, Photogrammetrie, Kulturtechnik, S. 254-260.

GORDON, B. (2008): *Zur Bestimmung von Messunsicherheiten terrestrischer Laserscanner*. TU Darmstadt, Dissertation, http://tuprints.ulb.tu-darmstadt.de/1206/, last accessed on March, 5 2015.

HAGEN, G. (1837): *Grundzüge der Wahrscheinlichkeits-Rechnung.* Berlin.

HENNES, M. (2002): *Zum Refraktionseinfluss auf terrestrische geodätische Messungen im Kontext der Messtechnik und der Instrumentenentwicklung*. FuB - Flächenmanagement und Bodenordnung, Heft 2/2002, S. 73-86.

LICHTI, D. D., LAMPARD, J. (2008): *Reflectorless total station self-calibration*. Survey Review, Vol. 40, pages 244-259.

LICHTI, D. D. (2010): *Terrestrial laser scanner self-calibration: Correlation sources and their mitigation*. ISPRS Journal of Photogrammetry and Remote Sensing, Vol. 65, pages 93–102.

NEITZEL, F. (2006a): *Gemeinsame Bestimmung von Ziel-, Kippachsenfehler und Exzentrizität der Zielachse am Beispiel des Laserscanners Zoller + Fröhlich Imager 5003*. In: Luhmann/Müller [Hrsg.], Photogrammetrie - Laserscanning - Optische 3D-Messtechnik, Beiträge der Oldenburger 3D-Tage 2006, Herbert Wichmann Verlag.

NEITZEL, F. (2006c): *Untersuchung des Achssystems und des Taumelfehlers terrestrischer Laserscanner mit tachymetrischem Messprinzip*. In: Beiträge zum 72. DVW-Seminar am 9. und 10. November 2006 in Fulda, Band 51, Wißner-Verlag.

SCHWIEGER, V. (1999): *Ein Elementarfehlermodell für GPS Überwachungsmessungen*. Schriftenreihe der Fachrichtung Vermessungswesen der Universität Hannover, Vol. 231.

SCHWIEGER, V. (2001): *Zur Konstruktion synthetischer Kovarianzmatrizen*. ZfV - Zeitschrift für Vermessungswesen, 3/2001, Seite 143-149.

STAHLBERG, C. (1997): *Eine vektorielle Darstellung des Einflusses von Ziel- und Kippachsenfehler auf die Winkelmessung*. ZfV - Zeitschrift für Vermessungswesen, 5/1997, S. 225-235.

ZÁMEČNIKOVÁ, M., NEUNER H. (2014): *Der Einfluss des Auftreffwinkels auf die reflektorlose Distanzmessung*. In: Beiträge zum 139. DVW-Seminar am 11. und 12. Dezember 2014 in Fulda, Band 78, Wißner-Verlag.

Denoising of the Point Cloud for Deformation Analysis

Lifan Zhang[1], Bimin Zheng[2]
[1]The master study course "Geodesy and Geoinformatic", University of Stuttgart, Germany
[2]Intitute of Engineering Geodesy, University of Stuttgart, Germany

Abstract
Aggregates are defined as large amounts of elements being in loose contact. In architecture they are mainly known as an additive in concrete construction (Figure 1). The construction from aggregate elements does not have a homogeneous form and surface. It is necessary to find a method to measure the deformation of this construction.

Figure 2: Aggregate construction (ICD, 2015)

Nowadays the technology Terrestrial Laser Scanning (TLS) is widely used and plays a more and more important role in the field of geodetic applications. But the point clouds of TLS are often disturbed by the noise and outliers. Those measurement errors influence the quality of a parametric description of the surface during object the reconstruction. They reduce the quality of deformation analysis. In this paper three filters will be tested using noisy point cloud data of an aggregate element. It will be seen, the "comet tail" removal can delete the "comet tail" outlier effectively in this point cloud data.

Keywords
Terrestrial Laser Scanning (TLS), filter, outlier, edge effect, "comet tail" removal, deformation analysis

1 MOTIVATION

Nowadays, amongst many other applications, TLS is used for deformation measurement. Compared with traditional measuring method, an advantage of TLS is the efficient area based data acquisition. In comparison with the traditional photogrammetry, which can only deliver 2D information of the object during the measurement, TLS can give 3D positon information with the position accuracy of about 2 mm in a distance up to 10 m (Lichti et al., 2006). A type of TLS is the 3D triangulation system. The high resolution is an advantage of this system. But the field of view of this system is small. It has an operating range of about 2 m only (Richter, 2009). It is not suitable for monitoring measurements, especially for constructions like buildings. TLS is commonly based on the time-of-flight measurement or on the phase comparison method. Phase- or pulse-based scanners offer a much larger field-of-view. The operating range is up to some hundred meters (phase), respectively kilometres (pulse). In the close-range application the phase-based scanners have better noise behaviour than the pulse-based scanners. Therefore, in this research, a phase-based laser scanner Leica HDS 7000 was used for the data acquisition. The aggregate element was on a table during scanning. The measurement distance is around 2 m. The original point cloud has a resolution of 2 mm.

Problems appear using a phase-based laser scanner, when the object has a small structured surface (see, Figure 2). The aggregate element is made of wood. It has a diameter of 10 cm. Each branch of the aggregate element has a width of 6 mm. The scanner produces a variety of points with wrong positions in the vicinity of the edges. From this noisy point cloud it is difficult to reconstruct the shape of the aggregate element for the modelling process.

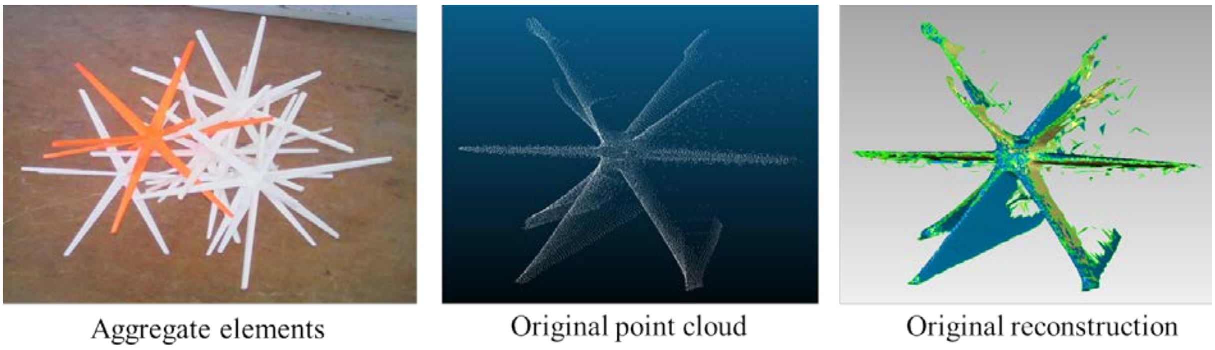

Figure 3: Aggregate element (left: image, middle: point cloud, right: reconstruction)

TLS has almost the same measurement principle like a total station. Many investigations and methods concerning measurement accuracy and point cloud smoothing have been already published (Hebert et al., 1992, Böhler et al., 2003, Gordon et al., 2003, Zogg, 2008, Gordon, 2008). Based on these publications the errors in TLS measurement can be divided as follows:

Influences of surface material properties and environment conditons:
Phase-based laser scanners receive the signal reflected back from the object surface. The returning signal is influenced by atmospheric conditions, incidence angle, temperature, interfering radiation and reflective abilities of the surface. Some investigations and the results of experiments can be read in Böhler et al. (2003).

Errors from angle measurement:
Vertical and horizontal angles are the results of the reading from encoder increments. The errors like eccentricities of angular encoders and random errors influence the angle measurements. In Lichti et al. (2006) some guideline values from the experiments can be found.

Errors from distance measurement:
The distance measurement is influenced by systematic errors like electronic and optical crosstalk. Random errors like receiver noise have also an effect during the distance measurement. The scale and offset distort the measured distance. More details about the calculation of these internal errors are described in Deumlich and Steiger (2002) and Joeckel et al. (2008).

Edge effects:
The measured intensity and the measured distance of the object part inside this footprint are approximately Gaussian-distributed. This causes problems especially in the area with lots of edge structures. The structures are rounded (Pfeifer et al., 2007, Richter, 2009, Böhler et al. 2003, Hebert et al., 1992). If the laser beam is distributed onto several surfaces with different distances from the scanner, another type of edge effects, the "mixed point" appear (Kern, 2003). Those "mixed points" stand scattered like "comet tail" behind the object (see Figure 2, middle). Actually the measuring laser beam is not only a ray without sectional area, but a thin cone with a very small opening angle γ and a certain sectional area with the diameter D, which depends on the size of laser emitting window (Figure 3). In our case, based on the manufacturer's data the laser beam has a divergence smaller than 0.3 mrad. The footprint of the laser beam has a diameter of about 4 mm in the distance of 2 m. When the laser beam is projected onto the edge of the measured object, a part of it touches the surface of the front object first and is reflected, while the other part continues to travel, and is reflected till it touches the other surface. The final measurement result is the weighted average distance of all measured distances. So the measured distance S_m ranges in the interval $[S_1, S_2]$ and belongs to a virtual point. If the front object is the object to be measured, the obtained distance will be larger than the true value. On the contrary, it will be smaller. This problem is also addressed by Sotoodeh (2006).

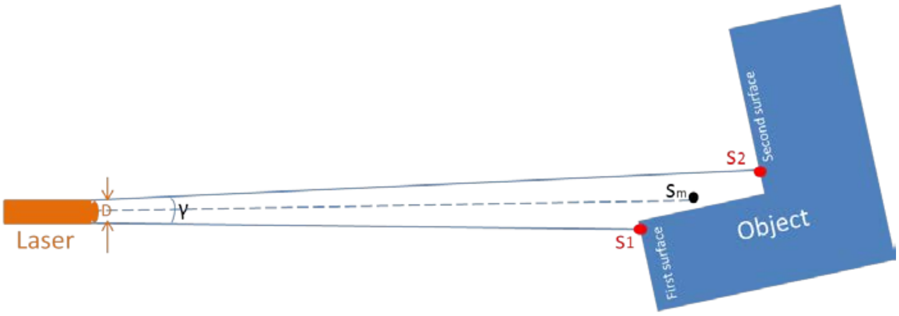

Figure 4: The "cometary tail" phenomenon

The focus of this research is set on the "comet tail" effect. A new own developed filter was investigated for the denoising process.

2 FILTER ALGORITHM

An extensive amount of research about outlier detection for point clouds has been presented in last years. In Papadimitriou et al. (2002) the distribution-based, depth-based and clustering approaches were described. In Sotoodeh (2006) the density-based approach was chosen for outlier detection, especially for the outliers in edge areas. More discussion and analysis of those approaches can be found in Sotoodeh (2006), Knorr et al. (2000) and Breunig et al. (2000). Based on this research the "comet tail" removal consists of radius outlier removal, normal estimation and conditional removal.

2.1 Radius Outlier Removal

The radius outlier removal (ROR) is a type of density-based approach. It points in a cloud based on the number of neighbours they have. The search region of a certain observed point is defined with a given radius *r* (Rusu, 2009). When the number of neighbouring points is greater than or equal to the given threshold *m*, this point will be retained as an inlier. On the contrary, the point which has less neighbours will be cut out from the point cloud. The threshold specifies the minimum number of the neighbours an inlier point should have. The threshold is defined by the user according to the actual situation based on the local density of its neighbourhood. It is exactly suitable for the denoising process in this research.

2.2 Normal Estimation

In the "comet tail" removal algorithm, the most important step is the estimation of the normal. The normal estimation is a quite important operation of 3D point clouds. In PCL (2014), Mitra et al. (2003) and Rusu et al. (2008) more details about the calculation of normal vectors can be found. This approximated computation of the surface's normal is based on the relationships of the observed point $\boldsymbol{p}(x,y,z)$ with the points in its neighbourhood with radius *r* (Rusu et al., 2008). This relationship can be mathematically represented by the neighbourhood's matrix **C.** After finding all the neighbours $\boldsymbol{q_i}(x_i, y_i, z_i)$ $(i = 1, 2, 3, \ldots, n)$ of the point $\boldsymbol{p}$, a weighted matrix with the term δ_i can be determined:

$$\mathbf{C} = \sum_{i=1}^{n} \delta_i \cdot (\boldsymbol{q_i} - \overline{\boldsymbol{p}})^T \cdot (\boldsymbol{q_i} - \overline{\boldsymbol{p}}) \tag{1}$$

with

$$\overline{\boldsymbol{p}} = \frac{1}{n} \cdot \sum_{i=1}^{n} \boldsymbol{q_i} \tag{2}$$

The term δ_i represents the weight for the point $\boldsymbol{q_i}$:

$$\delta_i = e^{\left(-\frac{d_i^2}{d_m^2}\right)} \tag{3}$$

d_i is the distance from the point $\boldsymbol{p}$ to a neighbour $\boldsymbol{q_i}$ and d_m is the mean value of all distances. The closer the point $\boldsymbol{q_i}$ is to $\boldsymbol{p}$ located, the bigger the term δ_i is. When d_i is very close to zero, δ_i is very close to *1*. The direction of the normal $\boldsymbol{n}$ at point $\boldsymbol{p}$ is given by the eigenvector corresponding to the smallest eigenvalue of the matrix **C**. Generally it requires at least three points to estimate the normal vector. There is also the possibility, that the neighbours in the given region are fewer than measured for the normal estimation. To ensure the definite computation of each point and also the calculation following, a filtering step using radius outlier removal will be processed before the normal estimation. Then all the points, which have less than two neighbours in the given neighbourhood, are removed.

2.2.1 Angle between Normal Vector and Target Direction

After the normal vector at the observed point $\boldsymbol{p}$ is estimated, the angle α between the normal and the vector from the view point to $\boldsymbol{p}$ can be calculated. The centre of the instrument is treated as the view point. It is defined the normal on the object surface points to the origin. Coordinates of $\boldsymbol{p}$ are $(x, y, z)^T$ and the normal $\boldsymbol{n}$ is stored in the form $(n_x, n_y, n_z)^T$. Thereby the angle α can be computed:

$$\alpha = \arccos\frac{<\boldsymbol{p}^T, \boldsymbol{n}>}{\|\boldsymbol{p}\|\cdot\|\boldsymbol{n}\|} = \arccos\frac{x\cdot n_x + y\cdot n_y + z\cdot n_z}{\sqrt{x^2+y^2+z^2}\cdot\sqrt{n_x^2+n_y^2+n_z^2}} \tag{4}$$

As shown in Figure 4, the angle of the point $\boldsymbol{p}$ on the object surface is nearly π. On the other hand the mixed point has an angle of about π/2. When α is close to $\pi/2$, the normal is nearly perpendicular to the view line, and the point is considered as mixed point. α=π/2 acts as the criterion used to determine whether the point is an outlier or not.

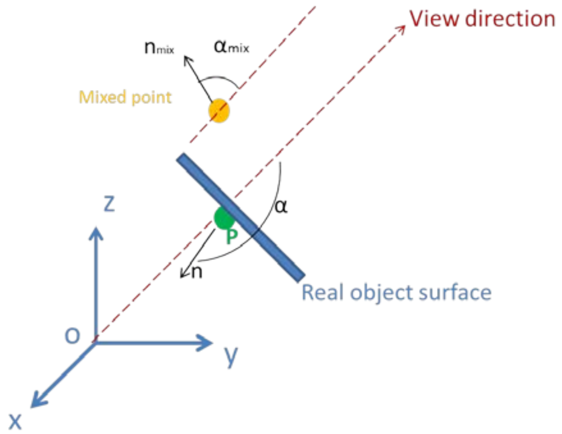

Figure 5: The angle between normal vector and view direction

2.2.2 Curvature Estimation

The points on edges have angles of about π/2. They should keep staying in the point cloud. But since the “comet tail” phenomenon occurs nearby the edge, those points can be almost removed together with mixed points. Typically, the edge of a surface has a certain curvature that is not equal to zero, while the “comet tail” points are assembled in a plane form with the curvature zero. The curvature of a point can be considered as the criterion for the judgment whether the point is on the edge or not. The curvature can be obtained using normal estimation algorithm. The matrix **C** has three eigenvalues $\lambda_1 \geq \lambda_2 \geq \lambda_3$. The curvature κ at this point is (Rusu et al., 2008):

$$\kappa = \frac{\lambda_1}{\lambda_1+\lambda_2+\lambda_3} \tag{5}$$

2.2.3 Conditional Removal

If a point has a curvature equal to zero and at the same time α is nearly π/2, it will be considered as a mixed point. This filtering process will be realized by the conditional removal algorithm. The whole procedure of “comet tail” removal is shown in Figure 5.

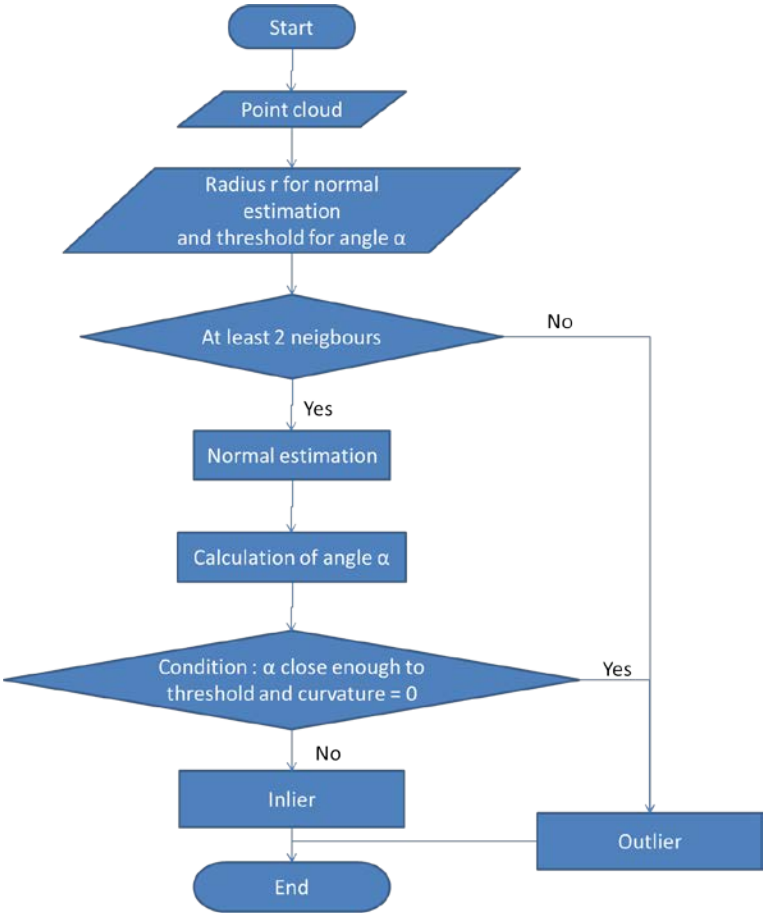

Figure 6: Flow chart of "cometary tail" removal algorithm

3 DATA ANALYSIS

3.1 Results of the Filtering Using "Comet Tail" Removal

The aggregate element presents a star shaped component with 14772 points. The "comet tail" removal begins with the radius outlier removal. Considering the distribution of all points in this point cloud and the point resolution of 2 mm, at first the search radius r and the minimum number of neighbours *m* are set to *0.002m* and *8*. In this case, 1192 points are removed as outliers. Lots of mixed points were deleted by the filter. But there are still many "cometary tail" points remaining, especially in the region behind the three branches which stand on the table during scanning (Figure 6, middle). The normal of all points was estimated with the search radius of 0.002 m. The number of neighbours stays at 8. As a result of the normal estimation the angles between the normal of the mixed points and the view direction vary from $\pi/2$ to 2.17. Therefore the threshold for the angle in the condition removal was set to 2.17. 2698 points was deleted as mixed points. The result is clearly improved (Figure 6, right).

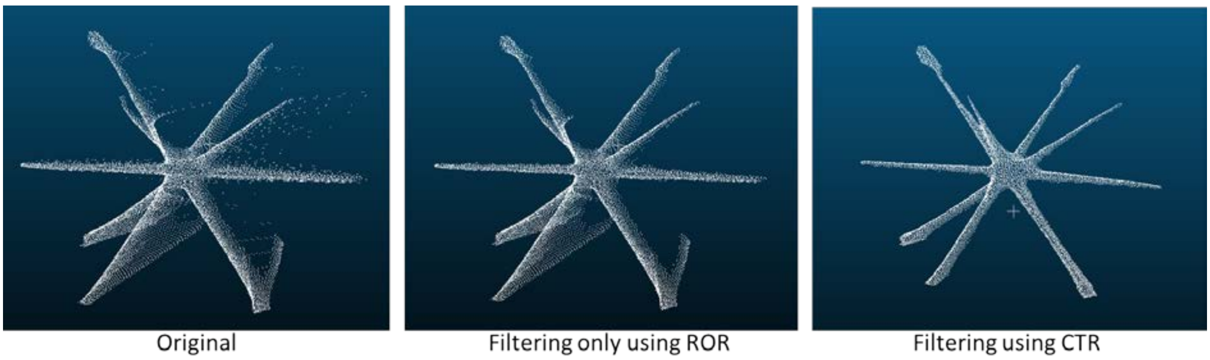

Figure 7: Point cloud before filtering and after filtering

3.2 3D Reconstruction in Geomagic 2012

Because of the curvature estimation a lot of points on the edges were kept after the filtering. This shows a high tolerance of the "comet tail" removal. After filtering the structure of the object can be clearly recognized.

The aggregate element was reconstructed using triangulation in Geomagic Studio 2012. Figure 7 shows the reconstruction's result of the point cloud before and after the filtering using "comet tail" removal. The large "cometary tail" plane does not exist anymore. Each branch can easily be recognized. However, at the ends of the upper branches, the reconstructed planes are not flat and complete. The reason is that in those areas there are not enough points that can be used to describe the object. This has to be improved in future work.

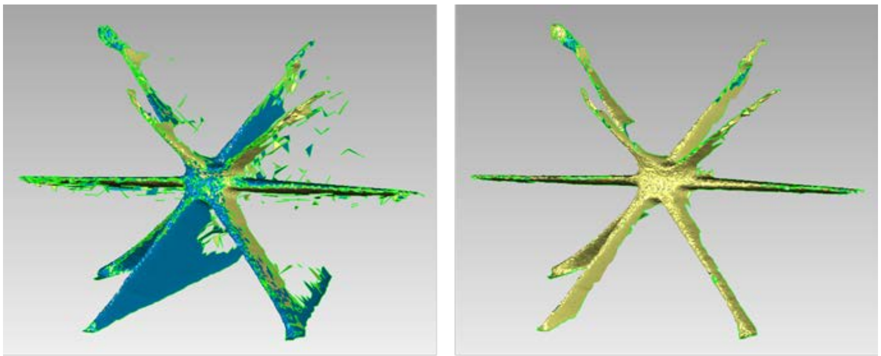

Figure 8: Results of the reconstruction before and after filtering

4 CONCLUSION AND OUTLOOK

The phase-based laser scanner can be used for area-wise data acquisition. The object with a lot of edges has a strong edge effect after scanning. Using available filters several clusters of points remain the point cloud that far away from the ideal model. The outliers can not be completely removed. The radius outlier removal deletes the mixed points which are very scattered behind the object. The angle between the normal of the mixed points and the view direction can be calculated. The curvature on each point can be estimated. Those two factors can be set as a condition to keep inlier and delete outlier. The "comet tail" removal can delete the outliers for the aggregate element very efficient.

Furthermore, since the location of the instrument is set as the origin of the coordinate system. Each scan has an own view direction during the normal estimation process. When several datasets are registered already, there will be many different views of the points in one scenario. The "comet tail" removal can only be used for the point clouds from the same scanning center.

In order to make it applicable for registered point clouds the filter algorithm "cometary tail" removal should be developed in the future research. Moreover, it still needs to be tested using other point clouds of different kinds of material, in different colors and with different shapes. Besides, it is necessary to find out, which influence this filtering algorithm has on the quality of the original point cloud.

REFERENCES

Books:

DEUMLICH, F., STAIGER, R. (2002): *Instrumentenkunde der Vermessungstechnik.* Wichmann, Heidelberg.

JOECKEL, R., STOBER, M., HUEP, W. (2002): *Elektronische Entfernungs-und Richtungsmessung und ihre Integration in aktuelle Positionierungsverfahren.* Wichmann, Heidelberg.

Journal articles:

BÖHLER, W., BORDAS VICENT, M., MARBS, A. (2003): *Investigating Laser Scanner Accuracy.* Originally presented at the XIX CIPA Symposium at Antalya, Turkey, 30 Sep-4 Oct 2003.

BREUNIG, M. M., KRIEGEL, H. P., NG, RAYMOND T., SANDER, J. (2000): LOF: *Identifying density-based local outliers.* In Proceedings of ACM SIGMOD Conf. 2000, p. 93-104.

PFEIFER, N., DORNINGER, P., HARING, A., FAN, H. (2007): *Investigating terrestrial laser scanning intensity data: quality and functional relations.* In: International Conference on Optical 3-D Measurement Techniques VIII, Zurich, Switzerland, 2007, p. 328-337.

GORDON, S., LICHTI, D., STEWART, M., FRANKE, J. (2003): *Structural Deformation Measurement Using Terrestrial Laser Scanners.* 11th FIG Symposium on Deformation Measurements, Santorini, Greece, 2003.

KNORR, E.M., NG R.T., TUCAKOV, V. (2000): *Distance-based outliers: Algorithms and applications.* VLDB Jounal, 8, p. 237-253.

LICHTI, D., LICHT, M. (2006): *Experiences with Terrestrial Laser Scanner Modelling and Accuracy Assessment.* IAPRS Volume XXXVI, Part 5, Dresden 25-27 September 2006, p. 155-160.

MITRA, N. J., NGUYEN, A. (2003): *Estimating Surface Normals in Noisy Point Cloud Data.* Symposium on Computational Geometry, p. 322 – 328.

PAPADIMITRIOU, S., HIROYUKI, K., GIBBONS, P. B., FALOUTSOS C. (2003): *Fast Outlier Detection Using the Local Correlation Integral*. IEEE 19th International Conference on Data Engineering (ICDE'03), Bangalore, India, March 5-8, 2003, p. 315-326.

RICHTER, E. (2009): *Denoising Point Cloud Data of Small-Structured Free Form-Surfaces Captured by A Phase-based Laserscanner.* In: Bretar F, Pierrot-Deseilligny M, Vosselman G (Eds) Laser scanning 2009, IAPRS, Vol. XXXVIII, Part 3/W8-Paris, France, September 1-2, 2009, p. 37-42.

RUSU, R. B., MARTON, Z. C., BLODOW, N., DOLHA, M., BEETZ, M. (2008): *Towards 3D Point Cloud based Object Maps for Household Environments*, Robotics and Autonomous Systems 56, 11/2008, p. 927 – 941, 2008.

SOTOODEH, S. (2006): *Outlier Detection in Laser Scanner Point Clouds.* IAPRS Volume XXXVI, Part 5, Dresden 25-27 September 2006, p. 297-302.

Dissertation:

GORDON, B. (2008): *Zur Bestimmung von Messunsicherheiten terrestrischer Laserscanner*. Institut für Photogrammetrie und Kartographie, Technische Universität Darmstadt, http://tuprints.ulb.tu-darmstadt.de/1206/ , last access: 01.03.2015

KERN, F. (2003): *Automatisierte Modellierung von Bauwerksgeometrien aus 3D-Laserscanner-Daten*. Institut für Geodäsie und Photogrammetrie, Technische Universität Braunschweig, 2003.

RUSU, B. R. (2009): *Semantic 3D Object Maps for Everyday Manipulation in Human Living Environments.* Disseration at Institut für Informatik, Technische Universität München, http://files.rbrusu.com/publications/RusuPhDThesis.pdf, last access: 03.03.2015

ZOGG, H. M. (2008): *Investigations of High Precision Terrestrial Laser Scanning with Emphasis on the Development of a Robust Close-Range 3D-Laser Scanning System*. Institute of Geodesy and Photogrammetry, Eidgenössische Technische Hochschule Zürich.

PCL (2014):
http://pointclouds.org/documentation/ , last accessed on June 23, 2014.

ICD (2015):
http://icd.uni-stuttgart.de, last accessed on March 09, 2015

TECHNICAL SESSION 6: GEOMETRIC AND DEFORMATION ANALYSIS

The Analysis of Methods for Determining the Geometric Parameters of Rotating Machines

Sergey G. Mogilny[1], Andrii A. Sholomytskyi[2], Vladimir A. Seredovich[2], Alexander V. Seredovich[2], Andrei V. Ivanov[2]
[1]Prydniprovs'ka State Academy of Civil Engineering and Architecture, Department of Land Management, Road-Building and Geodesy, Ukraine
[2]Siberian State University of Geosystems and Technologies, Russian Federation

Abstract
Rotating machines of various kinds are often used in industries that require regular measuring control. In this article, the analysis of contactless methods for the determination of the planned high-rise position of the rotating objects was conducted on the example of kilns for cement production. The paper discusses two methods of measurement with the use of total station and terrestrial laser scanner. The comparative analysis and accuracy assessment of the results were carried out.

Keywords: laser, total station, rotate kiln, measurement accuracy, terrestrial laser scanner

1 INTRODUCTION

Large-size rotary drum-type machines are often used in continuous production lines. The machine is an elaborate construction subject to load and deformation due to temperature and force effect in process of operation.

One of the main conditions for trouble-free efficient operation of such machine is strict correspondence of the machine slide units relative position to the design, i.e. the shell rotation axis linearity, relative position of bearing rollers and tyres, their rotation axes, etc. The process of the machine heating and operation is accompanied by the parts shift and wear resulting in the design geometric correlation failure. As rotary kilns heat up to extremely high temperature (the temperature of the shell outer surface amounts to 500°C) the tyres radii increase unevenly (up to 20 mm) causing the axis bending. Due to the defects of the kiln refectory lining and its uneven heating the shell shape gets curved. Thus, it is very important to determine the rotation axis shape in dynamics. I.e. in process of rotation of the machine heated up to the working temperature. It is called "hot" alignment. "Hot alignment" has been applied for a long time [1], but it is only lately that it has found wide application, probably due to the new measurement techniques and instrumentation permitting remote control of the process [2].

However, it is impossible to do without the cold alignment, as after the long-run repair works which require the kiln stoppage, it gets cool. After the repair works involving bearings, rollers, tyres or shell parts replacement or the works on lining restoration the kiln starts heating up to its working temperature. Changes in the kiln elements position or dimensions during the repair or replacement process result in the kiln axis getting curved and reduction of the subsequent overhaul period. "Hot" alignment of the kiln performed right away causes additional expenditure. Therefore, improvement of cold alignment and its accuracy seems to be an urgent problem. The authors consider the techniques of "hot" and "cold" alignment to be not mutually exclusive, but complementary ones.

Now there is a number of various types of cold alignment [3, 4, 5], with all of them permitting determination of only geometric axis of the kiln. Some of them may be applied to only short-length machines, ensuring desired accuracy for only short distances. In general, traditional geodetic methods for rotary machines alignment [3, 4[do not meet current requirements to the alignment precision. Precision of tyres leveling or lateral leveling most frequently used for cold alignment amounts to ±5 mm, with this level of precision being possible only under favorable conditions of measurements.

The time period of eight-support kiln cold alignment by tires leveling in four positions is 4÷5 days (with 12 hours shift).Moreover, this technique does not provide information on the kiln axis position between tyres.

A lot of the Internet commercials offer services of "hot" and "cold" alignment for rotary machines [for example, 6, 7]. However, the advertised services do not provide information on the applied technologies and accuracy of geodetic works for rotary machines alignment. State-of-the-art laser systems, laser tacheometers and trackers are mostly mentioned. The technique for cold alignment of rotary kiln using total station is described in details in [8, 9]. However, the technique has a number of drawbacks. First of all, it cannot be used remotely, so. the rackman (standing on the ladder at dangerous height) has to set the deformation mark on the machine surface. Secondly, this type of measurements may be made only for the machines on low supports. If the support height is more than 3 m, measurements may be made only for tyres and a limited part of the shell (only from the site under the tyre). Thirdly, common drawback for all the methods of laser alignment is lack of accuracy substantiation as regards determination of rotary machines parameters. The analysis results showed that the accuracy of rotary machines geometric parameters depends more on the geometric scheme of measurements than on the accuracy of angle and distance measurements by total station [2].

2 GEODETIC TECHNIQUE FOR COLD ALIGNMENT

The technique of cold alignment based on reflectionless laser measurements by total stations is presented. It is to be used for determination of geometric parameters of rotary machines.

Precise geodetic reference network serves as a geometric basis for measurements. To this end, light-reflecting targets are set on supporting structures around the object. The targets positions are determined by spatial linear-angular network (Fig.1). The network is used for referencing, when measuring certain elements of the machine, to refer all measurements to a single coordinate system. The size of reflective films is chosen depending on the object size (from 30×30 mm to 60×60 mm). If terrestrial laser scanning is used for the object, then the target size is 100x100 mm.

Measurements technique is chosen in accordance with the total station precision as regards measurement of angles and lengths as well as the network geometry, with the error of network points coordinates being max. 1 mm. Typical reference network of the rotary machine is shown in Fig. 2, where the points with the letter "T" are those of instrument setting, and the remaining – the points of the reference network. Rectangular columns of the diagram reflect relative measure of the network points coordinates errors. The network was established by the technique of free stations, by phase-by-phase station fixing. Current field network control in process of measurement provides its reliability.

Figure 1: Fixation of deformation benchmarks on the object structures.

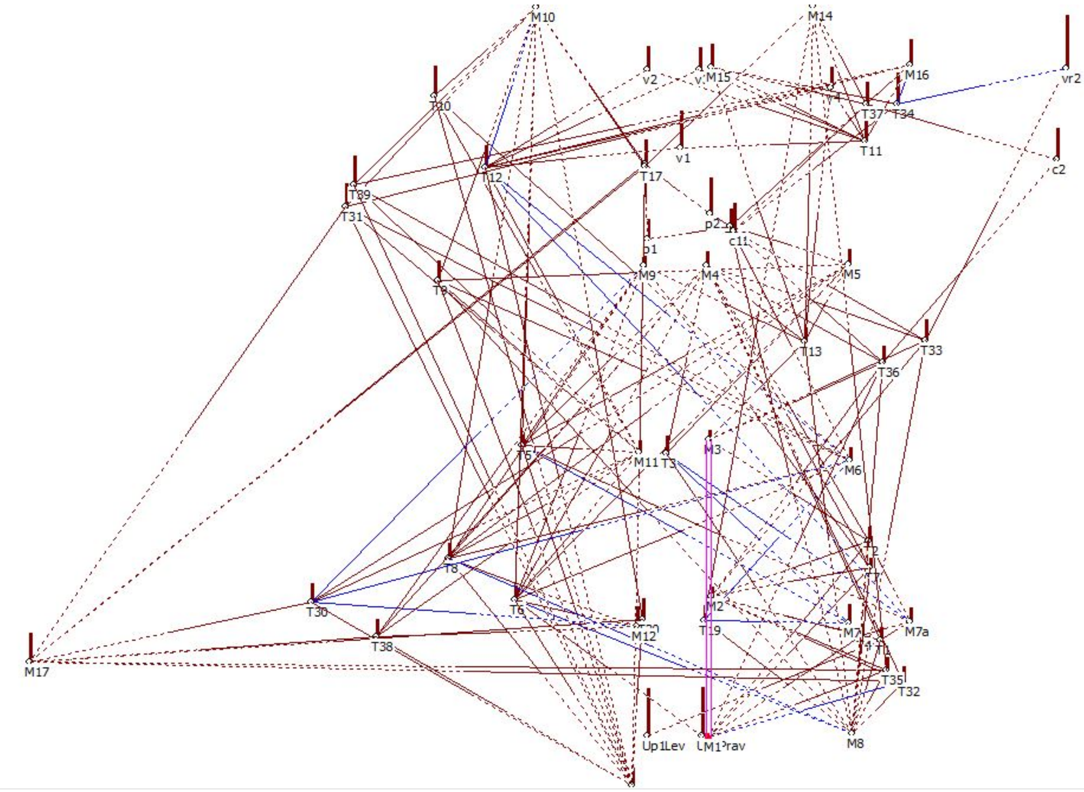

Figure 2: Reference geodetic network VP №4 of Azovstal plant (Mariupol)

The object was measured by characteristic sections. Measurement of the object tyres made from two sides to improve the accuracy is shown in Fig. 3. Tie measurements on reference points (designated by squares) are also shown.

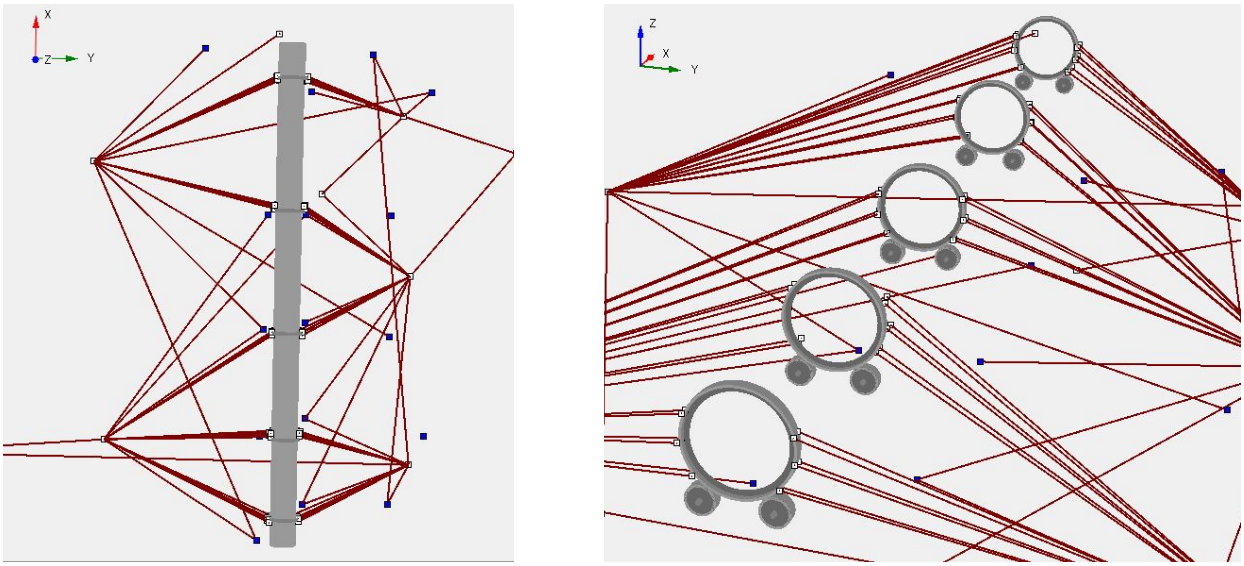

a) in plane б) 3D

Figure 3: Tyre geometry measurement scheme.

Measurements from the left and right sides of tyres are easily positioned on the object body, as they are usually made symmetrically as close as possible to the tyre edge which is free from stuck lubricant, dust and crumbling holes. Height measurements are distributed in the following way: in the centre – on the rotation axis, up and down – approximately half a radius apart. In case of significant misalignment, laser beam starts “grazing”, and the signal reflected from the tyre surface does not return to the total station receiving device.

Thus, six pairs of points are measured on the tyre surface. The points are used for constructing different geometrical figures (cylinder or cone). By average regular geometrical figure deviations real shape of the tyre may be determined, with the figure centre being the point of the machine geometrical axis.

To receive information on the geometrical axis of the shell the technique for section measurement is also used. However, as the shell has no visible reference points to determine the section position, measuring complex "Vizir 3D" is applied for the purpose [10]. Reference axis X and geometrical axis of the kiln being superposed (Fig. 3), all the points of the shell section are to have the same coordinate X, this being an indispensable condition for superposition of the kiln left and right sides sections. Measurement starts from any side of the kiln. When passing on to the other side, preliminary pointing is performed and the point coordinates on the shell surface are determined. After coordinate X analysis the point position on the shell is adjusted. Due to the online observation, the point adjusting by successive-approximations method (with accuracy of 2 cm) takes 15 – 20 seconds.

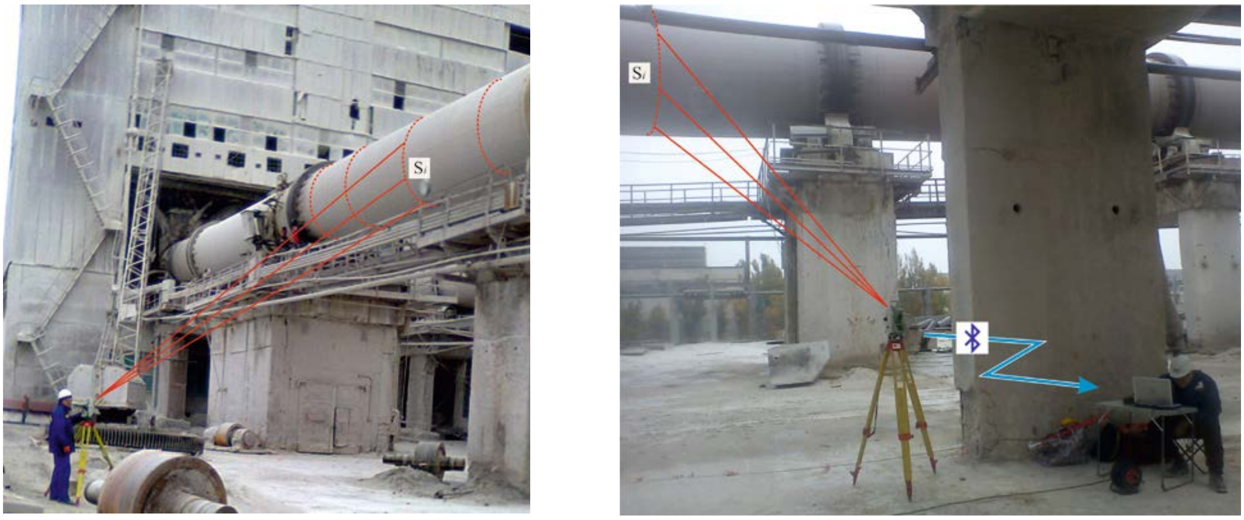

a) left side of the kiln b) right side of the kiln

Figure 4: Measurement of section S_i on the shell

Support rollers position in process of cold alignment is most accurately determined by direct measurement of the roller body and sections (Fig. 5). Two or three roller sections may be measured.

By means of measuring complex "Vizir 3D" (in cold alignment) all the elements of the rotary machine may be measured: center-to-center spacing, foundation framework marks, tyre clearance, central angle, etc. "Vizir 3D" measurements and processing being highly automated the results of measurement and adjustment may be applied immediately after measurement. The results are displayed in table 1, where summation correction actions for the left and right rollers (`dY left, dY right`) resulting from the axis correction in plane and height are presented.

Figure 5: Measurement of support rollers parameters

Table 1. Tyres position alignment

Tyre	X, mm	Y, mm	Z, mm	Zпр, mm	dZ, mm	dY, mm	dY left	dY right
№ 1	-1169.1	1.4	7040.5	7039.6	-0.9	-0.6	1.3	2.5
№ 2	10809.1	-3.5	7460.8	7458.8	-2.0	-1.5	2.5	5.5
№ 3	24858.8	-1.0	7955.4	7950.5	-4.9	-3.0	5.2	11.2
№ 4	42264.9	2.0	8559.7	8559.7	0.0	0.0	0.0	0.0
№ 5	59789.4	1.1	9174.7	9173.1	-1.6	-0.9	1.5	3.3

In the Table 1, X,Y,Z are actual coordinates (in millimeters) of tyre centres in the object coordinate system (Fig. 3). Zпр – tyres marks calculated from tyre #4 (whose position does not change, as it is close to the crown gear) with design kiln inclination. dY is the tyre shift in plane, with tyre #4 being immovable.

3 ACCURACY OF ROTARY MACHINE GEOMETRIC PARAMETERS DETERMINATION

The technique for static determination of the rotary machine geometric parameters is based on measurement of certain sections of the machine (an aggregation of cylindrical objects). Each object is measured separately in some general coordinate system as shown in Fig. 6.

Objects surface accessibility and possibility of reflectionless distance measurements permit coordinate determination (at each section of cylindrical object) for only six points with optimal position, designated in Fig. 6 as *1, 2,…,6*.

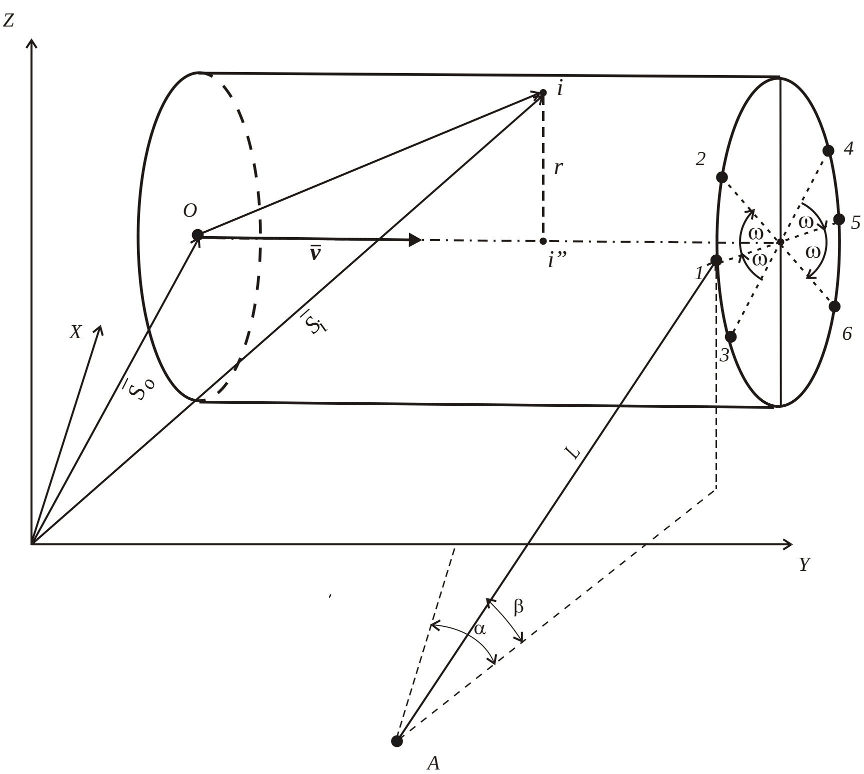

Figure 6: Geometrical scheme for cylindrical object measurement

The cylinder position and dimensions in the general case are determined by the following parameters: vector $\bar{S}_o$ of centre o of the rim section; unit vector $\bar{v}$ of axis direction and the value of radius r. For random point i on the cylinder surface, whose position is determined by vector $\bar{S}_i$, the following equation is used:

$$\varphi_i = \sqrt{|\bar{S}_i - \bar{S}_o|^2 - |(\bar{S}_i - \bar{S}_o) * \bar{v}\,|^2} - r = 0. \tag{1}$$

For measured coordinates of point *i*, due to the measurement errors, equation (1) will have the following form

$$\sqrt{|\bar{S}_i - \bar{S}_o|^2 - |(\bar{S}_i - \bar{S}_o) * \bar{v}\,|^2} - r = \varepsilon_i, \tag{2}$$

where ε_i – misalignment due to measurement errors of values α, β, L (Fig. 6). Expressing vectors through their projections we obtain the following system of parametrical equations for *n* measured points:

$$\left.\begin{array}{c}\sqrt{(x_i - x_o)^2 + (y_i - y_o)^2 + (z_i - z_o)^2 - \left((x_i - x_o)v_x + (y_i - y_o)v_y + (z_i - z_o)v_z\right)^2} - r = \varepsilon_i; \\ i = 1,2, \dots, n\end{array}\right\}, \tag{3}$$

to which we add condition

$$v_x^2 + v_y^2 + v_z^2 = 1, \tag{4}$$

to turn vector $\bar{v}$ into unit vector.
Combined solution of equations (3) and (4) is performed by the least square method, thereto they are reduced to linear form

$$\left.\begin{array}{l}\frac{\partial\varphi_1}{\partial x_o'}\delta_{x_o} + \frac{\partial\varphi_1}{\partial z_o'}\delta_{z_o} + \frac{\partial\varphi_1}{\partial v_x'}\delta_{v_x} + \frac{\partial\varphi_1}{\partial v_y'}\delta_{v_y} + \frac{\partial\varphi_1}{\partial v_z'}\delta_{v_z} + \frac{\partial\varphi_1}{\partial r'}\delta_r + l_1 = \varepsilon_1; \\ \frac{\partial\varphi_2}{\partial x_o'}\delta_{x_o} + \frac{\partial\varphi_2}{\partial z_o'}\delta_{z_o} + \frac{\partial\varphi_2}{\partial v_x'}\delta_{v_x} + \frac{\partial\varphi_2}{\partial v_y'}\delta_{v_y} + \frac{\partial\varphi_2}{\partial v_z'}\delta_{v_z} + \frac{\partial\varphi_2}{\partial r'}\delta_r + l_2 = \varepsilon_2; \\ \quad \dots \quad \dots \quad \dots \quad \dots \quad \dots \quad \dots \quad \dots \\ \frac{\partial\varphi_n}{\partial x_o'}\delta_{x_o} + \frac{\partial\varphi_n}{\partial z_o'}\delta_{z_o} + \frac{\partial\varphi_n}{\partial v_x'}\delta_{v_x} + \frac{\partial\varphi_n}{\partial v_y'}\delta_{v_y} + \frac{\partial\varphi_n}{\partial v_z'}\delta_{v_z} + \frac{\partial\varphi_n}{\partial r'}\delta_r + l_n = \varepsilon_n; \\ \qquad\qquad 2v_x'\delta_{v_x} + 2v_y'\delta_{v_y} + 2v_z'\delta_{v_z} \qquad + 0 = \varepsilon_v,\end{array}\right\} \tag{5}$$

where «′» designates approximate values of the desired cylinder parameters, and absolute terms are calculated by formulas

$$l_i = \sqrt{(x_i - x_o')^2 + (y_i - y_o)^2 + (z_i - z_o')^2 - \left((x_i - x_o')v_x' + (y_i - y_o)v_y' + (z_i - z_o')v_z'\right)^2} - r. \tag{6}$$

Value y_o is constant; it is taken as equal to the minimum value of coordinate y_i of measurements. Combined equations (5) are solved when performing the conditions of the least square method in the following form

$$\sum_1^n \varepsilon_i^2 + 100\varepsilon_v^2 = min. \tag{7}$$

Corrections and approximate values of unknowns are determined in matrix form by formula

$$\Delta = -(A^T A)^{-1} A^T L, \tag{8}$$

where A and L – matrices of coefficients and absolute members of combined equations (5); correction vector Δ has the form of

$$\Delta^T = \left|\delta_{x_o}, \delta_{z_o}, \delta_{v_x}, \delta_{v_y}, \delta_{v_z}, \delta_r\right| \tag{9}$$

Adding corrections to the approximate values of unknowns we find new improved values for the cylinder parameters. Iterations are performed until the norm of vector Δ is less than the established accuracy of iterations.
Diagonal elements of matrix Q

$$Q = (A^T A)^{-1} \tag{10}$$

are equal to the reversed weights of the corresponding parameters in the correction vector Δ. Then m_k, a mean-root-square error of k-rd parameter, is calculated by formula

$$m_k = \mu\sqrt{Q_{k,k}} \tag{11}$$

where μ – error of unit weight, which (when using total station Leica TM30, with angle measurement error 0,5″, distance in reflectionless conditions 2 mm + 2 ppm, for short distances 1 mm) may be taken as equal to the distance measurement accuracy, with angle error effect on misalignment ε_i being insignificant.

By the derived formula we may calculate the expected accuracy for the machine elements. Consider, as an example, measurement accuracy for the rotary kiln tyre, if its width is 0.5 m and radius 2.5 m.

Table 2. Accuracy of tyre parameters measurement ($\omega = 30°$)

Measurement points	Mean square errors of cylinder parameters, mm				
	m_{x_0}	m_{z_0}	m_{v_x}	m_{v_z}	m_r
1,2,3	6.42	1.27	3.68	7.95	5.90
1,2,3,4	0.60	0.96	3.56	6.65	0.49
1,2,3,4,5	0.41	0.87	3.11	6.61	0.34
1,2,3,4,5,6	0.32	0.70	2.60	5.62	0.29

The data of Table 2 correspond to the mean square error of 1 mm distance measurement with two sections measured and measurement points position at angle $\omega = 30°$ (Fig.. 6).Values m_{z_0} and m_{v_z} characterize accuracy of the cylinder axis inclination, mm per m. Accuracy results do not depend on the radius. With growing number of sections the accuracy increases in proportion to the square root of the number of sections, with the error of the axis inclination angle being inversely proportional to the cylinder length.

With angle ω of measurement points position growing up to $60°$ accuracy results improve (table 3), but the accuracy of reflectionless distance measurement decreases, therefore the data of table 2 are more reliable.

Accuracy analysis in process of “cold” alignment of rotary machines shows that modern total stations (when choosing optimal measurement techniques) allow for reliable estimation of the machine state and its efficient adjustment.

Table 3. Accuracy of tyre parameters measurement ($\omega = 60°$)

Measurement points	Mean square errors of cylinder parameters, mm				
	m_{x_0}	m_{z_0}	m_{v_x}	m_{v_z}	m_r
1,2,3	1.72	0.61	4.62	4.62	1.22
1,2,3,4	0.77	0.52	4.48	3.76	0.50
1,2,3,4,5	0.46	0.38	3.55	3.75	0.33
1,2,3,4,5,6	0.41	0.41	3.27	3.27	0.29

4 COLD ALIGNMENT BY TERRESTRIAL LASER SCANNING

Experience of cold alignment by terrestrial laser scanner Surphaser is presented in [11], cylindrical surface deviations are shown (for one section of the shell). Neither technical details nor the achieved accuracy and measurement and processing techniques are given. According to the presented photographs the kiln under consideration is set on very low supports, so the measurements involve major surface of the network.

The authors carried out the experiment of the kiln cold alignment at one of the cement mills of West Siberia by scanner RIEGL VZ400, with the following certificate characteristics:

- medium range of action is 400 m;
- distance measurement accuracy – 3mm;
- coordinate determination accuracy – 5 mm;
- angular resolution of inclinometer 0,008°.

The kiln was set on supports of considerable height (up to 12 m), survey was conducted on the land, from two sides. In Fig. 7, the process of scanning at the station (7a) and the result of 3D point model (Point Cloud - data array XYH described by the object surface), obtained after scanning data preprocessing (7b) are shown.

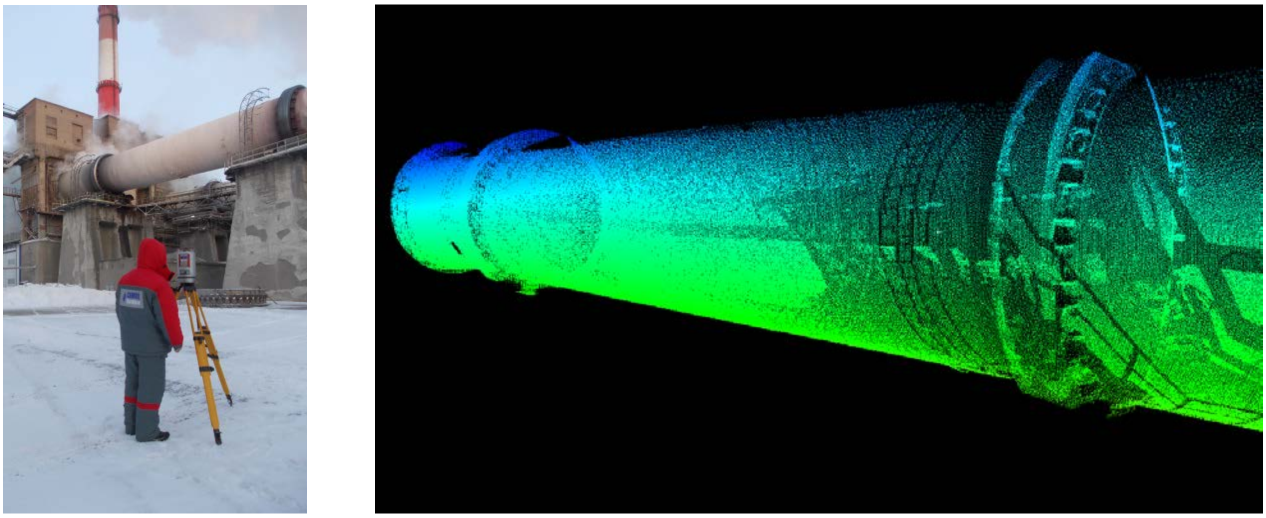

a) object surveying b) scanning data integration (point cloud)

Figure 7: Process of laser scanning at the station, and the segment of the kiln point model result

Terrestrial laser scanning has been done at 9 stations with average density of six measurements per 100^2 cm and average rate of 10 min per station. Scanning was arranged so that each station field of view covered the structure fragment of the kiln under study. The condition of measurements overlapping minimum 50 % of neighboring scanning stations (Fig. 8) was met. The overlapping condition was observed for further data preprocessing to establish reference scanning network based on the received scanning data. This function is provided by the producer of *RIEGEL* TLS. It permits considerable facilitation of engineering object surveying as it skips the stage of preparation and measurement of reference geodetic network.

The process of data adjustment and calculation (registration) of measurements MSE in uniform point model (point cloud) was performed in software Riscan PRO. For convenience, the object was divided into two sites (workshop 1-2 (A) and workshop 2-3 (Б)) for further data processing. That made it possible to visually estimate the scheme of all scanning stations distribution with regard to the local situation for further choosing of the reference point. Scanning station # 1 was taken as a reference point (reliable data for further adjustment, the middle of the scanning range), as its position allowed for maximum coverage (from two sites, A and B) of the kiln to be measured. Final MSE of all stations data registration after the adjustment process was 4 mm.

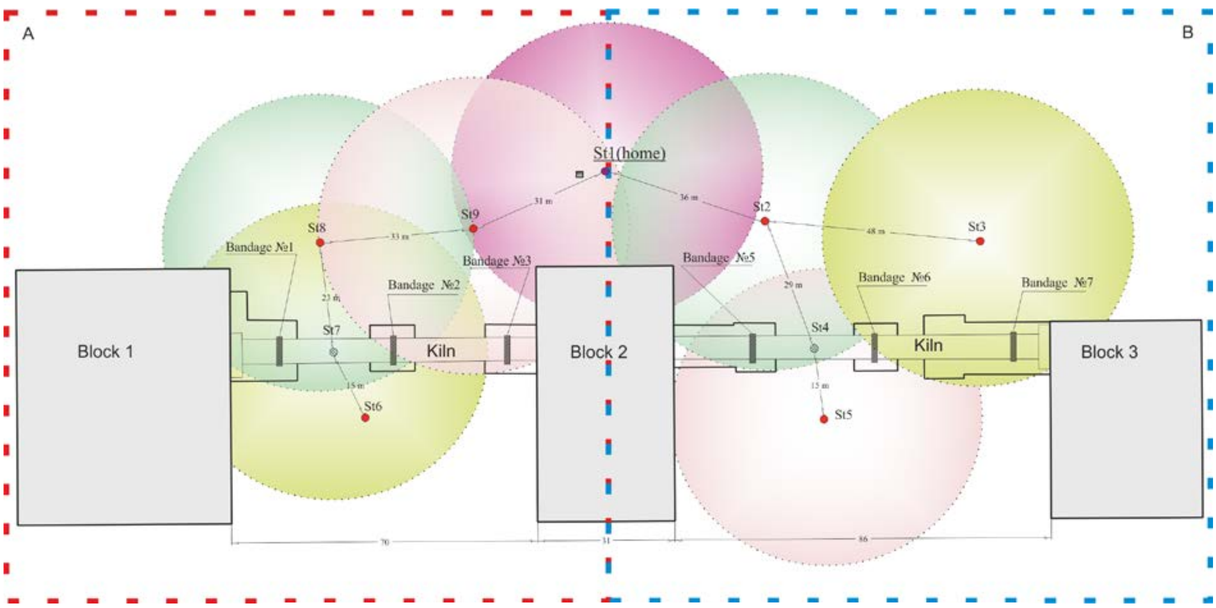

Figure 8: The scheme of scanning stations location and overlapping

In addition to the above said, visual estimate was conducted by longitudinal and cross sections in plane and height by Cyclone software to determine actual accuracy of scanning data integration in uniform model. The estimate made it possible to reveal maximal discrepancy between the scanning data, which amounted to 8 mm, Fig. 9.

The next stage of TLS data processing involved establishment of the working coordinate system, so that one of the axes was in agreement with the kiln body direction, and vector model-building by spatial Triangulated Irregular Network (TIN). It is the simplest and most efficient technique for 3D model-building based on TLS data (Fig. 10). The authors used software Rapidform XOR3 with special toolbox for TIN model-building.

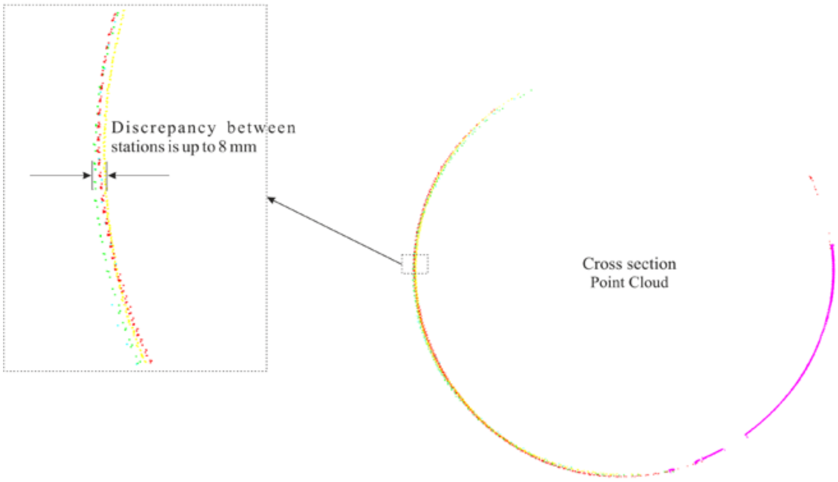

Figure 9: Construction of sections by the built model of the kiln body.

As a result of processing, the object model, built by terrestrial laser scanning covers (with its measurements) on average 210° of the kiln body.

Using TIN model and Rapidform XOR3 software functions the authors obtained cross sections of the kiln body with 1 m step and polyline inscribed in each section. On the basis of this polyline regular figure of a circle was approximated. Later the circle centre coordinates maximally approximated to the actual axis of the given tilt were determined (Fig. 11).

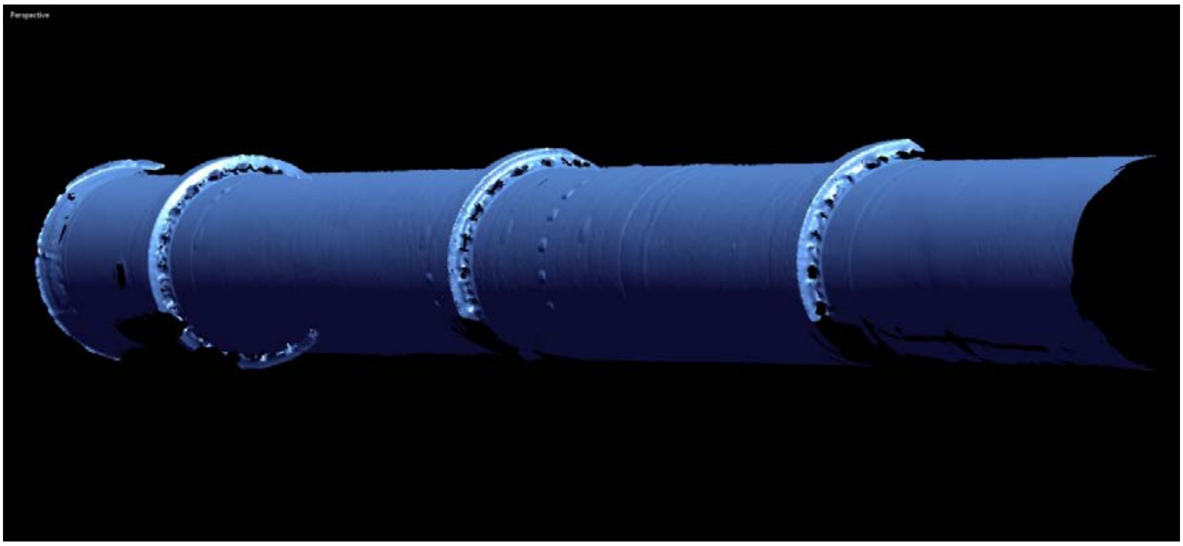

Figure 10: 3D model of the kiln body based on TLS data

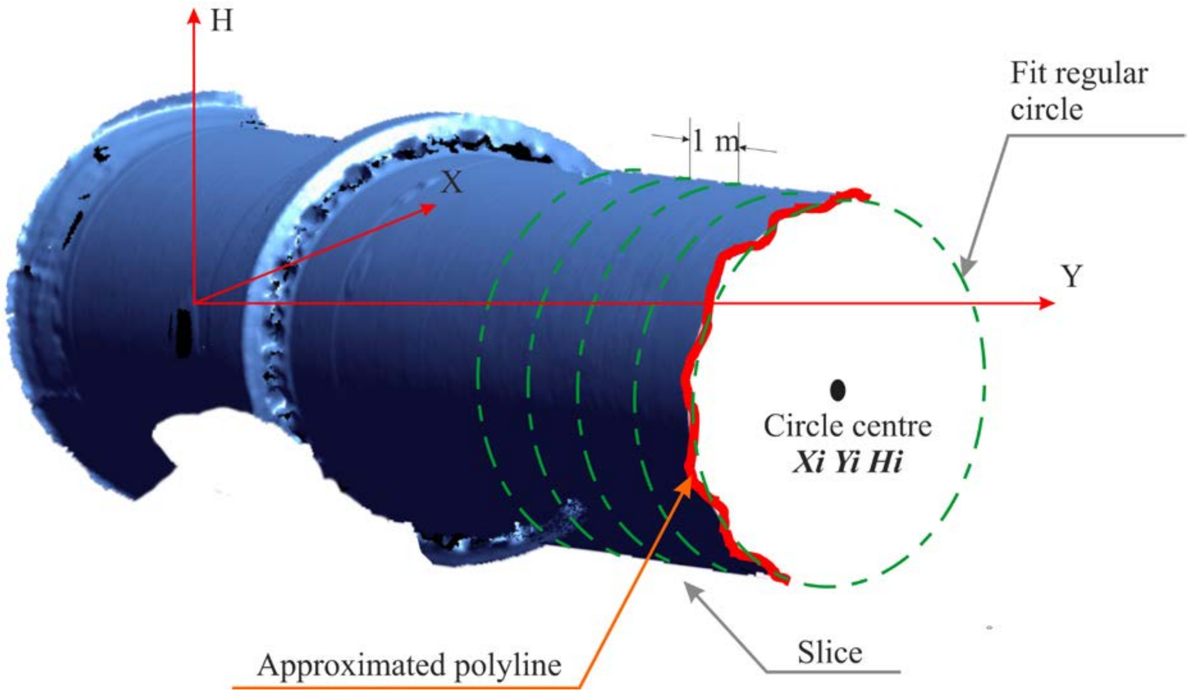

Figure 11: Setting the coordinate system and construction of sections

Accuracy analysis for the kiln geometrical parameters obtained in process of scanning was conducted for the tyre at the same conditions as in case with total station. The tyre parameters were determined by scanning its surface section ($30°$ of the cylinder circular arc). In tables 4 and 5 the errors of tyres parameters are shown for distance measurement accuracy ± 5 mm.
The statement of accuracy improvement due to the point cloud is purely theoretic in character, it is true only in case of measurements errors being free from the systematic component.

Table 4. Accuracy of one-way scanning of the tyre ($\omega = 30°$)

Measurement points number	Mean square errors of cylinder parameters, mm				
	m_{x_0}	m_{z_0}	m_{v_x}	m_{v_z}	m_r
440	9.48	24.13	1.45	4.82	5.85
860	6.91	17.68	1.03	3.54	4.39
1700	4.97	12.73	0.73	2.54	3.21
3380	3.55	9.09	0.52	1.82	2.31

Table 5. Accuracy of two-way scanning of the tyre ($\omega = 30°$)

Measurement points number	Mean square errors of cylinder parameters, mm				
	m_{x_0}	m_{z_0}	m_{v_x}	m_{v_z}	m_r
880	5.12	17.06	1.02	3.41	0.17
1720	3.66	12.50	0.73	2.50	0.12
3400	2.60	9.00	0.51	1.80	0.09
6760	1.84	6.42	0.37	1.28	0.06

On the basis of the determined coordinates of sections centres the graph for the kiln body axis deviation from the end line in plane and the graph of height marks were constructed (Fig. 12 – 13).

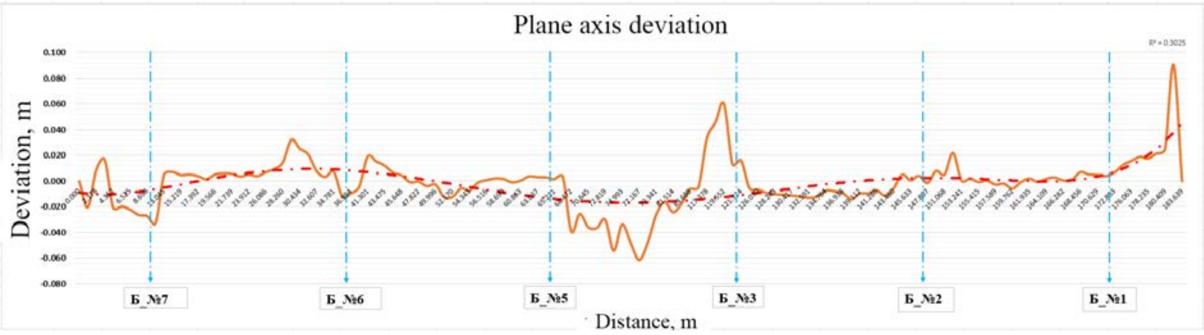

Figure 12: Deviation of the kiln body longitudinal axis from the end line

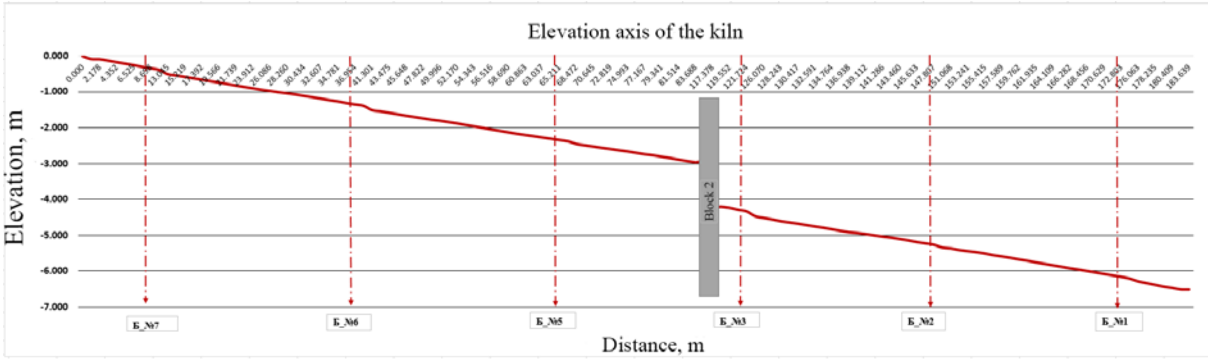

Figure 13: Height marks of the kiln body inclination

5 CONCLUSIONS

Accuracy analysis of rotary machines "cold" alignment revealed that modern total stations (when choosing optimal measurement techniques) allow for reliable estimation of the machine state and providing its efficient adjustment. The time of measurement and adjustment will be reduced twice relative to the traditional method of alignment – leveling of tyres in four positions of the kiln.

Cold alignment technique using terrestrial laser scanning provides more information on the kiln surface and tyres geometry, as it permits conducting practically continuous control of deformations throughout the kiln surface and supplementary equipment. It also facilitates and automates field works, and with the improved accuracy of reference geodetic networks, the technique may find wide application for rotary machines alignment in cold-static state. The authors believe terrestrial laser scanning is a promising technique for cold alignment of rotary machines as it allows for remote measurements and greater safety of works at the object [12].

REFERENCES

Books:

Manufacturing machinery for metallurgy industry. Alignment manual.// T.G. SHEVCHENKO, S.G. KHROPOT, V.P. PIVOVAROV, A.A. IGNATOV, V.F. MENSHIKOV, Ministry of Metallurgy, USSR, 1991, - 212 p.

Journal articles:

B.KRYSTOWCZYK "Ausrichten von Drehofen und Korrektur der Tragrollen-Verdrehunden waehrend des Betriebes" // "Zement Kalk Gips International", № 5, –1983. p. 288–292

MOGILNY, S.G., SHOLOMYTSKYI A.A., LUNEV A.A., SOTNIKOV A.L., FROLOV I.S. Kinematic location measurements of rotary machines. Research works of Donetsk National Technical University, Series "Mining and Geological". Issue № 1(18), Donetsk, - 2013, -P. 3-14

KUZYO, I.V. Calculation and control of continuous production machines installation// KUZYO I.V., SHEVCHENKO T.G. – Lvov: Visha shkola. – 1987.- 176 p.

PETROV, V.V. Technique for control of rotary kilns geometric characteristics / PETROV V.V., TYURIN S.V. Cellulose. Paper. Cardboard., -2005, #7.- p. 66-70

MOGILNY, S.G. measurement complex "Vizir 3D" at Ukraine enterprises: geodetic control and alignment of manufacturing equipment/ S.G. MOGILNY, A.A. SHOLOMYTSKYI, V.N. REVUTSKY, V.A. PRIGAROV/Geoprofil. -2009. - №3(6). – P. 12-19

SEREDOVICH V.A. Terrestrial laser scanning/ SEREDOVICH V.A., SHIROKOVA T.A., KOMISSAROV A.V., KOMISSAROV D.V//Novosibirsk SSGA, - 2009, P. 1-20

Links:

http://www.korabel.ru/news/comments/bum_tehno_zao_razrabativaet_i_vnedryaet_tehnologii_viverki_vrashchayushchihsya_pechey.html – Electronic resource [text] – "Bum Techno" close corporation develops and introduces technologies for rotary kilns alignment– [Date: 21.01.2015]

http://prostroymat.ru/tags/vyverka - Electronic resource [text] – Library of cement mills [date: 21.01.2015]

http://www.cemex.com – Electronic resource [text] – Site of Cemex [Date: 21.01.2015]

http://www.thyssenkrupp.ru/polysius – Electronic resource [text] – Site of ThyssenKrupp Polysius [Date: 21.01.2015]

http://promgeo.com/services/kiln – Electronic resource [text] Site of open corporation «Industrial geodesy» Works under way. [Date: 1.02.2015]

Deformation Analysis of a Timber Pavilion

Annette Schmitt
Institute of Engineering Geodesy, University of Stuttgart, Germany

Abstract

The presented investigations are part of the project *Robotics in Timber Construction*. The behaviour of the pavilion should be investigated over the time. Three measurement epochs in the range of five month are made. However, first of all a geodetic network has to be settled to georeferenced the scanner. This tachymeter network was measured in each epoch to compare the results and detect possible deformations. The second epoch is not comparable with the first and third epoch, because ATR-mode was used for the measurements. There are no significant deformations between the first and the third epoch.

The second step of the investigation and the main task is to scan the pavilion in each epoch and compare the results to detect deformations. Due to the incomparable results of the network measurements different approaches than georeferencing have to be realized to compare the second epoch with the first epoch. A local and a best-fit approach were chosen. The third epoch is compared by georeferencing. Between all three epochs significant deformations could not be detected.

Keywords

Geodetic network, laser Scanning, TIN, deformation analysis

1 INTRODUCTION

In the context of the project *Robotics in Timber Construction* an architectural prototype building was developed. Goal of the project is to develop a lightweight timber construction system with robotic prefabrication, computational design and simulation processes (ICD, 2014a). A pavilion, which is used as an exhibition hall for the horticultural show Landesgartenschau 2014 in Schwäbisch Gmünd, is a lightweight timber shell with robotically prefabricated beech plywood plates. The pavilion has a ground floor of 125m^2 and a volume of 605 m^3, but only 12m^3 wood is used. (ICD, 2014b). The structure of the pavilion remembers the skeletal shell of a sand dollar, a species of sea urchin (Krieg, et al., 2014).

The uniqueness of this building and the fact that wood is a working material, makes it necessary to investigate the pavilion for deformations. These investigations are made with the Laser Scanner Leica HDS7000. The pavilion was build up in March and April 2014. After finishing the interior fittings and the outdoor facilities the pavilion was scanned the first time at the beginning of May 2014, the second scan was at End of June 2014 and the third one in November 2014. In **Fig. 1** the pavilion is presented.

Figure 1: Pavilion at Landesgartenschau 2014

2 GEOREFERENCING

To simplify and speed-up the calculations a geodetic network is set up around the pavilion. This network includes five points in a local coordinate system, shown in **Fig. 2**, and was measured with a tachymeter Leica TS30. The network was measured in each epoch to ensure that there are no movements in the network. In Addition to the five points around the pavilion same unmarked points inside the pavilion were measured.

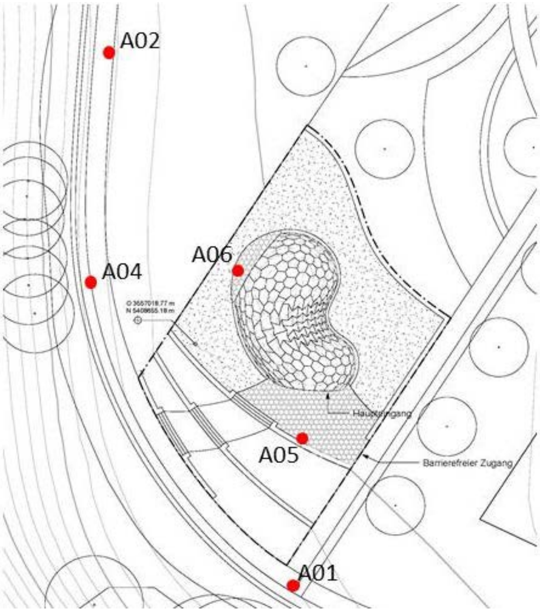

Figure 2: Location of reference points

With the freeware JAG3D the adjustment of the network and deformation analysis was realized. JAG3D uses the Gauß-Markov-Model for the adjustment; free adjustments are programmed with inner constraint solution (Lösler, 2014). Observations are directions, distances and vertical angles, as well as heights of the reflectors. The approximated coordinates are calculated by polar survey. The supposed accuracy for the measurements are 3 mgon for directions, 6 mgon for vertical angels and 1mm+1 ppm for distances. The mean accuracies of the coordinates for all epochs are shown in **Table 1**.

Table 2: Accuracy of coordinates for all epochs

	$s_x[m]$	$s_y[m]$	$s_z[m]$	$s_{3D}[m]$
Epoch 1	0.0004	0.0003	0.0003	0.0006
Epoch 2	0.0054	0.0043	0.0032	0.0076
Epoch 3	0.0007	0.0006	0.0003	0.0010

The results from epoch 1 and epoch 3 are useable for the georeferencing of the point clouds. The deformation analysis, which is realized with JAG3D (Lösler, 2014), is based on the implicite hypothesis. Before starting the deformation analysis the networks of both epochs were adjusted to detect measurement errors and to develop the stochastic model. For the congruency analysis, a common adjustment for both epochs is calculated. First the reference points were checked for invariance before checking the object points. For this check, the deformation vectors d_k between the two epochs were calculated and tested for significance. The variance-covariance-matrix Q_{ddk} is calculated, too (Lösler, 2014). The following tests were made:

$$T_{prio,k} = \frac{d_k^T Q_{\bar{d}\bar{d}k}^{-1} d_k}{m\sigma_0^2} \sim F_{m,\infty} \tag{1}$$

$$T_{post,k} = \frac{d_k^T Q_{\bar{d}\bar{d}k}^{-1} d_k}{m\hat{\sigma}_0^2} \sim F_{m,f-m} \tag{2}$$

with m for the number of degrees of freedom of the coordinates, σ_0^2 the a priori variance factor and $\hat{\sigma}_0^2$ the a posteriori variance factor. $F_{m,\infty}$ or $F_{m,f-m}$ are the quantiles of Fisher-distribution (Lösler, 2014). This method is described in detail in (Jäger, et al., 2005).

The analysis between these two epochs shows there are no movements in the network. The adjustment results of epoch 2 are less accurate compared to the results of epoch 1 and epoch 3. The reason for that is that the ATR-mode was used. This mode to find the target automatically what is helpful for long distance measurements, but not for short distances like in this project. The mode falsifies the measurements for the vertical angle. In the second epoch this mode is misleadingly used and the results for the epoch 2 are difficult to compare.

3 SCANNING AND MODELING THE PAVILION

After measuring the geodetic network the pavilion is scanned with the laser scanner HDS7000 from Leica Geosystems. During the first and the second epoch an exhibition was implemented, for that reason it was necessary to scan the pavilion from six positions. In the third epoch three positions were adequate, because the exhibition was finished and disappeared. For registration and georeferencing targets were used.

The registration and georeferencing was carried through using Leica Cyclone. The registration was realized classically, which means first a rough registration was made, followed by a fine registration. For the first epoch the mean error for registration is 2 mm, for the second epoch it is 3 mm. In the third epoch the mean registration error is 6 mm. For georefencing the mean error in the first epoch is 2 mm and for the third epoch it is 7 mm.

After registration and georeferencing, the point clouds were bowdlerized. However, all points which are not representing the pavilion were deleted. In **Fig. 3** the origin and cleaned point clouds are shown. For the deformation analysis the floor of the pavilion is deleted, since it is oscillating in case of kinematic louds e.g. by pedestrians.

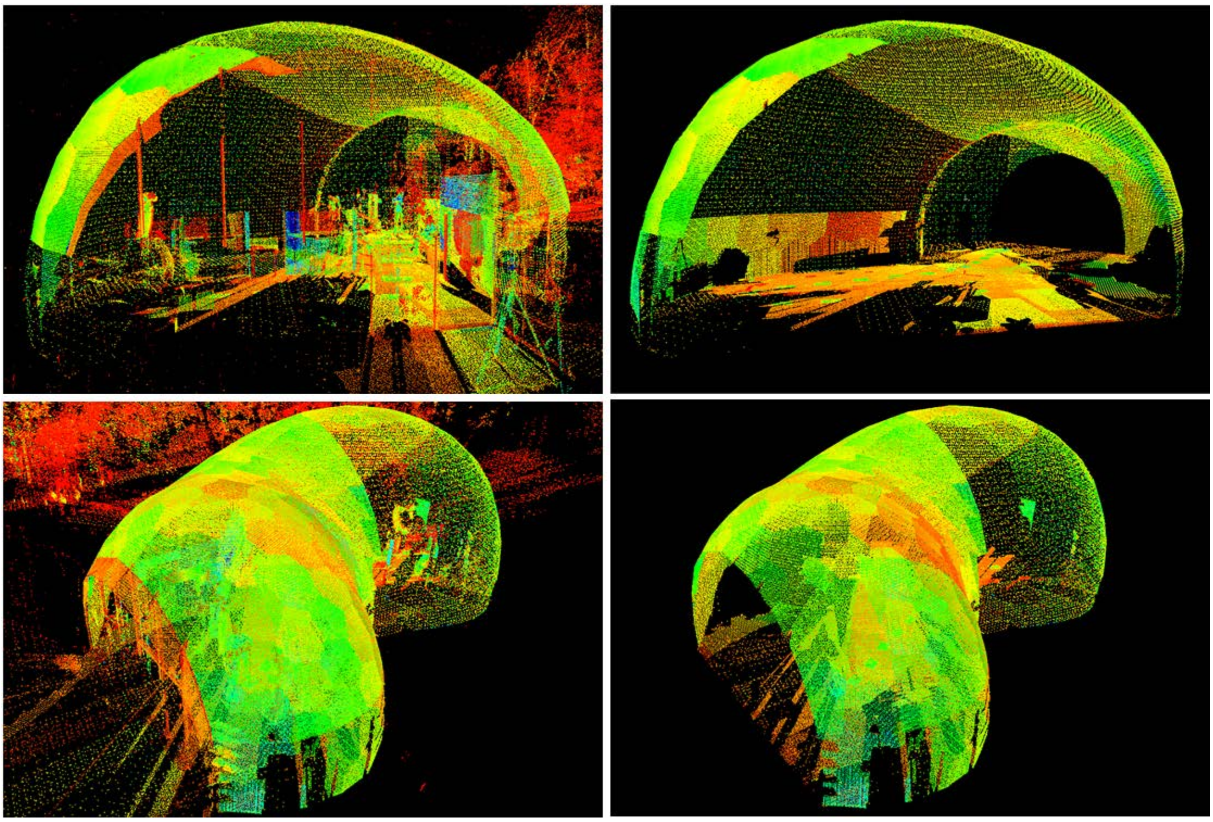

Figure 3 Left: registrated point cloud; Right: cleared point cloud (Wilhelm, 2014)

For the deformation analysis the point clouds were modelled. In this case, a triangulation irregular network (TIN) is calculated with Geomagic Studio 2012. The advantage is the in a TIN outliers could be detected and eliminated. Small holes could be closed. With the cleaned TINs the deformation analysis could be done using Geomagic Qualify 2012.

4 DEFORMATION ANALYSIS

For the deformation analysis the first epoch is the reference model. For both models, the reference model and the test model, the normal vectors were calculated and compared. The normal vectors are always showing apart from the scanners. However, positive deformations are shrinkage and negative deformations are expansion (Wilhelm, 2014).

The significance test to calculate the threshold value is made according (Welsch, et al., 2000). The test value is:

$$T = \frac{|\Delta x|}{\sigma_{\Delta x}}, \tag{3}$$

with $\sigma_{\Delta x}$ the standard deviation of the detected deviation, which is calculated as followed, unless there is no correlation between the epochs:

$$\sigma_{\Delta x} = \sqrt{\sigma_{xE_1}^2 + \sigma_{xE_2}^2}, \tag{4}$$

σ_{xE_i} is the standard deviation of the indicated epochs. They are given by the law of error propagation:

$$\sigma_{x\mathrm{E_i}} = \sqrt{\sigma_R^2 + \sigma_L^2} \tag{5}$$

with σ_R as standard deviation of registration, which is 3 mm for the comparison of the first and second epoch and 6 mm for comparison between the first and the third epoch. σ_L is the standard deviation of single point determination of the laserscans with 1 mm (Wilhelm, 2014).

By means of $\sigma_{\Delta x}$ a threshold value can be calculated, which signal significant deviations between both epochs. The test value T is Gaussian distributed and the confidence probability is 95%. This leads to a quantile of $y_{1-\alpha/2} = 1{,}96$. However the threshold is set to (Wilhelm, 2014):

$$|\Delta x| \geq y_{1-\frac{\alpha}{2}} \cdot \sigma_{\Delta x} \tag{6}$$

4.1 Comparison Approaches

The orientation of the TINs to each other is made in three different approaches, because the results of the tachymeter network in the second epoch can't be used.

The comparison between the first two epochs is made in two approaches. One of these approaches is the best-fit-approach. The orientation is made by ICP, where the distances between the two TINs are minimized. The second approach is a local approach. In this case a coordinate system is manually defined in both TINs.

In the case of the comparison between the first and the third epochs, the tachymeter network fot georeferencing is used. Both TINs are in the same coordinate system, so no transformation necessary and the TINs could be compared directly.

4.2 Deformation analysis between Epoch 1 and Epoch 2

Within a master's thesis at the Institute of Engineering Geodesy the deformation analysis between the first and second epoch is made. The results are summarized in the following. The threshold value is:

$$|\Delta x| \geq y_{1-\frac{\alpha}{2}} \cdot \sigma_{\Delta x} = 8{,}8\,mm \tag{7}$$

For the best-fit-approach, 99.6% of the deviations are in a range between -2 mm and +2 mm. In the local approach are 98.6% of the deviations lie in a range between -2 mm and +2 mm. In both approaches 99.999% of the deviations are not significant. The significant deviations are in the lower area of the pavilion, were a lot of shadings influence the results.

The difference of the potential deformations in both approaches could be ensured by the manual definition of the coordinate systems for the local approach, because the distribution apparently contains an offset and a rotation. However, the result of best-fit-approach was to be considered with caution because the distances between the two TINs will be minimized within the best-fit-approach. In Fig. 1 and Fig. 2 the results of the two approaches are shown.

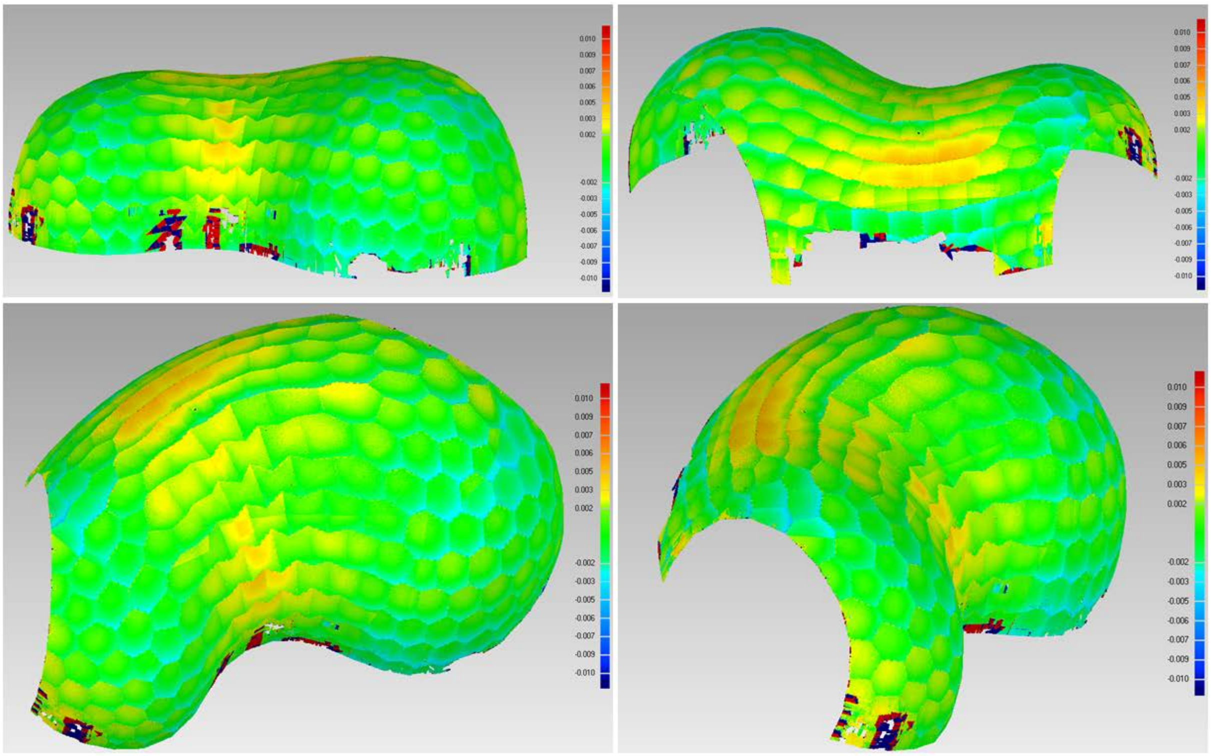

Figure 4: Overview of the results from best-fit-approach, epoch 2-epoch 1 – Geomagic 2012 (Wilhelm, 2014)

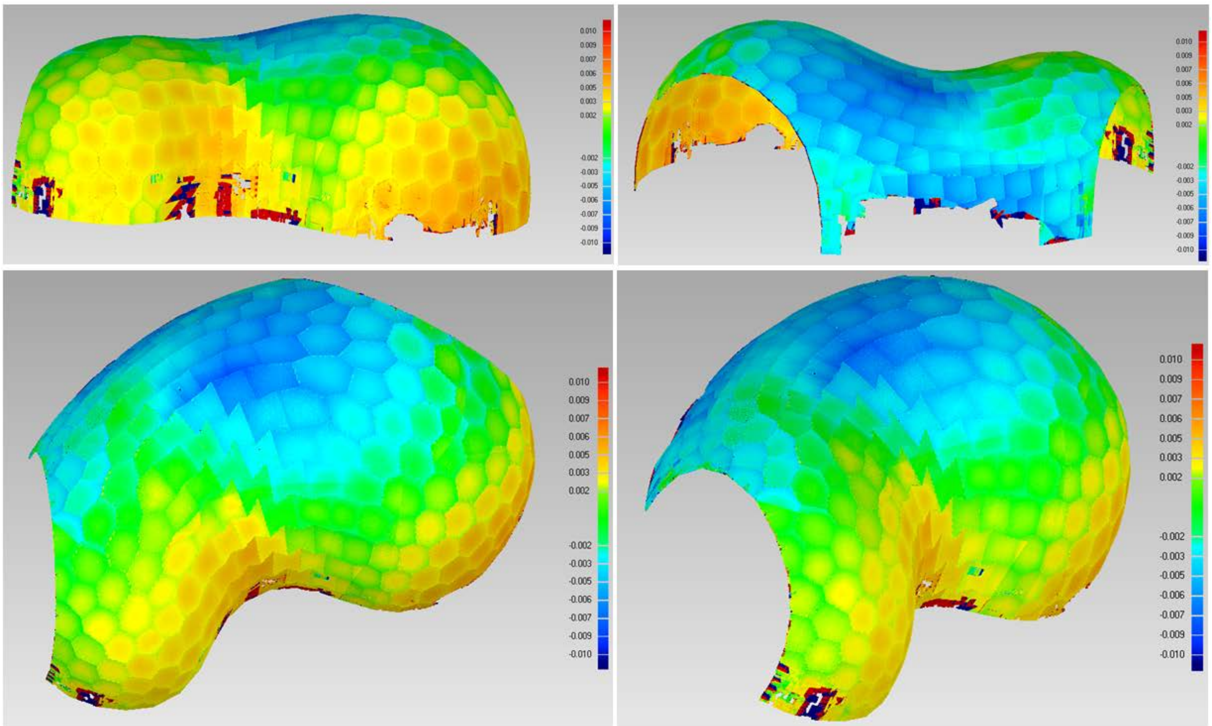

Figure 5: Overview of the results from local approach, epoch 2-epoch 1 – Geomagic 2012 (Wilhelm, 2014)

4.3 Deformation analysis between epoch 1 and epoch 2

The first and third epoch will be compared directly using the georeferencing which was realized by tachmeter network. In this case the standard deviation between both epochs is $\sigma_{\Delta x} = 6{,}9\,mm$. However, the threshold value is calculated by using the following equation:

$$|\Delta x| \geq y_{1-\frac{\alpha}{2}} \cdot \sigma_{\Delta x} = 13{,}4\,mm \tag{8}$$

The comparison shows that 99.6% of the deviations are in the range between -2 mm and 2 mm. The deviations are shown in Fig 6.

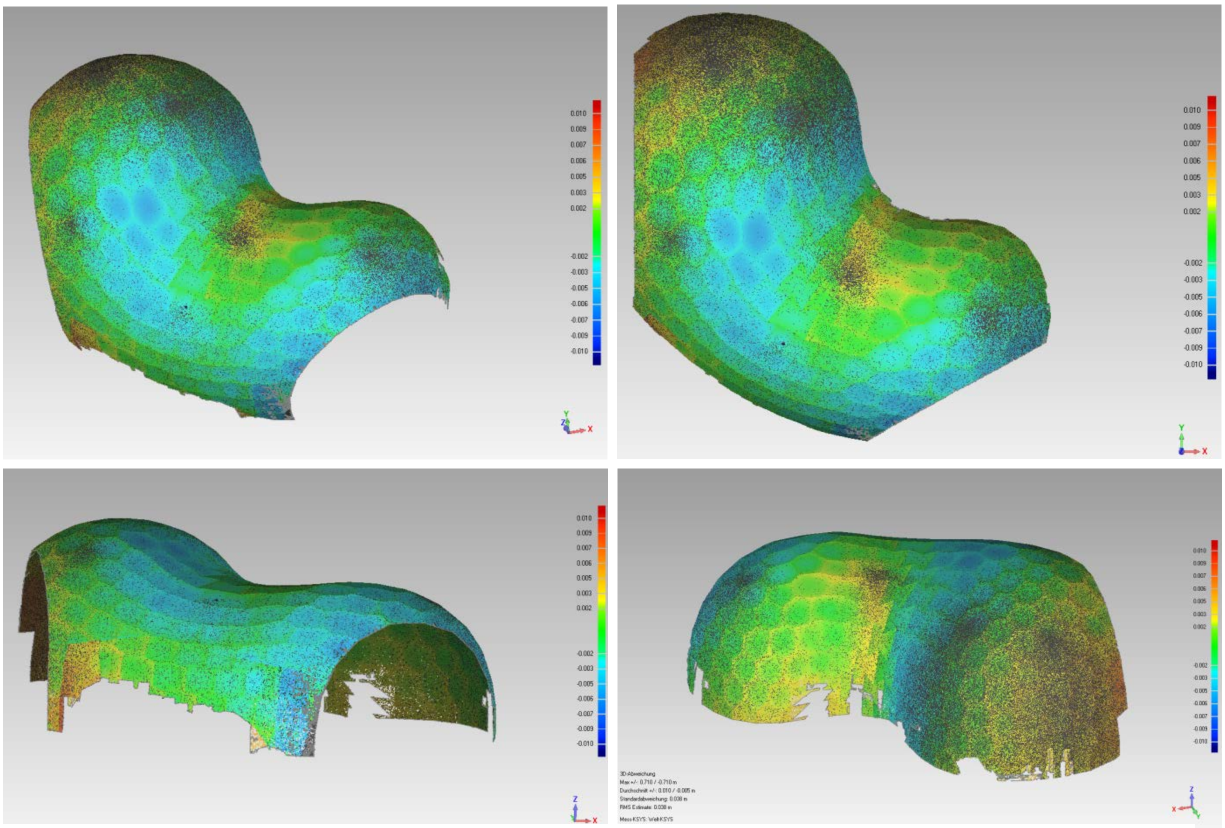

Figure 6 Overview of the results, epoch 3-epoch 1 - Geomagic 2012

5 RESULTS, CONCLUSION AND OUTLOOK

The first and the third measurements epochs of tachymeter network deliver exact results, which can be used for georeferencing. There is no significant deformation between these two epochs in the tachymeter network. Due to the use of the ATR-mode in the second epoch, the results of the network are difficult to compare. However, the deformation analysis of the TINs is realized with the best-fit-approach and the local approach.
The deformation analysis between the first and the second epoch shows for both approaches no significant deformations. The alleged deformations, which are shown, are in the borders of the TINs, where a lot of shadings influence the results. Between the first and third epochs no significant deformations occur too. But there are tendencies like a expansion in front area of the pavilion.
In all three epochs no significant deformations occur. In the middle part of the pavilion tendencies are divined in all three TINs, they could point to deformations. But the period, for deformation analysis was short, lasting five months only. Further monitoring could be interesting, because wood is always deforming under the influence of temperature and humidity. It would be interesting, too, to investigate the pavilion with snow load.
In the future one has to investigate, how the single plates of the pavilion behave over time, because the deformation of the single plates vary between the borders of the plates and the middle of the plates. The

question is, if the meshes between the different plates are the reason for the phenomenon or it is the result of the dishing of the plates.
Additionally a measurement mode or configuration should be developed to improve the georeferencing, because the mean error of registration from 7 mm in the third epoch has a big influence on the significance tests.

ACKNOWLEDGEMENTS

The author would like to thank her project partners Oliver Krieg, Tobias Schwinn and Achim Menges from the Institute of Computational Design, Jian-Min Li and Jan Knippers from the Institute of Building Structures and Structural Design as well as Müllerblaustein Holzbau GmbH, Landesgartenschau Schwäbisch Gmünd 2014 GmbH, KUKA Roboter GmbH and Forst BW. Furthermore, these investigations are funded by EFRE European Union and Cluster Forst und Holz, Baden-Württemberg. The author would like to thank Johannes Wilhelm for the investigation and analysis of the first and second epochs.

REFERENCES

Books:

JÄGER, R., MÜLLER, T., SALER, H., SCHWÄBLE, R. (2005). *Klassische und robuste Ausgleichungsverfahren.* Heidelberg: Herbert Wichmann Verlag.

WELSCH, W., HEUNECKE, O. & KUHLMANN, H., 2000. *Handbuch der Ingenieurgeodäsie – Auswertung geodätischer Überwachungsmessungen.* Heidelberg: Herbert Wichmann.

WILHELM, J. (2014). *Deformationsanalyse eines Holzpavillons.* Masterarbeit, IIGS - University Stuttgart, Stuttgart, unpublished.

Journal articles:

KRIEG, O., SCHWINN, T., MENGES, A., LI, J.-M., KNIPPERS, J., SCHMITT, A., SCHWIEGER,V. (2014). Biomimetic Lightweight Timber Shells: Computational Integration of Robotic Fabrication, Architectural Geometry and Structural Design. In P. Block, J. Knippers, N. Mitra, W. Wang (Hrsg.), *Advances in Architectural Geometry 2014.* London: Springer.

Links:

ICD (2014). *Landesgartenschau Exbition Hall.* Abgerufen am 18. February 2015 von http://icd.uni-stuttgart.de/?p=11173

ICD (2014). *Robotic Fabrication in Timber Construction.* Abgerufen am 18. February 2015 von http://icd.uni-stuttgart.de/?p=10046

LÖSLER, M. (2014). *Freie Netzausgleichungssoftware Java Graticule 3D.* Abgerufen am 11. 12 2014 von http://derletztekick.com/software/netzausgleichung

Deformation Analysis of Cable-Stayed Bridges Using Neural Networks

Boris Mazurov[1], Fawzi Zarzou[2], Samira Ahmed[3]
[1]Siberian State University of Geosystems and Technologies, Russian Federation
[2, 3]Mansoura University, Egypt

Abstract

Bridge safety will become a serious problem faced by bridge authorities. Cable-stayed bridges are important and widely used elements of regional and urban infrastructure for traffic and transportation. One of the system elements for providing their safety is geodetic monitoring using GNSS technologies. The displacements of bridges points depend not only on time but also on the impact of traffic capacity, wind temperature and humidity on the natural- technical system of suspension bridge should be taken into consideration. This makes the task of constructing a predictive model difficult. The most significant are the temperature change, the velocity of wind and vehicle movement loads. Here is given some analysis of these effects on the dynamics of cable-stayed bridge on real experimental data. Two analytical methods are Neutral Networks (NN) and Least-Squares Method (LS method). They were used for the adjustment of these data. The results obtained by the neural networks were much better than those obtained by the least-squares method.

Keywords:
Cable-stayed bridges, GNSS, neutral networks, least-squares method

1 INTRODUCTION

Bridges are important transport junctions and play an important role in the socio-economic development of municipalities and regions. In addition of cable-stayed bridges have multiple design options. Speed of cable-stayed bridge construction and their efficiency compared to conventional bridges on pillars are still accompanied by their limited use. For example, the railway traffic is impossible, etc. The position of typical bridge structural elements is significantly affected by traffic load, temperature and wind. It is evident that there is a problem of cable-stayed bridge security in their maintaining under conditions of a wide variety of external and climatic influences. When monitoring natural-technical systems by geodetic methods a systematic approach to the mathematical treatment of observations and determination of adequate predictive models is required. When GNSS technologies are used in monitoring, precision parameters of coordinate determination and high temporal frequency of their getting have to be considered. The following correct mathematical treatment should bind to include the definition (selection) of approximating models.
The Global Navigation Satellite System (GNSS) has been utilized for more than two decades in the deformation monitoring of a variety of structures, such as dams, building, bridges, slopes, etc., around the world [3, 4]. With the technological advent of GPS positioning, telecommunications and signal processing as well as public awareness, GPS has been widely tested in recent years for monitoring structures such as large suspension bridges and high-rise buildings and gradually becomes an alternative tool for structural health monitoring (SHM). GPS-based bridge monitoring has many appealing advantages over traditional bridge monitoring sensor systems. For instance, GPS monitoring could be carried out in a real-time and automatic manner for the provision of timely geometric displacements under different weather condition. The focus of this research is the comparison between the NN and LS method in GPS data processing to determine the deformations of cable-stayed bridge at its time of happening.

2 BRIDGE DESCRIPTION

Cable-stayed bridges are a type of bridges in which the deck is hung below suspension cables on vertical suspenders. Cables suspended between towers, plus vertical suspender cables that carry the weight of the deck below, upon which traffic crosses. The suspension cables must be anchored at each end of the bridge, since any load applied to the bridge is transformed into a tension in these main cables. The main cables continue beyond the pillars to deck-level supports and further continue to connections with anchors in the ground. The roadway is supported by vertical suspender cables or rods, called hangers.

Important practical consequences are reasonably optimization design of bridges and tracks and their safe state during operation. The current study is to clarify the mathematical models, which will provide real-time kinematic data processing (RTK)-GPS for structural monitoring and predicting will ensure obtaining displacements and deformations in time. Note that the structural properties of engineering structures, which include in particular cable-stayed bridge is determined largely a description of predicting the movements of structures and taking into consideration the effect of external influences on the natural and technical systems. For cable-stayed bridges, basically, is the effect of wind and vehicle movement.

3 MATHEMATICAL MODELS

There are several mathematical algorithms of the experimental data with a choice of approximating models. In the first place is the least-squares method (LS method) with possible modifications. We used the classical method of least-squares algorithm. For example, if the reference was a power polynomial function, the coefficients of the matrix obtained

$$A = \begin{bmatrix} (t_1 - t_0)^n & (t_1 - t_0)^{n-1} & \cdots & 1 \\ \vdots & \vdots & \ddots & \vdots \\ \vdots & \vdots & \ddots & 1 \\ (t_i - t_0)^n & (t_i - t_0)^{n-1} & \cdots & 1 \end{bmatrix}$$

Where: t_0, t_1 and t_i - time of observations and n - degree of the polynomial.

Using the same estimation of the parameters with Kalman filter, which is a device to determine the adequate predictive model of several models of applicants of different structures (Fig. 1).

The main objective of this study was to compare the creation of predictive models of the dynamics of cable-stayed bridges according to the GNSS monitoring obtained by LS method using the power polynomials, cubic splines and also using neural networks ANN (Neural Network). An Artificial Neural Network (ANN) is an information processing paradigm that is inspired by the way biological nervous systems, such as the brain, process information. (Fig. 2, 3).

The behaviour of NN depends on both the weights and the input-output function. This function typically falls into one of three categories: linear, threshold and sigmoid. Sigmoid units bear a greater resemblance to real neurons more than linear or threshold units, but all three categories must be considered rough approximations.

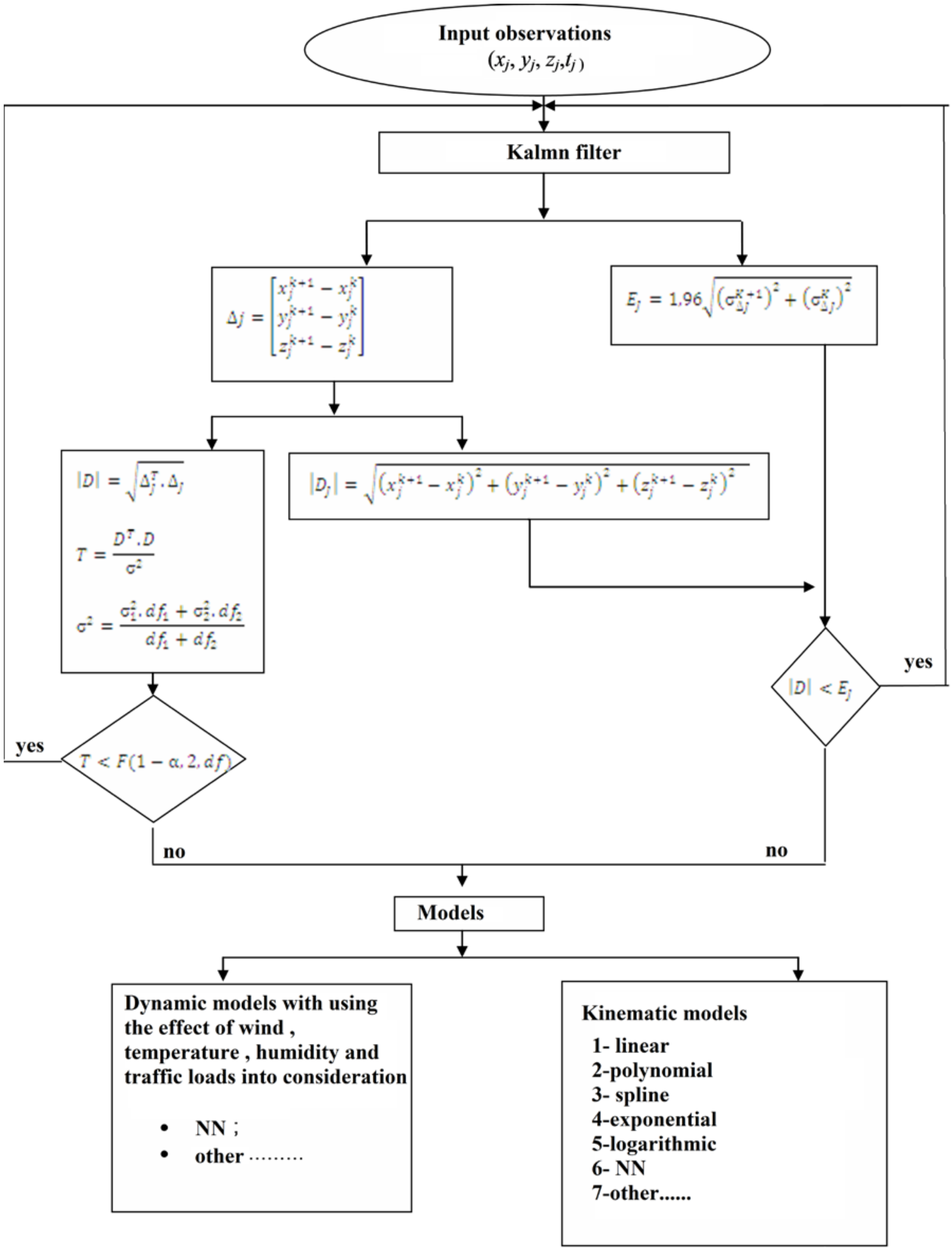

Figure 1: Prediction algorithm

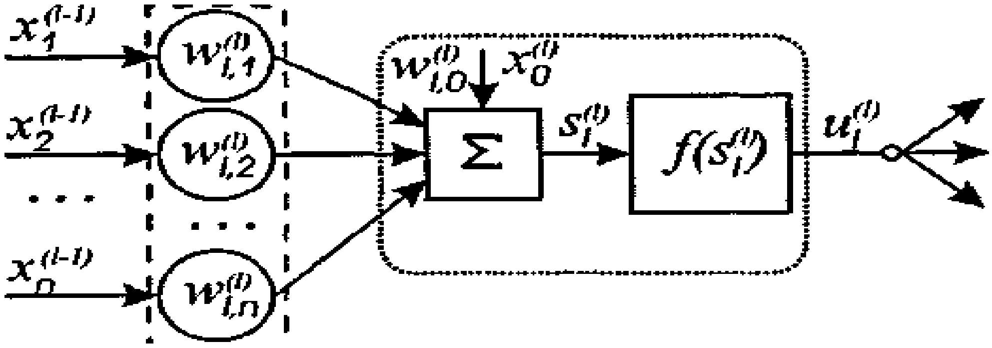

Figure 2: Neural network

The ability of the neural network to predict directly result is depends on its ability to compile and release hidden dependencies between the input and output data. After training, the network is able to predict the future value of a certain sequence based on several previous values and (or) any currently existing factors. It should be noted that the prediction is possible only if the previous changes to some extent determine the future. In practice, for training the neural network the most commonly used is receptors rule, which is the following simple algorithm.

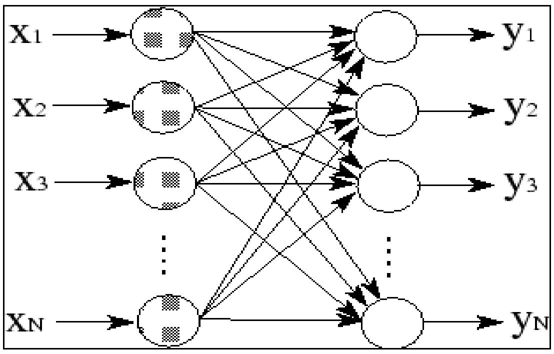

Single-Layer Network

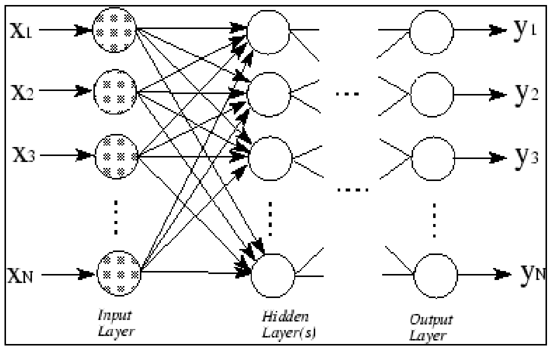

Multilayer Network

Figure 3: Classification of artificial neural networks

The above approximation properties and great practical confirmation of the effectiveness of ANN prompted to compare this model with models based on the degree of polynomials and splines. However, some conclusions about the comparative qualities of approximation of these models may be obtained on real data GNSS monitoring.

4 OBSERVATIONS METHODOLOGY AND DATA ANALYSIS

The bridge under study is a road bridge, which crosses the new Yongding River, located in the eastern of Tianjin in China. Its total length is 512.4m, adopting the prestressed concrete cable-stayed bridge with double pylons, whose main span is 260m. The entire width of the bridge deck is 13.6m, including lane road of 9m and the pavement on both sides of the bridge. The GPS observations are real time kinematic (RTK) with differential GPS (DGPS) system. The receivers are LEICA GMX902 antenna (24 channel L1/L2 code and phase, 20 Hz data rate two-rover observation stations were considered along the bridge in two tower of bridge, every rover station is observed for 24 hr, the number of data collection are 72000/hr, and each epoch is corrected with the base station.
Several options were considered modelling the displacement of bridge pylons derived from GNSS observations. Further, the estimate of approximating models for power polynomials choice was made to minimize the sum of squared deviations of the predicted values of displacement from the real displacements. Model building (training) was carried out from five temporary sites and received predictive models from subsequent sixth and seventh temporary site (Fig. 4, 5).

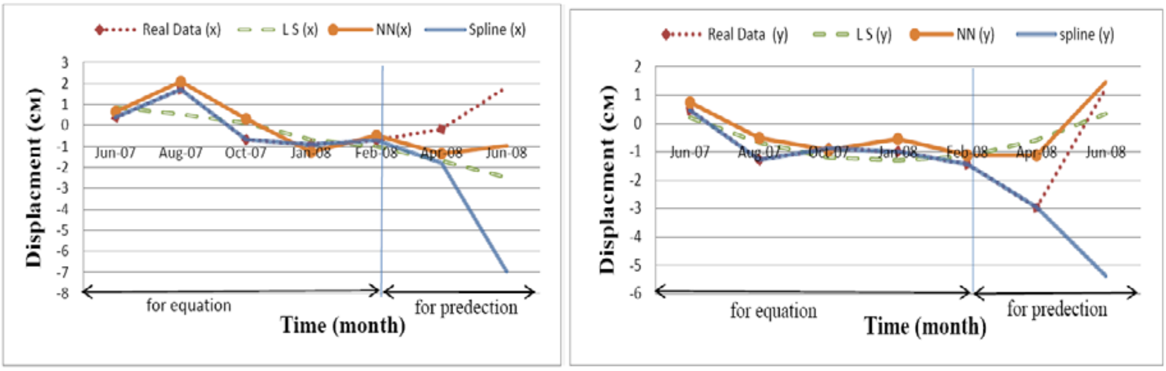

Figure 4: Displacements x and y for the pylon №1

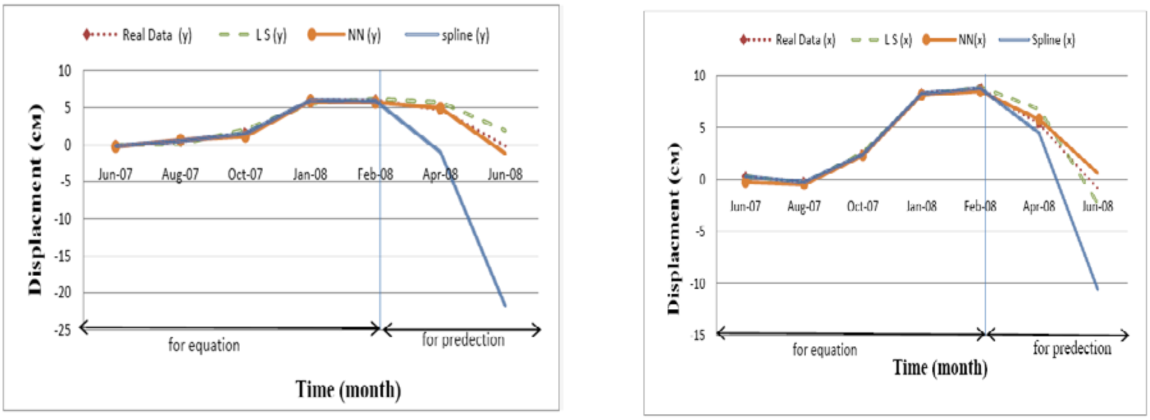

Figure 5: Displacements x and y for the pylon №2

The most matching description of kinematics bridge pylons have been installed by power polynomials of 3rd degree for the displacements x and y pylon №1 and by power polynomials of 2nd degree for the displacements x and y pylon №2.

From the same data were obtained an approximation model based on cubic splines. However, it was found that the differences between observation and prediction values were high. This confirms that the reliability of the predict displacements depends not only on time but also on the traffic load and wind.

Sufficiently conclusive results for the purposes of predicting displacements suspension bridge in the conditions of exposure to external forces were obtained with the use of neural networks. Differences between actual and predicted values of displacement did not exceed 3 cm. Clearly shows the results of comparison of forecast quality degree polynomials, cubic splines and neural networks (Fig. 4, 5).

It is noted that the increase in the frequency of the input data, respectively, increases the accuracy of the prediction estimates.

5 CONCLUSIONS

Important information about the dynamics movements of suspension bridge can be obtained by analyzing several alternative mathematical models of varying degrees of complexity and the selection of the support functions. This may be the degree polynomials, splines. In some cases, monitoring GNSS using DGPS - RTK is possible to obtain more accurate information about the dynamics displacement of structural elements and prediction using neural network technology. An important advantage is the possibility of implicit account not only time, but also the traffic load, wind, etc. An algorithm is choice of predictive models in the programming system MATLAB. Empirically derived mathematical equations of the displacements of bridges using into consideration weather factors (wind, temperature, humidity).

REFERENCES

Books:

HAYKIN, S. *Kalman filtering and neural networks,* Communication Research Laboratory, McMaster University, Hamilton, Ontario, Canada. (2001).

MARTIN H., *Matlab Recipes for Earth Sciences,* second ed., Springer, Berlin Heidelberg, New York, 2007.

KAPLAN, D. AND HEGARTY, J. *Understanding GPS Principles and Applications,* Second Edition, Artech House, Inc., UK. (2006).

MENG, X. *Real-time deformation monitoring of bridges using GPS/Accelerometers,* PhD Thesis, Institute of Engineering Surveying and Space Geodesy, the Nottingham University, UK. (2002).

USACE (2002b). *Structural Deformation Surveying* (EM 1110-2-1009). US Army Corps of Engineers, Washington, DC. 2002.

Journal articles:

ACAR, M., ÖZLÜDEMIR, M.T., AKYILMAZ, O., CELIK, R.N. AND AYAN, T. *Deformation Analysis with Total Least Squares.* Natural Hazards and Earth System Sciences 6(4), p. 663-669. (2006).

AZAR, R. S. , SHAFRI, H. Z. *"Mass structure deformation monitoring using low cost differential global positioning system device."* J. Applied Sciences, ASCE, Vol. 6, No.1, pp. 152-156. (2009).

CANKUT, D. I., MUHAMMED, S. *Real-Time Deformation Monitoring with GPS and Kalman Filter.* Earth Planets Space. Vol. 52(No. 10), p. 837-840. (2000).

EICHHORN, A. *Tasks and Newest Trends in Geodetic Deformation Analysis*: A Tutorial. Institute for Geodesy and Geophysics, Department of Engineering Geodesy. Vienna, Austria: Vienna University of Technology. Pp. 1156-1160 (2007).

EROL, S., EROL, B., AYAN, T., A *General Review of the Deformation Monitoring Techniques and a Case Study:* Analyzing Deformations Using GPS/Levelling. Civil Engineering Faculty, Geodesy Division. International Society for Photogrammetry and Remote Sensing. Commission VII, WG VII/5. Istanbul, Turkey: Istanbul Technical University. 2004

KALOOP M.R., LI H., *Monitoring of bridges deformation using GPS technique,* KSCE J. Civil. Eng. (KSCE), p. 423–431 (2009).

YU, M., GUO, H., AND ZOU, C. *"Application of wavelet analysis to GPS deformation monitoring."* Proc. of IEEE/ION PLANS 2006, San Diego, California, pp. 670-676. (2006).

ZARZOURA, F., EHIGIATOR R., MAZUROV, B. *Investigating Accuracy Enhancement of Global Navigation Satellite System.* British Journal of Earth Sciences Research, Vol.1, No.1, p.1-9. December 2013.

ZARZOURA, F., EHIGIATOR R., MAZUROV, B. *Utilizing of Mathematical Frame Work in Bridge Deformation Monitoring,* Asian Journal of Engineering and Technology (ISSN: 2321 – 2462) Volume 02 – Issue 04, p. 293-300. August 2014.

Positioned Displacements of Engineering Constructions and Natural Objects Obtained from Geodetic Monitoring

Igor G. Vovk
Siberian State University of Geosystems and Technologies, Russian Federation

Abstract
The position of monitored object points is determined by geodetic monitoring data. The data comprise those on the object displacement, its shape and size. The problem of determining object position from geodetic monitoring is considered.

Keywords
Position of engineering structures and natural objects

1 INTRODUCTION

Specialists in any field of activity deal with systems. Classical examples of systems are various engineering structures and natural objects. Any systems interact with the environment, i.e. other systems. The surrounding world is a system interacting with other systems [1].
Basic characteristic of any system is its spatio-temporal state (STS). The system shape, size and spatial position, considered as functions of time, characterize their STS. Changes of systems' STS show in their displacements and deformations. The system displacements are the changes of its spatial position relative to the invariable reference system, and deformations are displacements of system parts relative to each other which are accompanied by the changes in system shape and size as a whole or some of its parts [8].

Direct examination of system's STS may turn to be impossible, dangerous and expensive. Therefore, real systems are replaced by their models [10]. When studying systems' STS, each system is referred to some geometric object, which is uniquely determined by some set of scalar values and geometrical images. Spatio-temporal properties of these geometric objects are taken as models for the corresponding properties of systems under study.

2 GENERAL

For positioning of engineering structures and natural objects geodetic monitoring data are used. In process of geodetic monitoring of engineering structures and natural objects at moments t_j, $(j = 1,2, \dots, n)$ distances between initial (reference) points with known spatial position and the points to be determined M_i $(i = 1,2, \dots, m)$ are measured as well as the directions to these points relative to some reference direction. These data are used to determine the position of engineering structures or natural objects [3], [12]. It means that the initial data for estimation, analysis and prediction of engineering structures and spatio-temporal state of natural objects are the values of vector – functions $\bar{R}(t)$, measured in points M_i at moments t_j , i.e.

$$\bar{R}_{i,j} = \bar{R}_i(t_j) \tag{1}$$

It is known [2], [3] that to determine the point position in 3D one is to know either equations of three noncoplanar planes or the equations of two noncollinear straight lines, or the equation of a straight line and a plane. Therefore, to determine the position of engineering structures or natural objects by the results of monitoring (measured directions and/or distances), it is necessary to know these equations. Theoretical basis for this problem solution is considered in the courses of analytical geometry and linear algebra [4, 5]. Here we consider practical solution of these problems.

In three-dimensional space the equation of line and plane passing through fixed point Q have the following forms, respectively:

$$\bar{r}(t) = \bar{r}_Q + t \cdot \bar{u}, \tag{2}$$
$$\bar{r}(t1, t2) = \bar{r}_Q + t1 \cdot \bar{u}1 + t2 \cdot \bar{u}2. \tag{3}$$

By means of such combined linear equations we determine the spatial point position of engineering structures and natural objects.

2.1 Determination of the Equation of Plane by Measured Distances

Set up the equation of plane PP, passing through point P to be determined, orthogonal to vector $\overline{N} = \overline{r2} - \overline{r1}$, by distances *d1* and *d2*, measured from the initial points 1 and 2 (Fig. 1).

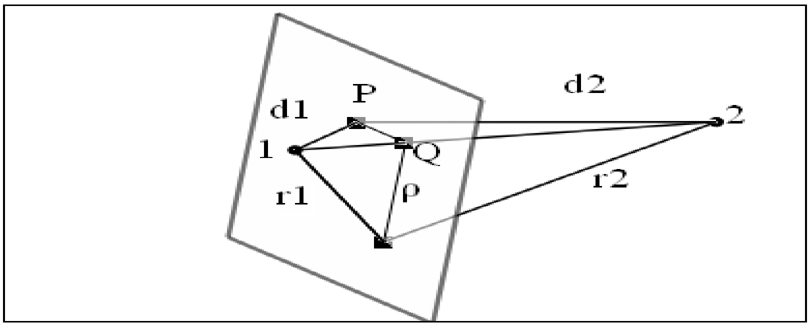

$(M11^{\langle 0 \rangle}, M11^{\langle 1 \rangle}, M11^{\langle 2 \rangle}), (M22^{\langle 0 \rangle}, M22^{\langle 1 \rangle}, M22^{\langle 2 \rangle}), (M33^{\langle 0 \rangle}, M33^{\langle 1 \rangle}, M33^{\langle 2 \rangle}), PL$

Figure 1: Determination of plane PP

The equation of the desired plane [9], [10] has the following form:

$$\overline{N}\left(\bar{r} - \bar{\rho}_Q\right) = 0, \tag{4}$$

where

$$\bar{\rho}_Q = \frac{\bar{r}_1 + \lambda \cdot \bar{r}_2}{1+\lambda}, \tag{5}$$

$$d = |\overline{r2} - \overline{r1}|\,, \tag{6}$$

$$\lambda = \frac{d^4 - (d_2^2 - d_1^2)^2}{\left(d^2 + (d_2^2 - d_1^2)\right)^2}\ . \tag{7}$$

is a scalar factor numerically equal to the ratio of the segment lengths into which point Q divides segment $\overline{r2} - \overline{r1}$. The desired point P is that of the three noncoplanar planes intersection (Fig. 2).

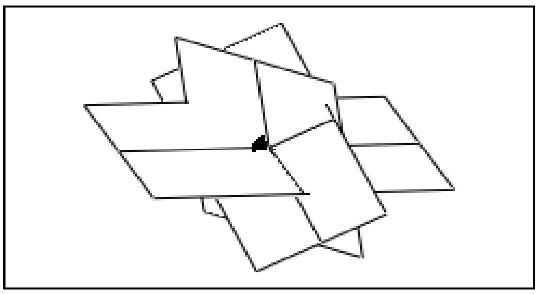

$P1, P2, P3, (FM^{\langle 0 \rangle}, FM^{\langle 1 \rangle}, FM^{\langle 2 \rangle})$

Figure 2: Determination of point position by intersecting three noncoplanar planes

Thus, coordinates of the desired point P may be determined by combined three linear equations (4) set up according to the given technique.

2.2 Formulation of the Equation of a Straight Line by the Horizontal Angle, Measured at the Initial Point, and Zenith Distance

Set up an equation of line passing through reference point B in the direction of the desired point *P* (Fig. 3). In Fig. 3, OXY plane projections are shown in lowercase letters. The given problem solution is considered in [11].

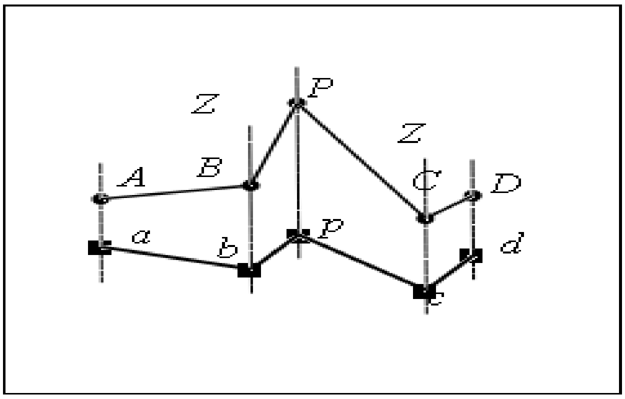

$\left(M1^{\langle 0\rangle}, M1^{\langle 1\rangle}, M1^{\langle 2\rangle}\right), \left(M0^{\langle 0\rangle}, M0^{\langle 1\rangle}, M0^{\langle 2\rangle}\right), Z1, Z2, Z3, Z4, Z5$

Figure 3: Initial situation for BP direction determination

Write $\overline{p1}$ for unit vector of direction $\overline{BP}$, $\overline{p0}$ - for projection $\overline{p1}$ on plane OXY. The known unit vector of direction *ba* in plane OXY write as $\overline{b0}$. Horizontal angle *abp* measured clockwise from direction *ba* denote by *U* and write the combined equations

$$\begin{cases} \overline{b0} \cdot \overline{p0} = \cos(U), \\ \overline{b0} \times \overline{p0} = -\overline{k} \cdot \sin(U) \end{cases} \quad (8)$$

where $\overline{k}$ – unit vector of coordinate axis OZ.

From the combined equations (8) solution we find the vector $\overline{p0}$. Taking into account that

$$\begin{cases} \overline{p1} \cdot \overline{k} = \cos(Z), \\ \overline{p1} \cdot \overline{p0} = \sin(Z) \end{cases} \quad (9)$$

we find vector $\overline{p1}$ and write the equation of line passing through point B in the direction of the desired point P.

$$\bar{r}(t) = \bar{r}_B + t \cdot \overline{p1}. \quad (10)$$

Solving the combined linear equations (10), set up for two initial points B and C, we can determine the coordinates of the desired point P (Fig. 3).

2.3 Formulation of the Equation of Line by Horizontal Angles Ω1, Ω2 and Zenith Distances Measured at the Desired Point P

The given situation arises while determining coordinates by horizontal angles Ω1, Ω2, and zenith distances measured at the desired point P (Fig.4). In this figure points *A, B, C* are initial, i.e. their coordinates are known.

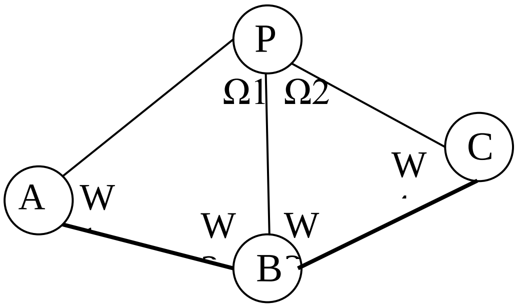

Figure 4: Geometry of the initial situation

The defined problem can be solved if angle W1 is determined by angles Ω1 and Ω2, therewith there arises the situation considered in Section 2.2.
In work [1] it is shown that values of angles w1 and w4 may be determined by combined equations

Where

$$\begin{cases} w1 + w4 - \Omega = 0 \\ ]\overline{AB}[\cdot \dfrac{\sin(w1)}{\sin(\Omega 1)} = |\overline{BC}| \cdot \dfrac{\sin(w4)}{\sin(\Omega 2)}, \end{cases} \tag{12}$$

$$\Omega = 2 \cdot \pi - w2 - w3 - \Omega 1 - \Omega 2. \tag{13}$$

Knowing angles W1 and W4 by analogy with equation (10), we write the equation of two lines directed at the desired point *P*. One of the lines passes through the initial (reference) point *A*, the other – through point *C*. By the combined two linear equations we can find coordinates of point *P*.

2.4 Formulation of the Equation of Plane by Measured Horizontal Angle and Zenith Distance

Vectors $\bar{p}0$ and $\bar{p}1$ (formulae 8 and 9) lie in the same orthogonal plane OXY, vector $\bar{p}1$ is directed at the desired point *P* (Fig. 3). So we can write the equation of plane, passing through initial point B and desired point *P*.

$$\bar{r}(t1, t2) = \bar{r}(B) + t1 \cdot \bar{p}0 + t2 \cdot \bar{p}1. \tag{14}$$

When determining the point position, equations of lines and planes can be used simultaneously (Fig. 4). In this regard it is sufficient to solve the set of two linear equations, with one of them being the equation of plane (3), (4), (14), the other – the equation of line (10). Such situation is shown in Fig.5.

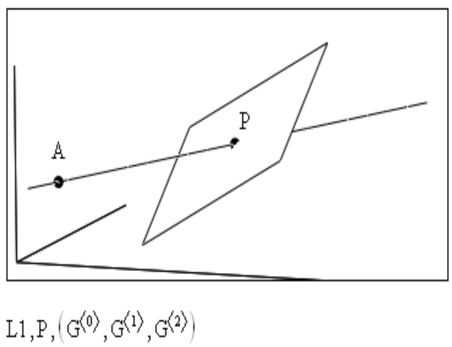

Figure 5: Point P positioning by line and plane intersection.

Thus, the task of positioning the points of engineering structures and natural objects at a fixed time reduces to the solution of combined linear equations (equations of lines and planes). The procedures of setting up such equations by measured distances and directions were considered above.

4 DETERMINATION OF RIGID BODY TRAJECTORY

In the course of time, STS of engineering structures and natural complexes changes under the impact of the environment and internal processes. These changes may be integral, inherent in all the points, and differential, inherent to certain points or some of their subsets. Integral changes of STS show in displacements of engineering structures and natural objects as a perfectly rigid body, while differential changes of STS reveal their deformations.

Taking into account the above mentioned, to determine the position of engineering structure or natural object as functions of time, it suffices to determine a trajectory of their model (perfectly rigid body). The fundamental theorem of rigid body kinematics [6] states that any motion of the body in space is a translational motion together with the pole and a turn about the axis, passing through the pole. Any point of a body may be chosen as a pole.

Here are some geometrical motion models for one of the rigid body points (Fig.6).

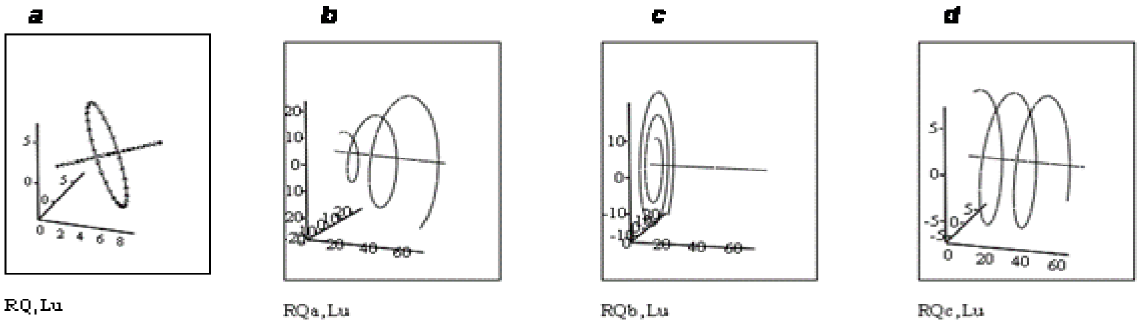

Figure 6: Rigid body trajectories

In Fig.6 four different scenarios of rigid body trajectory are presented. In all the scenarios translational and angular velocities are constant with invariable direction of translation. The rotation axis is fixed. Scenario *a* – no translational movement. The body rotates about the fixed axis; scenario *b* – the body rotates and moves translationally in the direction making up angle γ with rotation axis; scenario *c* - the body rotates and moves translationally in the direction perpendicular to the rotation axis; scenario *d* - the body rotates and moves translationally in the direction parallel to the rotation axis.

The scenarios are not confided to the given examples but in this article we restrict our consideration to these ones.

5 CONCLUSIONS

Hence, to determine the displacement of engineering structures and natural objects by geodetic monitoring data, vector functions values (1) should be calculated using algorithms (4), (10), (11). Then engineering structure or natural object is to be considered as a perfectly rigid body. Applying the known algorithms of theoretical mechanics we can define the trajectory of their spatial movement.

REFERENCES

Books:

PEREGUDOV, F.I., TARASENKO, F.P., *Fundamental of system analysis.:* Tomsk, NTL,1997.

POSTNIKOV, M.M., *Lectures on geometry. Semester II.:* Moscow, Nauka, 1979.

KORN, G., KORN, T., *Reference book on mathematics for research workers and engineers*.: Moscow, Nauka, 1976.

ILYIN, V.A., POZNYAK, V.G., *Linear algebra.:* Moscow, Main editorial board of physical and mathematical literature, 1974.

LAPTEV, G.F. Elements of vector calculus.: Moscow: Nauka, 1975.

LOYTSYANSKY, L.G., LURYE, A.I., *Course of theoretical mechanics*.: Moscow, Nauka, Vol. 1., 1982.

FOX, A., PRATT, M., *Computational geometry. Application in designing and production*.: Moscow, “Mir”, 1982.

Journal articles:

VOVK, I.G., *System analysis and modeling of time-space state of engineering systems*.Collected materials, IV International Scientific Congress “GEOSiberia 2008”, Vol.3, p. 132 – 135.

VOVK, I.G., *One more algorithm for coordinate determination by spatial linear intersection*. Vestnik SSGA, SSGA, Vol. 5, p. 137 – 139, 2000.

VOVK, I.G., *Mathematical modeling in applied geomatics*. Vestnik SSGA, Vol. 1(17), p. 94 – 103, 2012.

VOVK, I.G., *Linear geometric models and their application in applied geomatics*. Vestnik SSGA, Vol. 2(26), p. 107-116, 2014.

VOVK, I.G., *Shape modeling and size estimation of systems in applied geomatics*. Vestnik SSGA, Vol. 2(22), p. 115-124, 2013.

TECHNICAL SESSION 7: OPTICAL METHODS FOR STREET MAPPING

Street Inventory Based On Mobile Laser Scanning

Rolf Kemper-Böninghausen[1], Nico Zill[2]
[1]Emschergenossenschaft/ Lippeverband Germany, [2]technet-rail 2010 GmbH, Germany

Keywords: MLS systems, infrastructure monitoring and documentation

Abstract

The evolution of the laser scanning technology during the last decade offers a new possibility for surveying of large areas. The rapid development of the MLS technology in the last years makes it an irreplaceable part in various engineering fields such as measurements of highways, streets, railways and cities areas. The MLS techniques methods provide fast, high accurate and complete scanning of infrastructure objects (dam walls, bridges, railways, highways, street network). The data acquisition and processing are done in a continuous way which excludes the impact of operator errors. The software data processing ensures high quality, reliability, and accuracy of the adjusted measurements. The end products are base for performing of real time deformation analysis and monitoring of structure objects. The height density of the resulted point clouds in combination with algorithms for a-posteriori data adjustment prove the usage and the accuracy of the MLS systems for the needs of the engineer surveying in the area of deformation analysis and for monitoring and documenting the as-built street network. The investigation of results from various measurements proves the fully integration of MLS technology with the a-posteriori software data processing and adjustment as unprecedented method for the monitoring of any changes in the streets infrastructure objects and surface conditions.

1 INTRODUCTION

The maintenance of the streets infrastructure objects is one of the major challenges in the engineering geodesy in the last decades. In the same time a fast progress in the development and application of the Mobile Laser Scanning (MLS) in many areas of the surveying was realized. In response of the interest and tasks for the purposes of street inventory control and documentation a set of measurements with a-posteriori data adjustment were performed. The target was to be found solution and to be proved the usage of the MLS for fast and high-accurate measurement and monitoring of the street infrastructure objects.

2 STREET MONITORING WITH THE USAGE OF MOBILE LASER SCANNING

2.1 Purposes of the Measurement with MLS

The aim of the street inventory using mobile laser scanning was to identify street deformations due to tunnelling. In this process the vertical deformations on the street surface (because of the tunnelling) should be calculated.
At first a zero measurement is to be made. After that daily measurements have to be performed along the street. At the end the daily measurements are compared to the zero measurement and the resulting deformations can be calculated.
The former method with creation of vertical control points (benchmarks) outside of the street and levelling daily to these points shall be exchanged by the new and future-oriented method by using of Mobile Laser Scanning.

The following specifications have been made for the street monitoring:

Table 1: Framework for the street inventory by using of Mobile Laser Scanning

Specification	Content
Detection of significant deformations on the street / street surface	An accuracy of the result (vertical deformation) of +/- 3 mm must be reached.
Overview of the vertical deformations on the whole street surface on the basis of 3D scan data	A color-coded overview of the visualized image scan data (3D) showing the vertical deformations must be sent to the project participants.
Overview of the vertical deformations in defined areas	Creation of 2D-diagrams to visualize the vertical deformation along a reference line (for example: fast lane, lane center or side of the street)
Warning to the project participants when an exceedance of the security value of deformation occurs	If there exist more than 15 mm of a vertical deformation alert is given. A blocking of the street is possible.

Using this procedure, the necessary technical equipment (test vehicle, sensors, scanner) was created by the project partners.

2.2 Necessary Technical Equipment for Street Monitoring by Using of MLS

For the realization of the mobile laser scanning different components are required. In addition to the necessary scanner (in the example the ZF 5006 Zoller & Fröhlich) also sensors (2 IMU's, tilt sensor, position sensor, data collector for sensors) were used. Also the GNSS for absolute positioning (antenna and receiver) was necessary in the measurement system.

Figure 1: Used scanner ZF 5006 (© ZOLLER UND FRÖHLICH)

The necessary technical equipment has to be attached on the measurement vehicle.

2.3 Planning and Realization of the Daily Measurements

In the specific example the axis of tunnelling was directly under a highway (West Germany, Ruhr area). There were defined 3 areas for the daily measurements:
Area 1 / measurement run 1: South side of the highway
Area 2 / measurement run 2: North side of the highway
Area 3 / measurement run 3: Driveway on the south side of the highway

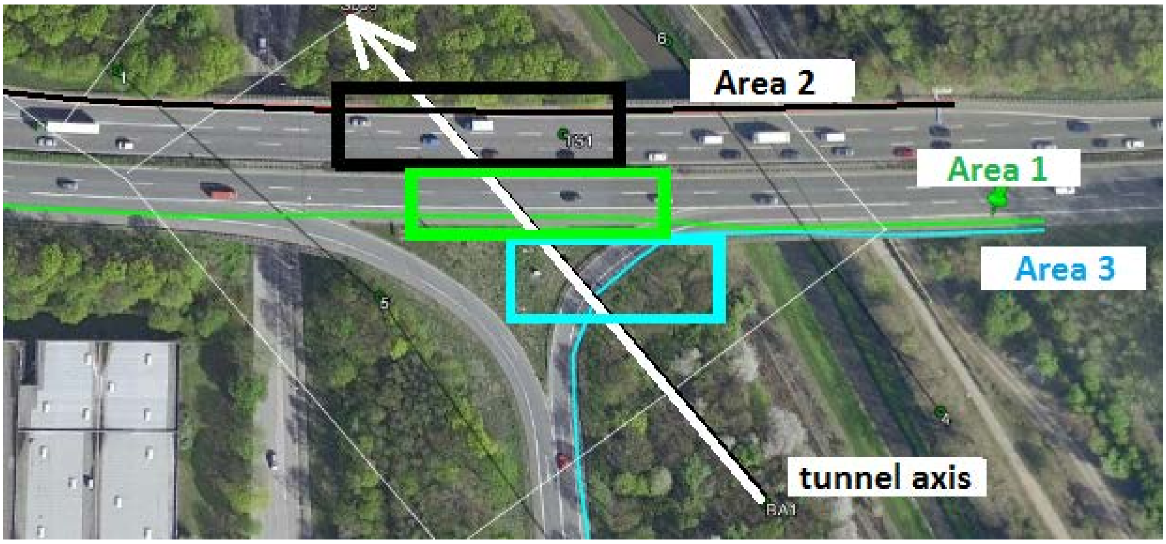

Figure 2: Overview of the areas of the measurement

The security area of the measurement amounted to +/- 30m from the tunnel axis (area of expected deformations). The measurement runs were planned so that at least an area of 100m before and behind the tunnel axis was measured. In addition to the zero measurement were performed at 8 measurement days (each day with 3 runs). The last day corresponded to a final measurement.
Below is an overview screen with the tunnel axis (direction of view of the scan data from west to east). The scan data are the result of the zero measurement:

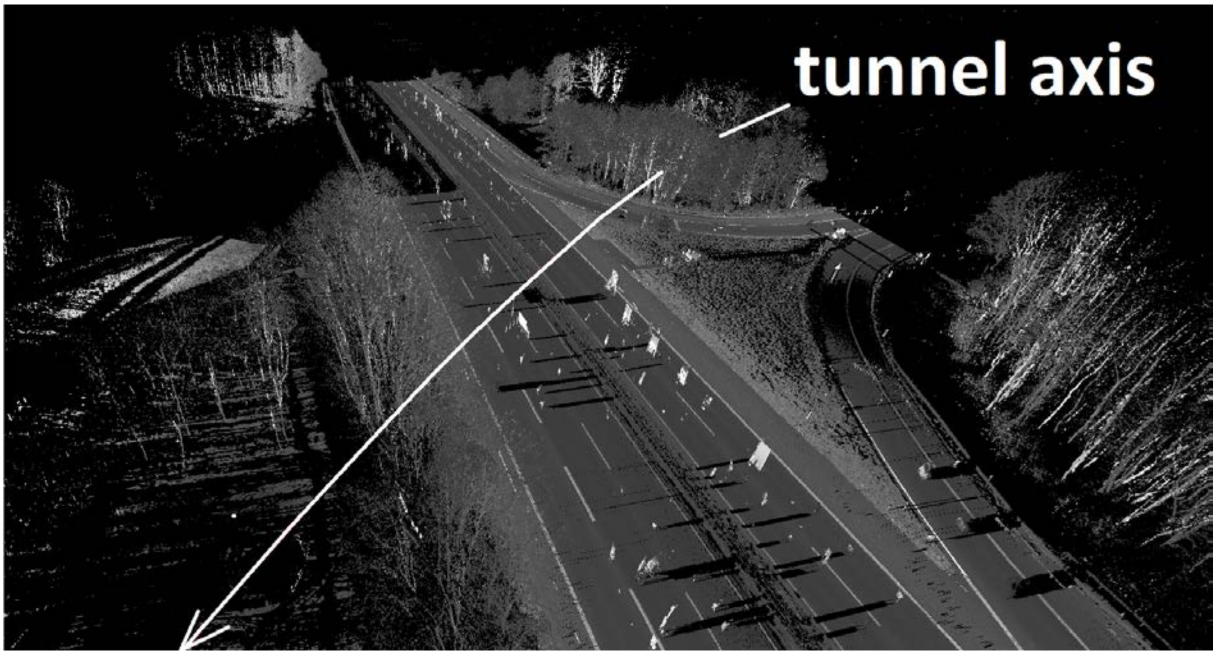

Figure 3: Overview of the scan data of the zero measurement with tunnel axis (© technet-rail 2010)

2.4 Analysis of measurement runs

The absolute positioning of the start and end point of a measurement run was determined by post-processing of GNSS data using existing SAPOS stations (reference stations in Germany)
in the vicinity of the survey area.

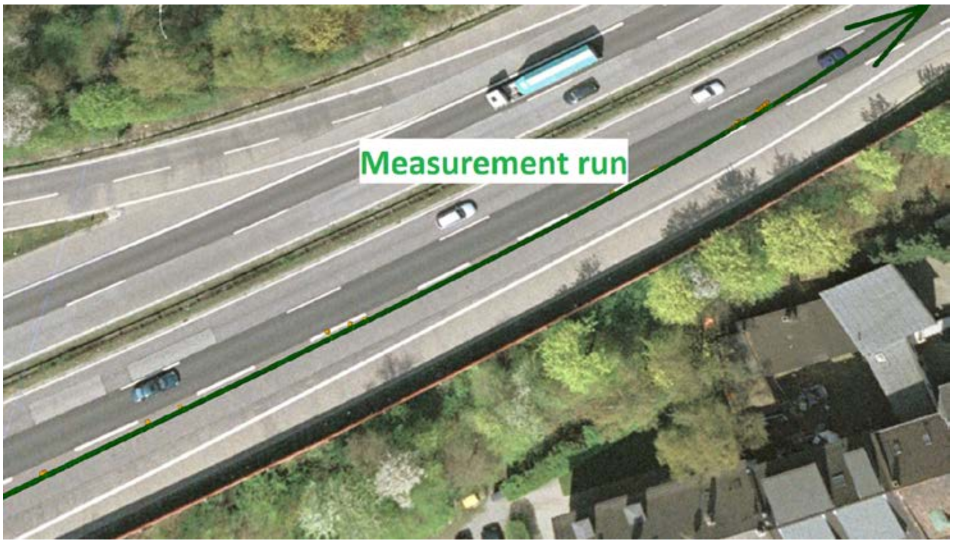

Figure 4: GNSS-Fixing of a measurement run

The GNSS fixing is used for determining the start and end point of each measurement run. The 3D-Scans are then calculated in a complex process of synchronization the sensor data (tilt sensor, position sensor, IMU's) and scan data. After the post-processing and visualization of the scan data have to be defined invariant areas in a minimum 30 meters away from the tunnel axis and outside of the expected deformation area. In the next step follows the deformation analysis process.
As program for the evaluation of the scan data is used the developed form technet-rail 2010 GmbH software solution SiRoadScan.
The scan data of the zero measurement and the scan data of the measurement runs were imported together in the software. Thereafter, the scan data of the zero measurement were compared with those of the measurement runs. Finally there was used a highly developed analysis tool to calculate and visualize the deformations.

2.5 Results of street monitoring with using of Mobile Laser Scanning

The results of the deformation analyses could be generated as a color-coded images and 2D-deformation diagrams. To create the color-coded scan images from the 3D point cloud the scan data of the measurement runs were compared with the scan data of the zero epoch / zero measurement.

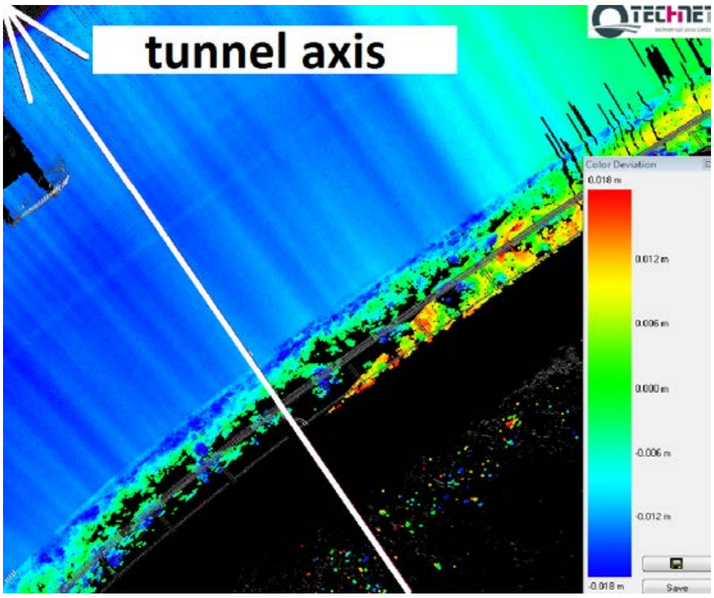

Figure 5: Deformation Analysis – color-coded scan image (© technet-rail 2010)

In addition, the vertical deformations can be also generated in 2D-diagrams. The diagrams can refer to any reference lines (for example fast lane, street way center and edge of the street).

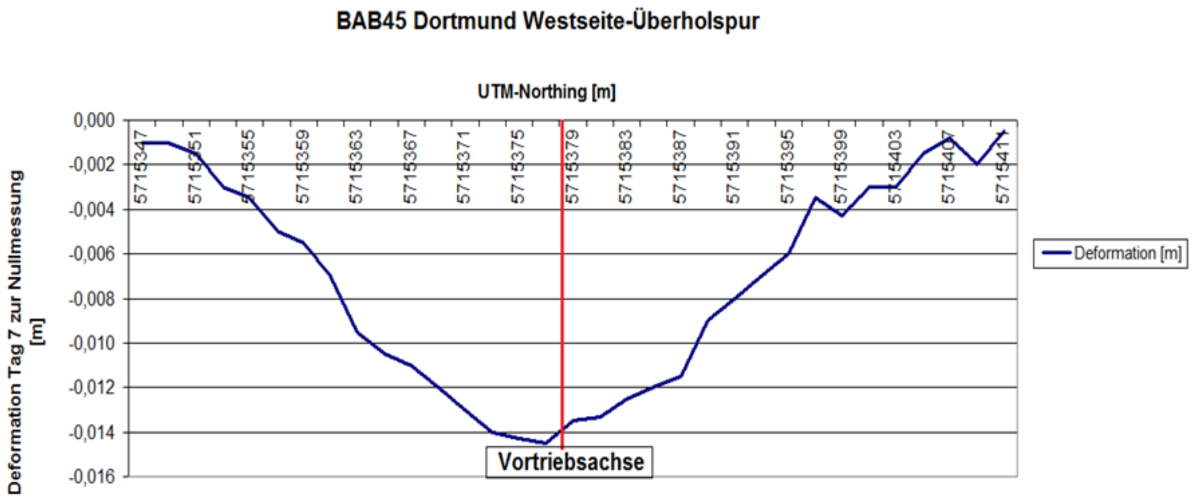

Figure 6: Deformation Analysis - 2D diagram of the fast lane (© technet-rail 2010)

The determination of the results of the deformation analysis is realized daily. Information about the actual state of the streets (and the occurred deformations) is possible.

3 HYBRID ANALYSIS OF IMAGES AND 3D SCAN DATA

The MLS method for maintenance of the street infrastructure is extended for any street inventory tasks. For example a hybrid evaluation of pictorial and 3D Street View (Scan data) is developed:

Figure 7: Hybrid analysis of pictures and 3D scan data (© technet-rail 2010)

This example shows that through the combination of time stamped georefenced images and the acquired scan data enables the detection and documentation of the street infrastructure objects and their correspondent attributes.

4 CONCLUSIONS

The maintenance and monitoring of the streets infrastructure objects is one of the major challenges in the engineering geodesy in the last decades. The combination of MLS technique ensuring fast, dense and high accurate data acquisition and the special developed software solutions proved the fully integration of this method for monitoring and documenting the as-built street network.

REFERENCES

Books:

MÖSER, MÜLLER, SCHLEMMER, WERNER, 2000, Handbuch Ingenieurgeodäsie „Grundlagen“

BEUTH UNIVERSITY OF APPLIED SCIENCE, Berlin, Germany

Journal articles:

MILEV I., STAYKOVA D., TLS for structure monitoring, 2014,*International Wokshop"Integration of Point- and Area-wise Geodetic Monitoring for Structures and Natural Objects"*, Novosibirsk, Russian Federation, pp.

Links:

Emschergenossenschaft/Lippeverband,Essen, Germany www.eglv.de

technet-rail 2010 GmbH: www.technet-rail.de

ZOLLER UND FRÖHLICH: Scannerbild, www.zf-laser.com/Z-F-IMAGER-R-5006h.3d_laserscanner1.0.html

Automated Detection for Pavement Crack for Mobile Mapping Data

Bara' AL-Mistarehi, Volker Schwieger
Institute of Engineering Geodesy, University of Stuttgart, Germany

Abstract
Considerable developments and improvements have been made in the field of automated crack detection in the last years. Digital image processing techniques for crack detection are already widely adapted on large highways maintenance projects. No standard scenario of digital image processing algorithms for crack detection is available and guarantees in all crack pavement images cases. Previously several image processing algorithms for crack detection are suffering from various shortcomings on crack detection sides. In this study, the development of a four stage approach closes these weak points by developing a new approach combining and modifying the digital image processing techniques. Combination of different morphological operation techniques is used to correct background illumination. Automatic local adaptive (dynamic) thresholding is realized to distinguish between cracks and extrinsic objects. An automatic fusion approach for the third crack connection stage is set up. This fusion approach is based on a Hole filling algorithm and the connected component algorithm. For the fourth crack detection stage, an automatic approach is developed. This integration approach is based on the contouring algorithm and a modified binary mask detection algorithm. This integration approach can automatically extract cracks and its characteristics with a high rate of correctness. This developed algorithm achieves an increase in automation in order to meet the requirements of the end-user.
The overall developed algorithm is used for testing various pavement crack images. The performance is checked by comparing the results with well-known crack detection algorithms. The developed algorithm with a false detection rate of 1.04% in 3.8 min processing time detects the cracks on around 96 continuous mobile mapping images.

Keywords
Crack detection, Pavement, Digital image processing techniques.

1 INTRODUCTION

The main objective of this paper was to present the feasibility to fuse and integrate several digital image processing tools in order to detect and analyse different crack types automatically. One case study including various mobile mapping pavement images was tested for this prototype study.
Several tasks (data pre-processing, thresholding, segmentation, and post processing) have been solved efficiently in order to ensure a high correctness rate. So different distress types, automatic methods, related work, and well known segmentation methods are briefly introduced in the following sections. A description of the detection algorithm is presented in Sections 2 and 3. Section 4 describes experimental results. Section 5 demonstrates the performance evaluations.

1.1 Classification of Basic Pavement Distress

The distresses of asphalt pavement are any defects or deterioration in the pavement. They can be grouped into general categories. Definitions are conform to those found in German regulations of road state determination (FGSV 2006):

1. Cracking is defined as individual crack or network crack. The network crack is connected to one another like a net. The network crack is classified as crack accumulation (block type). Open and sealed cracks are equally considered.
2. Patching is an area of damaged road surface that is restored by repairing. There are two types of repairing for patching either laid-on patched or pickled patched\excavation.
3. Out-Breaks (Potholes) is the detachment of the road surface parts due to traffic, weather, etc.

4. Open Work Seams is defined as a fine, not connected gap between two asphalt layers.
5. Binder Enrichment is escape of bituminous binder on the road surface.

The frame of this paper is constrained to extract cracking types only. This is done due to their correspondence to the types of distresses on the available datasets pavement images of this paper.

1.2 Automatic Acquisition Methods

Automated survey methods are done using vehicles traveling at highway speeds to gather data. These automated vehicles are called mobile mapping vehicles. Different kinds of automated pavement survey vehicles are obtainable wide world with various data collection techniques. Mobile mapping vehicles consist of different sensors like cameras, laser scanner, inertial measurement unit and lighting unit.

In this paper the sequence pavement images were observed by LEHMANN + PARTNER GmbH Company using S.T.I.E.R mobile mapper system. The S.T.I.E.R measuring vehicle is a system for surveying the longitudinal and transverse evenness. It measures texture and 3-dimensional road surface. This system records surface images. It is certified by the German Federal Highway Research Institute. The S.T.I.E.R mobile mapper system implements the idea of storing geo-referenced digital images. This system is considered as the basic unit and combining an arbitrary number of such image units. This S.T.I.E.R mobile mapper system consists of different sensors with different specifications as follows: (i) Macro picture cameras (Surface cameras) (two in the rear) which take "nearly orthofotos" with a very short overlapping, resolution (1920 x 1080) pixels, every image pixel equals (1.2mm) per ground point; (ii) Fraunhafer Institute Lider, 900 points per transverse profile; (iii) Applanix POS LV 420 positioning system (Combination of POS-LV positioning system); (iv) Lighting unit (L+P 2014).

1.3 Crack Detection Algorithms

The complete automation of crack detection is still an open topic of research in particular in case of complex compound cracks (TEOMETE et al. 2005, YING/SALARI 2009). TEOMETE et al. (2005) presented an algorithm based on dividing images into blocks, determining sub-block size in pixels and noting the pixel intensities during pre-processing stage. Localized (adaptive) thresholding is done by computing relative mean values of intensity for each row during segmentation stage. Finally during crack detection stage a binary mask detection algorithm is implemented to define the region of interest. The binary mask must be defined in two ways as follows: (i) either based on colour and intensity values using several trial and errors (setting threshold to the crack size) (ii) or further automated methods exploit the knowledge of the shape. These methods require pre-defined conditional statements for binary shape mask (square, rectangle, ellipse).

YING/SALARI (2009) presented an algorithm for crack detection and classification. Statistical properties for pavement distress images were investigated for amplitude factor correction calculation. This factor is important to correct background illumination during pre-processing stage. Beamlet transform concept was introduced by DONOHO/HUO (2001). This concept is used during segmentation stage for extraction of linear objects. Beamlet transform is able to detect all line segments at variant locations, orientations and scales.

CHOU/ SALARI (2012) suggested an algorithm based on using region growing concept and labelling connected components algorithm. These algorithms are able to differentiate road surface from background region during segmentation stage (BALLARD/ BROWN (1982). SALARI et al. (2010) offered an algorithm to remove non-uniform illumination effects using morphological operations during pre-processing stage. Otsu's, Niblack's, and Sauvola's thresholding algorithms are implemented during segmentation stage. WELLNER (1993) exploits the knowledge of the intensities for the surrounding pixels around current pixel. The average value is computed around each required pixel. In other words an approximate moving average of the last *s* pixels seen is calculated while traversing the image. Then a comparative study is implemented during segmentation stage. This algorithm needs only single pass through the image. The disadvantages are related to the moving average and distribution of pixels in all directions. Particularly, the neighbourhood pixels are not distributed equally in all directions.

Segmentation stage is considered as one of most important stage during any crack detection algorithm. As a matter of fact, no direct straightforward approach is known to the author for segmentation. The well-known binarization techniques are summarized as following:

1. Niblack's Method (Local Thresholding by NIBLACK'S (1985)): this method is suggested to use a local adaptive method for threshold surface computations. Niblack's represented the threshold value for a pixel with a fixed neighbourhood window as a linear relationship of mean and standard deviation of the neighbourhood pixels with a constant gradient of k.

2. Sauvola's Method (Local Threshold by SAUVOLA/ PIETIKAKINEN (2000)): the main difference between Niblack's algorithm and Sauvola's algorithm is that the latter one uses a dynamic range for the standard deviation R rather than a fixed one like the former algorithm (SAUVOLA/ PIETIKAKINEN 2000). Sauvola's algorithm can select a threshold value based on image properties.

3. Beamlet Transformation for Crack Detection: different locations, orientations, and scaled line segments were hatched by using Beamlet transform principle (YING/SALARI 2009). DONOHO/ HUO (2001) used this principle as a tool to detect and extract linear edges without noise with high accuracy.

As a logical follow-up, all the mentioned algorithms face some obstacles and problems. So the algorithm to be developed will base on the ability to achieve more correct results for detection of pavement cracks from continuous pavement images.

2 ALGORITHM OF PRELIMINARY STAGES FOR CRACK DETECTION

This paper presents a proposed uniform preliminary algorithm for processing digital pavement images. This proposed algorithm is based on a combination of different image processing techniques and some modifications of previous algorithms exactly during thresholding stage. The algorithm suggests a threshold-setting algorithm. This threshold-setting algorithm allows to set the best threshold value for each pixel in the image automatically. This adaptive local thresholding is able to separate all of the crack and only the crack from the reminder of the image. Then for the purpose of improving the thresholding results, this paper employs some combinations of image processing techniques. This general strategy aims to remove the remaining noise, check the crack continuity, and fill all the crack holes. Moreover, it provides an accurate crack image ready for crack detection stage. These preliminary stages pave the way for better crack extraction process.

2.1 Image Enhancement Algorithm

The reason for this first stage is that the pavement images are collected under different lighting situations. This creates the need for correction of the background illumination. This stage is optional based on images nature. As a consequence, conversion of all the source images to standardize the background conditions requires a robust corrected illumination algorithm, which is insensitive to illumination, scale differences and employs region properties (CHENG/MIYOJIM 1998). In this paper the image enhancement algorithm can be divided into the following steps:

1. Erode Operation: The essential erode functions based on Boolean operations for binary images are utilized for morphological image processing (DROOGENBROECK/TALBOT 1996). The erode operation will be applied on the original image. The implementation of this operation must be utilized using the linear structural element.

2. Opening by Reconstruction: The original image and the eroded image are combined using the opening by reconstruction process. The opening by reconstruction process is implemented based on VINCENT (1993). Furthermore, the algorithm makes the process to work best by setting the original image as a mask and the eroded image as a marker. For this purpose, opening by reconstruction is implemented between mask and marker several times during opening by reconstruction through dilation process. The operation will be continued automatically until all the peaks values in the mask

image will become flat. The final resulting image of this operation will help in order to get similar intensity values as well as to reduce illumination differences.

3. Dilate Operation: Dilate was described as one of the Boolean operations for binary images (DROOGENBROECK/TALBOT 1996). Consequently, the opening by reconstruction image will be applied to a similar operation of erode using linear structural element also. This results in expanding every boundary and extracting redundant information about it from the resulting image.

4. Closing by Reconstruction: The closing by reconstruction has been used for illumination correction and smoothness. Also, it enables to convert images into a suitable form for segmentation stage. The algorithm follows this operation having some analogy with VINCENT (1993). This operation will be implemented using the same concept as opening by reconstruction process. The complementary of dilated image is used as a marker while the opening by reconstruction image is utilized as a mask. The aim of this operation is to remove all peaks from the opening by reconstruction image through continuous erosion process (GONZALEZ/ WOODS 2008). So this operation plays a key role to provide accurate information for the thresholding stage.

2.2 Thresholding Algorithm

The integration and combination of different morphological operations during image enhancement stage delivers images with uniform distribution of illumination. After that, as a second stage, the threshold setting algorithm requires a robust dynamic automated algorithm. This algorithm is insensitive to noise, obstacles and employs region properties (GONZALES/WOODS 1992). The threshold setting algorithm (adaptive or local dynamic thresholding) can be defined by a simple extension of Wellner's method (WELLENER 1993). Accordingly, a convolution concept (NEWTON/MITCHELL 2006) is introduced and its parameters are estimated. This latter concept is done using the mean statistical operator within an *s x s* window of pixels around each pixel. This is usually followed by Sobel edge detector to clearly extract edges of crack. Then the algorithm can use the extracted objects which correspond to cracks or to other noise as an input for post processing stage. The proposed approach consists of the following steps:

1. Convolve the image with a mean statistical operator within an *s x s* window of pixels centred around each pixel.
2. Subtract the original from the convolved image.
3. Threshold the difference image with a constant c where (mean-c) is the local threshold.
4. Convert the difference image to a binary image.
5. Invert the threshold image.
6. Sobel edge detector is applied on the final resulted local adaptive threshold image.

2.3 Crack Connection Algorithm

Using different integration and combination of morphological operation during pre-processing stage with the help of adaptive thresholding algorithm can lead to: (i) noise due to the pixels intensity change, some background pixels displaced as foreground pixels. (ii) Crack discontinuity. (ii) Holes inside crack regions. In order to overcome these problems and improve results, an integration algorithm for post processing stage has been implemented.

1. Hole Filling algorithm: in this paper based on previous described properties, previous algorithms and literature review Hole pixel initial algorithm (GONZALEZ/WOODS 2008) has been tested for crack holes filling. After that, several dilation processes (DROOGENBROECK/TALBOT 1996) are implemented using disk structuring element. This operation plays a key role to facilitate the distinction between crack and other extrinsic objects during the next detection stage.

2. Labelling Connected Components algorithm: this step is designed, at first to accurately and quickly divide binary image pixels into connected components (*CC*). The connected component process is done on the resulting hole filling binary image to segment its pixels into connected components (*CC*). All the pixels in each connected component have the same intensity values (0 or 1) due to the binarization. Firstly the connected components (*CC*) process has been completed and all the pixels

have been separated into different groups. Secondly the labelling connected components algorithm is run for each group of pixels. The latter one is labelled with two possibilities either by grey level value (value labelling) such as 1, 2, 3,...etc; or by a colour (colour labelling) (GONZALEZ/WOODS 2008). Thus, in this paper connected components algorithm is realized as follows (GONZALEZ/WOODS 2008):

(i) Assuming 8-connected pixels which are defined as a neighbour to every pixel that touches one of their edges or corners. These pixels are linked vertically, horizontally, and diagonally.

(ii) The connected component is built by scanning a binary image pixel-by-pixel from top to the bottom and left to right. This process is done in order to specify connected pixel regions that have the same set of the intensity values.

(iii) The connected components regions are formed by (8-connectivity checks) around each pixel. Where the question will be for example as followed: Does the pixel on the left have the same intensity value as the current pixel, if the answer is yes, this pixel is put in the same connected component region of the current pixel. If the answer is no, this pixel is out the connected component region of the current pixel. This question must be repeated over all pixel neighbours during 8-connectivity.

The first pass labelling algorithm is realized as follows (GONZALEZ/WOODS 2008):

(i) Scan the image by moving along a row until it comes to element h.
(ii) If element h is not the background (h symbolized the pixel to be labelled for which I=1 (white not black)); when it is true, the following steps must be done:
   a. Examine the neighbours of *h* that have been obverted in the scan.
   b. If there are no neighbouring (all neighbours are 0 (black)), specify a new label to *h*.
   c. If only one neighbour has *I*=1; specify its label to *h*.
   d. Otherwise if more than one of the neighbours have *I*=1, find the neighbours with the smallest label and specify it to *h*. Then record the note of equivalence between neighbours labels. After completing first pass labelling algorithm the equivalent label pairs are recorded and saved into equivalent classes.

The second pass labelling algorithm is utilized as follows (GONZALEZ/WOODS 2008):

(i) Scan for each element of the image data by column then row and identify if element h is in the background or not.
(ii) If it is not in the background, the following steps must be done:
   a. Find the smallest label within the equivalence class concludes element h.
   b. Relabel element h with the smallest equivalence class labels.
   c. Display the final results where each equivalence class has its unique value and its unique colour (BALLARD/BROWN 1982).

3 ALGORITHM FOR CRACK DETECTION

A direct crack extraction from sequence pavement images based on the combination between different image processing techniques and some modifications of previous algorithms is presented. The proposed algorithm suggests to apply the contouring algorithm (SALARI et al. 2010; JONES 1971). This contouring algorithm specifies the location of the crack in the original image. Then for the purpose of extracting the crack, this study modifies the binary mask detection algorithm based on geometric relationship for crack regions (TEOMETE et al. 2005). This modification strategy aims to extract the crack alone and its characteristics.

3.1 Contouring Algorithm

The contouring algorithm aim is to exactly specify the probable cracks' locations automatically in the original image. This will be helpful to extract the real crack measurements from the original image after detecting it. The contouring algorithm is used as a tool for the projection of all coloured equivalence classes (probable crack regions) on the original image.

The overall algorithm for contouring is described as follows (JONES 1971, SALARI et al. 2010):

1. Define the feature.
2. Find the minimum and the maximum height (z_{min} , z_{max}) over the feature.
3. If $z_{min} \leqslant c \leqslant z_{max}$ then go to step (4), else go to step (6).
4. Dash the contour over the feature.
5. Save the contour.
6. If not all the features are handled, then consider the next feature and go to step (2), else go to step (7).
7. Connect the contours that have the same level.
8. Scheme the contours.

3.2 Binary Mask Detection Algorithm

The resulting contouring images indicate different probable crack regions (green colour regions). The binary mask detection algorithm (TEOMETE et al. 2005) has been selected in this paper with some modifications and extensions. In the following, a detailed description of the modified binary mask algorithm is explained in order to introduce the steps.

a. Perform statistical analysis for most of the crack images, the results of the statistical analysis are as follows: (1) the range of crack areas length is between 0.1 to 1 m on the ground which equals 100-833 pixels on the image. (2) The range of crack areas width is between 0.04 to 0.2 m on the ground which equals 35-166 pixels on the image. The minimum crack width on the available case study of this paper is 3 mm (2.5 pixels). Based on German regulations of road state determination (FGSV 2006), cracks thicker than 1 mm should be detected.

b. The overall modified binary mask detection algorithm (TEOMETE et al. 2005) is introduced as follows:

   (i) Define binary ellipse mask based on the pre-defined conditional statements values mentioned above.

   (ii) Move the binary ellipse mask over the resulting image after applying Hole filling algorithm as shown in figure 1.

   (iii) When the pre-defined conditional statements values are satisfied, the ellipse will be printed over the contour on the resulting image after applying the contouring algorithm. This is done to define the region of interest. Until this limit, binary mask detection algorithm is utilized as in TEOMETE et al. (2005). After that, in order to be fit the crack connectivity for detection and filter out incorrect noise this paper modifies and extends the algorithm in the following steps:

   (iv) Some conditions must be checked as follows: (a) if there are different continuous ellipses (binary masks) printed over continuous contours; (b) and if these contours are corresponding with connected components (equivalence classes) having the same or nearly the same intensities and colours, the continuous binary ellipse masks will be merged around the continuous contour regions automatically. Otherwise each binary ellipse mask will be drawn for each contour part alone automatically.

   (v) Draw the major axis and minor axis for each ellipse by a geometric method.

   (vi) Detect cracks automatically where each contour region will be surrounded by ellipse shape. It will be automatically considered as a crack region. Otherwise any other thing (other green regions) is neglected automatically as shown in figure 3-b.

   (vii) Extract crack characteristics automatically from the geometrical characteristics of binary ellipse mask shape (region properties) as follows:

      a. Crack area length is represented by length of the major axis given in pixels.
      b. Crack area width is represented by length of the minor axis given in pixels.

c. Crack area orientation (Ω) is represented by the orientation of the major axis inside binary ellipse mask region. A virtual vertical axis ranging from -90° to 90° is claimed and passed through the ellipse shape center. Then the algorithm can move directly through a path within the range -90° to 90° from positive horizontal axis to the major axis of the ellipse shape. The orientation angle will be generated from this movement either clockwise or counterclockwise. So the final orientation angle will be measured as a value in degree with a positive or negative sign. The sign will represent the direction of the path from positive horizontal axis to the major axis of the ellipse shape. The orientation angle will automatically be got from the region properties.

d. Area of crack region: In this paper the area of crack region is determined by calculating the area of the ellipse surrounded for each crack region by equation (1) below. This parameter is useful in the case of crack accumulation (block type). The modified algorithm generates a group of ellipse masks in the block type region. The affected areas by the block crack type are measured by summation of the areas for all ellipses inside block crack region automatically, as shown in figure 4.

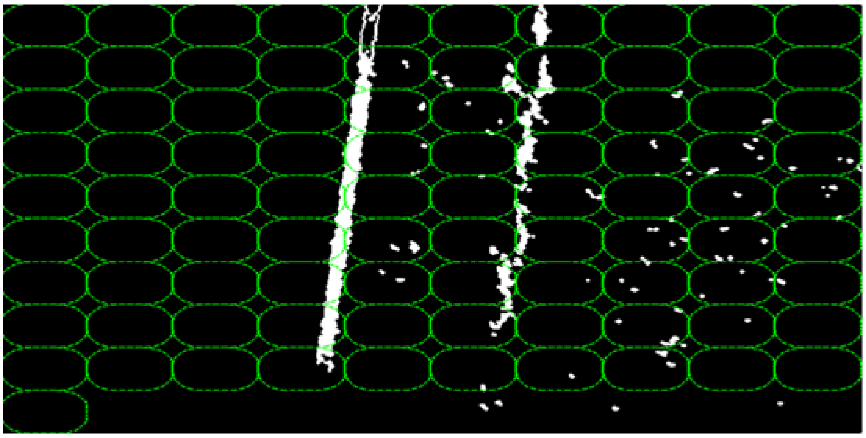

Figure 1: Moving binary ellipse mask over the image in crack detection stage.

$$A = \pi \cdot 0.5^2 \cdot r_a \cdot r_b \tag{1}$$

A : Area of the crack region that equals the ellipse area (pixels).
r_a : Major axis length (pixels).
r_b : Minor axis length (pixels).

4 CASE STUDY OF THIS REASEARH

4.1 Case Study Description

To achieve the objectives of this study, mobile mapping continuous pavement images for this research work were captured by LEHMANN + PARTNER GmbH Company in Germany (S.T.I.E.R mobile mapper system). This case study contains 96 sequence pavement images. The length of this case study is 100 m on the street ground. The pavement images of this case study have a resolution of 1920 x 1080 pixel. Every image pixel equals 1.2 mm per ground point. Generally the images of this case study contain: cracks with various shapes, noisy pavement texture, lane markings, tire marks, stop lines, repaired road, skid markings, railways trucks, grates, sidewalk (curbs), manholes covers, signs on the ground, oil spot on the ground, line stripping, lighting columns, water pipelines, traffic loops and bicycles, lighting conditions changing with shadows, shades from road traffic, persons, trees and different illumination conditions. The developed algorithm regarding different stages was applied to this case study. The aim was to extract cracks and its characteristics automatically for all sequence images together without human interaction.

4.2 Experimental Results

The results of the automatic fusion, combinations and modifications for crack recording are highlighted. Particularly, the efficiency of the algorithm is shown by presenting an interest to different pavement images. The outputs of digital image processing techniques combination and modification are evaluated and assessed. The aim was to extract cracks automatically for all sequence images without human interaction. Moreover, some pavement images contain some extrinsic objects such as marking and oil spot on the ground in cases of different pavement textures. This creates a challenge from the algorithm side, if it enables to detect the crack only (marked in figure 2-a) and neglects any other things. Figures 2, 3 and 4 demonstrate one of the tested samples and their corresponding results after applying the detection algorithm. The algorithm can be evaluated using the following criteria's:

a. The bias of false detection rate can be calculated using equation (2)

$$B = (\frac{N}{T} \cdot 100) \qquad (2)$$

B : False detection rate [%]
N : Number of false detected images.
T : Total number of images.

b. The processing time to complete crack detection is got automatically from the algorithm [seconds]. Table 1 summarizes the evaluation results for this case study.

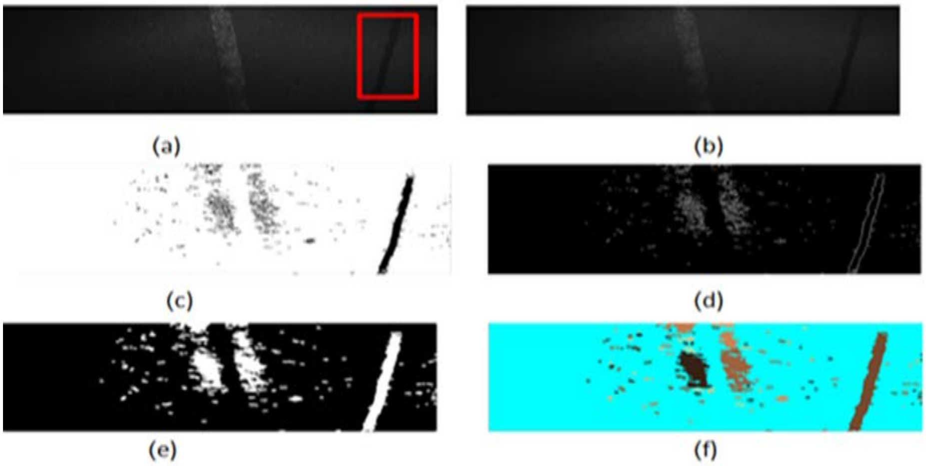

Figure 2: Behaviour of the algorithm for the preliminary stages of crack extraction within image; (a) original image, (b) the image after applying image enhancement algorithm, (c) image after applying adaptive local threshold algorithm, (d) image after applying Sobel edge detector, (e) the image after applying Hole pixel initial algorithm including several dilation processes, (f) the image after applying labelling connected components algorithm.

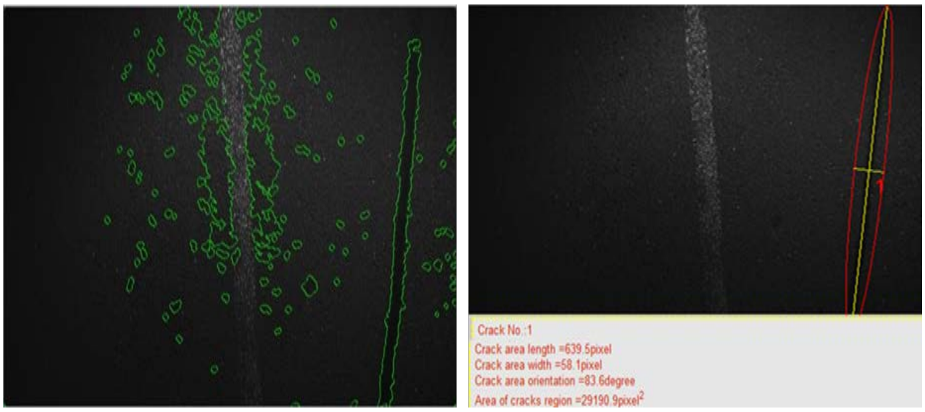

Figure 3: Behaviour of the algorithm for crack extraction; (a) the image after applying contouring algorithm, (b) the final image after applying modified binary mask detection algorithm.

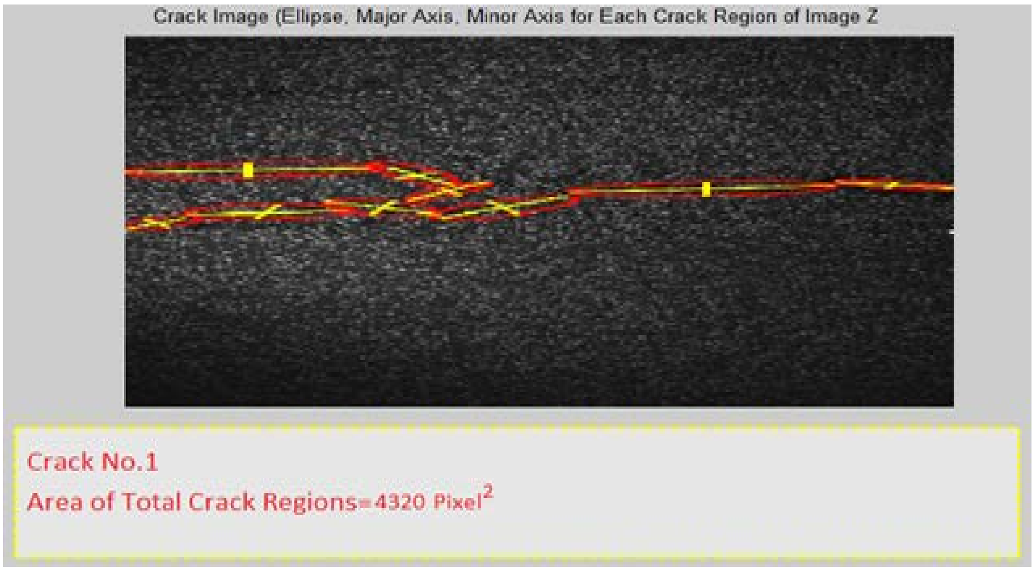

Figure 4: The behaviour of the algorithm in the case of crack accumulation (block crack)

Table 1: Evaluation the results of this case study

Category	Quality
Total number of crack's images	70 image
Total number of non crack's images	26 image
False detection (number of images)	1 image
False detection rate (%)	1.04%
Processing time to complete crack detection	3.8 min

5 RFORMANCE EVALUATION

As a matter of fact a perusal of the literature strongly confirms that none of the previous algorithms detects crack from continuous pavement images. Most of the previous algorithms detect cracks for each individual image alone. Several methods in the literature had been used to test individual images for comparison. These methods include NIBLACK'S (1985), SAUVOLA/PIETIKAKINEN (2000), and Beamlet transformation for crack detection (YING/SALARI 2009). These methods are chosen because either they have been formerly utilized to threshold individual pavement images efficiently or they were used to separate textual information from its application. In this section, a comparative study is done between the algorithm of this study and the latter three well-known methods for individual images as shown in figures 5, 6 and 7 below. Table 2 shows the performance of the algorithm in comparison to the other methods.

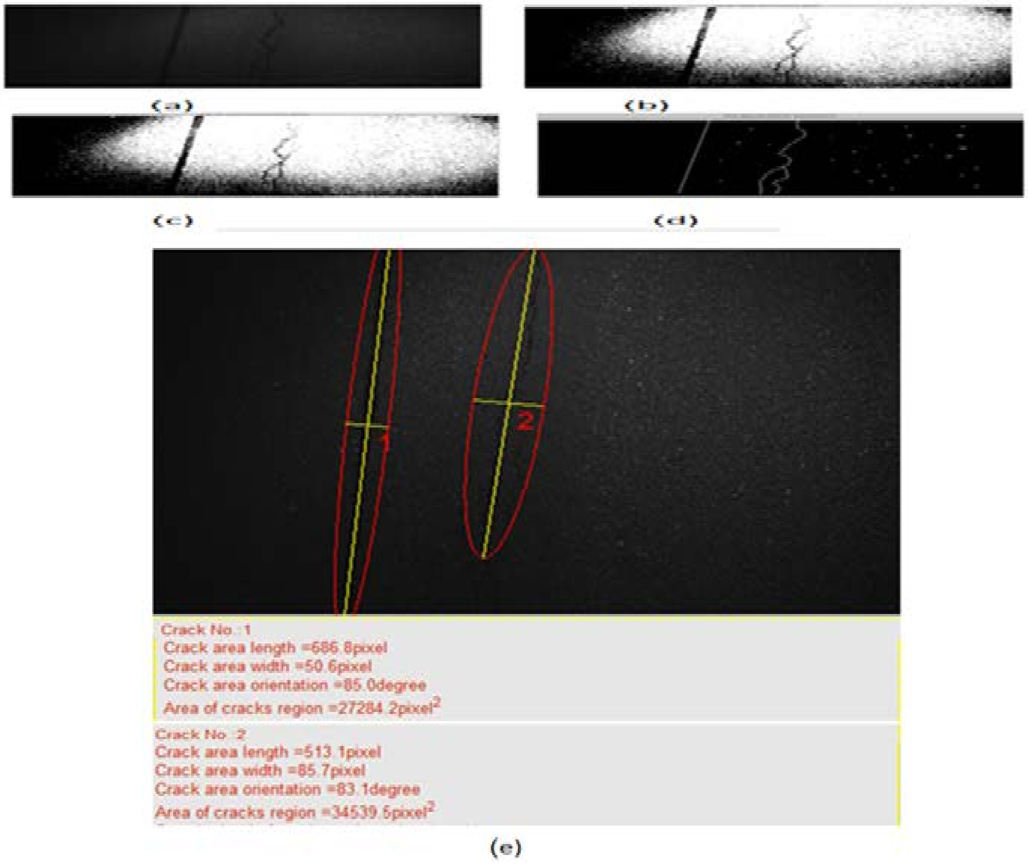

Figure 5: Comparative study between the algorithm of this study and other methods; (a) original image, (b) the image after applying Niblack's method, (c) the image after applying Sauvola's method, (d) the image applying Beamlet transformation method, (e) the image after applying the algorithm of this study.

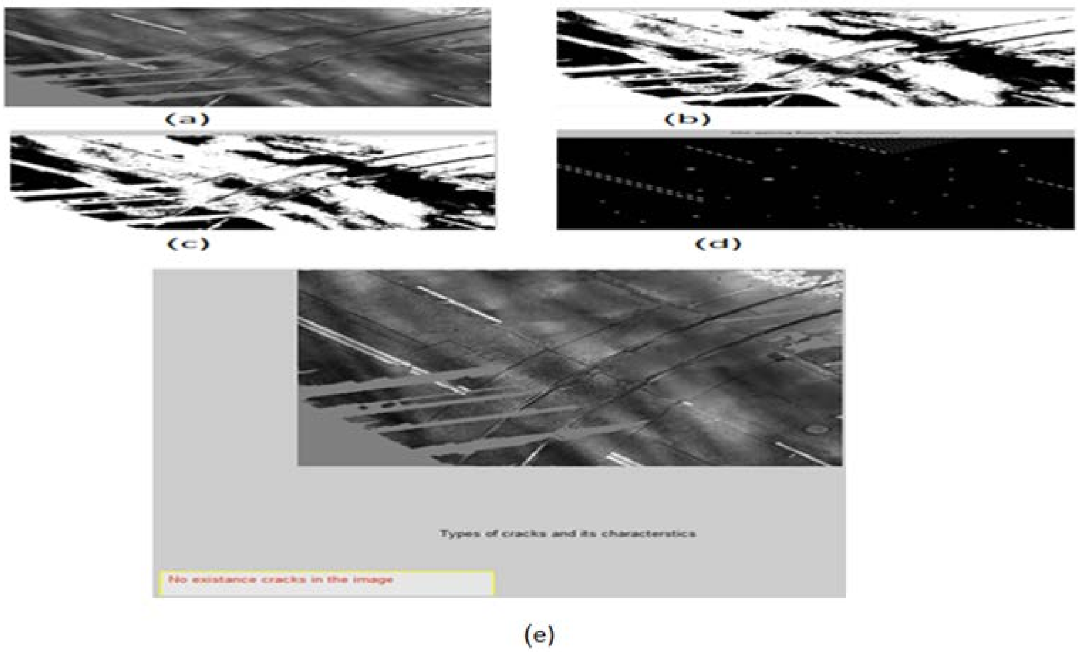

Figure 6: Comparative study between the algorithm of this study and other methods; (a) original image, (b) the image after applying Niblack's method, (c) the image after applying Sauvola's method, (d) the image applying Beamlet transformation method, (e) the image after applying the algorithm of this study.

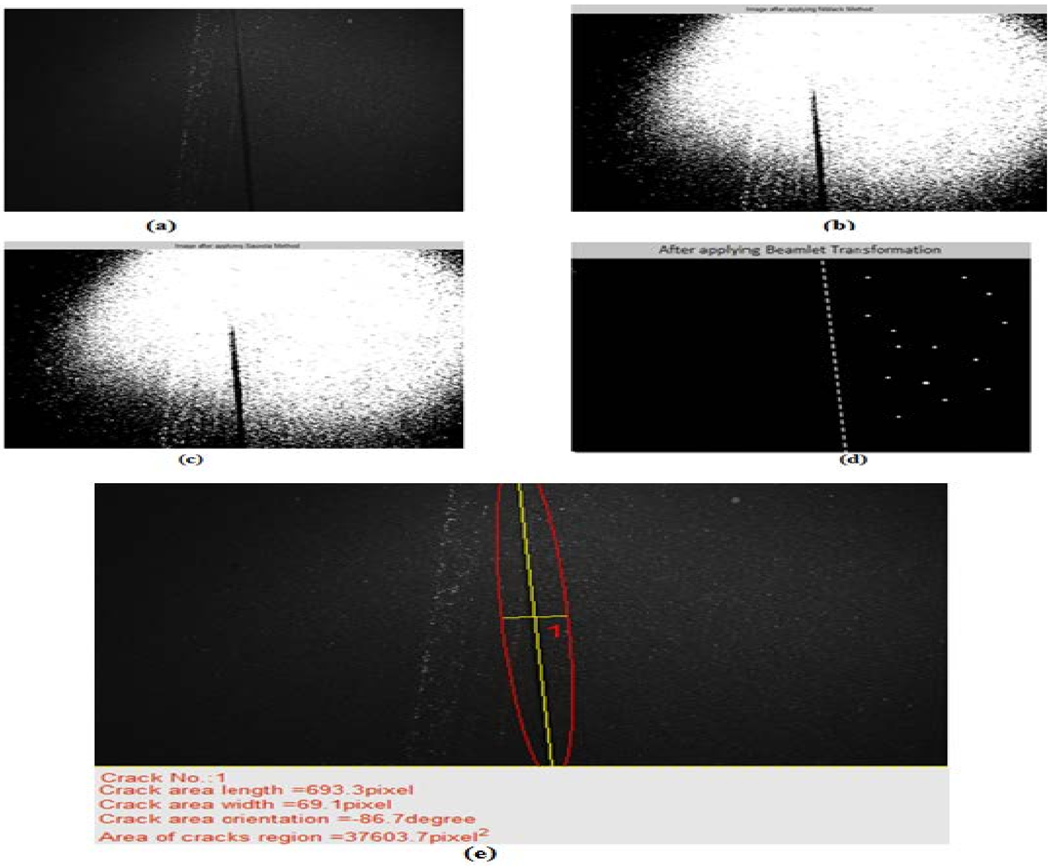

Figure 7: Comparative study between the algorithm of this study and other methods; (a) original image, (b) the image after applying Niblack's method, (c) the image after applying Sauvola's method, (d) the image applying Beamlet transformation method, (e) the image after applying the algorithm of this study.

Table 2: Computation time for the algorithm compared with other methods

Input image	Dimension (pixels)	Processing time for Niblack's Method (seconds)	Processing time for Sauvola's Method. (seconds)	Processing time for Beamlet Transformation Method. (seconds)	Processing time for the aligorthm in this paper (seconds)
Figure 5	1920 x 1080	5	4	3.5	2.4
Figure 6	1920 x 1080	4.1	3.8	3.9	2.6
Figure 7	1920 x 1080	3.4	3.5	3.7	2.8

The visual evaluation of the experimental results confirms that the developed algorithm performs better than the other cited methods. Results from Sauvola’s algorithm (SAUVOLA'S/PIETIKAKINEN 2000) are similar to the results from Niblack's algorithm. These two latter methods could not perform well enough to binarize the crack images. The result is worse than the developed algorithm because both Niblack’s and Sauvola’s algorithm count the background information especially around foreground texture as an important feature for local threshold calculation. So the crack pixels are considered as a part of the background pixels. Moreover, the Beamlet transformation algorithm (YING/SALARI 2009) works better than Niblack's (NIBLACK'S 1985) and Sauvola’s algorithms (SAUVOLA'S/PIETIKAKINEN 2000). Beamlet transform based method is very effective if cracks are present in pavement images. It can be applied for pavement images with a high rate of detection and a very low rate of false detection. But the processing time in this method is higher than the processing time using the developed algorithm (see table 2). Also this method detects cracks and some noise around the crack unlike the developed algorithm in this paper. In addition it is sensitive to different pavement texture (asphalt binder appears as noise). Moreover, it cannot distinguish between crack and extrinsic objects such as lane markings, sidewalks (curbs) and railways whereas the developed algorithm in this paper could separate.

Finally the results of the developed algorithm in this study have a better performance than former methods. The latter algorithm preserves the intended information very well after thresholding. It is based on a simple technique and low computational cost. Sequentially, the processing time of this latter algorithm is lower than all former methods for individual images as shown in table 2.

Also as presented in the previous section, the processing time for crack detection in the case of sequence mobile mapping images is low and acceptable. For example the case study of this paper contains 96 sequence mobile mapping images. The developed algorithm delivers an average computation time of 3.8 min and the false detection rate is 1.04% to complete crack detection.

6 CONCLUSIONS

In this paper, experimental results provided in section five, have demonstrated that the developed algorithm is very effective in the presence of noise, extrinsic objects such as lane markings, sidewalks, railways, different lighting conditions, and shades in different pavement texture images. It can be applied on noisy pavement images and detect different types of cracks with a high rate of detection and a low rate of false detection. The developed algorithm achieves better quality results compared to other methods shown by exemplary visualization. It can achieve a significant improvement of the computation time. In general, the overall proposed integration and combination approach presents an effective solution which enables to fuse different modified image processing algorithms for crack extraction applications.

REFERENCES

Books:

FGSV, (ED.).: *ZTV ZEB-STB_1- Zusätzliche Technische Vertragsbedingungen und Richtlinien zur Zustandserfassung und- bewertung vonStraßen_1*. FGSV-Nr.489, Köln, 2006.

GONZALEZ, R., WOODS, R.: Digital Image Processing, Pearson Prentice Hall, First edition,Upper Saddle River, New Jersey, United State, 1992.
GONZALEZ, R., WOODS, R.: Digital Image Processing, Pearson Prentice Hall, thrid edition, Upper Saddle River, New Jersey, United State, 2008.

NEWTON, I., MITCHELL, H.L.*: Close Range Photogrammetry and Machine Vision*, Whittles Publishing, Caithness, Scotland, UK, 2006.

NIBLACK'S, W.*: An Introduction to Digital Image Processing*, Prentice Hall,1985.

Journal articles:

BALLARD, A., BROWN, C.*M.: Computer Vision*, Prentice-Hall, Chap. 2, 1982.

CHENG, H.D., MYOJIM, M.*: Automated Pavement Distress Detection System*, Journal of Information Sciences, 1/2008, p. 219-240, 1998.

CHOU, E.Y., SALARI, J.*: Transportation Informatics: An Image Analysis System for Managing Transpotation Facilities-Phase 2*, final report, the University of Toledo-University Transportation Center, 2012.

DONOHO, D.L., HUO, X.*: Beamlets and Multiscale Image Analysis*, International Journal of Computer Science and Network Security, vol. 8, No. 1, p. 213-216, 2001.

DROOGENBROECK, M., TALBOT, H.: Fast Computation of Morhological Operations with Arbitrary Structuring Elements, Pattern Recognition Letters Journal, USA, Vol. 17(14), 1451-1460, 1996.

JONES, R.L.*: A Generalized Digital Contouring Program*, NASA Langley Research Center, Hampton, Virginia, NASA TN D-6022, p. 78, 1971.

SALARI, E., CHOU, E.Y-J, LYNCH, J., DUTTA, U.*: Transportation Informatics: Advanced Image Processing Techniques for Automated Pavement Distress Evaluation*, Report No: MIOH UTC TS18-Final, Department of Electrical Engineering and Computer Science, University of Toledo, Toledo, OHIO, and Department of Civil and Environmental Engineering, University of Detroit Mercy, Detroit., p. 2, 2010.

SAUVOLA, J., PIETIKAKINEN, M.*: Adaptive pavement image binarization Machine Vision and Media Processing Group*, Infotech Oulu, University of Oulu, P.O. BOX 4500, FIN-90401 Oulu, Finland, Pattern Recognition 33, p. 225-236, 2000.

TEOMETE, E., VIREN, R.A, HALIL, C., SMADI, O.*: Digital Image Processing for Pavement Distress Analysis*, Proceedings of the 2005 Mid-Continent Transportation Research Symposium, Ames, Iowa, Iowa State University, 2005.

VINCENT, L.*: Morphological Gray-scale Reconstruction in Image Analysi: Applications and Efficient Algorithms*, IEEE Transactions on Image Processing, Vol.2, No.2, p. 176-201, 1993.

WELLNER, P.D.*: Adaptive thresholding for the digitaldesk*, Tech. Rep. EPC-93-110, EuroPARC., 1993.

YING, L., SALARI, E.*: Beamlet Transform Based Technique for Pavement Image Processing and Classification*, Department of Electricall Engineering and Computer Science, University of Tolodo, Teledo, Ohio 43606, 2009.

Links:

L+P: *Lahmann+Partner GmbH company*, *Germany*, http://vectragermany.com/technologie/system-stier, last accessed on June 17, 2014.

Modelling of Spatio-Temporal Variations for Engineering Structures and Natural Objects by Geodetic Monitoring Data

Tatyana Yu. Bugakova
Siberian State University of Geosystems and Technologies, Russian Federation

Abstract
One of the main objectives of modern science is investigation of natural and man-made objects state (seismic areas of the Earth surfaces, engineering structures, precision facilities, environment pollution areas, etc.) in order to secure the safety of citizens and housing resources, accident prevention, etc. Natural and anthropogenic catastrophes taking place in the world necessitate development of the new techniques for research and forecasting of such conditions. The authors put forward the idea of modeling spatio-temporal variations of engineering structures and natural objects by geodetic monitoring data. The examples presented here deal with the solution of problem concerning determination of shape, size, orientation, and position of the object in time and space by mathematical simulation.

Keywords
Modeling, mathematical simulation, spatio-temporal state, engineering structures, natural objects, geodetic monitoring, size, shape, spatial position.

The object state is determined by the variety of its properties, with each of them expressed in qualitative and quantitative indices referred to some fixed instants of time. Object properties tend to changes due to some internal processes or environment impact. Each object has an infinite set of properties. When describing the object state, the purpose of its determination should be formulated, and (depending on the set purpose) out of the numerous properties (characteristics) only those which are necessary for its description should be selected.
To solve the problem of the object state determination by geodetic data its spatio-temporal state (STS) should be described. It is to embrace the shape, size, orientation, position in time and space, i.e., the spatio-temporal object state (STOS) of the is determined by function (1)

$$STS(t) = STS(F(t), R(t), P(t), O(t)) \tag{1}$$

where $F(t)$ is an object shape, $R(t)$ - size, $P(t)$ - spatial location relative to the coordinate system, $O(t)$ - spatial orientation, determined as functions of time.
Current geodetic techniques (e.g., terrestrial laser scanning) combined with special software packages allow for developing static model of the object state. Laser scanning of engineering structures and natural objects results in the development of points cloud with coordinates *X,Y,Z*, determined relative to the set coordinate system. The software for laser scanning data processing makes it possible to represent the object as a 3D scan, determine its dimensions and orientation relative to the set coordinate system, and monitor its geometric parameters.
Determination of the object state variations in time and space requires time series of the data obtained as a result of repeated object observation cycles. The most common systems nowadays are automated monitoring systems, which allow for continuous observation of the object with the set time interval despite weather condition. To this effect, control points (sensors) are fixed in the object body, they are to transfer signaling information on the object state.
The modeling of spatio-temporal object state variations is a complicated problem. Producing time series of coordinates *X(t),Y(t),Z(t)* by laser scanning seems to be costly, and the data obtained by automated monitoring systems are not sufficient as a whole for the determination of spatio-temporal object state variations.
Therefore, to develop dynamic model of STS variations and forecasting the object future state, mathematical simulation techniques should be applied.
Two basic techniques for mathematical modeling used now are analytical and simulation modeling.

Analytical technique for mathematical simulation consists in obtaining modeling results in the form of statements, whose truth is to be proved. If analytical modeling does not seem possible then simulation is applied. Any representation of the dynamic process on the computer and analysis of its alternate solutions are called simulation.

Simulation modeling resulted from the necessity of designing and studying complicated objects, which cannot be investigated by laboratory or natural experiment to optimize their structural and functional characteristics. In geodesy simulation models are used for simulating physical or information processes for revealing time dependence of phase variables (for example, spatio-temporal object state variations).

Variations of the spatio-temporal object state show in motions and deformations. Analyzing motions and deformations one can judge on the object state danger and take due measures on reducing the risk and damage caused by hazardous conditions. The object motions is the change of its position in space relative to the accepted invariable reference system, and deformation is motions of the system parts relative to each other accompanied by the changes in shape and size of the whole structure or its parts. The shape, size, orientation and spatial position of the object referred to some instant of time determine its spatio-temporal state, and the functions characterizing the system's STS – its state characteristics.

Based on the principles of system approach, decomposition of this compound motion into the sum of more simple ones may be performed.

Three-dimensional motion of object $\overline{D}$ is traditionally represented by the set of vectors of translational, $\overline{Dp}$, $\overline{Dw}$ rotational, and relative $\overline{Do}$ motions. To determine the enumerated types of motions in explicit form perform decomposition procedure:

$$\overline{D} = \overline{Dp} + \overline{Dw} + \overline{Do} \tag{2}$$

Characteristics of translational motion $\overline{Dp}$ are estimated by the motion of hypothetical point whose coordinates are determined as the arithmetical mean of the cloud points coordinates. In rotational motion $\overline{Dw}$ of the object the rotation axis may either change or not change its direction.

Develop the model for point cloud rotation about invariable axis. The results of rotation modeling for the cloud of $N = 7$ points in $M = 6$ measurement cycles are given in Table 1.

Spatial position of the point cloud is represented by plane *S*, with the sum of squares of the cloud points' distances from the plane being minimal (Fig. 1). Spatial orientation of the plane is completely defined by normal $\overline{N}$ (to this plane) passing through the point of S.

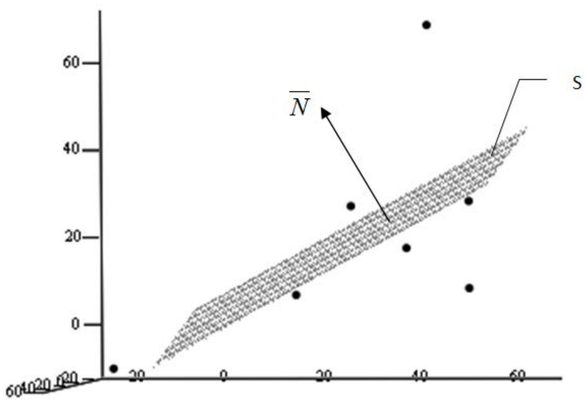

Figure 1: Geometrical model of spatio-temporal condition of point cloud

Table 1: Results of point cloud rotation modeling

Cycle numbers	Coordinates	Cloud point number						
		1	2	3	4	5	6	7
1	X	50.0000	20.0000	-20.0000	40.0000	60.0000	10.0000	20.0000
	Y	40.0000	60.0000	-20.0000	50.0000	30.0000	50.0000	60.0000
	Z	30.0000	10.0000	-10.0000	20.0000	10.0000	70.0000	30.0000
2	X	49.9983	19.9915	-19.9983	39.9949	59.9966	10.0034	19.9949
	Y	40.0054	60.0024	-20.0024	50.0048	30.0092	49.9945	60.0003
	Z	29.9955	10.0027	-9.9986	19.9983	9.9928	70.0034	30.0027
3	X	49.9965	19.9829	-19.9965	39.9898	59.9932	10.0068	19.9898
	Y	40.0109	60.0048	-20.0048	50.0095	30.0184	49.9891	60.0007
	Z	29.9911	10.0054	-9.9973	19.9965	9.9857	70.0068	30.0054
4	X	49.9949	19.9744	-19.9949	39.9846	59.9898	10.0102	19.9847
	Y	40.0164	60.0071	-20.0072	50.0143	30.0276	49.9836	60.0010
	Z	29.9867	10.0082	-9.9959	19.9949	9.9785	70.0010	30.0082
5	X	49.9932	19.9659	-19.9932	39.9795	59.9863	10.0136	19.9795
	Y	40.0218	60.0095	-20.0095	50.0191	30.0368	49.9782	60.0013
	Z	29.9823	10.0109	-9.9945	19.9932	9.9714	70.0136	30.0109
6	X	49.9914	19.9574	-19.9915	39.9744	59.9829	10.0171	19.9744
	Y	40.0273	60.0119	-20.0120	50.0238	30.0460	49.9727	60.0017
	Z	29.9778	10.0136	-9.9932	19.9915	9.9642	70.0170	30.0136

When the point cloud is rotating about the invariable axis, normal $\overline{N}$ remains perpendicular to the cloud rotation axis, i.e.

$$ORT_{k,k+1} = \frac{\overline{N}_k \times \overline{N}_{k+1}}{\left|\overline{N}_k\right| \cdot \left|\overline{N}_{k+1}\right|} \tag{3}$$

where k - measurement cycle number.

$$ORT(\overline{N}) = \begin{pmatrix} 0-1 & 1-2 & 2-3 & 3-4 & 4-5 \\ 0.032 & 0.032 & 0.032 & 0.032 & 0.032 \\ 0.858 & 0.858 & 0.858 & 0.858 & 0.858 \\ 0.513 & 0.513 & 0.513 & 0.513 & 0.513 \end{pmatrix} = \overrightarrow{const} \tag{4}$$

where $\overrightarrow{const}$ - invariable unit-vector of rotation axis.

As $ORT_{k,k+1} = \overrightarrow{const}$ we can draw a conclusion that rotation axis is invariable.

Thus, to determine position of the object in space $P(t)$ relative to the coordinate system we are to know the parameter $\overline{Dp}$. Orientation of $O(t)$ cloud of points in space is determined by $\overline{Dw}$.

It should be noted that the solution of the problem of parameter $\overline{Dw}$ determination, presented in the article is not unique. For example, if we superpose the origin of coordinates with the point whose coordinates are determined as the arithmetic mean of the point cloud coordinates, then spatial orientation of this point cloud will be defined through the Euler's angles (Fig. 2).

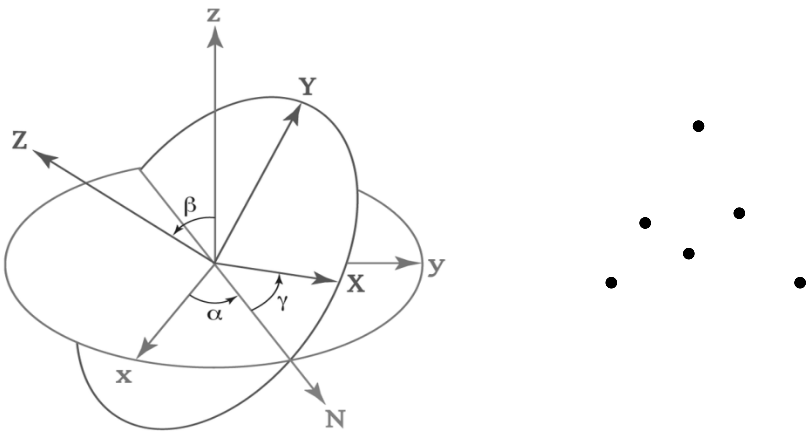

Figure 2: Spatial orientation of point cloud through the Euler's angles

To determine relative motion of object $\overline{Do}$ we should know its shape $F(t)$ and dimensions $R(t)$. Changes in the shape and size testify to the integral or differential deformations.

The shape and size of the system are determined by the border separating it from the external environment. The shape of any system is defined by the set of integral and differential characteristics. Integral characteristic, for example, involve geometrical properties of the whole system, i.e. the possibility of its representation by a single geometrical body, its dimensions, surface area, volume of the occupied space, and numerical values of invariant characteristics. Differential characteristics of the system are directions of tangents and normals to the surfaces and/or lines limiting the system, their curvature, areas of the parts of surface and lengths of lines embracing these parts, etc.

To determine the shape of the object by the data on the coordinates of finite set (cloud) of points it is necessary (in accordance with the purpose) to choose geometrical image which is taken as the shape model and determine the requirements (criteria) this image is to satisfy. Then the values of the finite number of parameters required for mathematical description of the chosen geometrical image of the system shape (in accordance with the made requirements) are to be estimated.

For example, to determine relative motion $\overline{Do}$ of the cloud (Fig. 3) we present it as a sphere A, whose radius r is equal to

$$r = r_i - r_0 \tag{5}$$

where r_i - is a point number i, $r_0 = \frac{1}{N}\sum r_i$, N – number of points.

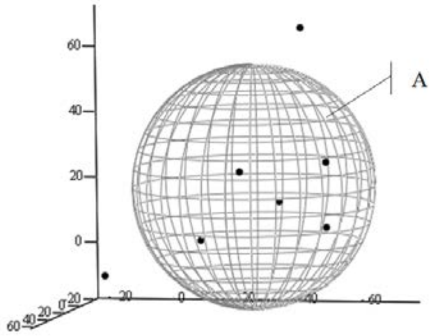

Figure 3: Spherical object model

The number of spheres is equal to the number of observations cycles. By changes in radius of spheres A and B referred to different cycles, we can estimate compression or widening of the cloud, i.e. its integral deformations (Fig. 4).

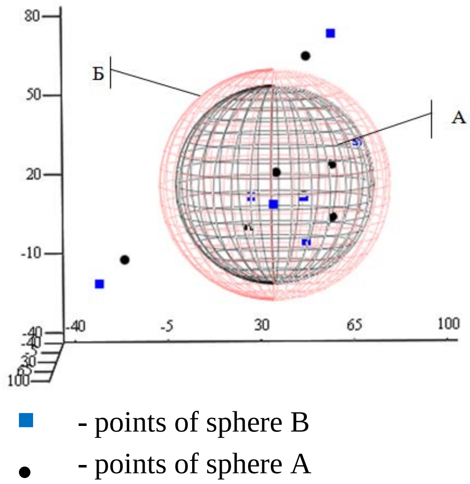

Figure 4: Sphere model changes with uniform widening of the cloud

After eliminating integral deformations from measurements results we can estimate differential deformations.

Thus, the above mentioned circumstances and examples testify to the possibility of modeling spatio-temporal variations of engineering structures and natural objects by geodetic monitoring data.

REFERENCES

Books:

LOYTSYANSKY, L.G., LURYE, A.I.: *Course of theoretical mechanics*; 2 volumes. Vol.1. Statics and kinematics. - second edition, revised and supplemented. – M.: Nauka, Chief editorial board of physical and mathematical literature, 1982.

LAPTEV, S.F.: *Elements of vector calculus*, M.: Nauka, 1975.

Journal articles:

BUGAKOVA, T.YU., *Objects state stability estimation by geodetic data using phase space method,* Author's abstract of dissertation for Candidate's degree, SSGA, Novosibirsk, 2005.

VOVK, I.G., BUGAKOVA, T. YU., *Mathematical simulation of spatio-temporal states of systems by geometrical properties, and anthropogenic risk estimation by exponential smoothing*, Vestnik SSGA, Issue 4(20), p. 47-58, 2012.

BUGAKOVA, T.YU., VOVK, I.G., *Mathematical simulation of systems spatio-temporal state,* Material of V Russian scientific and technical conference "Urgent problems of civil engineering", Novosibirsk:NGASU (Sibstrin), Vol.2, p. 100-105, 2012.

BUGAKOVA, T. YU., VOVK, I.G., *Mathematical simulation of systems spatio-temporal variations by geometric properties,* VIII International scientific congress, 10-20 April, 2012. Novosobirsk:International scientific conference "Geodesy, geomatics, cartography, mine survey", collected materials, Novosibirsk: SSGA,Vol.3, p. 26 – 31, 2012.

BUGAKOVA, T. YU., VOVK, I.G., *Mathematical simulation of systems spatio-temporal variations by geometric properties, and anthropogenic risk estimation by exponential smoothing,* Vestnik SSGA, Issue 4, p. 47-58, 2012.

VOVK, I.G., *Mathematical simulation in applied geomatics,* Vestnik SSGA, Novosibirsk: SSGA, Issue 1(17), p. 94 – 103, 2012.

VOVK, I.G., BUGAKOVA, T. YU., *Theory of technogenic geodynamic risk determination for engineering systems spatio-temporal state*, Geo-Siberia-2010, collected material of V International congress "Geo-Siberia-2010", Novosibirsk: SSGA, Vol. 1, part 2, p. 21-24, 2010.

VOVK, I.G., *Modeling in applied geomatics,* Vestnik SSGA, Issue 1(14), p.69 -75, 2011.

VOVK, I.G., *Shape modeling and size estimation of systems in applied geomatics*, Vestnik SSGA, № 2 (22), p.17-25, 2013.

VOVK, I.G., *Determination of geometric invariants of spatial curve in applied geomatics*, Vestnik SSGA, Issue 3(19), p. 51-62, 2011.

VOVK, I.G., *Determination of geometric invariants of surface in applied geomatics,* Vestnik SSGA, Issue 4(20), p. 59-69, 2012.

VOVK, I.G., *System-target approach in applied geomatics*, Vestnik SSGA, Issue 2 (18), p. 115-124, 2012.

BUGAKOVA, T.YU., *Problem of geoengineering systems risk evaluation by geodetic data*, Interexpo Geo-Siberia -2011, Vol.1, № -1, p. 151-157, 2011.

BUGAKOVA, T. YU., VOVK, I.G., *Determination of object rotational motion by results of repeated geodetic measurements*, Interexpo Geo-Siberia- 2013, IX International scientific congress, 15-26 April 2013, Novosibirsk; International scientific conference “Early warning and management under crisis and emergency situations: measures and their realization by means of cartography, geoinformation, GPS and remote sensing”, Novosibirsk, SSGA, p. 88-92, 2013.

LIST OF AUTHORS

Ashraf Abdallah
Institute of Engineering Geodesy, University of Stuttgart
Geschwister-Scholl-Str. 24D
70174 Stuttgart
GERMANY
Phone : + 49 711 68584051
Fax + 49 711 68584044
Email: ashraf.abdallah@ingeo.uni-stuttgart.de
Website: www.uni-stuttgart.de/ingeo

Samira Ahmed
Siberian State University of Geosystems and Technologies
10, Plakhotnogo St.
Novosibirsk, 630108
Russian Federation
Phone: +79537618216
Email: semsem.nosha@yahoo.com

Bara' Al-Mistarehi
Institute of Engineering Geodesy, University of Stuttgart
Geschwister-Scholl Str. 24D, D-70174 Stuttgart, Germany
Phone: +49 (0711) 685-8-4058
Fax: +49 (0711) 685-8-4044
Email: bara.al-mistarehi@ingeo.uni-stuttgart.de

Maxim A. Altyntsev
Siberian State University of Geosystems and Technology
Department of Engineering Geodesy and Mine Surveying
10, Plakhotnogo St.
630108, Novosibirsk
Russian Federation
Phone: +7 9529152980
Email: mnbcv@mail.ru

Evgeny I. Avrunev
Head of the Department of Cadastre and Territorial Planning
Siberian State University of Geosystems and Technology
10, Plakhotnogo Str. Office 106
Novosibirsk, 630108, Russian Federation
Phone: +7 (383) 344-31-73
Email: avrynev_ei@ngs.ru

Tatyana Yu. Bugakova
Siberian State University of Geosystems and Technology
Department of Applied Informatics and Information Systems
10, Plakhotnogo St.
Novosibirsk, 630018
Russian Federation
Phone: +7(383)343-18-53
Email: Bugakova-TU@yandex.ru

Alexander Yu. Chermoshentsev
Siberian State University of Geosystems and Technologies
Department of Physical Geodesy and Remote Sensing
10, Plakhotnogo St.
630108, Novosibirsk
Russian Federation
Phone: +79607985506
Email: fdz2004@gmail.com

Julia Diekert
Institute of Applied Research, University of Applied Sciences Karlsruhe (HSKA)
Molkestr. 30, 76133 Karlsruhe, Germany
Phone: +49 (0721) 925-2329
Email: julia.diekert@hs-karlsruhe.de

AlexeyV. Dubrovsky
Siberian State University of Geosystems and Technology
Department of Cadastre and Territorial Planning
10, Plakhotnogo St.
Novosibirsk, 630108
Russian Federation
Phone: +7 9529235141
Email: avd5@mail.ru

Sergey R. Gorobtsov,
Siberian State University of Geosystems and Technologies
Department of Cadastre and Territorial Planning
10, Plakhotnogo St.
Novosibirsk, 630108
Russian Federation
Phone: +7 913 471 55 67
Email: sergey.gorobtsov@mail.ru

Ekaterina I. Gorokhova
Siberian State University of Geosystems and Technologies
Department of Engineering Geodesy and Mine Surveying
10, Plakhotnogo St.
Novosibirsk, 630108
Russian Federation
Phone: +7 (383) 343-29-55
Email: e.gorohova@ssga.ru

Andrei V. Ivanov
Siberian State University of Geosystems and Technology
Department of Engineering Geodesy and Mine Surveying
10, Plakhotnogo St.
630108, Novosibirsk
Russian Federation
Phone: +7(913)893-35-36
Email: geoid@ngs.ru

Reiner Jäger
Institute of Geomatics at IAF/HSKA
University of Applied Sciences Karlsruhe
Moltkestr. 30
76133 Karlsruhe
Germany
Phone: +49(0)7219252620, -2598
Fax: +49(0)721-9252597
E-mail: reiner.jaeger@hs-karlsruhe.de
Website: www.goca.info

Stephanie Kauker
Institute of Engineering Geodesy, University of Stuttgart
Geschwister-Scholl Str. 24D, D-70174 Stuttgart, Germany
Phone: +49 (0711) 685-84068
Fax: +49 (0711) 685-84044
Email: stephanie.kauker@ingeo.uni-stuttgart.de

Olesya I. Malygina
Siberian State University of Geosystems and Technology
Department of Cadastre and Territorial Planning
10, Plakhotnogo St.
Novosibirsk, 630108
Russian Federation
Phone: +7 9133729326
Email: 131379@mail.ru

Boris Mazurov
Siberian State University of Geosystems and Technologies
Department of Physical Geodesy and Remote Sensing
10, Plakhotnogo St.
Novosibirsk, 630108
Russian Federation
Phone: +79139137399
Email: btmazurov@mail.ru

Sergey G. Mogilny
Prydniprovs'ka State Academy of Civil Engineering and Architecture
Department of Land Management, Road-Building and Geodesy
24a, Chernyshevs’kogo St.
Dnipropetrovs’k, 49600
Ukraine
Phone: +38(050)6064354
Email: mogilnysg@mail.ru

Vyacheslav N. Nikitin
Siberian State University of Geosystems and Technologies
Department of Physical Geodesy and Remote Sensing
10, Plakhotnogo St.
630108, Novosibirsk
Russian Federation
Phone: +79137123750
Email: vslav.nikitin@gmail.com

Annette Schmitt,
Institute of Engineering Geodesy, University of Stuttgart
Geschwister-Scholl Str. 24D, D-70174 Stuttgart, Germany
Phone: +49 (0711) 685 84065
Fax: +49 (0711) 685 84065
Email: annette.schmitt@ingeo.uni-stuttgart.de

Volker Schwieger,
Institute of Engineering Geodesy, University of Stuttgart
Geschwister-Scholl Str. 24D, D-70174 Stuttgart, Germany
Phone: +49 (0711) 685-84040
Fax: +49 (0711) 685-84044
Email: volker.schwieger@ingeo.uni-stuttgart.de

Andrii A. Sholomytskyi
Siberian State University of Geosystems and Technologies
Department of Engineering Geodesy and Mine Surveying
10, Plakhotnogo St.
Novosibirsk, 630108
Russian Federation
Phone: +7(913)373-07-51
Email: sholomitskij@mail.ru

Andrey V. Sementsov
Siberian State University of Geosystems and Technologies
10, Plakhotnogo St.
630108, Novosibirsk
Russian Federation
Phone:+79607790679
Email: andsemencov@mail.ru

Alexander V. Seredovich
Siberian State University of Geosystems and Technology
Department of Engineering Geodesy and Mine Surveying
10, Plakhotnogo St.
630108, Novosibirsk
Russian Federation
Phone: +7(913)987-07-42
Email: alexanders04@mail.ru

Vladimir A. Seredovich
Vice Rector for Scientific and Innovative Activities
Siberian State University of Geosystems and Technology
10, Plakhotnogo Str. Office 106
Novosibirsk, 630108, Russian Federation
Phone: + 7 (383) 343 39 57,
Fax: + 7 (383) 344-30-60
Email: v.seredovich@llst.ru

Mariya M. Shlyakhova
Siberian State University of Geosystems and Technology
Department of Applied Informatics and Information Systems
10, Plakhotnogo St.
Novosibirsk, 630018
Russian Federation
Phone: +7(383)343-18-53Email: plazma_space@mail.ru

Desislava Staykova
technet-rail 2010 GmbH
Goethestrasse 42
10625 Berlin
Germany
Phone: +49 (030)54840785
Fax: +49 (030)54826798
Email: desi.staikova@technet-rail.de
Web site: www.technet-rail.de

Dmitry N. Vetoshkin
Director of the Institute of Cadastre and Environmental Management
Siberian State University of Geosystems and Technologies
10, Plakhotnogo St.
Novosibirsk, 630108
Russian Federation
Phone: +7 952 938 73 75
Email: dmitry.vetoshkin@gmail.com

Igor G. Vovk
Siberian State University of Geosystems and Technology
Department of Applied Informatics and Information Systems
10, Plakhotnogo St.
Novosibirsk, 630108
Russian Federation
Phone: +7 (383)351-61-19
Email: kaf.pi@ssga.ru

Fawzi Zarzoura
Public Works Department (Surveying)
Faculty of Engineering
Mansoura University
Mansoura
EGYPT
Phone: +79658238189
Email: fawzyhamed2011@yahoo.com

Li Zhang
Institute of Engineering Geodesy
University of Stuttgart
Geschwister-Scholl Str. 24D
70174 Stuttgart
Germany
Phone: +49(0)71168584049
Fax: +49(0)71168584044
Email: li.zhang@ingeo.uni-stuttgart.de

Lifan Zhang
University of Stuttgart
Master Program Geodesy and Geoinformatics
Keplerstrasse 7
D-70174 Stuttgart
GERMANY
Phone: +49 176 41619133
Email: zhanglf_1989@126.com

Wei Zhang
University of Stuttgart
Master Program Geodesy and Geoinformatics
Keplerstrasse 7
D-70174 Stuttgart
GERMANY
Phone: +49 176 41551743
Email: zw158535165@gmail.com

Bimin Zheng,
Institute of Engineering Geodesy
University of Stuttgart
Geschwister-Scholl Str. 24D
70174 Stuttgart
Germany
Phone.: +49(0)71168584061
Fax: +49(0)71168584044
Email: bimin.zheng@ingeo.uni-stuttgart.de

Nico Zill
technet-rail 2010 GmbH
Goethestraße 42
10625 Berlin
Phone: +49 (0) 30 89616941
Fax: +49 (0) 30 54826798